

Lateral-Directional Static and Dynamic Stability Analysis at High Angles of Attack for the X-31 Configuration

by

Jose Rafael Villeta

B.S. Aeronautical Engineering, May 1990
Massachusetts Institute of Technology

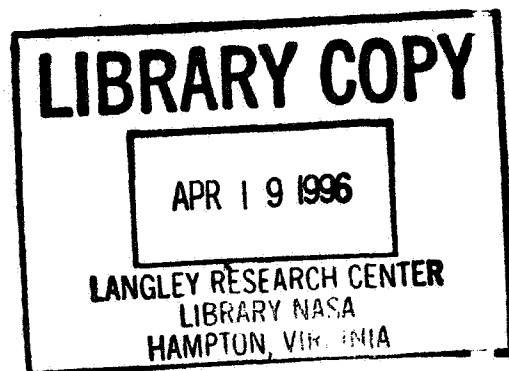
A thesis submitted to the faculty of
the School of Engineering and Applied Sciences of
The George Washington University in partial satisfaction of
the requirements for the degree of Master of Science

August 1992

Thesis directed by
Dr. Vladislav Klein

Professor of Engineering and Applied Sciences

This research was conducted at
NASA Langley Research Center



ABSTRACT

Wind-tunnel and Drop model flight data were analyzed to document the lateral-directional static and dynamic characteristics of the X-31 configuration at high angles of attack. Special emphasis was given to the analysis of the lateral-directional dynamic instabilities exhibited by this configuration, in particular, wing rock and high incidence kinematic roll (HIKR) departure. Results showed that wing rock for the X-31 configuration was triggered by the interaction of forebody flow with the forward fuselage and sustained by poor roll damping characteristics coupled with strong lateral static stability and nonlinear sideslip effect on rolling moment. A nonlinear simulation based on wind-tunnel data accurately predicted wing rock motions at high angles of attack. Without lateral-directional stability augmentation, as the angle of attack increased, the wing rock motions became divergent and the X-31 configuration exhibited a HIKR departure. Data analysis showed that a reversal from restoring to propelling rolling moment at sideslip angles larger than 30° was the cause for HIKR departure. A high-gain roll damper, implemented on the Drop model Flight Control System, demonstrated the viability of this control augmentation approach to suppress the wing rock and the HIKR departure.

ACKNOWLEDGEMENTS

The author wishes to thank the NASA Langley Research Center for providing the opportunity to perform this research. Mr. Mark A. Croom and Mr. Luat T. Nguyen deserve special recognition for their assistance and guidance during the conduct of these studies. Appreciation and special thanks go to Dr. Vladislav Klein who acted as academic advisor, Mr. Stanley H. Husch for his exceptional work in preparing the figures, and the colleagues of the Flight Dynamics Branch for their great support. Last, but not least, the author wishes to thank his family that without their love and support, this work would not have been possible.

TABLE OF CONTENTS

	Page
ABSTRACT.....	i
ACKNOWLEDGEMENTS.....	ii
TABLE OF CONTENTS.....	iii
LIST OF TABLES.....	v
LIST OF FIGURES.....	vi
LIST OF SYMBOLS.....	xi
 Chapter	
1.0 INTRODUCTION.....	1
2.0. BACKGROUND.....	3
2.1 Previous Investigations.....	3
2.2 Wing Rock Theory.....	11
3.0 TEST METHODS.....	15
3.1 Description of Models.....	15
3.2 Captive Wind-tunnel Tests.....	16
3.2.1 Static-Force Test.....	16
3.2.2 Forced-Oscillation Test.....	17
3.2.3 Rotary Balance Test.....	17
3.2.4 Free-to-Roll Test.....	18
3.3 Drop Model Test.....	19
3.4 Nonlinear Math Modeling.....	20
4.0 RESULTS AND DISCUSSION.....	21
4.1 Captive Test Results.....	21
4.1.1 Longitudinal Static Stability and Control.....	21
4.1.2 Lateral-Directional Static Stability and Control.....	23
4.1.3 Lateral-Directional Dynamic Stability.....	29

4.1.3.1	Forced-Oscillation Results.....	29
4.1.3.2	Rotary Balance Test Results.....	32
4.1.3.3	Free-to-Roll Results.....	33
4.1.3.3.1	Wing Rock Characteristics.....	34
4.1.3.3.2	HIKR Departure Characteristics.....	40
4.2	Drop Test Results.....	44
4.2.1	Data Analysis System.....	44
4.2.2	Wing Rock Test.....	45
4.2.2.1	Wing Rock Characteristics (Open Loop).....	45
4.2.2.2	Wing Rock Suppression Techniques.....	49
4.2.3	HIKR Departure Test.....	51
4.3	Nonlinear Simulation Results.....	55
5.0	CONCLUSIONS/RECOMMENDATIONS.....	58
5.1	Conclusions.....	58
5.2	Recommendations for Further Study.....	61
	REFERENCES.....	62
	APPENDIX	
A. -	BLOCK DIAGRAMS FOR NONLINEAR SIMULATION.....	66
B. -	DROP MODEL DATA ANALYSIS SYSTEM- PROGRAM LISTING.....	71
C. -	LINEAR 3 D.O.F. LATERAL-DIRECTIONAL MATH MODEL.....	88
	TABLES.....	90
	FIGURES.....	97

LIST OF TABLES

TABLE I. X-31 Mass and Geometric Characteristics.....	91
TABLE II. Scale Factors for Dynamic Models.....	92
TABLE III. Summary of Qualitative Free-To-Roll Results.....	93
TABLE IV. Wing Rock Free-To-Roll Characteristics.....	94
TABLE V. Wing Rock Simulation Characteristics.....	95
TABLE VI. Wing Rock Comparison.....	96

LIST OF FIGURES

Figure 1.	Wing Rock Suppression on the Handley Page aircraft.....	9 8
Figure 2.	Wing Rock on the F-4 aircraft	9 9
Figure 3.	Low Speed Wing Rock on the F-5 aircraft.....	1 0 0
Figure 4.	Frequency and Amplitude Effect on Roll Damping for the F-5 aircraft.....	1 0 1
Figure 5.	F-5 Wing Planforms Tested on NASA Wind-tunnel.....	1 0 2
Figure 6.	Roll Damping for the F-5 Wing Planforms.....	1 0 2
Figure 7.	Wing Rock Onset α for the Gnat aircraft.....	1 0 3
Figure 8.	Effect of Wing Fences on the Harrier aircraft.....	1 0 4
Figure 9.	Wing Rock on the HIRM model.....	1 0 5
Figure 10.	Wing Rock Envelope for the F-14 aircraft.....	1 0 6
Figure 11.	Wing Rock Build Up for the 80° Delta Wing.....	1 0 7
Figure 12.	Roll Damping Variation with Sideslip for the 80° Delta Wing.....	1 0 7
Figure 13.	Vortex Patterns for the 80° Delta Wing.....	1 0 8
Figure 14.	Comparison of one D.O.F. Results for the 80° Delta Wing.....	1 0 8
Figure 15.	Forebody Study for a Generic Fighter Model.....	1 0 9
Figure 16.	Wing Rock on the X-29 Drop Model.....	1 1 0
Figure 17.	Roll Damper Effect on Wing Rock for the X-29.....	1 1 1
Figure 18.	Wing Rock on the F-18 aircraft.....	1 1 2
Figure 19.	X-31 Full-scale aircraft.....	1 1 3
Figure 20.	X-31 13.3-percent-scale Model.....	1 1 3
Figure 21.	X-31 19-percent-scale Model.....	1 1 4
Figure 22.	X-31 27-percent-scale Drop Model.....	1 1 4
Figure 23.	X-31 Full-Scale 3-D Configuration Sketch.....	1 1 5
Figure 24.	System of Axes.....	1 1 6

Figure 25.	Forced-Oscillation Test Setup on Roll.....	117
Figure 26.	Rotary Balance Test Setup.....	117
Figure 27.	Free-to-Roll Test Setup.....	118
Figure 28.	Drop Model Operation at NASA Plum Tree Test Facility.....	119
Figure 29.	Drop Model Flight Control System.....	120
Figure 30.	Canard Effect on Longitudinal Characteristics.....	121
Figure 31.	Trailing-edge Flap Effect on Longitudinal Characteristics.....	122
Figure 32.	Maximum Nose-up and Nose-down Controls.....	123
Figure 33.	Sideslip Effect on Lift and Pitching Moment.....	124
Figure 34.	Large Sideslip Effect on Lift and Pitching Moment.....	126
Figure 35.	Canard Effect on Lateral-Directional Static Stability.....	127
Figure 36.	Flaps Effect on Lateral-Directional Static Stability.....	128
Figure 37.	J13 Noseboom Effect on Directional Static Stability.....	129
Figure 38.	Canard Effect on Lateral-Directional Characteristics.....	130
Figure 39.	Lateral Control Power for Trailing-edge Flaps Differential	131
Figure 40.	Directional Control Power for Rudder.....	132
Figure 41.	Sideslip Effect on Rolling and Yawing Moments.....	133
Figure 42.	Large Sideslip Effect on Rolling Moment.....	136
Figure 43.	Longitudinal Control Effects on Dynamic Directional Stability.....	138
Figure 44.	Aileron Rudder Interconnect Gain Effect on LCDP.....	139
Figure 45.	Departure and Spin Susceptibility Criteria.....	140
Figure 46.	Canard Effect on Yaw Damping.....	141
Figure 47.	Frequency Effect on Roll Damping.....	142
Figure 48.	Amplitude Effect on Roll Damping.....	142
Figure 49.	J13 Noseboom Effect on Roll Damping.....	143
Figure 50.	Canard Effect on Roll Damping.....	143

Figure 51.	M86 Body Strake Effect on Roll Damping.....	144
Figure 52.	Leading-edge Flaps Effect on Roll Damping.....	144
Figure 53.	Trailing-edge Flaps Effect on Roll Damping.....	145
Figure 54.	Vertical Tail Effect on Roll Damping.....	146
Figure 55.	Moment Slope Criteria for the Rotary Balance Test data....	146
Figure 56.	Sideslip Effect on Rolling Moment from Rotary Balance Test.....	147
Figure 57.	Normalized Sideslip Effect on Roll Damping from Rotary Balance Test Data.....	149
Figure 58.	Wing Rock Suppression Body Strakes Location.....	149
Figure 59.	Wing Rock Flow Visualization Results.....	150
Figure 60.	Free-to-Roll Results for $\theta_{\text{sting}} = 28^\circ$	151
Figure 61.	Free-to-Roll Results for $\theta_{\text{sting}} = 30^\circ$	152
Figure 62.	Free-to-Roll Results for $\theta_{\text{sting}} = 32^\circ$	153
Figure 63.	Energy Exchange Effect on Rolling Moment.....	154
Figure 64.	Roll and Sideslip Angle Effects on Rolling Moment	154
Figure 65.	Roll Rate Effect on Rolling Moment for $\theta_{\text{sting}} = 32^\circ$	155
Figure 66.	Phase Plane Theoretical Diagram.....	156
Figure 67.	Phase Plane Diagram for $\theta_{\text{sting}} = 32^\circ$	157
Figure 68.	Free-to-Roll Results for $\theta_{\text{sting}} = 45^\circ$	158
Figure 69.	HIKR Departure Characteristics from the Free-to-Roll Tests.....	159
Figure 70.	Static Rolling Moment Dependence with Roll Angle.....	160
Figure 71.	HIKR Departure Characteristics from the Static-Force Tests.....	161
Figure 72.	HIKR Departure Flow Visualization Results.....	162
Figure 73.	Wing Rock Drop Test Results.....	164

Figure 74.	Wing Rock Drop Test Results.....	165
Figure 75.	Wing Rock Drop Test Results.....	166
Figure 76.	Wing Rock Drop Test Results.....	167
Figure 77.	Wing Rock Drop Test Results.....	168
Figure 78.	Wing Rock Drop Test Results.....	169
Figure 79.	Wing Rock Drop Test Results.....	170
Figure 80.	Wing Rock Drop Test Results.....	171
Figure 81.	Wing Rock Drop Test Results.....	172
Figure 82.	Wing Rock Drop Test Results.....	173
Figure 83.	Wing Rock Drop Test Results.....	174
Figure 84.	Wing Rock Drop Test Results.....	175
Figure 85.	Wing Rock Drop Test Results.....	176
Figure 86.	Wing Rock Suppression Results from X-31 Free-Flight Test.....	177
Figure 87.	Roll Damper Gain Variation Effect on Wing Rock	178
Figure 88.	HIKR Departure Drop Test Results.....	179
Figure 89.	HIKR Departure Drop Test Results.....	180
Figure 90.	HIKR Departure Drop Test Results.....	181
Figure 91.	HIKR Departure Drop Test Results.....	182
Figure 92.	HIKR Departure Drop Test Results.....	183
Figure 93.	HIKR Departure Drop Test Results.....	184
Figure 94.	HIKR Departure Drop Test Results.....	185
Figure 95.	HIKR Departure Drop Test Results.....	186
Figure 96.	HIKR Departure Drop Test Results.....	187
Figure 97.	HIKR Departure Drop Test Results.....	188
Figure 98.	HIKR Departure Drop Test Results.....	189
Figure 99.	Nonlinear Simulation Results for $\theta_{\text{sting}} = 28^\circ$	190

Figure 100. Nonlinear Simulation Results for $\theta_{\text{sting}} = 28^\circ$	191
Figure 101. Nonlinear Simulation Results for $\theta_{\text{sting}} = 28^\circ$	192
Figure 102. Nonlinear Simulation Results for $\theta_{\text{sting}} = 30^\circ$	193
Figure 103. Nonlinear Simulation Results for $\theta_{\text{sting}} = 30^\circ$	194
Figure 104. Nonlinear Simulation Results for $\theta_{\text{sting}} = 30^\circ$	195
Figure 105. Nonlinear Simulation Results for $\theta_{\text{sting}} = 32^\circ$	196
Figure 106. Nonlinear Simulation Results for $\theta_{\text{sting}} = 32^\circ$	197
Figure 107. Nonlinear Simulation Results for $\theta_{\text{sting}} = 32^\circ$	198

LIST OF SYMBOLS

a_x	longitudinal acceleration, positive along positive X axis, g units
a_y	lateral acceleration, positive along positive Y axis, g units
a_z	normal acceleration, positive along positive Z axis, g units
b	wing span, ft
C_D	drag coefficient, $\frac{\text{Aerodynamic drag force}}{\bar{q}S}$
C_ϕ	histogram curve of $C_{l_{aero}}$ versus ϕ
C_L	lift coefficient, $\frac{\text{Aerodynamic lift force}}{\bar{q}S}$
C_l	total rolling moment coefficient
$C_{l_{aero}}$	rolling-moment coefficient about X body axis, $\frac{\text{Aerodynamic rolling moment}}{\bar{q}Sb}$
C_{ld}	dynamic rolling moment coefficient
C_{lic}	rolling moment coefficient due to inertia coupling, $\frac{(I_{yy}-I_{zz})qr}{\bar{q}Sb}$
C_{licx}	rolling moment coefficient due to inertia cross coupling, $\frac{I_{xz}(pq+r)}{\bar{q}Sb}$
$\overline{C_{lp}}$	$C_{lp}+C_{lp}\sin \alpha$, roll damping obtained from Forced-Oscillation test
$\overline{C_{lr}}$	$C_{lr}-C_{lp}\cos \alpha$, yaw rate effect on roll obtained from Forced-Oscillation test
C_{ls}	static rolling moment coefficient
C_m	total pitching moment coefficient
$C_{m_{aero}}$	pitching moment coefficient about Y body axis, $\frac{\text{Aerodynamic pitching moment}}{\bar{q}Sc}$

$C_{m_{ic}}$	pitching moment coefficient due to inertia coupling, $\frac{(I_{zz}-I_{xx})pr}{\bar{q}S\bar{c}}$
$C_{m_{icx}}$	pitching moment coefficient due to inertia cross coupling, $\frac{I_{xz}(r^2-p^2)}{\bar{q}S\bar{c}}$
C_n	total yawing moment coefficient
$C_{n_{aero}}$	yawing moment coefficient about Z axis, $\frac{\text{Aerodynamic yawing moment}}{\bar{q}Sb}$
$C_{n_{ic}}$	yawing moment coefficient due to inertia coupling, $\frac{(I_{xx}-I_{yy})pq}{\bar{q}Sb}$
$C_{n_{icx}}$	yawing moment coefficient due to inertia cross coupling, $\frac{I_{xz}(\dot{p}-qr)}{\bar{q}Sb}$
$\overline{C_{n_p}}$	$C_{n_p}+C_{n_{\beta}}\sin \alpha$, roll rate effect on yaw obtained from Forced-Oscillation test
$\overline{C_{n_r}}$	$C_{n_r}-C_{n_{\beta}}\cos \alpha$, yaw damping obtained from Forced-Oscillation test
C_X	total X-axis force coefficient along positive X body axis
C_Y	total Y-axis force coefficient along positive Y body axis
$\overline{C_{Y_p}}$	$C_{Y_p}+C_{Y_{\beta}}\sin \alpha$, roll rate effect on side force obtained from Forced-Oscillation test
$\overline{C_{Y_r}}$	$C_{Y_r}-C_{Y_{\beta}}\cos \alpha$, yaw rate effect on side force obtained from Forced-Oscillation test
C_Z	total Z-axis force coefficient along positive Z body axis
\bar{c}	wing mean aerodynamic chord, ft
f	frequency of oscillation, Hz
g	acceleration due to gravity, 1 g = 32.2 ft/sec ²
h	altitude, ft
I_{XX}, I_{YY}, I_{ZZ}	moments of inertia about X, Y and Z body axes, slug-ft ²

I_{xz}	product of inertia with respect to X and Z body axes, slug-ft ²
K_{ARI}	Aileron Rudder Interconnect gain
k	reduced frequency, $\frac{\pi fb}{V}$
M	Mach number
N	model-to-airplane scale ratio
m	airplane mass, slugs
P	period, seconds
P_{stk}	roll stick, -1 (full left roll) to 1 (full right roll) unit
p	roll rate about X body axis, deg/sec
\dot{p}	roll acceleration about X body axis, deg/sec ²
\bar{q}	dynamic pressure, $\frac{\rho V^2}{2}$, lb/ft ²
q_{stk}	pitch stick, -1 (full pitch down) to 1 (full pitch up) unit
q	pitch rate about Y body axis, deg/sec
\dot{q}	pitch acceleration about Y body axis, deg/sec ²
Re	Reynolds number, $\frac{V\rho\bar{c}}{\mu}$
r_{stk}	yaw stick, -1 (full left yaw) to 1 (full right yaw) unit
r	yaw rate about Z body axis, deg/sec
\dot{r}	yaw acceleration about Z body axis, deg/sec ²
S	wing area, ft ²
t	time, seconds
u, v, w	components of airplane velocity along X, Y and Z axes, ft/sec
WEIGHT	airplane weight, lb
V	airplane resultant velocity, ft/sec
X, Y, Z	airplane body axes (c.f., Figure 23)
α	angle of attack, deg

$\dot{\alpha}$	time rate of change of angle of attack, deg/sec
β	angle of sideslip, deg
$\dot{\beta}$	time rate of change of sideslip angle, deg/sec
ΔC_l	incremental rolling moment coefficient
ΔC_n	incremental yawing moment coefficient
ΔC_Y	incremental side force coefficient
$\Delta \phi$	roll angle amplitude, deg
ΔE	energy exchange
δ_c	canard deflection, deg
δ_{fLE}	leading-edge flap deflection, deg
$\delta_{fTEDIFF}$	trailing-edge flap differential deflection, deg
$\delta_{fTESYMM}$	trailing-edge flap symmetric deflection, deg
δ_r	rudder deflection, deg
ϕ	roll Euler angle, deg
$\dot{\phi}$	rate of roll angle, deg/sec
$\ddot{\phi}$	acceleration of roll angle, deg/sec ²
μ	coefficient of viscosity, lb/ft-sec
ν	kinematic viscosity, ft ² /sec
θ	pitch Euler angle, deg
θ_{sting}	angle between fuselage center line and wind, deg
ρ	air density, lb/ft ³
σ	ratio of air density to sea-level density
Ω	total angular velocity, rad/sec
ψ	yaw Euler angle, deg
ζ	damping coefficient

Stability and Control Derivatives

$$C_{Y_p} = \frac{\partial C_Y}{\partial \frac{pb}{2V}}$$

$$C_{Y_r} = \frac{\partial C_Y}{\partial \frac{rb}{2V}}$$

$$C_{Y_{\dot{\beta}}} = \frac{\partial C_Y}{\partial \frac{\dot{\beta}b}{2V}}$$

$$C_{l_p} = \frac{\partial C_l}{\partial \frac{pb}{2V}}$$

$$C_{l_r} = \frac{\partial C_l}{\partial \frac{rb}{2V}}$$

$$C_{l_{\delta r_{TEDIFF}}} = \frac{\partial C_l}{\partial \delta r_{TEDIFF}} \quad C_{l_{\dot{\delta r}}} = \frac{\partial C_l}{\partial \dot{\delta r}}$$

$$C_{n_p} = \frac{\partial C_n}{\partial \frac{pb}{2V}}$$

$$C_{n_r} = \frac{\partial C_n}{\partial \frac{rb}{2V}}$$

$$C_{n_{\delta r_{TEDIFF}}} = \frac{\partial C_n}{\partial \delta r_{TEDIFF}} \quad C_{n_{\dot{\delta r}}} = \frac{\partial C_n}{\partial \dot{\delta r}}$$

$$C_{l_{\beta}} = \frac{\partial C_l}{\partial \beta}$$

$$C_{n_{\beta}} = \frac{\partial C_n}{\partial \beta}$$

$$C_{n_{\beta, dyn}} = C_{n_{\beta}} \cos \alpha - \frac{I_{ZZ}}{I_{XX}} C_{l_{\beta}} \sin \alpha$$

$$C_{l_{\Omega}} = \frac{\partial C_l}{\partial \frac{\Omega b}{2V}}$$

$$C_{l_d} = \overline{C_{l_p}} \frac{C_{l_{\Omega}}(\beta)}{C_{l_{\Omega}}(\beta=0)}$$

$$C_{l_{\dot{\beta}}} = \frac{\partial C_l}{\partial \frac{\dot{\beta}b}{2V}}$$

$$C_{n_{\dot{\beta}}} = \frac{\partial C_n}{\partial \frac{\dot{\beta}b}{2V}}$$

Subscripts

CMD	command value
CPT	control position transducer (i.e., surface position)
dr	Dutch Roll
max	maximum value
o	initial value
wr	Wing Rock
sting	referenced to the Free-to-Roll wind-tunnel setup

Abbreviations

c.g.	center of gravity
D.O.F.	degree of freedom
FCSMODE	flight control system mode
F2 ϕ	Free-to-Roll tests
HIKR	high incidence kinematic roll
LCDP	lateral control divergence parameter
L.E.D.	leading-edge down
SIM	simulation
T.E.D.	trailing-edge down
T.E.L.	trailing-edge left
T.E.R.	trailing-edge right
T.E.U.	trailing-edge up

1.0 INTRODUCTION

New agility requirements are being placed on fighters bringing additional maneuverability considerations into the mission design goals (Reference 1). The ability to expand the flight envelope of future combat fighter aircraft requires an in-depth understanding of high angle-of-attack aerodynamics and aircraft maneuverability demands. Aircraft flying at high angles of attack have encountered static and dynamic stability and control problems. In particular, many fighters have encountered moderate to severe lateral-directional instabilities such as wing rock and nose slice departures. Therefore, to alleviate these undesirable flight characteristics, it is imperative to understand the triggering and driving mechanisms behind these instabilities.

This study provides the methodology to better understand the lateral-directional characteristics of a given configuration, the X-31. Special emphasis was given to the lateral-directional dynamic instabilities exhibited by this configuration, in particular, wing rock and high incidence kinematic roll (HIKR) departure. Wind-tunnel tests, including Static-Force, Forced-Oscillation and dynamic Free-to-Roll tests, were conducted at the NASA Langley Research Center with several scale models of the X-31 configuration. From the Static-Force tests, the lateral-directional static stability and control characteristics were obtained and analyzed. The lateral-directional dynamic stability derivatives were obtained from the Forced-Oscillation tests. From the Free-to-Roll tests, the wing rock characteristics were obtained, and the triggering and driving flow mechanisms causing wing rock were shown using different flow

visualization techniques. Using the data from the wind-tunnel force tests, a nonlinear, one D.O.F. math model was constructed to predict the wing rock and HIKR departure characteristics on the X-31. These predictions were compared to the results from the wind-tunnel dynamic Free-to-Roll tests and from the analysis of the X-31 Drop model flight data. Aerodynamic body strakes and a roll damper control law were tested to suppress wing rock motions on the X-31 configuration.

2.0 BACKGROUND

2.1 Previous Investigations

Studies of the wing rock phenomenon have been conducted for more than half a century. One of the first wing rock research studies was done at the NASA Langley Research Center around the late 1940's by McKinney and Drake on slender delta wings (Reference 2). Free-flight experiments showed that these slender delta wings were susceptible to large amplitude undamped roll oscillations at moderate angles of attack well below the stall region. Since this initial study, several other investigations were conducted (Reference 3, 4, and 5), but it was only within the last decade that a clearer understanding of the nonlinear aerodynamics and the flow triggering mechanisms was established. In 1961, the British research aircraft Handley Page 115 first flew and exhibited a roll oscillation building up to a limit cycle of 30° roll. The Royal Aircraft Establishment (RAE) study stated that the wing rock behavior was due to an undamped Dutch roll oscillation at high angles of attack (Reference 6). Moreover, this research showed "the effects of nonlinearities in static sideslip data on limiting the amplitude of the diverging oscillation to give wing rock" (Reference 7). Recovery from this motion, as seen in Figure 1 from Reference 7, was achieved by lowering the angle of attack or by driving the aileron against the roll oscillations. In the 1960's, the McDonnell Douglas F-4 high angle-of-attack flight studies concentrated primarily on yaw divergence and spin characteristics. These studies showed that the F-4 experienced wing rock followed by a nose slice departure (Reference 8). In Figure 2 from Reference 7, flight time histories of the F-4 at 25,000

feet and $M = 0.4$ show wing rock and spin motions. Notice that the entry to these motions was a combined rolling and pitching up maneuver. As the angle of attack increased, rolling oscillations began and their amplitudes increased until the wing rock motions diverged into yawing motions that build up into a spin. Again, in Reference 9, it was concluded that the wing rock was caused primarily by an unstable Dutch roll oscillation. Although it was concluded from the HP-115 and F-4E studies that wing rock is caused by an unstable Dutch roll, it cannot be generalized for all aircraft configurations because the Dutch roll response can be derived in a linear aerodynamic model whereas the wing rock phenomenon consists of nonlinear aerodynamics. Other studies showed that the wing rock characteristics depend greatly on configuration geometry and flow interaction over the configuration at high angles of attack specially around the forebody region. For example, changing the configuration geometry of the F-4 by adding leading-edge slats was shown to cause a delay in the wing rock onset angle of attack (Reference 10).

Another example of the effect that wing rock can have on the lateral-directional stability of an aircraft can be seen on the Northrop T-38A aircraft. During a 1-g deceleration, the T-38A experienced moderate-to-heavy airframe buffet and wing rock with an amplitude of up to 20° roll with no heading excursions (i.e., no nose wandering). Because the T-38A is control limited longitudinally, the aircraft will not enter full stall and post stall flight regimes. This allowed easy recovery from moderate wing rock by lowering the aircraft angle of attack or increasing afterburner thrust (Reference 11). Nevertheless, if flight envelope expansion is required to enhance agility and combat effectiveness, longitudinal control limitation is

undesirable. Therefore, modern fighters need to have stable lateral-directional stability characteristics through the stall and post stall regions. If lateral-directional stability is lost, it is possible to encounter an immediate departure from controlled flight unless the pilot response is quick enough to lower the aircraft angle of attack below the stall region. Moreover, this behavior in a landing approach would be disastrous. Examples of aircraft prone to directional departure are the Vought A-7 and F-8 series.

Around the late 1960's, more attention was given to combat aircraft design due to a high number of stall/spin out-of-control accidents. The lessons learned from the T-38A flight test helped in the design of the Northrop F-5. Its forebody was designed primarily to improve the lateral-directional static stability characteristics. The final design of the F-5 forebody showed excellent lateral-directional static stability characteristics. To alleviate wing rock on the F-5, the final forebody design was improved by reducing the nose apex angle, which lead to the shark nose design on some aircraft in the F-5 series. The shark nose, in conjunction with the wing-root leading-edge extension (LEX), proved to be a noteworthy wing rock suppression technique on the F-5 series (Reference 12). During flight test, the F-5 experienced two different types of wing rock. One type of wing rock occurred at low speeds and high angle of attack ($\alpha > 30^\circ$) with large amplitude roll oscillations as seen in the 1-g stall flight time histories of Figure 3. It was found that the observed wing rock, through inertia and kinematic coupling, will increase the angle of attack and can cause a departure from controlled flight (Reference 13). The second type of wing rock occurred at higher speeds ($M > 0.8$) but at a

lower angle of attack ($\alpha = 10^\circ$) with smaller amplitude roll oscillations. Data from the Forced-Oscillation tests (c.f., Figure 4 from Reference 14) of the F-5 showed that the roll damping parameter, $\overline{C_{lp}}$, varied at high angle of attack not only with the oscillation frequency but also with oscillation amplitude. Also, the basic F-5 configuration was tested with different wing planforms (c.f., Figure 5). The roll damping data results from the Forced-Oscillation tests on the different wing planforms were astounding. In Figure 6 from Reference 14, the data showed highly unstable roll damping characteristics for $30^\circ < \alpha < 42^\circ$ indicating susceptibility to wing rock. Moreover, the roll damping instability did not appreciably change with the drastically different wing planforms. These results strongly suggest that the wing is not primarily responsible for the roll damping instabilities at high angle of attack. Finally, the data analysis has shown the two types of wing rock experienced by the F-5 are caused by entirely different phenomena. The high speed wing rock is driven "by shock-induced separation, and is a wing-dominated phenomenon". On the other hand, the low speed wing rock is driven "by vortical-flow dynamics, and is a forebody-dominated phenomenon" (Reference 7).

In the 1970's, the RAE expanded its research activities to better understand the buffet and wing rock characteristics of the Gnat aircraft with parallel studies using the British Aerospace Harrier, Panavia Tornado, and two RAE High Incidence Research Models (HIRM) (Reference 7). The Gnat flight test data, as seen in Figure 7 from Reference 15, showed that a Gnat carrying fuel tanks under its wings compared to a Gnat with no tanks experienced a delay in wing rock onset angle of attack. More evidence on

wing geometry and forebody flow interaction effects on wing rock motion was observed on the Harrier. In Figure 8 from Reference 16, Static-Force wind-tunnel tests on a Harrier model showed the effect of wing fence separation distance on rolling moments where lateral unsteadiness was encountered. Notice that well-placed wing fences improved wing rock suppression by reducing lateral oscillations. During the Tornado design phase, it was concluded that wing rock motion should be damped using the flight control system (Reference 7). The HIRM research activities were aimed at mathematically modelling the aerodynamics observed during dynamic wind-tunnel and flight tests. The HIRM planes experienced wing rock and divergent Dutch roll oscillations. One of the most important aspects found in these tests was the coupling characteristic of the motions. If the angle of attack was not controlled (i.e., inactive longitudinal controls), the wing rock motions were highly coupled. On the other hand, when longitudinal controls were used to eliminate angle-of-attack excursions, the wing rock motions were uncoupled as seen in Figure 9 from Reference 7.

Around the same time frame, the NASA embarked on a number of research activities including Static-Force wind-tunnel tests, dynamic Forced-Oscillation wind-tunnel tests, dynamic Free-to-Roll wind-tunnel tests, dynamic Free-Flight wind-tunnel tests, Drop model flight tests, and computer simulations. Special emphasis was given to aerodynamic and control system designs to suppress wing rock motion. The first aircraft family to integrate these newly developed aerodynamic and control designs into their high angle-of-attack control system was the Grumman F-14 fighter series. In Figure 10 from Reference 17, the wing rock region

for the F-14 was indicated as a function of α and M . Notice that the wing rock motions were limited to low speeds ($M \leq 0.65$) and the onset angle of attack occurred around 17° . At $M = 0.65$ and above, the wing rock susceptibility decreased gradually due to higher wing sweep, which reduced the roll damping instability. Flight time histories for a wing rock motion encountered in the F-14 showed that the lateral oscillations were primarily body axis motions. Also, from the flight test, it was found that special attention must be given to the design of the high roll damper gain (i.e., the wing rock suppression system) to avoid degradation of the airframe spin resistance characteristics (Reference 17).

A key NASA research activity relating to the wing rock phenomenon involved the investigation of aerodynamic factors that cause the low speed wing rock on slender delta wings (Reference 18). An 80° flat-plate delta wing was subjected to Static-Force and dynamic wind-tunnel tests in addition to flow visualization studies. In the dynamic Free-to-Roll wind-tunnel tests, the delta wing, under symmetric conditions, exhibited self-induced large amplitude wing rock at angles of attack greater than 25° (c.f., Figure 11 from Reference 18). It was also found that the delta wing always reached the same limit cycle conditions independent of initial roll angle or wind disturbances. From the Rotary Balance and Forced-Oscillation wind-tunnel tests, a roll damping dependence on sideslip was shown. At angles of attack where the roll damping was unstable, increasing the sideslip angle substantially reduced the roll damping instability (c.f., Figure 12 from Reference 19). Flow visualization studies suggested a roll damping dependence with asymmetric leading-edge vortex locations and patterns (c.f., Figure 13 from Reference 18). A one

degree-of-freedom nonlinear wing rock simulation resulted in time histories that reasonably matched the wing rock analytical solution and Free-to-Roll results (c.f., Figure 14 from Reference 18).

Additional wing rock experimental studies were conducted at the NASA Langley Research Center to investigate the effects of forebody geometry on high angles-of-attack static and dynamic stability (Reference 34). A generic fighter model with cylindrical fuselage was tested with five different forebodies (c.f., Figure 15a from Reference 34). The results showed a strong effect of forebody cross-sectional shape on static lateral-directional stability (c.f., Figure 15b and c from Reference 34). The forebody shape did not affect the wing rock onset, but strongly changed the wing rock amplitude (c.f., Figure 15d from Reference 34). It was noted that the forebody shapes that provided the highest level of static lateral-directional stability caused the highest wing rock amplitude.

In the 1980's, the NASA participated vigorously in the testing of the Grumman X-29 technology demonstrator aircraft. The X-29 was subjected to many wind-tunnel and flight tests. In the Free-Flight and Drop model flight tests, the X-29 showed self-induced roll instabilities at high angles of attack (c.f., Figure 16 from Reference 20). The wing rock onset occurred around $\alpha = 20^\circ$. As the angle of attack increased beyond 20° , the wing rock oscillations increased in amplitude until the motions diverged into violent roll departures at angles of attack greater than 32° . Consequently, a high-gain roll damper was effectively incorporated into the Free-Flight, Drop model, and full-scale flight control systems to alleviate these wing rock motions (c.f., Figure 17 from Reference 20). In the dynamic Free-to-Roll

wind-tunnel tests, the X-29 exhibited wing rock at angles of attack greater than 25° . Moreover, configuration component breakdown showed that the X-29 still exhibited wing rock without canards, wings, or vertical tail. These results strongly supported the wing rock theory that the nonlinear roll damping characteristics are primarily dependent on the forebody flow fields. It is interesting to note that the X-29 forebody and fuselage geometry was derived from the F-5. This brings into attention two important conclusions. First, the wing planforms, in particular the X-29 forward-swept wing and the F-5 wings tested at the NASA Langley Research Center, had no strong effects on the unstable roll damping characteristics. Second, the forebody geometry produced strong asymmetric vortical flows at high angles of attack that caused nonlinear roll damping characteristics.

Currently, the NASA and other national agencies are involved in the High Alpha Research Vehicle (HARV) program. A modified McDonnell Douglas F/A-18 aircraft is used as a high angle-of-attack aerodynamics testbed. The basic F/A-18 without the Research Flight Control System (RFCS) exhibited self-induced, low frequency, moderate amplitude wing rock between 35° and 50° angle of attack (c.f., Figure 18 from Reference 21). On the other hand, the modified F/A-18 HARV with leading-edge extension (LEX) fences, thrust vectoring system, and RFCS on, showed no strong, undesirable wing rock motions.

2.2 Wing Rock Theory

Wing rock is a lightly damped oscillatory rolling-yawing motion dominated by a body axis roll oscillation with a constant amplitude. It can be induced by asymmetric flight (i.e., $|\beta| > 0^\circ$) or by flow asymmetries around the aircraft during symmetric flight (i.e., $\beta = 0^\circ$). Previous studies show that there are primarily two basic types of wing rock. As explained in Reference 7, "the first type is manifested as lateral unsteadiness at moderate-to-high angles of attack with small-amplitude intermittent oscillations in roll, which can become sufficiently developed in a random manner". The second type is "an initially diverging oscillation which usually becomes a limit cycle, with larger amplitude in roll". The second type of wing rock is the most analyzed because of the potential capability of motion predictions based on the understanding of the aerodynamics and flow behavior around a given flight vehicle. Depending on its amplitude and frequency, the wing rock motion can affect landing approaches, weapon aiming accuracy (Reference 22), aircraft agility, missile avoidance capability, turning and combat effectiveness (Reference 23). Wing rock is being encountered at low speed, high angle of attack and at high speed, low angle of attack.

Presently, at least six theoretical models describing wing rock triggering and/or driving mechanisms have been proposed.

First, the RAE showed that by including a cubic term in the roll damping derivative, a reasonable agreement was obtained between flight and simulated time responses for the sideslip and roll rate of a Gnat

aircraft exhibiting wing rock (Reference 15). The lateral-directional equations of motion were reduced to a fourth order differential equation in sideslip. Nevertheless, when same model was used for the HP 115 aircraft, there was a considerable difference (i.e., 40%) between simulated motions and experimental responses (Reference 6).

Second, the Naval Postgraduate School showed that "aerodynamic hysteresis of the form of relay action can lead to lateral-directional limit cycle motions" (Reference 24). The main disadvantage of this model is that "limit cycles are obtained only when an external disturbance is large enough to induce a sideslip angle to lie outside of the β -range in the hysteresis loop" (Reference 23).

Third, the NASA Langley Research Center showed that "the wing rock phenomenon is caused by a dependence of aerodynamic damping in roll on sideslip such that unstable roll damping is obtained at smaller sideslip angles and stable roll damping is obtained at the larger angles" (Reference 18). From the one D.O.F. math model of an 80° delta wing, simulated motions were in close agreement with the dynamic Free-to-Roll test results. However, the one D.O.F. equation of motion analysis showed a disagreement (i.e., 15% difference) between the analytical solution and simulated motions.

Fourth, at Lockheed Missiles & Space Co., studies showed that "limit cycles oscillations in roll of advanced aircraft can result from three different fluid mechanical flow processes" (Reference 25). One of the processes was found as the result of studies on slender wings. Wing rock

on slender wings is caused by "asymmetric vortex shedding from highly swept wing leading-edges" (Reference 25). For aircraft with moderate sweep leading-edges, the fluid mechanical flow process causing wing rock is the dynamic airfoil stall. For aircraft with slender forebodies, wing rock is caused by "asymmetric body vortices from the nose, which interact with an asymmetric aft body" (Reference 25). Another important finding from these studies is that "asymmetry caused by the aircraft canopy can be enough to establish a rocking motion" (Reference 25).

Fifth, the Virginia Polytechnic Institute and State University studies showed that "the dynamical equation governing the rolling motion of a flat delta wing about an axis parallel to its mid-span chord is coupled with the unsteady vortex-lattice method" (Reference 26). The solution of the one D.O.F. equation of motion and the unsteady incompressible inviscid flow equations yielded time histories of the rolling motion of the wing and the flow field. However, this model could not predict the maximum wing rock amplitude for the 80° flat-plate delta wing without changing the original model formulation.

Sixth, the Flight Research Laboratory of the University of Kansas performed a detailed investigation on wing rock theory. Studies concluded that "wing rock is triggered by flow asymmetries, developed by negative or weakly positive roll damping, and sustained by nonlinear aerodynamic roll damping" (Reference 23). The models consisted of nonlinear aerodynamics parameters for one D.O.F. and three D.O.F. equations of motion. Although these math models are more theoretically complete, they include nonlinear terms that are very difficult to obtain from existing

experimental test methods. For their studies, these terms were estimated at some average dynamic conditions (Reference 23).

Finally, it should be noted that these models have been verified only for a particular configuration. They cannot predict motions for any generic configuration. Nevertheless, these models indicate possible scenarios for wing rock susceptibility depending on the aircraft configurations. Therefore, "when preparing the equations of motions for predicting the dynamic behavior of a new, unknown configuration, the mathematical model, at least initially, should be made sufficiently general to encompass all such scenarios" (Reference 27).

3.0 TEST METHODS

3.1 Description of Models

For the wind-tunnel captive tests, two dynamically scaled models of the Rockwell/MBB X-31A (c.f., Figure 19) were used: a 13.3-percent-scale model (c.f., Figure 20) and a 19-percent-scale model (c.f., Figure 21). Additionally, a 27-percent-scale model of the X-31 was used for the Drop model flight tests (c.f., Figure 22). The geometry of the models is presented in a three-view sketch of the X-31 full-scale aircraft (c.f., Figure 23). A summary of weight and inertias, geometric, and control-surface deflections for the X-31 is presented in Table I. The effect that the model-to-airplane scale factor (i.e., N) has on various parameters for dynamically scaled models is included in Table II.

The longitudinal control surfaces include the all-movable canard and full-span, symmetrically deflected trailing-edge flaperons. Also, movable inboard/outboard leading-edge flaps are included in the double-delta wing to improve aircraft performance. The lateral-directional control surfaces include asymmetrically deflected trailing-edge flaperons for roll control and a rudder on the center-line vertical tail for yaw control. The propulsive controls include a thrust-vectoring system for pitch and yaw augmentation. In addition to the above control surfaces, the X-31 is equipped with a movable inlet lip and left/right speed brakes, and fixed M86 nacelle strakes and low-positioned J13 noseboom. The X-31 nose cross-sectional shape is a combined circular and vertical ellipse. All models tested in this investigation had no active thrust vectoring system

except the 19-percent-scale model used during the Free-Flight tests. Unless otherwise noted, all data presented in this thesis were measured with the model in the basic high angle-of-attack test configuration. This basic configuration consisted of the canard at -40° , the inboard/outboard leading-edge flaps at $40^\circ/32^\circ$, the trailing-edge flaperons at 0° , the inlet lip at 0° , and the rudder at 0° .

3.2 Captive Wind-Tunnel Tests

Extensive captive wind-tunnel tests were conducted prior to the radio-controlled Drop model flight tests. The objectives of these tests were to define the predominant aerodynamic characteristics of the configuration at high angles of attack and to explore the wing rock susceptibility.

3.2.1 Static-Force Tests

The Static-Force tests were conducted using the 13.3-percent-scale X-31 model in a low-speed wind-tunnel with a 12-foot octagonal test section at a dynamic pressure of 4 lb/ft^2 , which corresponds to a Reynolds number, Re , of 0.6×10^6 based on \bar{c} . Conventional six-component body-axis force and moment data (c.f., Figure 24) were measured through angle of attack and sideslip ranges of $0^\circ \leq \alpha \leq 85^\circ$ and $-30^\circ \leq \beta \leq 30^\circ$, respectively. The Static-Force tests included component buildup tests and measurements of control effectiveness. For sideslip ranges of $|\beta| > 30^\circ$, conventional Static-Force tests were conducted using the 19-percent-scale X-31 model in the NASA Langley 30-by-60-Foot wind-tunnel at a dynamic pressure of 5 lb/ft^2 , which corresponds to a Reynolds number, Re , of

0.97×10^6 based on \bar{c} . Conventional six-component body-axis force and moment data were measured through angle of attack and sideslip ranges of $0^\circ \leq \alpha \leq 80^\circ$ and $-85^\circ \leq \beta \leq 85^\circ$, respectively. Both Static-Force tests were referenced to a c.g. location of 25-percent of \bar{c} .

3.2.2 Forced-Oscillation Tests

To determine the dynamic stability derivatives, Forced-Oscillation tests for the 19-percent-scale X-31 model were conducted by the Flight Dynamics Branch in the Langley 30-by-60-Foot wind-tunnel about all three body axes as described in Reference 28 and as illustrated in Figure 25. Only lateral-directional damping data are presented in this thesis. These measurements were made at oscillations frequencies, f , of 0.4, 0.6 and 1 Hz and at amplitudes, $\Delta\phi$, of $\pm 5^\circ$ and $\pm 20^\circ$. These tests were conducted for a free stream dynamic pressure of 10 lb/ft² and an angle-of-attack range of $0^\circ < \alpha < 90^\circ$ at zero sideslip.

3.2.3 Rotary Balance Tests

Rotary Balance tests were conducted in the Langley 20-Foot Vertical Spin Tunnel using the apparatus (c.f., Figure 26) and techniques described in Reference 29 at an airspeed velocity of 25 ft/sec, which corresponds to a Reynolds number, Re , of 2.62×10^5 based on the \bar{c} of the 13.3-percent-scale X-31 model. Data were measured for a range of rotation rates, $-0.4 < \frac{\Omega b}{2V} < 0.4$, for $0^\circ \leq \alpha \leq 90^\circ$ at sideslip angles of $10^\circ, 0^\circ, -5^\circ, -10^\circ, -15^\circ$,

-20°, and -30°. The aerodynamic data were referenced to the body axes system and c.g. location of 25-percent of \bar{c} .

3.2.4 Free-to-Roll Tests

To explore the dynamic roll stability of the X-31 configuration at high angles of attack, a series of wind-tunnel tests were conducted with the single degree-of-freedom test apparatus shown in Figure 27. The models were allowed to rotate freely about their roll axes with no angular limitation as described in Reference 18. The roll angle, $\phi(t)$, was measured with a high quality synchro resolver, and subsequently digitized and stored in a computer at 125 samples per second. Estimates of roll rate, $\dot{\phi}(t)$, and roll acceleration, $\ddot{\phi}(t)$, were computed by using the central difference method. The total aerodynamic moment was computed from

the following equation:
$$C_{l_{aero}}(t_i) = \frac{I_{XX} \ddot{\phi}(t_i)}{\bar{q} S b}$$
 . The roll inertia, I_{XX} , was experimentally determined using a conventional oscillation technique. The Free-to-Roll tests were conducted in a low-speed wind-tunnel with a 12-foot octagonal test section at a dynamic pressure range from 0.5 to 4 lb/ft², which corresponds to a Reynolds number, Re , of 0.2×10^6 to 0.6×10^6 based on \bar{c} for the 13.3-percent-scale X-31 model.

Flow-visualization tests were also conducted in the Langley 12-Foot Low-Speed wind-tunnel by using both tuft and smoke techniques. The tuft technique was used to observe the surface airflow over the model. On the other hand, the smoke technique was used to understand the off-surface flow field. Video footage was obtained from the flow visualization

studies. For a clearer understanding of the flow mechanisms observed during the flow studies, an image enhancement analysis was performed on selective video sequences. The video frames were digitized, and contour lines depicting changes in smoke density were overlaid on the original video frame. Additional color enhancement was used to distinguish between each contour region. The final video prints combine original frame in gray scale and contour regions in false color from a color look-up table. Each video print includes a color scale based on the color look-up table.

3.3 Drop Model Tests

The radio-controlled Drop model test was initially developed to study the stall/post-stall and spin-entry motions of aircraft. Currently, the investigations of high-rate maneuvers and other flight dynamics aspects over the low-speed flight envelope are included in the Drop model flight test plan. The Drop model test is conducted at the NASA Plum Tree Test Site and the overall operation is illustrated in Figure 28 (Reference 30). It involves dropping an unpowered, dynamically-scaled model from a helicopter at an altitude ranging from 6,000 to 10,000 feet, and flying it remotely from the ground through a series of predetermined maneuvers from the pilot flight cards. At approximately 1,000 feet altitude, the flight ends when an onboard parachute is deployed.

The X-31 Drop model is fully instrumented for the acquisition of rates, accelerations, Euler angles, control surfaces positions, and air data (c.f., Figure 29). The flight control system consists of digital flight control

laws designed from wind-tunnel aerodynamic data. These control laws use real-time measured data and pilot commands to compute the control surfaces commands necessary for aircraft stability augmentation.

3.4 Nonlinear Math Modeling

The results from wind-tunnel tests were used to develop a mathematical model of the wing rock dynamics. The simulation results were compared to Free-to-Roll results and Drop flight data. The equation of motion used in the nonlinear simulation is given by:

$$\ddot{\phi} = \frac{\bar{q} S b C_{l_{aero}}}{I_{xx}}$$

with the aerodynamics modelled as:

$$C_{l_{aero}} = C_{l_s}(\alpha, \beta) + C_{l_d}(\alpha, |\beta|) \frac{\dot{\phi} b}{2 V}$$

and requiring auxiliary equations:

$$\tan \alpha = \tan \theta_{sting} \cos \phi$$

$$\sin \beta = \sin \theta_{sting} \sin \phi$$

The static data, C_{l_s} , were taken from the NASA Langley 12-foot and 30-by-60-Foot wind-tunnels tests. The damping data, C_{l_d} , were combined from Forced-Oscillation and Rotary Balance tests. The Forced-Oscillation data include frequency and amplitude effects on the roll damping parameter, $\overline{C_{l_p}}$. The Rotary Balance data were used to define the sideslip dependency of C_{l_d} based on the measured effects of β on C_{l_d} . Detailed block diagrams of the nonlinear simulation are included in Appendix A.

4.0 RESULTS AND DISCUSSION

4.1 Captive Test Results

4.1.1 Longitudinal Static Stability and Control

The static longitudinal characteristics of the X-31 configuration are presented in Figure 30 to 32. The data shows maximum lift around $\alpha = 30^\circ$. The canard deflection effects on the longitudinal characteristics show minor change in lift and considerable pitching moment increase for all angles of attack. Below CL_{max} , full trailing-edge symmetric flap effects show a parallel shift in the lift curve and a greater pitching moment increase than with the partial canard deflection. Nevertheless, above CL_{max} , the positive trailing-edge deflection effectiveness decreases because the wing is fully stalled. On the other hand, the negative trailing-edge flap deflection causes a considerable loss in lift providing nose-up pitching moment control throughout the post stall region. In Figure 32, the maximum combined nose-up pitch controls for $\beta = 0^\circ$ show good nose-up pitching moment capability at all positive angles of attack. Also, the combined nose-down pitch controls show good pitching moment capability for low angles of attack. On the other hand, using the nose-down recovery guidelines from Reference 31, the combined nose-down pitch controls at high angles of attack show desired nose-down pitching moment capability at the reference c.g. of 25-percent of \bar{c} . However, aft c.g. movement degrades the nose-down capability into the marginal to unacceptable regions. As discussed below, this nose-down control limitation will affect

the X-31 flight characteristics if additional pitching moment is obtained from large sideslip angles.

The sideslip effects on lift and pitching moment are presented in Figure 33 for $|\beta| \leq 30^\circ$ and in Figure 34 for $|\beta| \leq 85^\circ$. For $|\beta| \leq 30^\circ$, at low angles of attack (i.e., $\alpha < 20^\circ$), the lift and pitching moment vary slightly with sideslip angle (c.f., Figure 33a). At moderate angles of attack (i.e., $20^\circ < \alpha < 50^\circ$), the lift and pitching moment show a nonlinear relationship with sideslip (c.f., Figure 33b). For small sideslip angles, the pitching moment slightly increases, but at larger sideslip angles, it increases significantly more. Moreover, this nonlinear behavior reverses at high angles of attack (i.e., $\alpha > 50^\circ$). At extremely high angles of attack, the lift and pitching moment curves remain flat for all sideslip angles (c.f., Figure 33c). On the other hand, for $|\beta| \leq 85^\circ$, large nonlinear sideslip effect on lift and pitching moment is evident (c.f., Figure 34). As the $|\beta|$ increases over 30° , the pitching moment grows increasingly large whereas the lift decreases significantly for all angles of attack. Finally, the evident sideslip effect in pitching moment could be critical to aircraft operations at high angles of attack if the pitching moment exceeds the available nose-down control power. As discussed in subsequent sections, this nonlinear sideslip effect will be influential on the X-31 flight characteristics at high angles of attack.

4.1.2 Lateral-Directional Static Stability and Control

The static lateral-directional stability characteristics of the X-31 configuration are presented in Figures 35 to 38. The static stability derivatives were computed using a sideslip range from -5° to 5° . The canard deflection effect on the static directional stability shows that at loaded canard deflections (i.e., canard incidence numerically greater than the negative of the angle of attack), the configuration experiences a less stable $C_{n\beta}$ than at unloaded canard deflections (c.f., Figure 35). At $\alpha > 60^\circ$, $C_{n\beta}$ becomes unstable for all canard deflections. This instability can be partially attributed to the vertical tail ineffectiveness at high angles of attack. On the other hand, the configuration experiences static lateral stability for all angles of attack, except for loaded canard deflections at $\alpha < 10^\circ$. Between $20^\circ < \alpha < 50^\circ$, $C_{l\beta}$ becomes considerably more stable for unloaded canard deflections. As also seen in the static directional stability, the canard deflection effect on the static lateral stability, $C_{l\beta}$, reinforces the interaction between canard loading and weaker stability. These results suggest a possible relationship between forebody flow field strength and canard incidence angles. The trailing-edge symmetric flap effect in the lateral-directional stability is shown in Figure 36. At moderate-to-high angles of attack (i.e., $35^\circ < \alpha < 50^\circ$), $C_{n\beta}$ becomes unstable for negative trailing-edge flaps, whereas for the positive and neutral flap settings, $C_{n\beta}$ remains stable. In the same region, the trailing-edge flap effect on $C_{l\beta}$ is less significant and a strong dihedral effect remains for all flap settings. The effect of noseboom location on static directional stability is illustrated in Figure 37. Notice the large effect of the J13 noseboom location on $C_{n\beta}$. The low position seems to be the optimal location for high angles of attack.

The static lateral-directional characteristics in Figure 38 show yawing and rolling asymmetries. At low angles of attack, these asymmetries could be the product of wind-tunnel angularities or model asymmetries. Of more consequence are the characteristics at high angles of attack, which show that the configuration exhibits considerable yawing asymmetries. These asymmetries can lead to nose wandering or yaw departures (i.e., nose slice).

The lateral-directional control power available at all angles of attack is presented in the form of deltas between deflected and neutral control data. In Figure 39, at $\alpha < 40^\circ$, the trailing-edge differential flap effectiveness shows a proverse yawing moment, whereas at higher angles of attack, there is an adverse yawing moment. Moreover, at low angles of attack, there is a high roll control effectiveness. Around the stall/post stall regions, the roll control effectiveness decreases, but it still retains a substantial level of roll control power for all high angles of attack. An interesting aspect from the roll control power available curves is the nonlinear effect of differential flap deflections on roll control power magnitude. At low angles of attack, a 10° differential deflection provides almost 50% of the roll control power for the 30° deflection. Nevertheless, as the angle of attack increases, a more linear relationship between the differential deflections and roll control power is established. This nonlinear roll control behavior can be attributed to two different phenomena. At low angles of attack, large differential deflections are less effective than smaller deflections because the large deflections create flow separation around the flap area, whereas the small deflections maintain attached flow characteristics. Flow separation will lead to a decrease in the

incremental lift obtained from the flap deflections. On the other hand, at high angles of attack, the wing is stalled and roll control is generated from the aft-wing projected area. In this case, the roll control generated is directly proportional to the flap deflection angles. As discussed in subsequent sections, the roll control power available will be of critical importance for the suppression of undesirable lateral instabilities such as wing rock.

The directional control power curve from Figure 40 shows good levels of rudder control effectiveness at low angles of attack up to CL_{max} . On the other hand, as the angle of attack increases, the rudder effectiveness decreases due primarily to the immersion of the center-line vertical tail into the low energy stalled wake shed from the wing and fuselage. Finally, the rudder roll control effectiveness shows an adverse rolling moment at low-to-moderate angles of attack (i.e., $\alpha < 45^\circ$).

The nonlinear sideslip effects in the lateral-directional characteristics for positive angles of attack and $|\beta| \leq 30^\circ$ are presented in Figure 41. At low angles of attack, the rolling moment slope (i.e., $C_{l\beta}$) switches from unstable to stable as the angle of attack increases (c.f., Figure 41a). Also, the degree of stability remains constant past 20° of sideslip. This sideslip nonlinearity is more evident at mid angles of attack (c.f., Figure 41b). For small sideslip, the most stable $C_{l\beta}$ is found at $\alpha = 32^\circ$, but it remains constant as the sideslip angle increases. Past this angle of attack, there is a steady reduction in lateral stability. At high angles of attack, the sideslip effects in rolling moment become linear for $|\beta| \leq 30^\circ$. The large sideslip effects on rolling moments are presented in Figure 42. At a given angle of

attack, the rolling moments are plotted versus sideslip ($-85^\circ \leq \beta \leq 85^\circ$) for neutral and cross-controls (i.e., right roll and left rudder). At $\alpha = 0^\circ$ (c.f., Figure 42a), the basic configuration experiences positive rolling moments for positive sideslip angles (i.e., unstable dihedral effect). The roll control effectiveness is good for most sideslip angles. Notice that at extremely large sideslips the roll power is considerably reduced. When the angle of attack is increased to 20° (c.f., Figure 42b), the existence of sideslip reversal effects in rolling moment emerges. A restoring rolling moment is obtained for small sideslips (i.e., stable dihedral effect). However, a destabilizing moment is encountered for $|\beta| > 30^\circ$ (i.e., unstable dihedral effect). The roll control effectiveness remains high for most sideslip, but the tendency to lose roll control at large sideslip angles strongly remains. At $\alpha = 40^\circ$ (c.f., Figure 42c), the dihedral effect is more stable for $|\beta| \leq 30^\circ$ than in the 20° case, but as sideslip further increases, a reversal occurs. For angles of attack greater than 40° , the main difference from the aforementioned behavior is the roll control effectiveness collapse for sideslip angles larger than 40° (c.f., Figures 42d and 42e). On the other hand, for small sideslip angles, roll control level remains. This nonlinear sideslip effect in rolling moment and roll control is a dominant factor on the configuration susceptibility to wing rock and HIKR departures as discussed in subsequent sections.

A calculated parameter that is useful for the analysis of high angle-of-attack lateral-directional stability is $C_{n\beta, \text{dyn}}$ (Reference 32), defined as:

$$C_{n\beta, \text{dyn}} = C_{n\beta} \cos \alpha - \frac{I_{ZZ}}{I_{XX}} C_{l\beta} \sin \alpha$$

Negative values of this parameter indicate a susceptibility to a directional divergence (i.e., nose slice). An unstable $C_{n\beta}$ combined with a weak dihedral effect will make the configuration susceptible to yaw departures, particularly for fighter aircraft that have a high inertia ratio of yaw to roll. In Figures 43a and 43b, $C_{n\beta, \text{dyn}}$ for different canard and trailing-edge symmetric flap deflections is plotted versus angle of attack. Notice that the configuration remains stable for all deflections. Nevertheless, a reduction in stability is seen for the deflections that showed a decrease in $C_{n\beta}$. A positive increase in canard deflection will make the configuration less resistant to directional departure.

A useful parameter to predict lateral control reversal is the Lateral Control Divergence Parameter (i.e., LCDP). This parameter is defined as:

$$\text{LCDP} = C_{n\beta} - C_{l\beta} \left(\frac{C_{n\delta r \text{TEDIFF}} + K_{\text{ARI}} * C_{n\delta r}}{C_{l\delta r \text{TEDIFF}} + K_{\text{ARI}} * C_{l\delta r}} \right)$$

where K_{ARI} is the aileron to rudder interconnect gain used to coordinate turns in the flight control system. This gain depends on the angle of attack, and lateral-directional stability and control power characteristics. Positive values of LCDP indicate a normal roll response, and negative

values indicate a reversed response. When reversed response is encountered, a right roll control input by the pilot will cause the airplane to roll to the left. In Figure 44, LCDP is given at each angle of attack for the basic configuration at three different gain settings. LCDP remains positive for up to $\alpha = 60^\circ$. Above 60° of angle of attack, there is a lateral reversal at all gain settings. The reduction in LCDP at high angles of attack is primarily due to the aileron adverse yaw and rudder ineffectiveness. Notice that as the gain increases, LCDP becomes more positive. Nevertheless, if the gain is too high, as in $K_{ARI} = 2$, there will be a lateral control reversal point caused by the Stability Augmentation System. Moreover, from the Static-Force data, the $Cl\delta_r$, when multiplied by a large gain, can negate the $Cl\delta_{fTEDIFF}$ contribution at $\alpha = 40^\circ$. Iterating through K_{ARI} for LCDP values, the maximum gain value at this angle of attack was computed to be 1.6. Therefore, the desired K_{ARI} should be tested at each angle of attack to ensure that no lateral control reversal points exist.

Knowing $C_{n\beta, dyn}$ and LCDP parameters, one can come up with the Departure and Spin Susceptibility Criteria described in Reference 33. In Figure 45a, plane regions are described depending on the parameter values. Notice that one needs to avoid the third quadrant, which represents the worst case scenario. For the X-31 configuration, the Departure and Spin Susceptibility Criteria is given in Figure 45b. Most points lie in the first quadrant (i.e., no departure). Nevertheless, there are points near the origin and fourth quadrant. These points indicate that the configuration could experience a "mild initial yaw divergence followed by roll reversal (mild rolling departure), low spin susceptibility" (i.e., Region B).

It should be noted that the stability derivatives used in calculating the $C_{n\beta, \text{dyn}}$ and LCDP parameters are applicable over only small sideslip angles (i.e., $\pm 5^\circ$). The higher the angle of attack, the more nonlinear effects will appear in the yawing and rolling moments. Therefore, it is possible to have positive values for $C_{n\beta, \text{dyn}}$ and LCDP at small sideslip angles, and negative values for $C_{n\beta, \text{dyn}}$ and LCDP at larger sideslip angles

4.1.3 Lateral-Directional Dynamic Stability

4.1.3.1 Forced-Oscillation Results

The yaw and roll damping data were obtained from Forced-Oscillation tests. In Figure 46, the yaw damping parameter, $\overline{C_{n_r}}$, is given as a function of α for a range of canard deflections including trim canard setting. At low angles of attack (i.e., $\alpha < 30^\circ$), the yaw damping parameter is stable for all canard deflections. On the other hand, at moderate-to-high angles of attack (i.e., $35^\circ < \alpha < 50^\circ$), it is unstable for all canard deflections specially at negative deflections. At $\alpha > 50^\circ$, the yaw damping becomes marginally stable for most canard deflections. Comparing the yaw damping data with the directional static stability characteristics, the damping becomes less stable as the directional static stability is increased.

The roll damping parameter, $\overline{C_{l_p}}$, was obtained for the basic configuration at different reduced frequencies and amplitudes. The frequency effects for $\Delta\phi = \pm 5^\circ$ are shown in Figure 47. At low angles of attack, the roll damping is stable and relatively insensitive to the

frequency of oscillation. Approaching the stall region (i.e., near CL_{max}), the roll damping becomes unstable for all frequencies tested, peaking at a value of 0.9 at $\alpha = 35^\circ$. Notice that the lower the frequency, the roll damping instability becomes more severe. This suggests a possible flow lag effect on roll damping. The flow lag effect would manifest itself as a change in the $C_{l\dot{\beta}}$ term of the measured $\overline{C_{l_p}}$ derivative. Past the stall region, $\overline{C_{l_p}}$, becomes marginally stable and insensitive to frequency of oscillation. The amplitude effect at a reduced frequency of 0.089 is shown in Figure 48. The roll damping becomes considerably less unstable between $30^\circ < \alpha < 45^\circ$ at the larger oscillation amplitude because the oscillation covers more $\Delta\beta$. This suggests a relationship between roll damping and sideslip angle. This relationship is reinforced from the Rotary Balance test data as discussed in subsequent section.

In addition to frequency and amplitude effects, configuration component effects on roll damping were obtained. The J13 noseboom was found to have a stabilizing effect on roll damping around $30^\circ < \alpha < 45^\circ$ as shown in Figure 49. The canard effect on roll damping is shown in Figure 50 for several canard deflections including canard off. At low angles of attack, roll damping is insensitive to canard deflection. Between $25^\circ < \alpha < 40^\circ$, roll damping is more unstable as the canard deflection becomes more negative. The worst instability occurs when canards are off. Notice that when the canard is at 0° and $+20^\circ$, the roll damping instability is delayed past $\alpha = 30^\circ$. The M86 body strake effect on $\overline{C_{l_p}}$ is shown in Figure 51 for canard of -40° . The destabilizing effect of the M86 strakes is only seen between $30^\circ < \alpha < 40^\circ$. At $\alpha > 50^\circ$, the M86 strake has a

considerable stabilizing effect on $\overline{C_{l_p}}$. The leading-edge flap effect on roll damping with canard deflections of -40° and 0° are shown in Figure 52a and 52b, respectively. The inboard/outboard leading-edge flaps of $40^\circ/32^\circ$ show slightly less instability than flaps at $0^\circ/0^\circ$. The inboard/outboard trailing-edge symmetric flap effect is mixed as seen in Figure 53. At low angles of attack ($\alpha < 25^\circ$), the trailing-edge flaps of $+30^\circ/+30^\circ$ produce the highest level of stability, but between $25^\circ < \alpha < 35^\circ$, the effect of the trailing-edge flaps of $0^\circ/0^\circ$ is more stable. For $\alpha > 35^\circ$ (i.e., in the post stall region), there is no considerable difference. The vertical tail effect is shown in Figure 54. Removing the vertical tail increases the roll damping instability for $30^\circ < \alpha < 40^\circ$.

In summary, the frequency effect on roll damping suggests the importance of vortex flow lag on roll damping around stall/post stall regions. Likewise, the amplitude effect shows the importance of roll (or sideslip) angle on roll damping in the same regions. From the configuration component effects, two important aspects of roll damping are shown. First, forebody flow interference changes the roll damping characteristics as seen from the J13 noseboom, canard, and M86 body strakes effects. Second, wing camber slightly influences the roll damping characteristics as seen from the leading-edge and trailing-edge flap effects. Finally, the roll damping instability encountered around the stall/post stall regions will be one of the crucial factors allowing the self-induced roll oscillations (i.e., wing rock) to build up as discussed in subsequent sections.

4.1.3.2 Rotary Balance Test Results

From the Rotary Balance test method, rolling moments under a steady rotating condition can be obtained for a given angle of attack. A configuration is damped in roll if the moment is in the second or fourth quadrant of the rotational data plots and is propelling if the moment is in the first or third quadrant as illustrated in Figure 55. Propelling moments may indicate a susceptibility to roll departures or spins. The X-31 configuration rotational data obtained in Reference 29 is plotted in Figure 56a and 56b. Data was obtained for rotational rates of $-0.4 < \frac{\Omega b}{2V} < 0.4$, for $0^\circ < \alpha < 90^\circ$ at sideslip angles of $10^\circ, 0^\circ, -5^\circ, -10^\circ, -15^\circ, -20^\circ$, and -30° . One positive sideslip angle was obtained to check for asymmetries in the moments. For angles of attack less than 20° , the configuration is damped in roll for all sideslip angles. As the angle of attack increases, the slope of the rolling moments becomes flatter. At $\alpha = 25^\circ$, the slope is almost zero indicating a tendency towards propelling moments. Approaching the stall region (i.e., $\alpha = 30^\circ$), the slope at $\beta = 0^\circ$ is positive but at larger sideslip the slope remains nearly flat. At $\alpha = 45^\circ$, propelling moments are shown at all sideslip angles tested, but the instability reduces as the sideslip angle increases.

These results were used to formulate a sideslip dependency in the roll damping term used in the one D.O.F. nonlinear simulation. First, at a given α , the rate of change of the rolling moment coefficient with respect to rotation rate was determined for each sideslip angle using a linear least squares method. Then, the slopes were normalized with respect to the

slope obtained for zero sideslip (c.f., List of Symbols). An example of the normalized slope versus sideslip is shown in Figure 57 for $\alpha = 45^\circ$. This process was repeated for each angle of attack. The normalized slope function will be used as a multiplier to the Forced-Oscillation roll damping data to bring in sideslip effects on the roll damping term of the nonlinear simulation. Symmetric behavior is assumed for positive sideslip angles.

4.1.3.3 Free-to-Roll Results

From the previous test results, the X-31 configuration at high angles of attack showed poor roll damping characteristics coupled with strong lateral static stability (i.e., strong dihedral effect), and a high inertia ratio of yaw to roll (i.e., $I_{ZZ}/I_{XX} \approx 12$). These characteristics indicate that the configuration may be susceptible to wing rock. To explore this possible behavior, Free-to-Roll tests were conducted. The Free-to-Roll results are divided into two categories: qualitative and quantitative results. The qualitative results summarize the configuration component effects on wing rock susceptibility, and on the forebody flow behavior during wing rock and into the HIKR departure. On the other hand, the quantitative results specify the X-31 wing rock characteristics including the aerodynamic moments responsible for driving the motion, and the HIKR entry characteristics.

4.1.3.3.1 Wing Rock Characteristics

The X-31 configuration experiences a self-induced wing rock when the angle of attack is increased toward the stall region. The wing rock onset angle of attack depends somewhat on the configuration. For the basic configuration, the roll motions are found to be lightly damped below $\alpha = 24^\circ$. As the angle of attack increases, limit cycle (undamped) wing rock motions are observed with an onset angle of attack of 25° . The wing rock amplitude, $\Delta\phi_{WR}$, increases with angle of attack and reaches a maximum amplitude limit cycle around $\alpha = 32^\circ$. For α greater than 32° , the wing rock motions diverge and a HIKR departure is experienced for angles of attack up to 45° . For α greater than 45° , lightly damped roll motions are experienced. The removal of J13 noseboom, canard, wings, or vertical tail did not largely alter or eliminate the fundamental wing rock characteristics experienced with the basic configuration. A summary of the effect of configuration changes on wing rock characteristics is included in Table III. Notice that the main differences reside in the onset and maximum amplitude angle of attack. With the canard at 0° , the onset and maximum amplitude angles of attack are delayed considerably. In this case, the canards are working like body strakes interfering with the forebody flow. Also, removing the wings delayed the onset α . This strongly suggest that the presence of the wing deteriorates the wing rock characteristics, but is not the source of the undamped motions. Moreover, the effect of replacing the X-31 nose with a hemispherical nose shows no fundamental change in the wing rock behavior. Therefore, these results show that the triggering mechanism for the wing rock motions in the X-31 configuration is due to the interaction of forebody flow with the forward fuselage body. The

effect of additional body strakes shows a delay of the wing rock onset α . These add-on strakes (3.5 ft by 0.88 ft full-scale) were placed behind the canard and above the engine inlet area as illustrated in Figure 58. As shown in Table III, the strakes delay the onset α past the stall region deep into the post stall region. Nevertheless, the wing rock motions become divergent within five degrees from the onset α . Also, without the M86 body strakes but with the add-on body strakes, the wing rock onset is brought back near the stall region indicating the need for both sets of body strakes. These results strongly support the theory that the forebody flow around the engine inlet area and canopy is a major source of the undamped motions.

The flow visualization results support the previous theory about the wing rock triggering mechanisms in the X-31 configuration. Although the flow studies are conducted at a slower wind speed than in the Free-to-Roll tests, the undamped roll motions are still present and no significant changes in onset α are seen. Using a smoke wand and moving it around the forebody and forward fuselage of the X-31 configuration, two vortex patterns are distinguished coming from the forward fuselage underneath the canard hinge line. The vortices positions change during wing rock motions. As seen from the dynamic flow visualization study in Figure 59, the windward vortex is stretched at small roll angles whereas the leeward vortex is compressed. This leads into an increase in the leeward vortex velocity generating an additional, destabilizing rolling moment in the same direction of the roll. As the roll angle keeps increasing, the spanwise position of the vortical cores moved. The leeward vortex is blown outboard whereas the windward vortex is blown inboard. The windward

vortex will move over the canopy eventually causing a restoring rolling moment. These flow mechanisms combined with strong dihedral effect and variation of roll damping with sideslip are considered to be the main driving mechanisms of the wing rock of the X-31 configuration.

For the basic configuration, wing rock characteristics in terms of the limit cycle amplitude ($\Delta\phi_{WR}$), period (P_{WR}), and reduced frequency (k_{WR}) were computed from the Free-to-Roll time histories. Because the wing rock frequency may vary throughout an oscillation cycle, the reduced frequency is computed from an average frequency. This reduced frequency is used to compare Free-to-Roll results with the nonlinear simulation results. A summary of the above wing rock characteristics for the basic configuration is given in Table IV. Notice that as the angle of attack increases, the reduced frequency slightly decreases, and the limit cycle amplitude greatly increases.

From the measured roll angle time histories, the total aerodynamic rolling moment, Cl_{aero} , was derived as discussed earlier. The moment of inertia, I_{XX} , was determined by the oscillation technique to be 0.19683 slug-ft². This I_{XX} compared to full-scale values corresponds to a scaled altitude of 15,350 feet. In Figure 60, aerodynamic data for the X-31 basic configuration at $\theta_{sting} = 28^\circ$ show mild limit cycle wing rock with $\Delta\phi_{WR} = 15^\circ$. Due to the one D.O.F. kinematic relationship between α , β , ϕ and θ_{sting} (c.f., auxiliary equations), α decreases with ϕ , whereas β increases with ϕ . The roll rate, $\dot{\phi}$, oscillates between $\pm 24^\circ/\text{sec}$ (full-scale). The aerodynamic rolling moment, Cl_{aero} , is 180° out-of-phase with ϕ . It is at a maximum positive value when ϕ is at its maximum negative value and vice versa. It

is noteworthy that the Cl_{aero} peak value is just under half of the Lateral Control power available with full trailing-edge flap differential deflection as determined from the Static-Force tests (c.f., Figure 39). The aerodynamic data at $\theta_{sting} = 30^\circ$ are plotted versus time (full-scale) in Figure 61. The same pattern is seen as in the $\theta_{sting} = 28^\circ$ case, but the wing rock is moderate with $\Delta\phi_{WR} = 25^\circ$. The roll rate, $\dot{\phi}$, oscillates around $\pm 41^\circ/\text{sec}$ (full-scale). The rolling moment from the wing rock motion is just under 85% of the Lateral Static Control power available. At $\theta_{sting} = 32^\circ$, the wing rock is large with $\Delta\phi = \pm 45^\circ$ (c.f., Figure 62). The roll rate, $\dot{\phi}$, oscillates between $\pm 70^\circ/\text{sec}$ (full-scale). In this case, there are considerable α changes and close to $\pm 20^\circ$ in sideslip. The angle of attack fluctuates from 32° to 20° . Notice that when the angle of attack is at its lowest value, the rolling moment reaches a peak positive value that is well below the available Lateral Control power (c.f., Figure 39). Nevertheless, when the rolling moment is at its peak negative value (i.e., $28^\circ < \alpha < 32^\circ$), Cl_{aero} exceeds the Lateral Static Control power available (c.f., Figure 39) by almost 10% (c.f., Figure 62). For $32^\circ < \theta_{sting} < 45^\circ$, the roll oscillations grow increasingly large and diverge never settling into limit cycles.

To better understand the wing rock aerodynamics, it is useful to include the concept of energy exchange as explained in Reference 18. The net energy exchanged over a cycle is given by:

$$\Delta E = \bar{q} S b \int_{C_\phi} C_{l_{aero}} d\phi$$

where C_ϕ is the histogram curve obtained by plotting $C_{l_{aero}}$ versus ϕ over a given time frame. For an ideal limit cycle, C_ϕ is a closed curve over one oscillation cycle. In Figure 63, two ideal histograms of $C_{l_{aero}}$ are plotted versus ϕ with the arrows indicating increasing time. From the above equation and aforementioned conceptual plots, it is concluded that the "net aerodynamic energy exchange in a cycle is directly proportional to the areas contained within the C_ϕ loops where $\Delta E > 0$ for clockwise loops so that the energy is added to the model (destabilizing) while $\Delta E < 0$ for counter-clockwise loops so that the energy is extracted from the model (stabilizing)" (Reference 18). In real-time experiments, C_ϕ can consist of none, one, or many of the conceptual loops from Figure 63.

For a single wing rock oscillation at $\theta_{sting} = 32^\circ$, histograms of $C_{l_{aero}}$ plotted versus ϕ and β are presented in Figure 64a and 64b. Based on the energy exchange concepts, it is seen that a large destabilizing, clockwise loop (i.e., $\Delta E > 0$) exists for roll angles between $\pm 20^\circ$ whereas smaller stabilizing, counterclockwise loops (i.e., $\Delta E < 0$) exist for larger roll angles. It is reasonable to assume that the area of the stabilizing loops equals the area of the destabilizing loop indicating an energy balance that is required to sustain the limit cycle. Moreover, in Figure 65, $C_{l_{aero}}$ is plotted against ϕ . Notice that the rolling moment magnitude increases to counterbalance

the non-zero roll rate until the roll rate becomes zero. Comparing to the previous energy exchange figures, when the rolling moment is zero, it means that a balance is achieved between the roll rate and roll angle contributions to $\dot{\phi}$. Finally, if the large sideslip effect on the rolling moment is destabilizing as shown in Static-Force tests, it will not allow the generation of stabilizing loops to sustain wing rock limit cycle. This will lead into a HIKR departure as discussed in subsequent sections.

Another conceptual tool used to understand the wing rock aerodynamics is the phase plane diagram. The phase plane diagrams consist of $\dot{\phi}$ versus ϕ . For a given angle of attack, one can get the system equilibrium point(s). For a damped, stable system, the phase plane diagram can consist of a single equilibrium point called a stable focus (c.f., Figure 66a). If the single equilibrium point is unstable (c.f., s1 in Figure 66b), it can build up into a limit cycle or move into two other unstable equilibrium points called saddle points (c.f., s2 and s3 in Figure 66b). From Figure 66b, one can see that any motion initiated in the shaded region will not form a limit cycle but diverge into complete revolutions (i.e., sustained HIKR). For a given aircraft, the phase plane might look like Figure 66a or 66b depending on the system stability at each angle of attack.

At $\theta_{\text{sting}} = 32^\circ$, the phase plane diagram for several cycles is given in Figure 67a. There are deviations from one cycle to another, but the same circular path is followed in time representing a limit cycle. For a single cycle, the arrows in the phase plane diagram in Figure 67b indicate an increase in time. As the roll angle increases, the roll rate magnitude decreases. Notice that at zero roll rate, the roll angle is at its maximum

value. Then, the roll angle decreases while the roll rate magnitude increases. At zero roll angle, the roll rate is at its maximum value. This pattern is repeated for all given cycles. The correlation of maximum angular velocity with zero roll position and zero angular velocity with maximum roll position is consistent with the physics of limit cycles. From the phase plane diagrams, it is observed that an offset exists in the neutral axis. This can be attributed to wind-tunnel angularities or a geometric asymmetry in the model. At $\theta_{\text{sting}} = 45^\circ$, the roll oscillations are rapidly divergent. As seen in the roll angle time history in Figure 68a, the configuration oscillates and departs into a sustained HIKR. This behavior is illustrated in the phase plane diagram of Figure 68b. The divergent, unstable spiral never established a limit cycle due primarily to nonlinear, destabilizing sideslip effects in the rolling moment as seen in the Static-Force results.

4.1.3.3.2 High Incidence Kinematic Roll Departure Characteristics

To understand the HIKR departure, it is important to consider not only the dynamic behavior but also the static conditions that might lead into it. From the Free-to-Roll results, the existence of static departure roll angles was revealed. If the open-loop configuration matches or exceeds these roll angles, it will not return to level-flight unless control surfaces are deflected to roll it back. These points were found by statically releasing the configuration at non-zero roll angles. If the configuration restores itself back to level-flight or oscillates into a limit cycle, the model initial release point is increased until a roll departure is imminent. In Figure 69a, ϕ_{max} values for the basic configuration at three symmetric

trailing-edge flap settings are plotted versus θ_{sting} . Typically, ϕ_{max} values fluctuate between 55° and 75° . The angle of attack and sideslip angle departure combination can be computed from the one D.O.F. auxiliary equations:

$$\tan \alpha = \tan \theta_{sting} \cos \phi$$

$$\sin \beta = \sin \theta_{sting} \sin \phi$$

In Figure 69b, the X-31 flight envelope guideline is depicted with regions where the configuration should experience a HIKR departure. The HIKR departure boundary is a statically-released departure boundary from experimental results obtained in the Free-to-Roll tests. It does not include dynamic effects, which could shift the boundary up or down. Therefore, this guideline is not at all a conservative guideline. Departure points could exist before or after the α and β conditions depending on the flight dynamics. The departure points are considered to be saddle points (i.e., unstable points) in the X-31 phase plane diagram.

On the other hand, from the Static-Force test data, the roll angle static effects on rolling moment can be obtained by using the α and β relationships from the one D.O.F. math model. At a given θ_{sting} , α and β are computed as the roll angle is varied from 0° to 90° . From the α and β combination, the static rolling moment can be computed by interpolating from the Static-Force test data. In Figure 70, the rolling moment at $\theta_{sting} = 40^\circ$ is plotted versus roll angle. As the roll angle increases, α decreases and β increases. The static rolling moment increases negatively to restore β back to zero. When the sideslip angle is over 20° (i.e., roll angle over 30°), the rolling moment decreases and eventually becomes positive (i.e.,

propelling moment). Further sideslip increase will lead to more propelling rolling moment (i.e., HIKR departure). The roll angle at the point where $C_{l_s} = 0$ correlates with the ϕ_{max} value obtained from the Free-to-Roll tests. Repeating the previous process for $20^\circ < \theta_{sting} < 85^\circ$ and $-90^\circ < \phi < 90^\circ$, the static departure roll angles from Static-Force tests are obtained for positive and negative ϕ_{max} values (c.f., Figure 71a). Comparing these values to the Free-to-Roll results, the HIKR departure values from Static-Force test results (i.e., $C_{l_s}(\phi_{max}) = 0$) are slightly higher. Using the auxiliary equations, the α and β combinations are plotted with the flight envelope guideline from Free-to-Roll tests (c.f., Figure 71b). Notice that the HIKR departure points from the Static-Force tests are higher than the HIKR departure points from the Free-to-Roll tests. This suggests that the HIKR departure can occur before $C_{l_s} = 0$. Because the rolling moment slope is positive (i.e., unstable) around this region, any perturbation could lead to a HIKR departure before reaching $C_{l_s} = 0$.

From the flow visualization studies (c.f., Figure 72), it was concluded that the HIKR departure occurs when the configuration rolls into very large roll angles; the windward vortex moves over the leeward vortex and pushes it up toward the leeward wing top surface. The vortex impacts the leeward wing causing a suction into the direction of the roll.

Finally, it should be noted that the HIKR departure is closely linked to wing rock motions because the wing rock motions are responsible for the sideslip angle build up. At a critical sideslip angle, the sideslip reversal effect in rolling moment from the Static-Force tests can propel the configuration into a HIKR departure. From the Free-to-Roll tests, a

sustained HIKR was seen for the X-31 configuration with neutral and full fixed trailing-edge flap differential deflections. A sustained HIKR is characterized by large roll rate. If the control surfaces are deflected in the direction of the roll motion or the energy build up is largely destabilizing, the configuration could experience a sustained HIKR.

4.2 Drop Tests Results

4.2.1 Data Analysis System

The data measured during Drop model tests were filtered and fitted with a spline curve to obtain the necessary first and second derivatives. The air data (i.e., α , β , and V) were corrected for sensor location. Also, linear accelerations were corrected for instrument location using the angular rates. Atmospheric parameters, such as ρ or μ , were calculated from altitude measurements assuming a standard atmosphere (c.f., Appendix B for program listing of the Data Analysis System). The body axes forces and moments were calculated from the following nondimensional equations of motion:

$$C_X = \frac{\text{WEIGHT} \cdot a_X}{\bar{q}S}$$

$$C_Y = \frac{\text{WEIGHT} \cdot a_Y}{\bar{q}S}$$

$$C_Z = \frac{\text{WEIGHT} \cdot a_Z}{\bar{q}S}$$

$$I_{XX}\dot{p} = (I_{YY} - I_{ZZ})qr + I_{XZ}(pq + \dot{r}) + \bar{q}SbC_{l_{aero}}$$

$$I_{YY}\dot{q} = (I_{ZZ} - I_{XX})pr + I_{XZ}(r^2 - p^2) + \bar{q}ScC_{m_{aero}}$$

$$I_{ZZ}\dot{r} = (I_{XX} - I_{YY})pq + I_{XZ}(\dot{p} - qr) + \bar{q}SbC_{n_{aero}}$$

These moments were broken down into three main components: aerodynamic, inertia coupling, and inertia cross-coupling terms. The lift and drag coefficients were calculated from C_X , C_Z , and corrected incidence angles as shown:

$$\begin{aligned}C_L &= C_X \sin \alpha_{\text{corr}} - C_Z \cos \alpha_{\text{corr}} \\C_D &= -C_X \cos \alpha_{\text{corr}} - C_Z \sin \alpha_{\text{corr}}\end{aligned}$$

In addition to these parameters, the Euler angles, pilot sticks, control surface commands and positions were available. All data presented in the figures, when appropriate, were scaled to full-scale aircraft values.

4.2.2 Wing Rock Test

A Drop model test was designed to explore the full six D.O.F. wing rock characteristics of the X-31 configuration. The test consisted first of trimming the aircraft into level-flight around $\alpha = 30^\circ$ with the flight control system active. Then, the lateral-directional flight controls were commanded to zero and the open loop response was recorded. The canard was still active during the test to minimize any α excursions. To facilitate data analysis, the Flight Control System mode signal (i.e., FCSMODE) marked the start and end points of the open loop section of the test.

4.2.2.1 Wing Rock Characteristics (Open Loop)

The results from the open loop test are summarized in Figures 73 to 85. The initial airspeed (c.f., Figure 73) is around 400 ft/sec ($M = 0.2$) at $\alpha = 30^\circ$ and near zero sideslip (c.f., Figure 74). The corresponding Reynolds

number based on \bar{c} is near 4.5×10^6 . As soon as the pilot selects the open loop mode, the X-31 Drop model experiences an undamped roll oscillation with a period of 2.0 seconds (full-scale) or an average reduced frequency of 0.1025. The oscillations grow exponentially with a rate time-to-double of about 1 second. From the angular rate data in Figure 75, the wing rock motions are predominantly body axis roll oscillations with peak roll rate values of $\pm 125^\circ/\text{sec}$ and sideslip angle of 42° . The yaw and pitch rates remain within $\pm 5^\circ/\text{sec}$ until the roll rate exceeded $\pm 100^\circ/\text{sec}$. This supports the assumption that the wing rock motions for small-to-moderate roll angles are predominantly body axis roll oscillations, which allows the use of nonlinear one D.O.F. simulations for wing rock prediction. In Figure 76, the θ_{sting} and ϕ_{sting} values calculated from the one D.O.F. auxiliary equations are compared to α and roll attitude, ϕ , respectively. Notice that the wing rock motion experienced in the Drop model reasonably matches the one D.O.F. values. The angle of attack never exceeds θ_{sting} and the ϕ_{sting} value slightly lags the model roll attitude. This reinforces the assumption that wing rock motions for small-to-moderate roll angles are predominantly body axis roll oscillations.

Nevertheless, as soon as the roll rate exceeds $100^\circ/\text{sec}$, the rolling motion couples with yawing and pitching motions, and subsequently, the configuration departs from controlled flight. The linear accelerations remain within normal operating values, but the lateral acceleration becomes oscillatory in response to the wing rock motion (c.f., Figure 77). The same pattern observed in the angular rates is seen in the angular accelerations (c.f., Figure 77). In Figure 78, the roll attitude starts around level flight and roll oscillations gradually build up. It is noteworthy that a

roll departure occurs before the static roll departure angles predicted from the Free-to-Roll tests (i.e., dashed line in Figure 78 represents ϕ_{\max} values at a given θ_{sting}). This reinforces the importance of the flight dynamics effect on the HIKR departure flight envelope guideline. Also, the α and β combination at the HIKR departure point is near the boundary depicted from the flight envelope guideline of Figure 71b. Another important finding is the close relationship between sideslip and roll attitude. As expected from one D.O.F. motions, both parameters are in phase with each other. Moreover, the roll attitude first derivative and roll rate show nearly the same amplitude and phase characteristics.

The configuration lift and drag coefficients are plotted in Figure 79. As expected, when the roll angle increases toward 50° , lift is lost and drag is increased. The calculated moment coefficients are presented in Figures 80 to 84. The total rolling moment is driven primarily by the aerodynamic term. In addition to the existing roll damping instability, as the roll oscillations build in amplitude, the total rolling moment exceeds the available lateral control power for the α region in question. In Figure 81, the phase plane diagram for these motions is included. It consists of an undamped, diverging spiral that never settles into a limit cycle. The rolling moment relationship with roll and sideslip angle is shown in Figure 81. The sideslip angle increased into the region of the sideslip reversal effect obtained from the Static-Force test. Also, the energy exchange for the last roll oscillation was a clockwise (i.e., destabilizing) loop causing a energy unbalance that resulted in the HIKR departure.

On the other hand, the yawing moment remains near zero until the yaw acceleration builds up and the product of roll rate and pitch rate becomes considerably large (c.f., Figure 82). At that point, the contribution from the yawing moment inertia coupling term becomes large and increasingly destabilizing. Since the configuration has a strong yaw damping instability, the total yawing moment continues to increase into large oscillations that exceeds the already reduced directional control. The combination of these lateral-directional moments propelled the configuration into a HIKR departure.

The Euler angles and rate of change for pitch and yaw are shown in Figure 83. The pitching moment remains near zero for most of the wing rock buildup (c.f., Figure 84). Nevertheless, when the pitch angular acceleration increases in magnitude, there is a considerable pitching moment increase. Also, the inertia coupling term becomes increasingly nose-down due to the extremely large roll and yaw rates that are out-of-phase. The aerodynamic pitching moment grows increasingly exceeding the inertia coupling term. The net result is a growing nose-up increase in total pitching moment. This increase at high angles of attack exceeds the pitch margin available for nose-down recovery as indicated previously. Notice from the control commands that after eight seconds, the canard is already saturated at its maximum nose-down deflection (c.f., Figure 85). The pitch attitude (c.f., Figure 83) shows a steady increase up to 20° . Its rate of change remains small. Nevertheless, as the pitching moment oscillations build up, the Drop model experience a steeper increase in pitch attitude up to 60° with a rate exceeding $30^\circ/\text{sec}$. Finally, the model

departs into an inverted hung stall and remains in it despite application of full nose-up controls.

4.2.2.2 Wing Rock Suppression Techniques

Ideally, the configuration should be aerodynamically designed to be wing rock resistant. Because of the nonlinear roll damping, strong sideslip effects, and forebody asymmetric flow behavior, the X-31 configuration is prone to wing rock at high angles of attack. To suppress the wing rock, two different approaches were taken. First, the configuration was altered by strategically mounting body strakes to interfere with the forebody flow mechanisms driving the wing rock motions. The body strakes tested in the Free-to-Roll study showed a considerable delay in the wing rock onset angle of attack. Nevertheless, one needs to look at the overall effect of the strakes on the X-31 configuration. From previous Static-Force tests (not shown), the strakes showed detrimental effects on the longitudinal and lateral-directional static stability. A second approach to wing rock suppression is to drive the lateral flight controls to negate the roll rate oscillations arising during wing rock. From the X-31 Free-Flight wind-tunnel test conducted by the NASA Flight Dynamics Branch, it was shown that using a high-gain roll rate damper scheduled with α effectively eliminated the roll oscillations. In Figure 86, angle of attack, roll rate and sideslip angle are shown versus time. Notice that before disengaging the roll damper, the angle of attack is close to 38° and the roll rate and sideslip angle remain near zero. As soon as the roll damper is disengaged, roll oscillations grow increasingly large with roll rate exceeding $\pm 50^\circ/\text{s}$. After twelve seconds, the roll damper is reengaged and roll oscillations are

immediately damped. From the Free-Flight wind-tunnel test, two important results are noteworthy. First, the roll damper is an effective wing rock suppression technique. Second, the X-31 configuration has sufficient roll control power to suppress small-to-moderate wing rock motions. From the Free-Flight tests, it was found that if the wing rock motions are allowed to grow to extremely large levels, the roll damper will not be able to suppress the motions. Moreover, two evident disadvantages of using the flight control system are that a high gain roll damper could (1) reduce the aircraft agility specially at high angles of attack and; (2) increase the system noise sensitivity. Therefore, if this approach is followed, one needs to optimize the roll damper gains for all flight conditions.

A Drop test was designed to show the roll damper gain effect on the wing rock motions. A nominal roll damper gain was designed from the wind-tunnel data at each angle of attack and tested in X-31 computer simulations. These nominal gains were designed to augment the roll damping to a satisfactory, stable level, which included a safety margin to account for possible discrepancies between wind-tunnel data and Drop model characteristics. Using the Drop model flight control system, one can change the roll damper nominal gain during flight while recording real-time dynamic responses. As illustrated in Figure 87, three levels of roll damper gains were tested for $\alpha = 38^\circ$. At 50% of the nominal gain, roll oscillations grow increasingly large. As the gain increases from 50% to 100% of the nominal gain, the roll oscillations are considerably reduced. Varying the roll damper gain, one could find the roll damper gain which

makes the configuration marginally stable (i.e., $\overline{C_{l_p}} = 0$). Analyzing the roll rate oscillations, this gain should lie between 70% and 100% of the nominal gain. At 70% of the nominal gain, the sideslip angle is within $\pm 2.5^\circ$ and the roll rate oscillates between $\pm 10^\circ/\text{sec}$. When the nominal gain is restored to 100%, the oscillations in roll rate and sideslip essentially die out. Also, later in flight (not shown), the nominal gain is reduced to 80% with similar results as in the 100% case. At this angle of attack, it is clear that a 20% reduction in the nominal roll damper gain is possible without adversely affecting the system roll stability. Although a gain reduction is possible at this angle of attack, it cannot be assumed that a reduction can be applied to all flight conditions without testing at each angle of attack.

4.2.3 High Incidence Kinematic Roll Departure Characteristics

From the Free-to-Roll tests, a body axis HIKR departure was experienced at high angles of attack. Likewise, during a Drop test designed to study spin characteristics, the Drop model departed from a spin into a HIKR departure. In Figures 88 to 98, time histories are presented for this flight. As the angle of attack increases, the model encounters a yawing asymmetry to the left. Then, the pilot puts the model into a spin by rapidly pulling nose-up and crossing the lateral-directional controls (c.f., Figures 88 and 89). Entering the spin, the pilot engages a flight control system mode that will produce full pro-spin trailing-edge flap differential and rudder deflections and disable all feedback states. The Drop model remains in a left spin with a maximum yaw rate of $-65^\circ/\text{sec}$ and angle of attack above 90° (c.f., Figure 90). Before reaching a steady spin, the model

departs into a sustained HIKR. During the HIKR, kinematic exchange of α and β is shown in Figure 90. Although the roll rate exceeded the instrument limit of $\pm 250^\circ/\text{sec}$ (c.f., Figure 91), the maximum roll rate was computed from video image analysis to be $374^\circ/\text{sec}$. During the sustained HIKR, the model yaw and pitch rate values from the spin decay significantly. The roll angle time history shows roll oscillations build up prior to the HIKR departure (c.f., Figure 92). The roll angle departure value correlates with the one D.O.F. static departure guidelines. In Figure 93, using the one D.O.F auxiliary equations, the θ_{sting} and ϕ_{sting} values were calculated and compared to the angle of attack, α , and roll attitude, ϕ , respectively. Notice that the HIKR motion experienced in the Drop model reasonably matches the one D.O.F. values. As expected from the one D.O.F. motions, the angle of attack never exceeds θ_{sting} . This suggest that the HIKR departure is predominantly a body axis roll motion (i.e., minimal yawing motion).

Presented in Figure 91, the model linear accelerations show oscillations in the normal acceleration between 1 and -1 g's and in the lateral acceleration between 0.5 and -2 g's for almost ten seconds. From the handling qualities point of view, these are very undesirable motions that could potentially disable the pilot. The angular accelerations are given in Figure 94, and as illustrated in Figure 95, the rolling moment is driven by the aerodynamic term even during the spin. Oscillations in the rolling moment coefficient of nearly ± 0.1 occur during the spin, which are primarily due to wing rock oscillations since there is no roll damper active during this phase of the test. The total rolling moment shows a large positive increase just before going into the sustained HIKR. In Figure 96,

the total yawing moment is shown to be quite low throughout the spin. Nevertheless, during the sustained HIKR, the total yawing moment is substantially large primarily due to the inertia coupling term. Notice that the aerodynamic term shows an additional small yawing moment in the same direction as the inertia term. In Figure 97, the model heading shows 3 full turns and then enters into a HIKR departure. During the sustained HIKR departure, there is a growing increase in heading oscillations due to the yawing moment oscillations. Also, the pitch attitude starts negative during the spin and settles around -5° entering the HIKR. During the sustained HIKR departure, some pitch oscillations are evident. As illustrated in Figure 98, the total pitching moment oscillates during the spin, but it increasingly grows into extremely large values during the HIKR departure. During the spin, the inertia coupling term is the dominant term, whereas the aerodynamic term remains near zero. As the HIKR departure emerges, the aerodynamic term grows larger than the inertia coupling term primarily due to large sideslip changes. This correlates well with the large sideslip effects on pitching moment shown from the Static-Force tests. After the cross-controls are released, the model subsequently recovers from the sustained HIKR into an inverted hung stall. Unfortunately, even with all longitudinal controls deflected to their nominal nose-up positions (i.e., $\delta_c = +20^\circ$, $\delta_{f_{TESYMM}} = -30^\circ$ shown in Figure 89), the maximum nose-up pitching moment available is not enough to bring the model back to level flight.

Finally, it should be noted that the HIKR departure was encountered primarily by a build up of wing rock oscillations. Also, the sideslip angle, as predicted from the Static-Force tests, is a dominant factor in the entry

to a sustained HIKR. Although the model exhibited a dominant body axis roll, there is a substantial build up of pitching moment due also to the large sideslip effects. The departure from controlled flight could disable the pilot or maneuver the model into unstable equilibrium points (i.e., hung stall). Notice that as the lateral-directional controls are relaxed, the sustained HIKR characteristics die out. Moreover, subsequent Drop model flights show that with an active roll damper, no HIKR departures are experienced during spin entries.

4.3 Nonlinear Simulation Results

The rolling moment differential equation in the nonlinear math model was solved by using the Runge-Kutta method. Initial conditions were varied to simulate different flight conditions. In particular, three different θ_{sting} settings (i.e., 28° , 30° and 32°) were tested in the math model. The initial perturbation to induce the wing rock behavior was a release at nonzero roll angle. An initial estimate of the oscillation frequency and amplitude is required for the calculation of the roll damping term as detailed in Appendix A. In order to compare simulation results to those obtained from other tests, the computed data was scaled to full-scale values.

At $\theta_{\text{sting}} = 28^\circ$, time histories were computed for the roll angle, roll rate, angle of attack, sideslip angle, and rolling moment. In Figure 99, roll angle and roll rate are plotted versus time. The roll angle settles into a limit cycle with a wing rock amplitude of $\pm 15^\circ$. The roll rate builds up to $\pm 25^\circ/\text{sec}$ and the sideslip angle grows to $\pm 8^\circ$. As illustrated in Figure 100, the aerodynamic rolling moment magnitude was under 0.02 for this limit cycle. Using the same conceptual tools as in the Free-to-Roll tests, the phase plane diagram shows a steady limit cycle. Moreover, the rolling moment dependence on roll angle is include in Figure 101. Notice the clockwise (i.e., destabilizing) loop for roll angle magnitudes lower than 8° , and the counterclockwise (i.e., stabilizing) loops for larger roll angles. By looking at the areas of the loops, it is reasonable to assume that the sum of the areas of the outer loops equals the area of the inner loop making the total energy exchange equal to zero. This condition will guarantee limit

cycle without a roll departure. As the sting pitch setting was increased, more critical responses were obtained. At $\theta_{\text{sting}} = 30^\circ$, the roll oscillation amplitude builds to 25° with a roll rate of $\pm 42^\circ/\text{sec}$ (c.f., Figure 102). There is an almost 100% increase in the aerodynamic rolling moment with sideslip angle under $\pm 15^\circ$ (c.f., Figure 103). The phase plane diagram shows an increasing-radius spiral which eventually settles into limit cycle (c.f., Figure 104). The energy loop areas are much larger than in the 28° case. Inner loops are shown with the same characteristics as in the previous case- stabilizing outer loops and destabilizing inner loop. Moreover, when the angle of attack is further increased to 32° , the roll oscillations amplitude gradually builds to $\pm 45^\circ$. The roll rate oscillates around $\pm 75^\circ/\text{sec}$ during the sustained limit cycles (c.f., Figure 105). The total aerodynamic rolling moment magnitude peaks around 0.07 (c.f., Figure 106). Again, this is a 100% increase from the $\theta_{\text{sting}} = 30^\circ$ case and almost 4 times the aerodynamic moment computed at the $\theta_{\text{sting}} = 28^\circ$ case. The sideslip angle increased to $\pm 22^\circ$. Notice from the rolling moment time history that there are indications of an impending roll departure. The restoring rolling moment almost changes direction when the roll angle is at its highest value. This implies that the sideslip angle is approaching its reversal effect region in the rolling moment curve as discussed in the Static-Force and Free-to-Roll results. From the energy exchange stand point, the rolling moment curve shows the existence of small, destabilizing outer loops (c.f., Figure 107). If the stabilizing loop area is not large enough to counteract these outer loops, the configuration will experience a propelling moment which in turn will be enough to cause a HIKR departure. The phase plane diagram for this case shows the configuration settling into a higher limit cycle than in the previous cases.

A summary of wing rock characteristics for the nonlinear simulation is presented in Table V. Comparing these results to the Free-to-Roll results, it is evident that the nonlinear math model well predicts the wing rock motions at a given angle of attack. A comparison of the wing rock parameters between the Free-to-Roll and simulation results is shown in Table VI. Notice the close match for roll rates and sideslips angles. The aerodynamic moments differ slightly except for the $\theta_{\text{sting}} = 32^\circ$ case. The nonlinear simulation motions match the Free-to-Roll amplitudes, but differ slightly in the average reduced frequencies.

Finally, the ability to predict wing rock motions using the nonlinear simulation requires a prior knowledge of the wing rock frequency. If Free-to-Roll tests are not available, one might not be able to accurately use the simulation unless one finds another way to obtain the wing rock frequency. From the previous wing rock studies, a relation between Dutch Roll and wing rock frequencies was established for some aircraft. Comparing the X-31 Dutch Roll frequency to the wing rock frequency obtained from the Free-to-Roll tests, it is fortunate that the wing rock average reduced frequencies obtained from the Free-to-Roll tests and nonlinear simulations are only slightly larger than the X-31 Dutch Roll natural reduced frequency. The Dutch Roll reduced frequency computed from a linear, 3 D.O.F. lateral-directional math model (i.e., see Appendix C for model description and results) is 0.10846 at $\alpha = 30^\circ$ and 0.1417 at $\alpha = 34^\circ$. Therefore, one can use the Dutch Roll frequency for the initial frequency value needed for the nonlinear simulation, allowing the possibility for wing rock predictions prior to Free-to-Roll tests.

5.0 CONCLUSIONS/RECOMMENDATIONS

5.1 Conclusions

Because of poor roll damping characteristics coupled with strong lateral static stability (i.e., strong dihedral effect) and nonlinear sideslip effect on rolling moment, the X-31 configuration at high angles of attack is susceptible to the wing rock phenomenon. From captive and free-flight tests, the results of the wing rock study for the X-31 configuration may be summarized as follows:

1. Self-induced body axis roll oscillations build to limit cycles for $\alpha > 24^\circ$. The wing rock amplitude increases with α . Between $32^\circ < \alpha < 45^\circ$, the wing rock motions become divergent.
2. Wing rock onset α varies with the configuration geometry. Forebody geometry changes do not significantly alter or eliminate the fundamental wing rock characteristics.
3. The triggering mechanism for the wing rock motions for the X-31 configuration is the interaction of asymmetric forebody flow with the forward fuselage. On the other hand, the main driving mechanism, which amplified the wing rock motions, is the interaction of the forward fuselage flow field with the wings and aft fuselage, including the vertical tail. Flow visualization studies reinforce the theory of forward fuselage flow interaction with wings and aft fuselage.
4. The nonlinear sideslip effect on rolling moment is shown to be a major factor in sustaining wing rock limit cycles. The aerodynamic rolling moment is dependent on sideslip angle. Large aerodynamic rolling

moments from the Free-to-Roll and Drop model wing rock tests exceed the lateral control power available at the given flight conditions.

5. Two wing rock suppression techniques were explored: a) an aerodynamic approach using configuration modifications and b) Flight Control System approach. Body strakes were tested on the forward fuselage. They successfully delay the onset α past the stall region deep into the post stall region. Also, wing rock motions can be effectively suppressed with a high-gain roll damper.

6. Phase plane diagrams reveal the presence of three unstable equilibrium points at high angles of attack: a) unstable focus, b) & c) two saddle points. The unstable focus trajectories settle into limit cycles or diverge into HIKR departures. The two saddle points are the static departure roll angles associated with the HIKR departure. The departure roll angles encountered in the Drop model flight data correlate well with Free-to-Roll and Static-Force results.

7. Nonlinear simulation based on wind-tunnel data successfully predicts wing rock motions at high angles of attack for the X-31 configuration.

If the wing rock motions are allowed to increasingly grow, the X-31 configuration can experience a High Incidence Kinematic Roll departure. HIKR departures are characterized by a high incidence angle between the fuselage center line and the wind, a nonlinear destabilizing sideslip effect on rolling moment, and the kinematic exchange of α and β . Flow visualization studies indicate that the interaction of the forward fuselage asymmetric vortical flow with the wings is the triggering mechanism for the HIKR departure. A flight envelope guideline was calculated for α and β

flight conditions which could drive the configuration into HIKR departures. The sustained HIKR characteristics are extremely undesirable. The pitching and rolling moments can grow increasingly large with sideslip angle, as predicted by the Static-Force tests. The sustained HIKR departure characteristics show that there is a possibility of disabling the pilot or maneuvering the configuration into unstable equilibrium points (i.e., hung stall). Nevertheless, the HIKR departure can be avoided by maintaining lateral-directional stability augmentation.

5.2 Recommendations for Further Study

1. Perform Forced-Oscillation tests around non-zero roll angle. This data should confirm the sideslip effects on roll damping found in Rotary Balance tests.

2. Perform Bifurcation analysis for the wing rock region. The analysis results should complete the phase diagrams obtained from the wing rock motions and HIKR departure.

3. Perform additional wing rock wind-tunnel tests, including a more rigorous flow study using different flow visualization techniques. This can precisely determine the wing rock vortex locations on wing and fuselage.

4. Design additional Drop model tests to verify sustained wing rock and HIKR departure characteristics at different angles of attack. Correlate results with wind-tunnel data.

5. Validate aerodynamic model from the Drop model and full-scale flight test results in order to optimize roll damper gains for all angles of attack. This could be accomplished by using the nonlinear math model with optimal control theory. Then, the simulation-derived gains should be verified using the Drop model or Free-Flight test techniques.

6. Perform generic fighter model investigation to determine wing planform geometry and placement effect on HIKR departure characteristics.

REFERENCES

1. Nguyen, L. T.; and Gilbert, W. P. : Impact of Emerging Technologies on Future Combat Aircraft Agility. AIAA-90-1304, May 1990.
2. McKinney, M.O.; and Drake, H.M. : Flight Characteristics at Low Speed of Delta-Wing Models. NACA RM No. L7R07, Jan.1948.
3. Paulson, J.S.; and Shanks, R.E. : Investigation of Low-Subsonic Flight Characteristics of a Model of a Flat-Bottom Hypersonic Boost-Glide Configuration Having a 78° Delta Wing. NASA TN D-894, 1961.
4. Shanks, R.E. : Low-Subsonic Measurements of Static and Dynamic Stability Derivatives of Six Flat-Plate Wings Having Leading-Edge Sweep Angles of 70° to 84° . NASA TN D-1822, 1963.
5. Boisseau, P.C. : Investigation of the Low-Subsonic Flight Characteristics of a Model of a Reentry Vehicle With a Thick Flat 78° Swept Delta Wing and a Half-Cone Fuselage. NASA TN D-1007, 1962.
6. Ross, A.J. : Investigation of Nonlinear Motion Experienced on a Slender-Wing Research Aircraft. Journal of Aircraft, Vol. 9, No. 9, Sept. 1972.
7. Ross, A.J.; and Nguyen, L.T. : Some Observations Regarding Wing Rock Oscillations at High Angles of Attack. AIAA-88-4371-CP, Aug.1988.
8. McElroy, C.E.; and Sharp, P.S. : Stall/Near Stall Investigation of the F-4E Aircraft. AFFTC Report FTC-SD-70-20, 1970.
9. Chambers, J.R.; and Anglin, E.L. : Analysis of Lateral-Directional Stability Characteristics of a Twin-Jet Fighter Airplane at High Angles of Attack. NASA TN D-5361, 1969.

10. Burris, W.R.; and Lawrence, J.T. : Aerodynamic Design and Flight Test of U.S. Navy Aircraft at High Angles of Attack. AGARD-CP-102, Paper 25, Apr. 1972.
11. Young, P.D.: Wing Rock as a Lateral-Directional Aircraft Limit Cycle Oscillation Induced by Nonlinear Aerodynamics Occurring at High Angle of Attack. M.S. Thesis, Naval Postgraduate School, June 1977.
12. Skow, A.M.; and Titiriga, A., Jr. : A survey of Analytical and Experimental Techniques to Predict Aircraft Dynamic Characteristics at High Angles of Attack. AGARD-CP-260, Paper 10, Sept. 1978.
13. Skow, A.M.; and Erickson, G.E. : Modern Fighter Aircraft Design for High-Angle-of-Attack Maneuvering. AGARD-LS-121, 1982.
14. Grafton, S.B.; Chambers, J.R.; and Coe, P.L., Jr.: Wind Tunnel Free-Flight Investigation of a Model of a Spin-Resistant Fighter Configuration. NASA TN D-7716, June 1974.
15. Ross, A.J.: Lateral Stability at High Angles of Attack, Particularly Wing Rock. AGARD-CP-260, Paper 10, Sept. 1978.
16. Bore, C.L. : Post Stall Aerodynamics of the Harrier GRI. AGARD-CP-102, Paper 19, Apr. 1972.
17. Nguyen, L.T.; Gilbert, W.P.; Gera, J.; Iliff, K.W.; and Enevoldson, E.K.: Application of High- α Control System Concepts to a Variable Sweep Fighter Airplane. AIAA Flight Mechanics Conference, Aug.1980.
18. Nguyen, L.T.; Yip, L.P.; and Chambers, J.R.: Self-Induced Wing Rock of Slender Delta Wings. AIAA-81-1883, Aug. 1981.
19. Nguyen, L.T.; Whipple, R.D.; and Brandon, J.M. : Recent Experiences of Unsteady Aerodynamic Effects on Aircraft Flight Dynamics at High Angles Of Attack. AGARD-CP-386, May 1985.

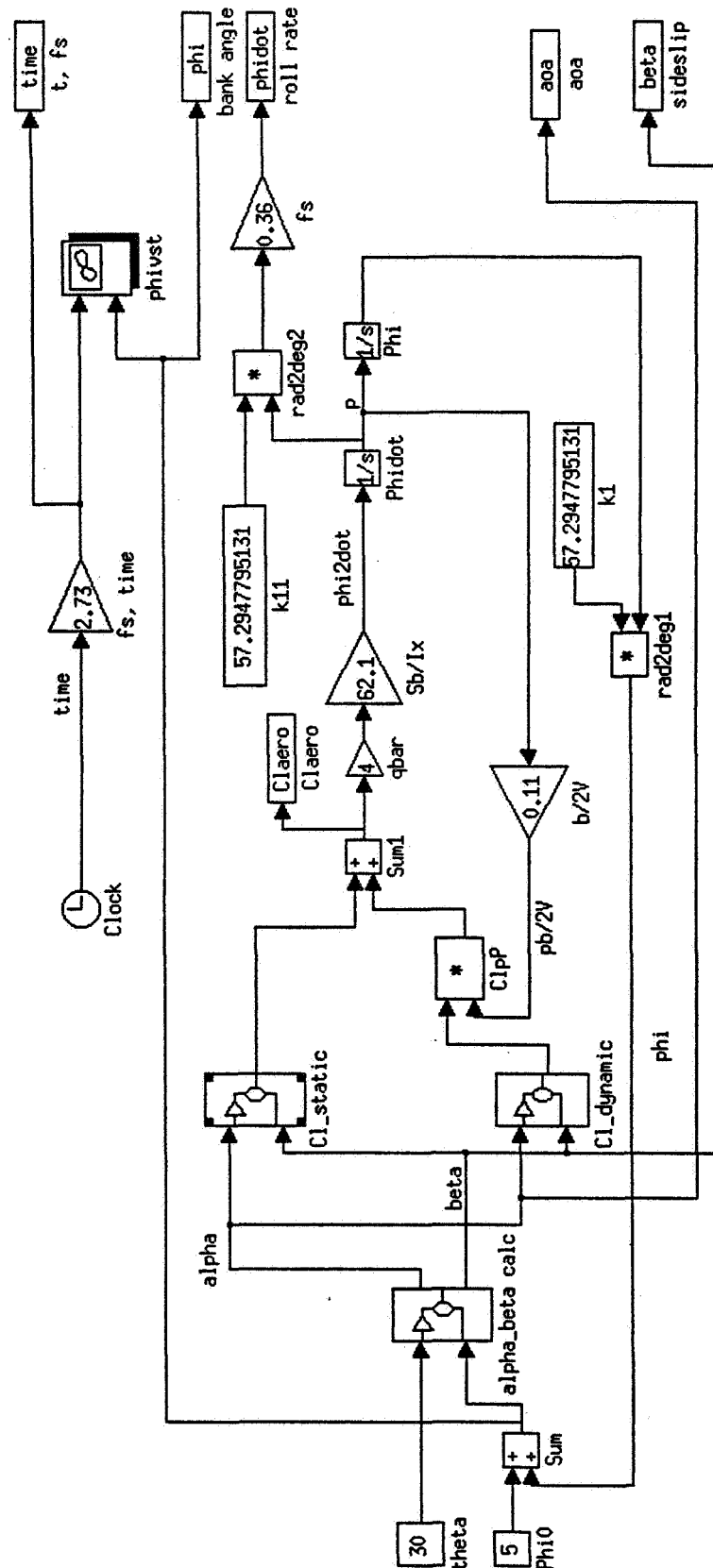
20. Croom, M.A.; Whipple, R.D.; Murri, D.G.; Grafton, S.B.; and Fratello, D.J. : High-Alpha Flight Dynamics Research On The X-29 Configuration Using Dynamic Model Test Techniques. SAE-88-1420, Oct. 1988.
21. Quast, T.; Nelson, R.C.; and Fisher, D.F. : High Alpha Dynamics and Flow Visualization for a 2.5 percent model of the HARV Undergoing Wing Rock. AIAA- 91-3267, Sept. 1991.
22. Chambers, J.R.; Gilbert, W.P.; and Nguyen, L.T.: Results of Piloted Simulator Studies of Fighter Aircraft at High Angles of Attack. AGARD-CP-235, Paper 33, May 1978.
23. Hsu, C.H.; and Lan, C.E.: Theory of Wing Rock. Technical Report CRINC-FRL-516-1, Feb. 1984. AIAA-85-0199, Jan. 1985.
24. Schmidt, L.V.: Wing Rock due to Aerodynamic Hysteresis. Journal of Aircraft, Vol. 16, No.3, Mar. 1979.
25. Ericsson, L.E.: Flow Phenomena Causing Wing and Body Rock. AIAA-84-2177, Aug. 1984.
26. Konstadinopoulos, P.; Mook, D.T.; and Nayfeh, A.H. : Subsonic Wing Rock of Slender Delta Wings. AIAA-85-0198, Jan. 1985.
27. Orlik-Ruckemann, K.J. : Aerodynamic Aspects of Aircraft Dynamics at High Angle of Attack. AIAA-82-1363, Aug. 1982.
28. Chambers, J.R.; and Grafton, S.B.: Investigation of Lateral-Directional Stability of a Tilt-Wing V/STOL Transport. NASA TN D-5673, 1970.
29. Dickes, E.; Barnhart, B.; and Bihrlé, W., Jr.: Analysis of Static and Rotational Aerodynamics at High Angles of Attack for Rockwell X-31A. BAR 91-7, Oct. 1991.

30. Fratello, D.J.; Croom, M.A.; and Nguyen, L.T.: Use of the Updated NASA Langley Radio-Controlled Drop-Model Technique for High-Alpha Studies of the X-29 Configuration. AIAA-87-2559, Aug. 1987.
31. Nguyen, L.T.; and Foster, J.V.: Development of a Preliminary High-Angle-of-Attack Nose-Down Pitch Control Requirement for High Performance Aircraft. NASA TM-101684, Feb. 1990.
32. Moul, M.T.; and Paulson, J.W.: Dynamic Lateral Behavior of High-Performance Aircraft. NACA RM L58E16, 1958.
33. Weissman, R.: Status of Design Criteria for Predicting Departure Characteristics and Spin Susceptibility. AIAA-74-791, Aug. 1974.
34. Brandon, J.M.; and Nguyen, L.T.: Experimental Study of Effects of Forebody Geometry on High Angle of Attack Static and Dynamic Stability. AIAA-86-0331, Jan. 1986

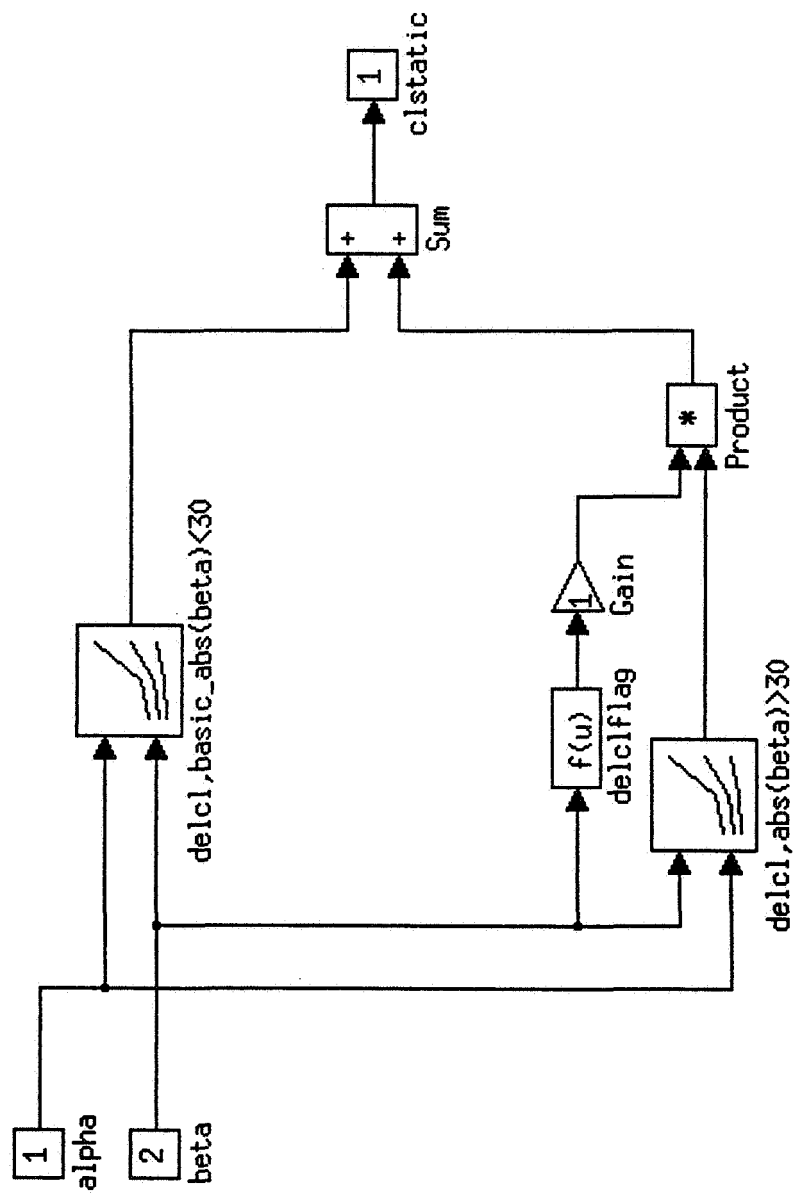
APPENDIX A
BLOCK DIAGRAMS FOR NONLINEAR SIMULATION

BLOCK DIAGRAMS FOR NONLINEAR SIMULATION

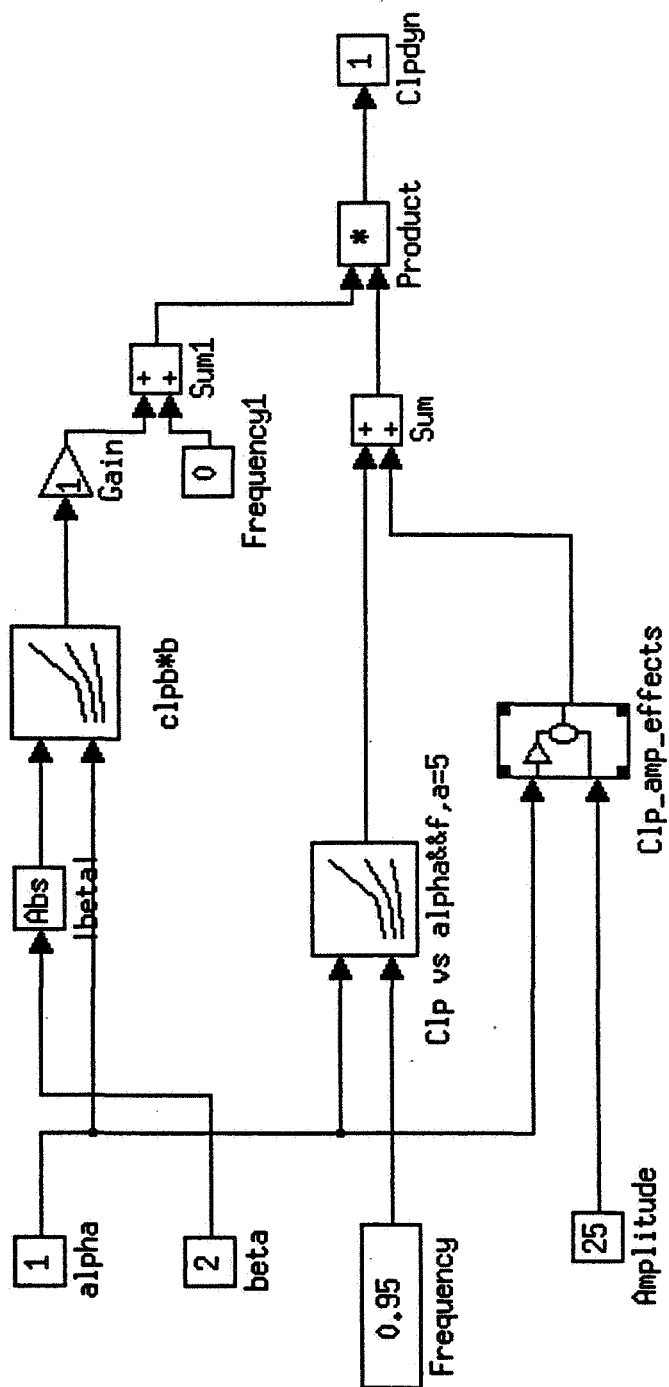
The X-31 Wing Rock one D.O.F. nonlinear math model is shown in Block Diagram 1. Given a constant θ_{sting} (i.e., theta) and initial roll angle (i.e., Φ_0), the corresponding α and β values are calculated using the one D.O.F. auxiliary equations (i.e., alpha_beta calc block). At this flight condition, the rolling moment from Static-Force tests and the roll damping term from Forced-Oscillation test including the sideslip dependency from Rotary Balance test are obtained. In Block Diagram 2, the increment in rolling moment depends on the sideslip angle. For $|\beta| \geq 30^\circ$, the large sideslip effect on rolling moment obtained from the Static-Force test results is included. Otherwise, the rolling moment is obtained from the Static-Force test results for $|\beta| \leq 30^\circ$. In Block Diagram 3, the roll damping term is calculated from the Forced-Oscillation test results for a given frequency and amplitude of oscillation. Notice that a roll damping multiplier from the Rotary Balance tests results for different sideslip angles is included. In Block Diagram 1, the roll damping term is multiplied by nondimensional roll rate and added to the static rolling moment. This total aerodynamic moment is used to solve for the roll acceleration. Subsequent integrations give roll rate and angle at this flight condition. The roll angle, like the roll rate, are used as state feedbacks in the model.



Block Diagram 1. X-31 Wing Rock one D.O.F. Nonlinear Math Model
68



Block Diagram 2. Rolling moment coefficient from Static-Force Tests



Block Diagram 3. Roll damping coefficient from Dynamic Tests

APPENDIX B
DROP MODEL DATA ANALYSIS SYSTEM
PROGRAM LISTING

```

/*X-31 Drop Aero Program 8-14-92*/
#include <math.h>
#include <stdio.h>
#include <stdlib.h>
#include <string.h>
#include <time.h>
#define PI 3.14159
#define rad2deg 180/PI
#define deg2rad PI/180
/*Drop model Specs*/
#define fsbird -1.7651667 /*bird and cg location in feet*/
#define fscg 6.0008333
#define blbird 0.4062500
#define blcg 0.0
#define wlcg -0.0466667
#define wlbird -0.5
#define xax -0.3850 /*accel location in feet from cg to instr*/
#define yax 0.0938
#define zax -0.3233
#define xay -0.2648
#define yay -0.0938
#define zay -0.4275
#define xaz -0.3742
#define yaz -0.0365
#define zaz -0.3650
#define WT 16.44907 /*slugs*/
#define ix 9.46 /*slugs-feet squared*/
#define iy 118.84 /*slugs-feet squared*/
#define iz 116.97 /*slugs-feet squared*/
#define ixz -0.39 /*slugs-feet squared*/
#define S 16.49727 /* feet squared */
#define b 6.16491 /*feet*/
#define cbar 3.3345 /*feet*/
#define G 32.2 /*feet per sec squared*/
#define BLANK ' '
#define NEWLINE '\n'
#define true 1
#define false 0

main(){
double datval ;
double tul[k[200000],cnrd_cmd[200000],f_rin_cmd[200000],f_rot_cmd[200000];
double f_lin_cmd[200000],f_lot_cmd[200000],rud_cmd[200000],in_lip_cmd[200000];
double pitch_stk[200000],roll_stk[200000],yaw_stk[200000],t1k[200000];
double qhigh[200000],beta[200000],plow[200000],qlow[200000],rlow[200000];
double cnrd_cpt[200000],f_rot_cpt[200000],f_rin_cpt[200000],f_lot_cpt[200000];
double f_lin_cpt[200000],rud_cpt[200000],phigh[200000],aoa1[200000],t2c[40000];
double rhigh[40000],axr[40000],azr[40000],roll[40000],Vbird[40000],ayr[40000];
double fcs_mode[200000],t1c[20000],theta1[20000],aoa2[20000],theta2[20000];
double psi[20000],in_lip_cpt[20000],t1dc[20000],h[20000],x[20000],y[20000];
double cnrd_cmd_dot[200000],f_rin_cmd_dot[200000],f_rot_cmd_dot[200000];
double f_lin_cmd_dot[200000],f_lot_cmd_dot[200000],rud_cmd_dot[200000];
double in_lip_cmd_dot[200000],pitch_stk_dot[200000],roll_stk_dot[200000];
double yaw_stk_dot[200000],f_symm_cmd[200000],f_symm_cmd_dot[200000];

```

```

double    f_diff_cmd[200000],f_diff_cmd_dot[200000],qhigh_dot[200000];
double    beta_dot[200000],plow_dot[200000],qlow_dot[200000],rlow_dot[200000];
double    cnrd_cpt_dot[200000],f_rot_cpt_dot[200000],f_rin_cpt_dot[200000];
double    f_lin_cpt_dot[200000],f_lot_cpt_dot[200000],rud_cpt_dot[200000];
double    phigh_dot[200000],aoa1_dot[200000],f_symm_cpt[200000],f_diff_cpt[200000];
double    f_symm_cpt_dot[200000],f_diff_cpt_dot[200000],rhigh_dot[40000];
double    roll_dot[40000],roll_2dot[40000],theta1_dot[20000],theta1_2dot[20000];
double    aoa2_dot[20000],theta2_dot[20000],theta2_2dot[20000],psi_dot[20000];
double    psi_2dot[20000],in_lip_cpt_dot[20000],h_dot[20000],qsel[20000];
double    qdot[20000],psel[20000],pdot[20000],rsel[20000],rdot[20000],aoa[20000];
double    aoadot[20000],aoarad,betarad,prad,qrad,rrad,ubird,u[20000],v[20000];
double    w[20000],vcorr[20000],aoacorr[20000],betacorr[20000],rho,temp,mu;
double    val,thetasting[20000],phisting[20000];
double    re[20000],qbar[20000],mach[20000],cax,cay,caz,ax[20000],ay[20000];
double    az[20000],fx,fy,fz,cx[20000],cy[20000],cz[20000],clift[20000];
double    cdrag[20000],ldratio[20000],txic,txicx,tyic,tyicx,tzic,tzicx,tx,ty,tz;
double    clic[20000],clix[20000],cl[20000],cmic[20000],cmicx[20000],cm[20000];
double    cnic[20000],cnicx[20000],cn[20000],claero[20000],cmaero[20000];
double    cnaero[20000],omega2[20000],u_dot[20000],v_dot[20000],w_dot[20000];
double    vcorr_dot[20000],de1,de2,de3,betacorr_dot[20000],aoacorr_dot[20000];
double    avg(),ti,tf;
int    n,l,i,c,s,bk,count,ok,nul k,n1k,n1c,n2c,n1dc,go,done;
char    signal[20],drop[4],ul[8],dl1k[8],dl2c[8],dl1c[8],dc[8];
FILE    *fp, *fopen();

```

```

ti=44.0;
tf=49.0;
drop[0]='1';
drop[1]='0';

/* data readings */
/*uplink 1000 Hz*/
l=0;
s=0;
bk=0;
go=false;
ok=false;
done=false;
strcpy(ul,drop);
strcat(ul,"ul1k");
fp = fopen (ul,"r");
while((c=fgetc(fp)) != EOF)
{
    if(c != BLANK && c != NEWLINE)
    {
        signal[s]=c;
        s++;
        bk=0;
        go=true;
    }
    else{
        bk++;
        if (bk==1 && go)
        {
            signal[s]='\0';
            count++;

```

```

        datval=atof(signal);
        if (count==1 && datval >= ti)
            ok=true;
        if (count==1 && datval > tf)
        {
            ok=false;
            done=true;}
        if(ok)
        {
            switch(count){
                case 1: tulk[l]=datval;
                    break;
                case 2: cnrd_cmd[l]=datval;
                    break;
                case 3: f_rin_cmd[l]=datval;
                    break;
                case 4: f_rot_cmd[l]=datval;
                    break;
                case 5: f_lin_cmd[l]=datval;
                    break;
                case 6: f_lot_cmd[l]=datval;
                    break;
                case 7: rud_cmd[l]=datval;
                    break;
                case 8: in_lip_cmd[l]=datval;
                    break;
                case 9: fcs_mode[l]=datval;
                    break;
                case 10: pitch_stk[l]=datval;
                    break;
                case 11: roll_stk[l]=datval;
                    break;
                case 12: yaw_stk[l]=datval;
                    break;
                default: break;
            }
        }
    }
    s=0;
}
if(c==NEWLINE)
{
    if (count != 17)
        printf("\n Column number mismatch error.....");
    count=0;
    if (ok)
        l++;
}
if (done)
    break;
}
fclose(fp);
nul1k=1;
printf("\nDone reading ul1k");

/*downlink 1000 Hz*/

```

```

l=0;
s=0;
bk=0;
count=0;
go=false;
done=false;
ok=false;
strcpy(dllk,drop);
strcat(dllk,"dllk");
fp = fopen (dllk,"r");
while((c=fgetc(fp)) != EOF)
{
    if(c != BLANK && c != NEWLINE)
    {
        signal[s]=c;
        s++;
        bk=0;
        go=true;
    }
    else{
        bk++;
        if (bk==1 && go)
        {
            signal[s]='\0';
            count++;
            datval=atof(signal);
            if (count==1 && datval >= ti)
                ok=true;
            if (count==1 && datval > tf)
            {
                ok=false;
                done=true;}
            if(ok)
            {
                switch(count){
                    case 1: t1k[l]=datval;
                        break;
                    case 14: qhigh[l]=datval;
                        break;
                    case 3: beta[l]=datval;
                        break;
                    case 4: plow[l]=datval;
                        break;
                    case 5: qlow[l]=datval;
                        break;
                    case 6: rlow[l]=datval;
                        break;
                    case 7: cnrd_cpt[l]=datval;
                        break;
                    case 8: f_rot_cpt[l]=datval;
                        break;
                    case 9: f_rin_cpt[l]=datval;
                        break;
                    case 10: f_lot_cpt[l]=datval;
                        break;
                    case 11: f_lin_cpt[l]=datval;
                        break;
                    case 12: rud_cpt[l]=datval;
                        break;

```



```

        case 13: phigh[l]=datval;
                break;
        case 2:  aoal[l]=datval;
                break;
        default: break;
    }
}
}
s=0;
}
if(c==NEWLINE)
{ if (count != 14)
    printf("\n Column number mismatch error.....");
    count=0;
    if (ok)
        l++;
}
if (done)
    break;
}
fclose(fp);
nlk=l;
printf("\nDone reading dl1k");

/*downlink 200 Hz*/
l=0;
s=0;
bk=0;
count=0;
ok=false;
done=false;
go=false;
strcpy(dl2c,drop);
strcat(dl2c,"dl2c");
fp = fopen (dl2c,"r");
while((c=fgetc(fp)) != EOF)
{ if(c != BLANK && c != NEWLINE)
    { signal[s]=c;
      s++;
      bk=0;
      go=true;
    }
    else{
      bk++;
      if (bk==1 && go)
      { signal[s]='\0';
        count++;
        datval=atof(signal);
        if (count==1 && datval >= ti)
            ok=true;
        if (count==1 && datval > tf)
        { ok=false;
          done=true;}
      }
    }
}

```

```

        if(ok)
        {
            switch(count){
                case 1: t2c[l]=datval;
                        break;
                case 2: rhigh[l]=datval;
                        break;
                case 3: axr[l]=datval;
                        break;
                case 4: azr[l]=(-1)*datval;
                        break;
                case 5: roll[l]=datval;
                        break;
                case 7: Vbird[l]=datval;
                        break;
                case 8: ayr[l]=datval;
                        break;
                default: break;
            }
        }
    }
    s=0;
}
if(c==NEWLINE)
{ if (count != 10)
    printf("\n Column number mismatch error.....");
    count=0;
    if (ok)
        l++;
    }
    if (done)
        break;
}
fclose(fp);
n2c=l;
printf("\nDone reading dl2c");

/*downlink 100 Hz*/
l=0;
s=0;
bk=0;
count=0;
ok=false;
done=false;
go=false;
strcpy(dl1c,drop);
strcat(dl1c,"dl1c");
fp = fopen (dl1c,"r");
while((c=fgetc(fp)) != EOF)
{ if(c != BLANK && c != NEWLINE)
    { signal[s]=c;
      s++;
      bk=0;
      go=true;

```

```

    }
    else{
        bk++;
        if (bk==1 && go)
        {
            signal[s]='\0';
            count++;
            datval=atof(signal);
            if (count==1 && datval >= ti)
                ok=true;
            if (count==1 && datval > tf)
            {
                ok=false;
                done=true;}
            if(ok)
            {
                switch(count){
                    case 1: tlc[l]=datval;
                        break;
                    case 2: theta1[l]=datval;
                        break;
                    case 4: aoa2[l]=datval;
                        break;
                    case 13: theta2[l]=datval;
                        break;
                    case 15: psi[l]=datval;
                        break;
                    case 16: in_lip_cpt[l]=datval;
                        break;
                    default: break;
                }
            }
        }
        s=0;
    }
    if(c==NEWLINE)
    { if (count != 27)
        printf("\n Column number mismatch error.....");
        count=0;
        if (ok)
            l++;
    }
    if (done)
        break;
}
fclose(fp);
nlc=l;
printf("\nDone reading dl1c");

/*downlink Data Converter 100 Hz*/
l=0;
s=0;
bk=0;
count=0;
ok=false;

```

```

done=false;
go=false;
strcpy(dc,drop);
strcat(dc,"dc");
fp = fopen (dc,"r");
while((c=fgetc(fp)) != EOF)
{
    if(c != BLANK && c != NEWLINE)
    {
        signal[s]=c;
        s++;
        bk=0;
        go=true;
    }
    else{
        bk++;
        if (bk==1 && go)
        {
            signal[s]='\0';
            count++;
            datval=atof(signal);
            if (count==1 && datval >= ti)
                ok=true;
            if (count==1 && datval > tf)
            {
                ok=false;
                done=true;}
            if(ok)
            {
                switch(count){
                    case 1: tldc[l]=datval;
                        break;
                    case 15: h[l]=datval;
                        break;
                    case 16: x[l]=datval;
                        break;
                    case 17: y[l]=datval;
                        break;
                    default: break;
                }
            }
        }
        s=0;
    }
    if(c==NEWLINE)
    {
        if (count != 27)
            printf("\n Column number mismatch error.....");
        count=0;
        if (ok)
            l++;
    }
    if (done)
        break;
}
fclose(fp);
nldc=l;
printf("\nDone reading dc");

```

```

/*time derivatives calc*/
/*1000 Hz Uplink Signals*/
/*dot(0.001,nul1k,tul1k,cnrd_cmd,cnrd_cmd_dot);
dot(0.001,nul1k,tul1k,f_rin_cmd,f_rin_cmd_dot);
dot(0.001,nul1k,tul1k,f_rot_cmd,f_rot_cmd_dot);
dot(0.001,nul1k,tul1k,f_lin_cmd,f_lin_cmd_dot);
dot(0.001,nul1k,tul1k,f_lot_cmd,f_lot_cmd_dot);
dot(0.001,nul1k,tul1k,rud_cmd,rud_cmd_dot);
dot(0.001,nul1k,tul1k,in_lip_cmd,in_lip_cmd_dot);
dot(0.001,nul1k,tul1k,pitch_stk,pitch_stk_dot);
dot(0.001,nul1k,tul1k,roll_stk,roll_stk_dot);
dot(0.001,nul1k,tul1k,yaw_stk,yaw_stk_dot);*/

/*computed Uplink 1000 Hz Signals*/
for(l=0;l<nul1k;l++)
{
    f_symm_cmd[l]=(f_rin_cmd[l]+f_rot_cmd[l]+f_lin_cmd[l]+f_lot_cmd[l])/4;
    f_diff_cmd[l]=(f_rin_cmd[l]+f_rot_cmd[l]-f_lin_cmd[l]-f_lot_cmd[l])/4;
}
/*dot(0.001,nul1k,tul1k,f_symm_cmd,f_symm_cmd_dot);
dot(0.001,nul1k,tul1k,f_diff_cmd,f_diff_cmd_dot);
printf("\nDone computing dot's for ul1k");
*/
/*1000 Hz Downlink Signals*/
dot(0.001,n1k,t1k,qhigh,qhigh_dot);
dot(0.001,n1k,t1k,beta,beta_dot);
dot(0.001,n1k,t1k,plow,plow_dot);
dot(0.001,n1k,t1k,qlow,qlow_dot);
dot(0.001,n1k,t1k,rlo,rlow_dot);
/*dot(0.001,n1k,t1k,cnrd_cpt,cnrd_cpt_dot);
dot(0.001,n1k,t1k,f_rot_cpt,f_rot_cpt_dot);
dot(0.001,n1k,t1k,f_rin_cpt,f_rin_cpt_dot);
dot(0.001,n1k,t1k,f_lot_cpt,f_lot_cpt_dot);
dot(0.001,n1k,t1k,f_lin_cpt,f_lin_cpt_dot);
dot(0.001,n1k,t1k,rud_cpt,rud_cpt_dot);*/
dot(0.001,n1k,t1k,phigh,phigh_dot);
dot(0.001,n1k,t1k,aoa1,aoa1_dot);

/*computed Downlink 1000 Hz Signals*/
for(l=0;l<n1k;l++)
{
    f_symm_cpt[l]=(f_rin_cpt[l]+f_rot_cpt[l]+f_lin_cpt[l]+f_lot_cpt[l])/4;
    f_diff_cpt[l]=(f_rin_cpt[l]+f_rot_cpt[l]-f_lin_cpt[l]-f_lot_cpt[l])/4;
}
/*dot(0.001,n1k,t1k,f_symm_cpt,f_symm_cpt_dot);
dot(0.001,n1k,t1k,f_diff_cpt,f_diff_cpt_dot);
printf("\nDone computing dot's for dl1k");
*/
/*200 Hz Downlink Signals*/
dot(0.005,n2c,t2c,rhigh,rhigh_dot);
dot(0.005,n2c,t2c,roll,roll_dot);
dot(0.005,n2c,t2c,roll_dot,roll_2dot);
printf("\nDone computing dot's for dl2c");

/*100 Hz Downlink Signals*/
dot(0.01,n1c,t1c,thetal,thetal_dot);

```

```

dot(0.01,n1c,t1c,theta1_dot,theta1_2dot);
dot(0.01,n1c,t1c,aoa2,aoa2_dot);
dot(0.01,n1c,t1c,theta2,theta2_dot);
dot(0.01,n1c,t1c,theta2_dot,theta2_2dot);
dot(0.01,n1c,t1c,psi,psi_dot);
dot(0.01,n1c,t1c,psi_dot,psi_2dot);
/*dot(0.01,n1c,t1c,in_lip_cpt,in_lip_cpt_dot);*/
printf("\nDone computing dot's for dl1c");

/*100 Hz Data Converter*/
dot(0.01,n1dc,t1dc,h,h_dot);
printf("\nDone computing dot's for dc");

/* data conversion to 100Hz*/
for(i=0;i < n1c;i++)
{
    /*1000hz Uplink data Conversion*/
    cnrd_cmd[i]=avg(i,10,cnrd_cmd);
    /*cnrd_cmd_dot[i]=avg(i,10,cnrd_cmd_dot);*/
    f_rin_cmd[i]=avg(i,10,f_rin_cmd);
    /*f_rin_cmd_dot[i]=avg(i,10,f_rin_cmd_dot);*/
    f_rot_cmd[i]=avg(i,10,f_rot_cmd);
    /*f_rot_cmd_dot[i]=avg(i,10,f_rot_cmd_dot);*/
    f_lin_cmd[i]=avg(i,10,f_lin_cmd);
    /*f_lin_cmd_dot[i]=avg(i,10,f_lin_cmd_dot);*/
    f_lot_cmd[i]=avg(i,10,f_lot_cmd);
    /*f_lot_cmd_dot[i]=avg(i,10,f_lot_cmd_dot);*/
    rud_cmd[i]=avg(i,10,rud_cmd);
    /*rud_cmd_dot[i]=avg(i,10,rud_cmd_dot);*/
    in_lip_cmd[i]=avg(i,10,in_lip_cmd);
    /*in_lip_cmd_dot[i]=avg(i,10,in_lip_cmd_dot);*/
    f_symm_cmd[i]=avg(i,10,f_symm_cmd);
    /*f_symm_cmd_dot[i]=avg(i,10,f_symm_cmd_dot);*/
    f_diff_cmd[i]=avg(i,10,f_diff_cmd);
    /*f_diff_cmd_dot[i]=avg(i,10,f_diff_cmd_dot);*/
    pitch_stk[i]=avg(i,10,pitch_stk);
    /*pitch_stk_dot[i]=avg(i,10,pitch_stk_dot);*/
    roll_stk[i]=avg(i,10,roll_stk);
    /*
    roll_stk_dot[i]=avg(i,10,roll_stk_dot);*/
    yaw_stk[i]=avg(i,10,yaw_stk);
    /*yaw_stk_dot[i]=avg(i,10,yaw_stk_dot);*/
    fcs_mode[i]=avg(i,10,fcs_mode);

    /*1000 hz Downlink data Conversion*/
    qhigh[i]=avg(i,10,qhigh);
    qhigh_dot[i]=avg(i,10,qhigh_dot);
    beta[i]=avg(i,10,beta);
    beta_dot[i]=avg(i,10,beta_dot);
    plow[i]=avg(i,10,plow);
    plow_dot[i]=avg(i,10,plow_dot);
    qlow[i]=avg(i,10,qlow);
    qlow_dot[i]=avg(i,10,qlow_dot);
    rlow[i]=avg(i,10,rlow);

```

```

        rlow_dot[i]=avg(i,10,rlow_dot);
        f_rot_cpt[i]=avg(i,10,f_rot_cpt);
/*
        f_rot_cpt_dot[i]=avg(i,10,f_rot_cpt_dot);*/
        f_rin_cpt[i]=avg(i,10,f_rin_cpt);
/*f_rin_cpt_dot[i]=avg(i,10,f_rin_cpt_dot);*/
        f_lot_cpt[i]=avg(i,10,f_lot_cpt);
/*
        f_lot_cpt_dot[i]=avg(i,10,f_lot_cpt_dot);*/
        f_lin_cpt[i]=avg(i,10,f_lin_cpt);
/*f_lin_cpt_dot[i]=avg(i,10,f_lin_cpt_dot);*/
        f_symm_cpt[i]=avg(i,10,f_symm_cpt);
/*f_symm_cpt_dot[i]=avg(i,10,f_symm_cpt_dot);*/
        f_diff_cpt[i]=avg(i,10,f_diff_cpt);
/*f_diff_cpt_dot[i]=avg(i,10,f_diff_cpt_dot);*/
        rud_cpt[i]=avg(i,10,rud_cpt);
        cnrd_cpt[i]=avg(i,10,cnrd_cpt);
/*rud_cpt_dot[i]=avg(i,10,rud_cpt_dot);*/
        phigh[i]=avg(i,10,phigh);
        phigh_dot[i]=avg(i,10,phigh_dot);
        aoa1[i]=avg(i,10,aoa1);
        aoa1_dot[i]=avg(i,10,aoa1_dot);

/*200hz Downlink data Conversion*/
        rhigh[i]=avg(i,2,rhigh);
        rhigh_dot[i]=avg(i,2,rhigh_dot);
        axr[i]=avg(i,2,axr);
        azr[i]=avg(i,2,azr);
        roll[i]=avg(i,2,roll);
        roll_dot[i]=avg(i,2,roll_dot);
        roll_2dot[i]=avg(i,2,roll_2dot);
        Vbird[i]=avg(i,2,Vbird);
        ayr[i]=avg(i,2,ayr);
    }
    printf("\nDone converting data to 100 hz");

    for(n=0;n<n1c;n++)        /*time independent parameters*/
    {
        if(fabs(qlow[n]) < 90)        /*rates selection*/
        {
            qsel[n]=qlow[n];
            qdot[n]=qlow_dot[n];}
        else
        {
            qsel[n]=qhigh[n];
            qdot[n]=qhigh_dot[n];}
        if(fabs(plow[n]) < 170)
        {
            psel[n]=phigh[n];
            pdot[n]=phigh_dot[n];}
        else
        {
            psel[n]=phigh[n];
            pdot[n]=phigh_dot[n];}
        if(fabs(rlow[n]) < 90)
        {
            rsel[n]=rlow[n];
            rdot[n]=rlow_dot[n];}
        else
        {
            rsel[n]=rhigh[n];
            rdot[n]=rhigh_dot[n];}
    }

```

```

if(aoa2[n] >= 180)
    aoa2[n]=aoa2[n]-360;
if((aoa1[n]>=-120)&&(aoa1[n]<=120))          /*aoa selection*/
{
    aoa[n]=aoa1[n];
    aoadot[n]=aoa1_dot[n];}
else if(((aoa2[n]>=120)&&(aoa2[n]<=180))||((aoa2[n]>=-
180)&&(aoa2[n]<=-120)))
{
    aoa[n]=aoa2[n];
    aoadot[n]=aoa2_dot[n];}
else
{
    aoa[n]=aoa1[n];
    aoadot[n]=aoa1_dot[n];}

/*deg to rad conversion*/
aoarad=aoa[n]*deg2rad;
betarad=beta[n]*deg2rad;
prad=psel[n]*deg2rad;
qrad=ysel[n]*deg2rad;
rrad=rse[n]*deg2rad;
if(Vbird[n] != 0) /*air data correction*/
{
    ubird=Vbird[n]/sqrt(1+pow(tan(betarad),2)+pow(tan(aoarad),2));
    u[n]=ubird+rrad*(blbird-blcg)-qrad*(wlcg-wlbird);
    v[n]=ubird*tan(betarad)-rrad*(fscg-fsbird)+prad*(wlcg-wlbird);
    w[n]=ubird*tan(aoarad)+qrad*(fscg-fsbird)-prad*(blbird-blcg);
    vcorr[n]=sqrt(u[n]*u[n]+v[n]*v[n]+w[n]*w[n]);
    aoacorr[n]=aoarad+qrad*(fscg-fsbird)/vcorr[n]+prad*(blcg-
blbird)/vcorr[n];
    betacorr[n]=betarad+rrad*(fsbird-fscg)/vcorr[n]+prad*(wlcg-
wlbird)/vcorr[n];
    if (fabs(aoacorr[n]-90*deg2rad) < 0.0017)
    {
        thetasting[n] = 0;

        phisting[n]=rad2deg*atan2(sin(betacorr[n]),tan(aoacorr[n]));
        else
        {
            val=(pow(tan(aoacorr[n]),2)+pow(sin(betacorr[n]),2))/(1+pow(tan(aoacorr[n])
,2));
            thetasting[n]=asin(sqrt(fabs(val)));

            phisting[n]=atan2(sin(betacorr[n]),(tan(aoacorr[n])*cos(thetasting[n])));
            thetasting[n]=thetasting[n]*rad2deg;
            phisting[n]=phisting[n]*rad2deg;
        }
    }
/*atmospheric parameters calc*/
rho=0.002378*pow((1-0.00000689*h[n]),4.256);
temp=59-3.57*h[n]/1000; /*temp in F*/
temp=(5/9)*(temp-32)+273.15; /*temp in K*/
mu=(3.0443e-8)*pow(temp,1.5)/(temp+110.4);
re[n]=vcorr[n]*rho*cbar/mu;
qbar[n]=0.5*rho*vcorr[n]*vcorr[n];
mach[n]=vcorr[n]/(65.79664*sqrt(temp));

/*accelerometer corrections*/

```



```

        cax=((qrad*qrad+rrad*rrad)*xax-(prad*qrad-rdot[n]*deg2rad)*yax-
(prad*rrad+qdot[n]*deg2rad)*zax)/G;
        ax[n]=axr[n]+cax;
        cay=((-
1)*(prad*qrad+rdot[n]*deg2rad)*xay+(prad*prad+rrad*rrad)*yay-(qrad*rrad-
pdot[n]*deg2rad)*zay)/G;
        ay[n]=ayr[n]+cay;
        caz=((-1)*(prad*rrad-qdot[n]*deg2rad)*xaz-
(qrad*rrad+pdot[n]*deg2rad)*yaz+(prad*prad+qrad*qrad)*zaz)/G;
        az[n]=azr[n]+caz;

/*forces and moments coefficients*/
fx=WT*ax[n]*G;
fy=WT*ay[n]*G;
fz=WT*az[n]*G;
cx[n]=fx/(qbar[n]*S);
cy[n]=fy/(qbar[n]*S);
cz[n]=fz/(qbar[n]*S);
clift[n]=(-1)*cz[n]*cos(aoacorr[n])+cx[n]*sin(aoacorr[n]);
cdrag[n]=(-1)*cx[n]*cos(aoacorr[n])-cz[n]*sin(aoacorr[n]);
if (cdrag[n]==0)
{   printf("\nDrag is zero, setting L/D to zero");
    ldratio[n]=0.0;}
else
    ldratio[n]=clift[n]/cdrag[n];
/*inertia and cross coupling calc*/
txic=qrad*rrad*(iy-iz);
txicx=(prad*qrad+rdot[n]*deg2rad)*ixz;
tx=pdot[n]*deg2rad*ix;
clic[n]=txic/(qbar[n]*S*b);
clicx[n]=txicx/(qbar[n]*S*b);
tyic=prad*rrad*(iz-ix);
tyicx=(rrad*rrad-prad*prad)*ixz;
ty=qdot[n]*deg2rad*iy;
cmic[n]=tyic/(qbar[n]*S*cbar);
cmicx[n]=tyicx/(qbar[n]*S*cbar);
tzic=prad*qrad*(ix-iy);
tzicx=(pdot[n]*deg2rad-qrad*rrad)*ixz;
tz=rdot[n]*deg2rad*iz;
cnic[n]=tzic/(qbar[n]*S*b);
cnicx[n]=tzicx/(qbar[n]*S*b);
/*total moments*/
cl[n]=tx/(qbar[n]*S*b);
cm[n]=ty/(qbar[n]*S*cbar);
cn[n]=tz/(qbar[n]*S*b);
/*aero moments*/
claero[n]=cl[n]-clic[n]-clicx[n];
cmaero[n]=cm[n]-cmic[n]-cmicx[n];
cnaero[n]=cn[n]-cnic[n]-cnicx[n];
/*omega2 (spin cm) term*/
if(fabs(sin(2*aoacorr[n])) <= 0.001)
{   aoarad=0.001;
    omega2[n]=qbar[n]*S*cbar*cmaero[n]/((ix-iz)*sin(2*aoarad));}
else

```

```

        omega2[n]=qbar[n]*S*cbar*cmaero[n]/((ix-iz)*sin(2*aoacorr[n]));
    }
else
    printf("\nVbird equals zero....");
}
printf("\nDone computing aero data");

/*calc of u,v,w, and vcorrected time derivatives*/
dot(0.01,n1c,t1c,u,u_dot);
dot(0.01,n1c,t1c,v,v_dot);
dot(0.01,n1c,t1c,w,w_dot);
dot(0.01,n1c,t1c,vcorr,vcorr_dot);
for(i=0;i<n1c;i++)
{
    /*rad to deg conversion*/
    aoacorr[i]=aoacorr[i]*rad2deg;
    betacorr[i]=betacorr[i]*rad2deg;
    /*aoa and beta dot corrected calc*/
    if(vcorr[i]!=0){
        de1=(qdot[i]*vcorr[i]-vcorr_dot[i]*qsel[i])/(vcorr[i]*vcorr[i]);
        de2=(pdot[i]*vcorr[i]-vcorr_dot[i]*psel[i])/(vcorr[i]*vcorr[i]);
        aoacorr_dot[i]=aoadot[i]+de1*(fscg-fsbird)+de2*(blcg-blbird);
        de3=(rdot[i]*vcorr[i]-vcorr_dot[i]*rsel[i])/(vcorr[i]*vcorr[i]);
        betacorr_dot[i]=beta_dot[i]+de3*(fsbird-fscg)+de2*(wlcg-wlbird);
    }
    else{
        printf("\nVbird equals zero");
    }
}

/*output section*/
fp=fopen("dataair","w");
fprintf(fp,"format asc 2 .1\n");
fprintf(fp,"nChans 23\n");
fprintf(fp,"names aoa aoadot beta betadot Vbird \n");
fprintf(fp,"qbar p pdot r rdot q \n");
fprintf(fp,"qdot ax ay az h hdot \n");
fprintf(fp,"roll rolldot roll2dot u v w \n");
fprintf(fp,"data001\n");
for(i=0;i<n1c;i++)
{
    fprintf(fp,"%13.6E%13.6E%13.6E%13.6E%13.6E%13.6E\n",t1c[i],aoacorr[i],aoacorr_dot[i],betacorr[i],betacorr_dot[i],vcorr[i]);

    fprintf(fp,"%13.6E%13.6E%13.6E%13.6E%13.6E%13.6E\n",qbar[i],psel[i],pdot[i],rsel[i],rdot[i],qsel[i]);

    fprintf(fp,"%13.6E%13.6E%13.6E%13.6E%13.6E%13.6E\n",qdot[i],ax[i],ay[i],az[i],h[i],h_dot[i]);

    fprintf(fp,"%13.6E%13.6E%13.6E%13.6E%13.6E%13.6E\n",roll[i],roll_dot[i],roll_2dot[i],u[i],v[i],w[i]);
}
fclose(fp);

fp=fopen("dataaero","w");

```

```

        fprintf(fp,"format   asc 2   .1\n");
        fprintf(fp,"nChans      23\n");
        fprintf(fp,"names      cx      cy      cz      thetasting phisting   \n");
        fprintf(fp,"mach      re      wdot      L/D      lift      drag      \n");
        fprintf(fp,"cl      clic      clicx      clae      cn      cnic      \n");
        fprintf(fp,"cnicx      cnaero      cm      cmic      cmicx      cmaero      \n");
        fprintf(fp,"data001\n");
        for(i=0;i<n1c;i++)
        {
            fprintf(fp,"%13.6E%13.6E%13.6E%13.6E%13.6E%13.6E\n",t1c[i],cx[i],cy[i],cz[i],th
etasting[i],phisting[i]);

            fprintf(fp,"%13.6E%13.6E%13.6E%13.6E%13.6E%13.6E\n",mach[i],re[i],w_dot[i],l
dratio[i],clift[i],cdrag[i]);

            fprintf(fp,"%13.6E%13.6E%13.6E%13.6E%13.6E%13.6E\n",cl[i],clic[i],clicx[i],clae
ro[i],cn[i],cnic[i]);

            fprintf(fp,"%13.6E%13.6E%13.6E%13.6E%13.6E%13.6E\n",cnicx[i],cnaero[i],cm[i
],cmic[i],cmicx[i],cmaero[i]);
        }
        fclose(fp);

        fp=fopen("datcon","w");
        fprintf(fp,"format   asc 2   .1\n");
        fprintf(fp,"nChans      23\n");
        fprintf(fp,"names      omega2      vcorrdot      theta1      theta2      psi
\n");
        fprintf(fp,"psidot      theta1dot      theta2dot      psi2dot      cnrdcmd      cnrdcpt
\n");
        fprintf(fp,"fsymmcmd      fsymmcpt      fdiffcmd      fdiffcpt      ruddercmd
ruddercpt   \n");
        fprintf(fp,"inlipcmd      inlipcpt      pitchstk      rollstk      yawstk      fcsmode
\n");
        fprintf(fp,"data001\n");
        for(i=0;i<n1c;i++)
        {
            fprintf(fp,"%13.6E%13.6E%13.6E%13.6E%13.6E%13.6E\n",t1c[i],omega2[i],vcorr_
dot[i],theta1[i],theta2[i],psi[i]);

            fprintf(fp,"%13.6E%13.6E%13.6E%13.6E%13.6E%13.6E\n",psi_dot[i],theta1_dot[i],
theta2_dot[i],psi_2dot[i],cnrd_cmd[i],cnrd_cpt[i]);

            fprintf(fp,"%13.6E%13.6E%13.6E%13.6E%13.6E%13.6E\n",f_symm_cmd[i],f_sym
m_cpt[i],f_diff_cmd[i],f_diff_cpt[i],rud_cmd[i],rud_cpt[i]);

            fprintf(fp,"%13.6E%13.6E%13.6E%13.6E%13.6E%13.6E\n",in_lip_cmd[i],in_lip_c
pt[i],pitch_stk[i],roll_stk[i],yaw_stk[i],fcs_mode[i]);
        }
        fclose(fp);
        printf("\nDone outputting data\n");
    }
    dot(a,n,t,in,ot) /*a=stepsize n=#pts t=t_array*/
    int n; /*in=input_signal ot=output_signal*/

```

```

double      a,t[],in[],*ot;
{
    double  temp1[200000],temp2[200000],wk1[200000],wk2[200000],wk3[200000];
    double  wk4[200000],wk5[200000],wk6[200000],dersp();
    int  i;
    /*fil(a,in,n);*/
    secder(3,3,t,in,temp1,temp2,n,0,0,.5,.5,wk1,wk2,wk3,wk4,wk5,wk6);
    for(i=0;i<n;i++)
        *(ot+i)=dersp(t[i],t,in,n,temp1,temp2);
}

double  avg(a,e,h) /*average routine*/
int  a,e;
double  h[];
{
    double  value,sum;
    int  l;
    sum=0;
    for (l=0;l < e; l++)
        sum=sum+h[a*e+l];
    value=sum/e;
    return  value;
}

```

APPENDIX C
LINEAR 3 D.O.F. LATERAL-DIRECTIONAL MATH MODEL

LINEAR 3 D.O.F. LATERAL-DIRECTIONAL MATH MODEL

Nondimensional Equations of Motion

$$\begin{aligned}
 \dot{\bar{\beta}} &= \frac{1}{2\eta} C_{y\beta} \beta + \left(\frac{1}{2\eta} \overline{C_{y_p}} + \alpha_0 \right) \bar{p} + \left(\frac{1}{2\eta} \overline{C_{y_r}} - 1 \right) \bar{r} + \frac{g b}{2 V^2} \cos \theta_0 \phi \\
 \dot{\bar{p}} &= \varepsilon (i_z C_{l\beta} + i_{xz} C_{n\beta}) \beta + \varepsilon (i_z \overline{C_{l_p}} + i_{xz} \overline{C_{n_p}}) \bar{p} + \varepsilon (i_z \overline{C_{l_r}} + i_{xz} \overline{C_{n_r}}) \bar{r} \\
 \dot{\bar{r}} &= \varepsilon (i_{xz} C_{l\beta} + i_x C_{n\beta}) \beta + \varepsilon (i_{xz} \overline{C_{l_p}} + i_x \overline{C_{n_p}}) \bar{p} + \varepsilon (i_{xz} \overline{C_{l_r}} + i_x \overline{C_{n_r}}) \bar{r} \\
 \dot{\bar{\phi}} &= \beta + \tan \theta_0 \phi
 \end{aligned}$$

where $\eta = \frac{2m}{\rho S b}$, $\varepsilon = \frac{1}{i_x i_z - i_{xz}^2}$, $i_a = \frac{8 I_{aa}}{\rho S b^3}$ with $a=x,y,z,xz$

Using nondimensional wind-tunnel data for the basic configuration, the characteristic equation was obtained at two angles of attack: 30° and 34°. The characteristic equation was solved, and the system eigenvalues were determined. The lateral-directional equations of motion contain three modes: one periodic and two aperiodic modes. The Dutch roll periodic mode characteristics were calculated from its corresponding complex conjugate eigenvalues. The natural reduced frequency, k_{dr} , and damping were calculated to be:

$$\begin{aligned}
 k_{dr} &= 0.108458 & \& & \zeta_{dr} &= 0.118018 & (\text{i.e., } \alpha = 30^\circ) \\
 k_{dr} &= 0.141676 & \& & \zeta_{dr} &= 0.280217 & (\text{i.e., } \alpha = 34^\circ)
 \end{aligned}$$

TABLES

TABLE I.- X-31 MASS AND GEOMETRIC CHARACTERISTICS

Weight, lb	12169
Moments of Inertia:	
I_{xx} , slug-ft ²	2861
I_{yy} , slug-ft ²	31022
I_{zz} , slug-ft ²	31910
I_{xz} , slug-ft ²	-145
Wing:	
Span , ft	22.83
Mean Aerodynamic Chord, ft	12.35
Area, ft ²	226.30
Aspect Ratio	2.30
Leading-edge Sweep, deg	57/45
Leading-edge Flap Deflection, deg	0/0 to -40/-32 (L.E.D.)
Leading-edge Area (Total), ft ²	14.70
Taper Ratio, (inboard/outboard)	0.343/0.356
Trailing-edge Flaperon Deflection, deg	+30 (T.E.U.) to -30 (T.E.D.)
Flaperon Area (Total), ft ²	31.74
Canard:	
Span, ft	2.5
Leading-edge Sweep,deg	45
Area (Total), ft ²	23.6
Aspect Ratio	3.18
Taper Ratio	0.169
Deflection, deg	+20 (T.E.D.) to -70 (T.E.U.)
Vertical Tail:	
Height, ft	6.81
Leading-edge Sweep,deg	50
Area (Total), ft ²	37.55
Aspect ratio	1.24
Taper Ratio	0.312
Rudder Area, ft ²	8.68
Rudder deflection, deg	+30 (T.E.L.) to -30 (T.E.R.)
Fuselage:	
Length, ft	43.33
Inlet Lip Deflection, deg	0 to -26 (L.E.D.)
Speed Brake Deflection, deg	0 to 46

TABLE II.- SCALE FACTORS FOR DYNAMIC MODELS

	SCALE FACTOR
Linear Dimension	N
Relative Density	1
Froude Number	1
Weight, mass	$N^3\sigma^{-1}$
Moment of Inertia	$N^5\sigma^{-1}$
Linear Velocity	$N^{1/2}$
Linear Acceleration	1
Angular Velocity	$N^{-1/2}$
Time	$N^{1/2}$
Reynolds Number	$\frac{v}{v_0}N^{1.5}$

Model values are obtained by multiplying airplane values by the above scale factors.

TABLE III.- SUMMARY OF QUALITATIVE FREE-TO-ROLL RESULTS

Configuration	Onset α , deg	Max Amplitude α , deg
1. Basic Configuration	2.5	3.2
2. Body, Wing, and Tail (J13 on, M86 on, Canard 0°)	2.5	5.0
3. Body, Wing, and Tail (J13 on, M86 on, Canard off)	2.5	3.5
4. Body, Wing, and Tail (J13 off, M86 on, Canard -40°)	2.5	3.2
5. Body, Wing, and Tail (J13 on, M86 off, Canard -40°)	2.7	3.0
6. Body (Hemispherical Nose), Wing, and Tail (J13 off, M86 on, Canard -40°)	2.5	3.0
7. Body (Hemispherical Nose), Wing, and Tail (J13 off, M86 on, Canard 0°)	3.2	4.2
8. Body (Hemispherical Nose), Wing, and Tail (J13 off, M86 on, Canard off)	2.5	3.0
9. Body, and Tail (J13 on, M86 off, Canard -40°)	4.0	4.7
10. Body (Canard -40°)	2.5	3.5
11. Body (Canard off)	2.5	3.5
12. Basic Configuration (S8A90 Strakes on)	5.5	6.0
13. Basic Configuration (S8A90 Strakes on, M86 off)	3.0	4.0

TABLE IV. WING ROCK FREE-TO-ROLL CHARACTERISTICS

α , deg	$\Delta\phi_{wr}$, deg	P_{wr} , sec	k_{wr}	Type
<hr/>				
$\leq 24^\circ$				(a)
28°	15°	3.6515	0.12358	(b)
30°	25°	3.6300	0.12432	(c)
32°	45°	4.5000	0.10029	(d)
$32 \leq \alpha \leq 45^\circ$				(e)
$50^\circ \geq$				(a)

Notes:

- (a) Lightly Damped Wing Rock: Roll motions eventually die out.
- (b) Mild Wing Rock: $\Delta\phi < \pm 15^\circ$
- (c) Moderate Wing Rock: $\pm 15^\circ < \Delta\phi < \pm 25^\circ$
- (d) Large Amplitude Wing Rock: $\Delta\phi > \pm 25^\circ$
- (e) Diverging Spiral Wing Rock

TABLE V. WING ROCK SIMULATION CHARACTERISTICS

α , deg	$\Delta\phi_{wr}$, deg	P_{wr} , sec	k_{wr}	Type
<hr/>				
$\leq 24^\circ$				(a)
28°	15°	4.0909	0.11032	(b)
30°	25°	3.7500	0.12035	(c)
32°	45°	4.3333	0.10414	(d)
$32 \leq \alpha \leq 45^\circ$				(e)
$50^\circ \geq$				(a)

Notes:

- (a) Lightly Damped Wing Rock: Roll motions eventually die out.
- (b) Mild Wing Rock: $\Delta\phi < \pm 15^\circ$
- (c) Moderate Wing Rock: $\pm 15^\circ < \Delta\phi < \pm 25^\circ$
- (d) Large Amplitude Wing Rock: $\Delta\phi > \pm 25^\circ$
- (e) Diverging Spiral Wing Rock

TABLE VI. WING ROCK COMPARISON

θ_{sting}	28°		30°		32°	
Magnitude	SIM	F2 ϕ	SIM	F2 ϕ	SIM	F2 ϕ
$\Delta\phi, ^\circ$	1 5	1 5	2 5	2 5	4 5	4 5
$\Delta\dot{\phi}, ^\circ/\text{s}$	2 5	2 4	4 2	4 1	7 5	7 0
$\Delta\beta, ^\circ$	8	7	1 2	1 2	2 2	2 0
$\Delta C_{l_{\text{aero}}}$	0.019	0.023	0.036	0.037	0.072	0.058
P_{wr}, s	4.09	3.65	3.75	3.63	4.33	4.5
k_{wr}	0.110	0.124	0.120	0.124	0.104	0.100

FIGURES

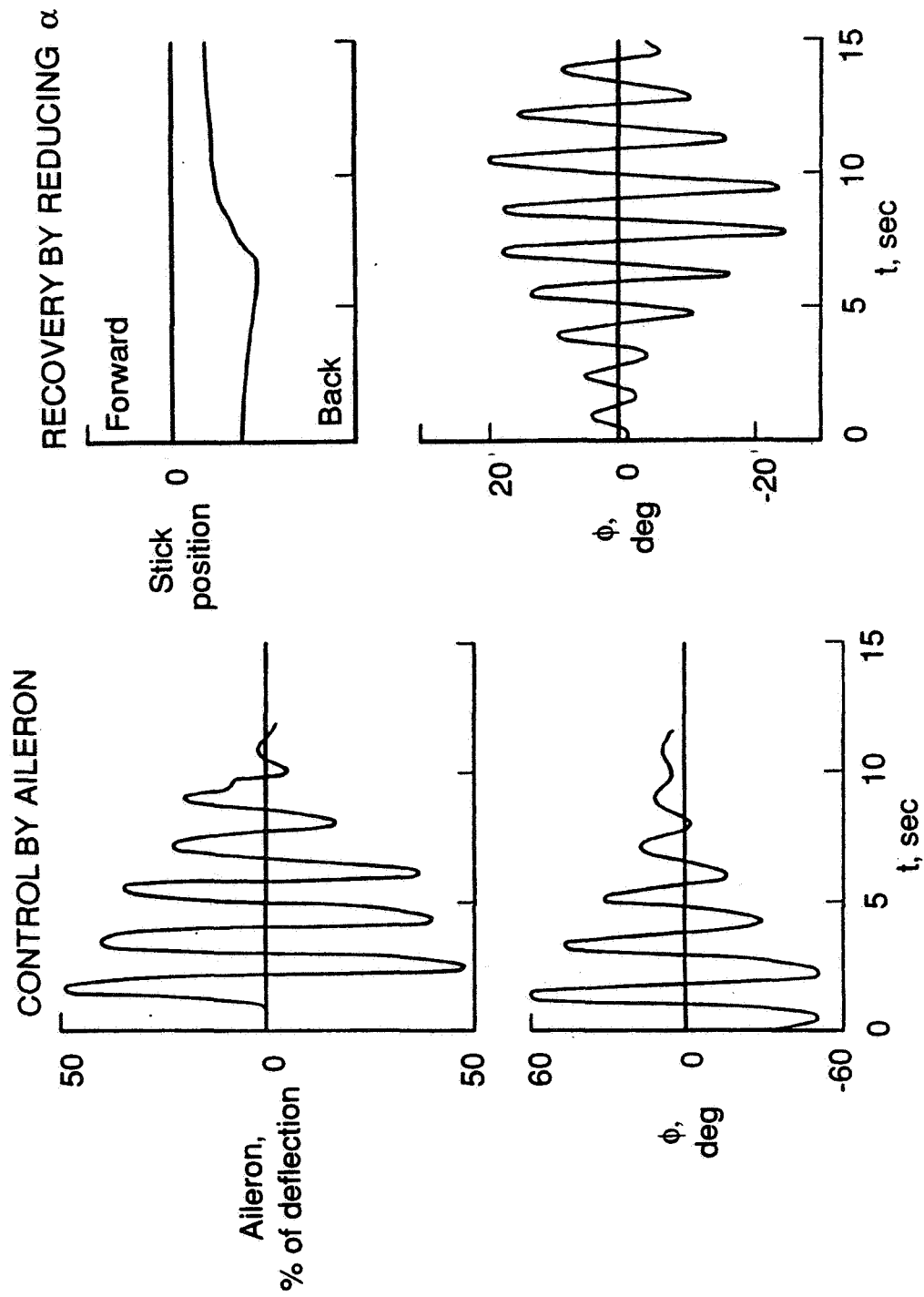


Figure 1. Wing Rock Suppression on the Handley Page aircraft (Ref. 7)

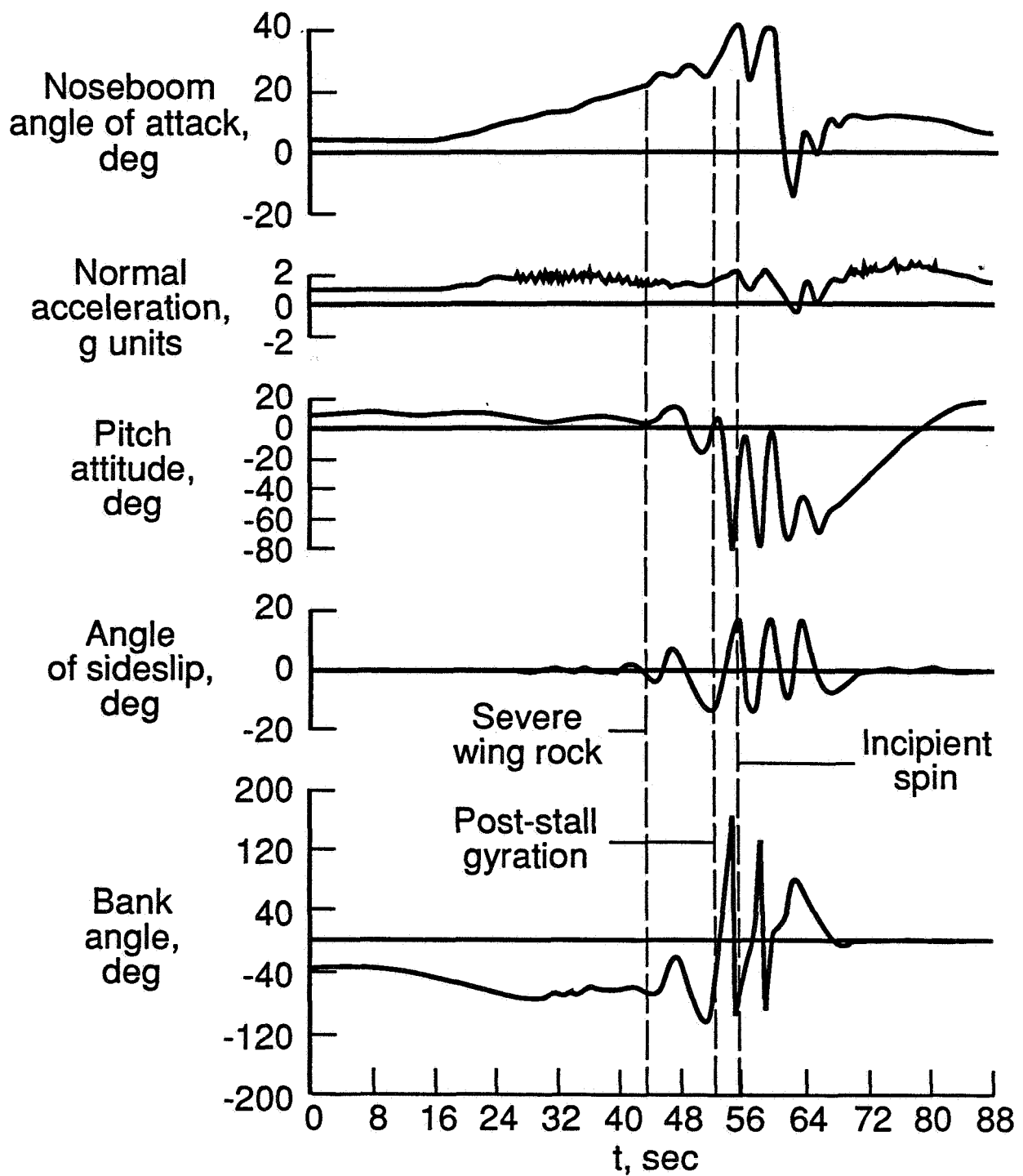


Figure 2. Wing Rock on the F-4 aircraft (Ref. 7)

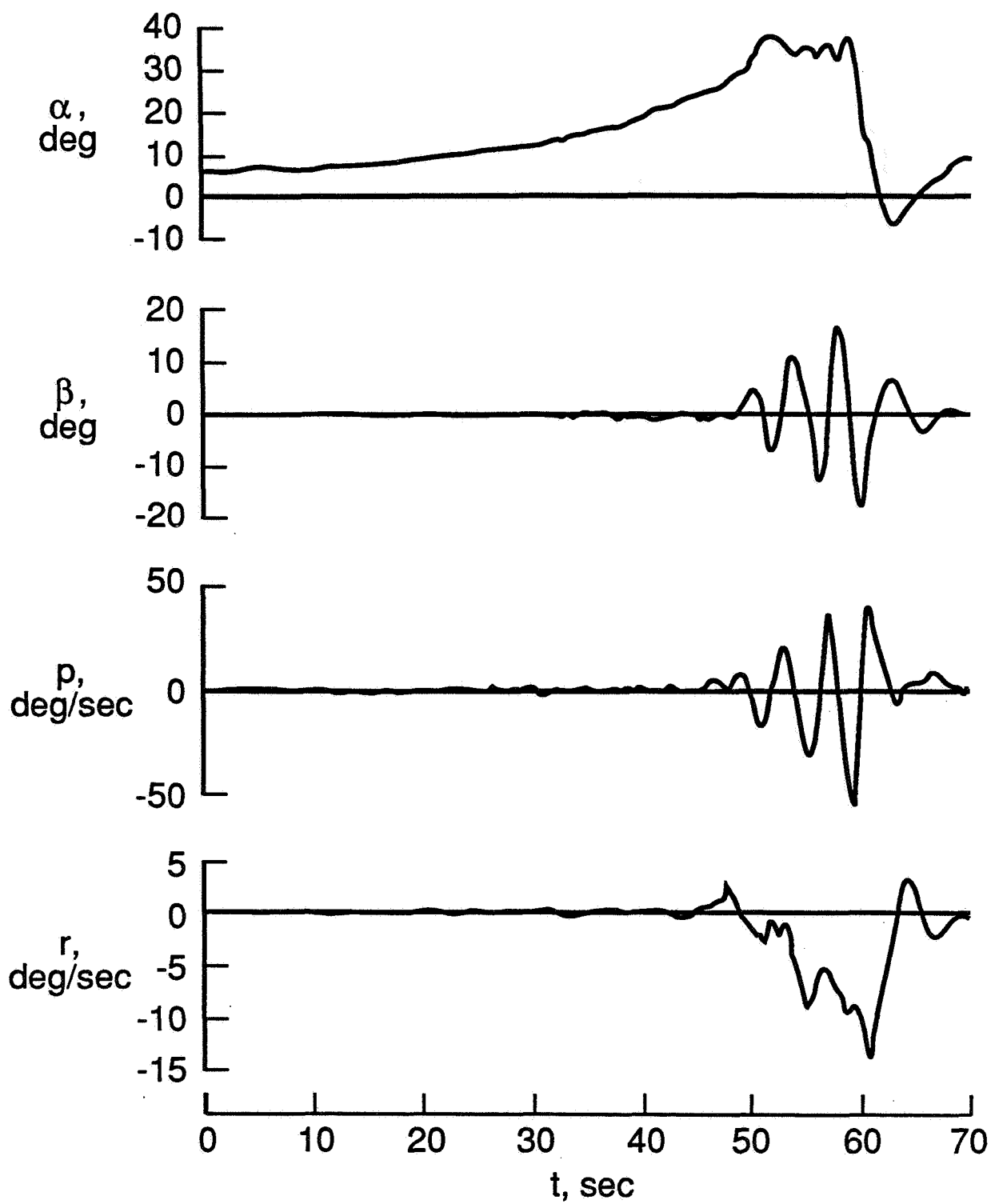


Figure 3. Low Speed Wing Rock on the F-5 aircraft (Ref. 7)

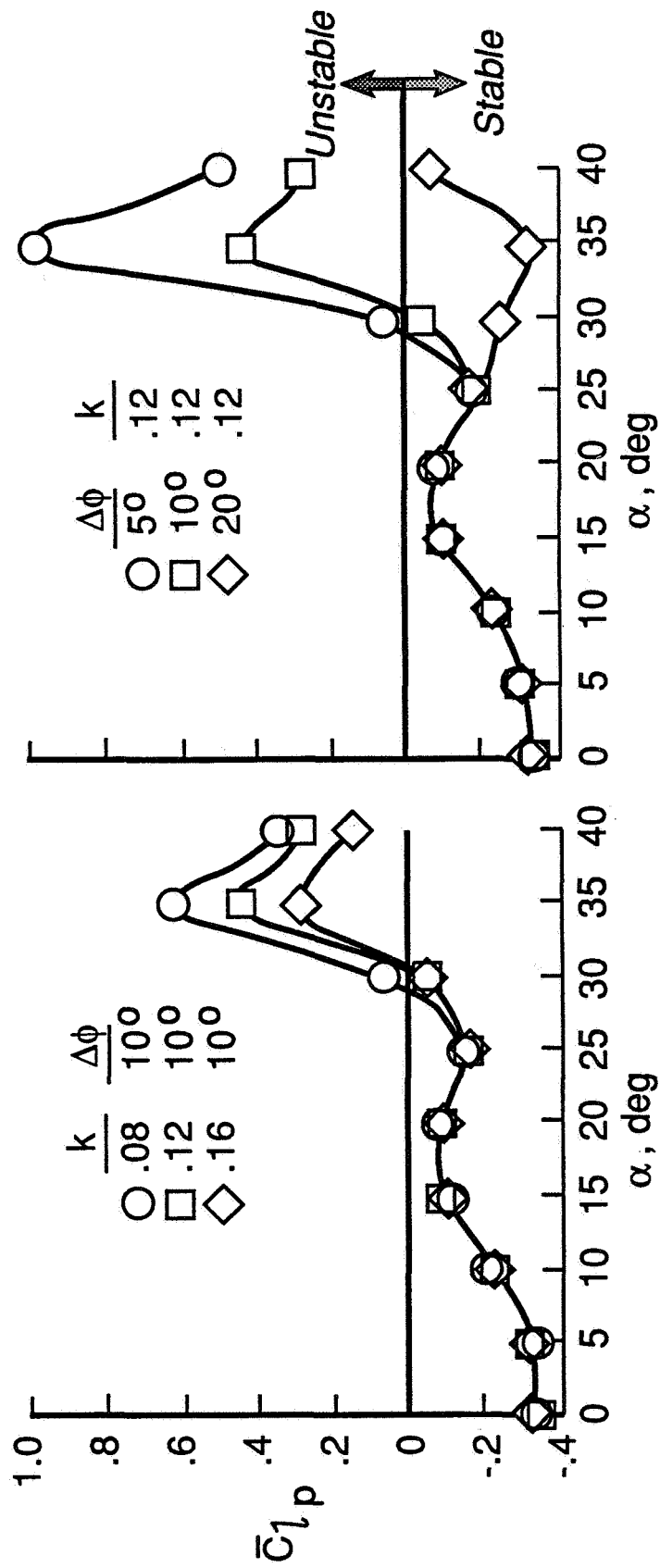


Figure 4. Frequency and Amplitude Effect on Roll Damping for the F-5 aircraft (Ref. 14)

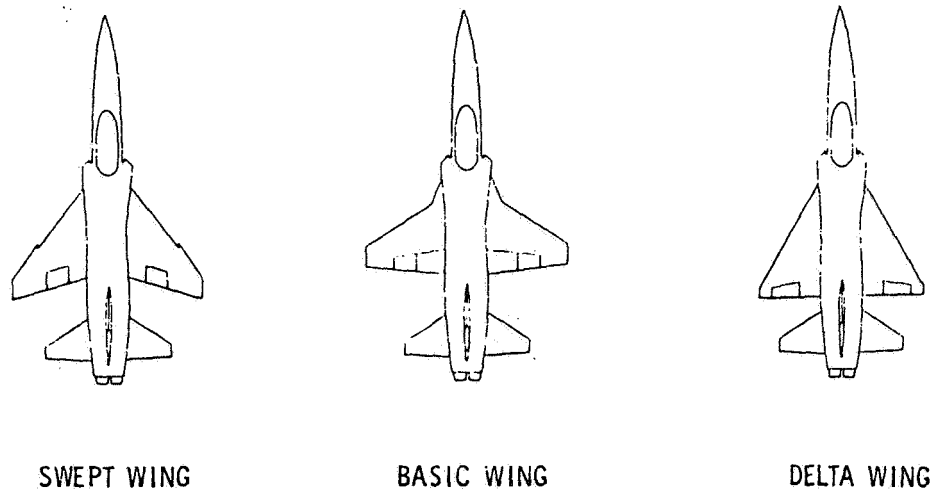


Figure 5. F-5 Wing Planforms Tested on NASA Wind-tunnel (Ref. 14)

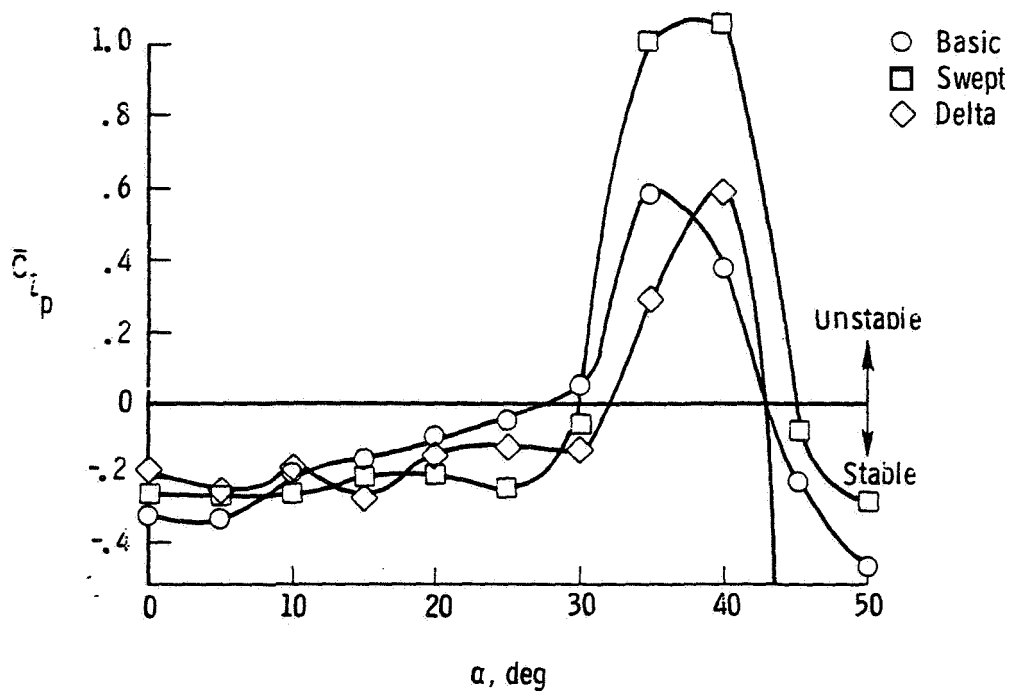


Figure 6. Roll Damping for the F-5 Wing Planforms (Ref. 14)

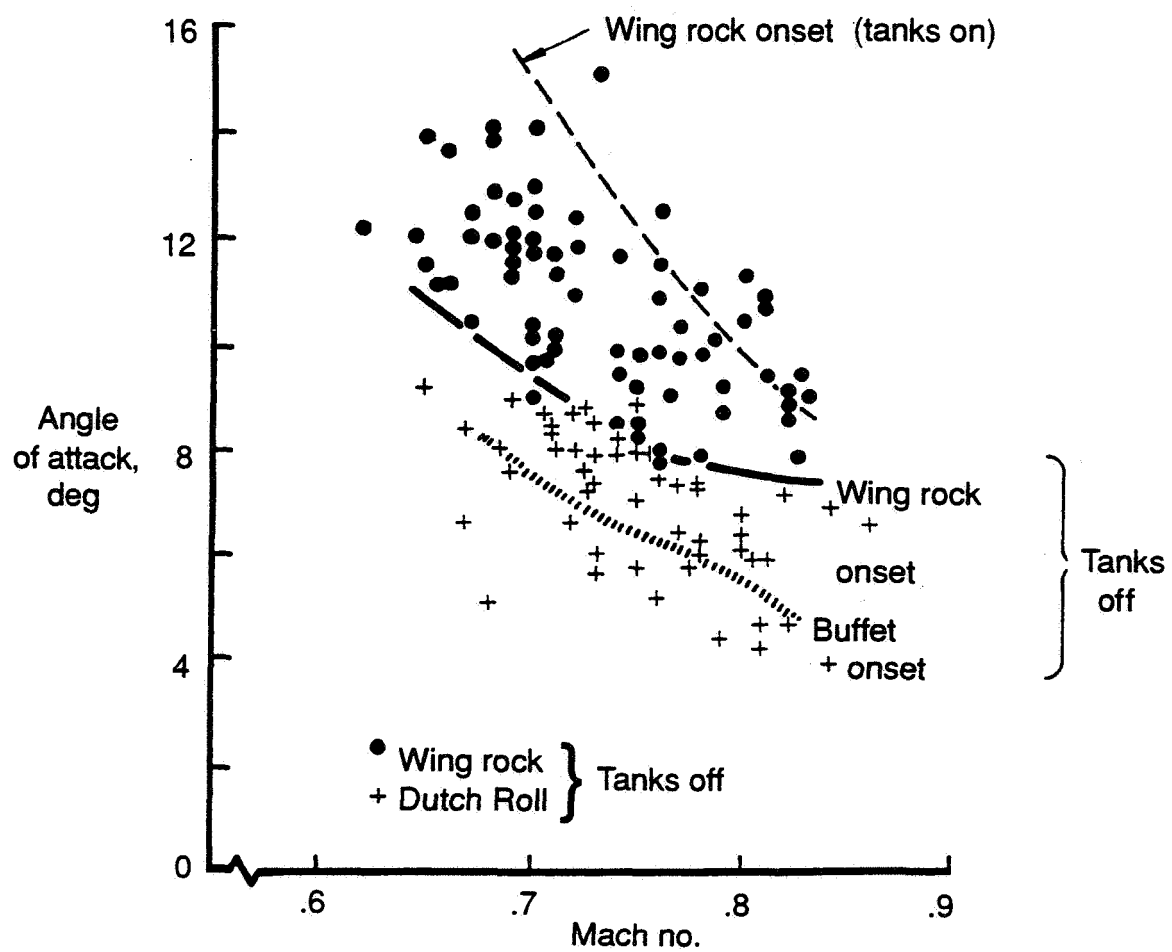


Figure 7. Wing Rock Onset α for the Gnat aircraft (Ref. 15)

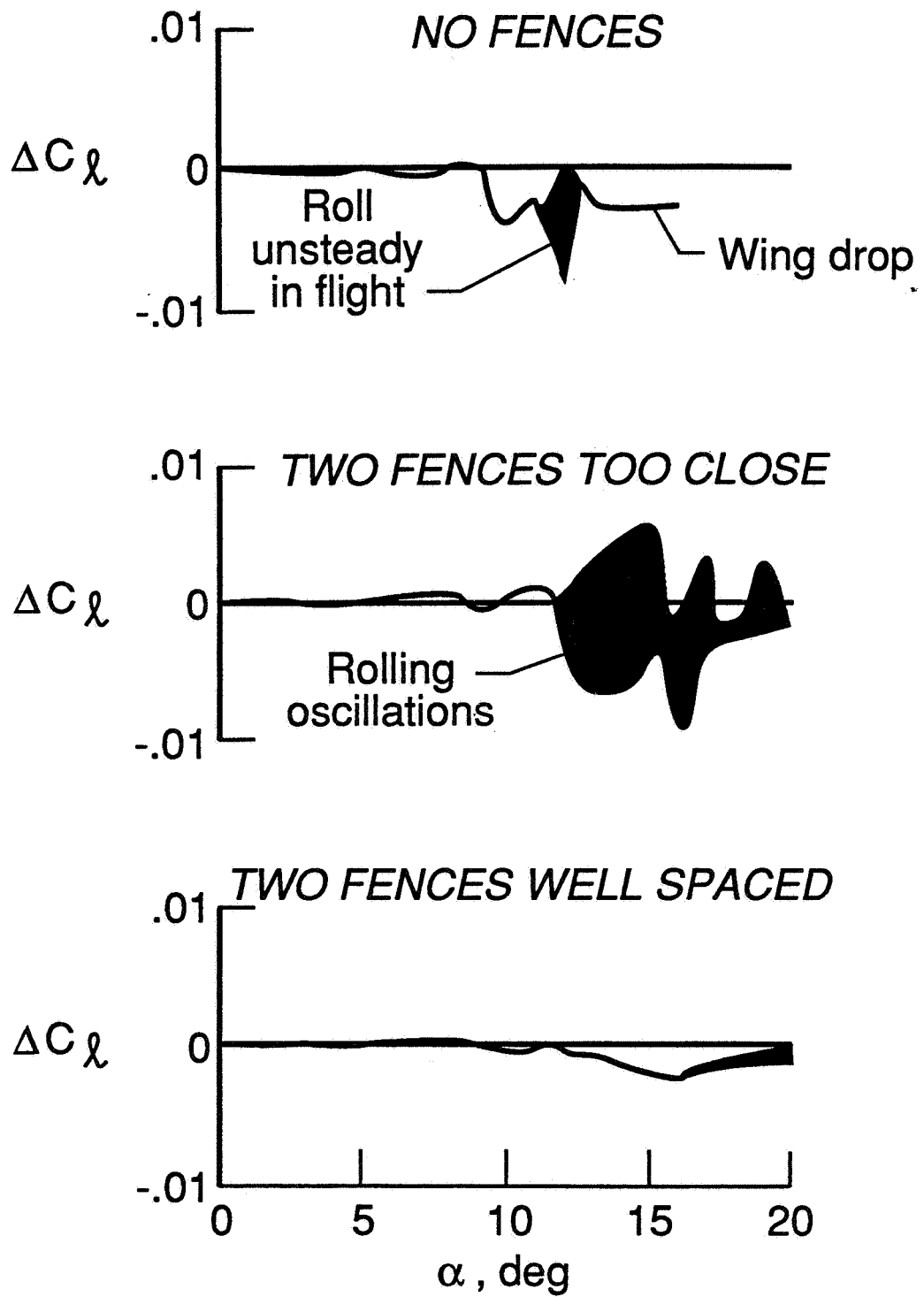


Figure 8. Effect of Wing Fences on the Harrier aircraft (Ref. 16)

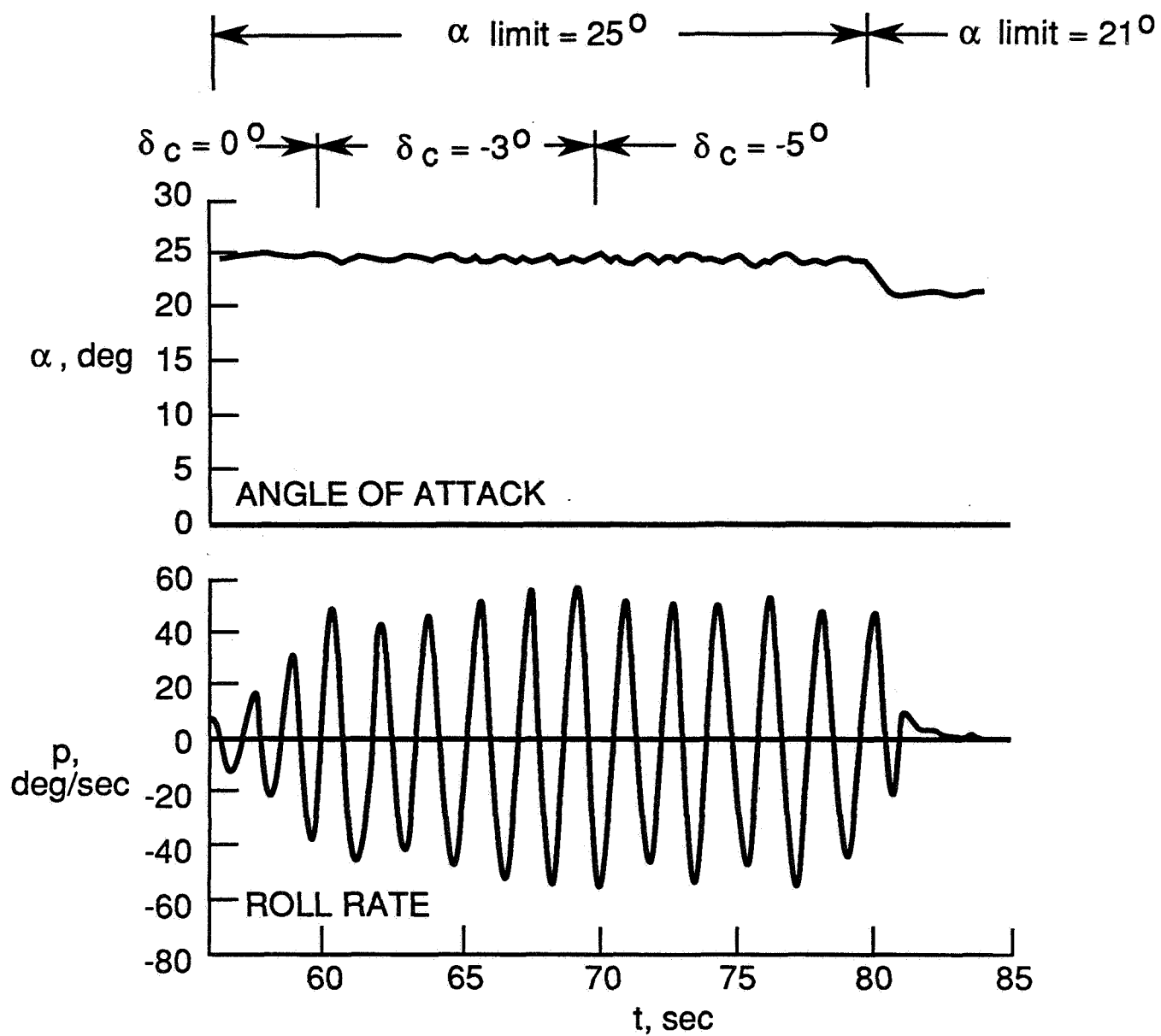


Figure 9. Wing Rock on the HIRM model (Ref. 7)

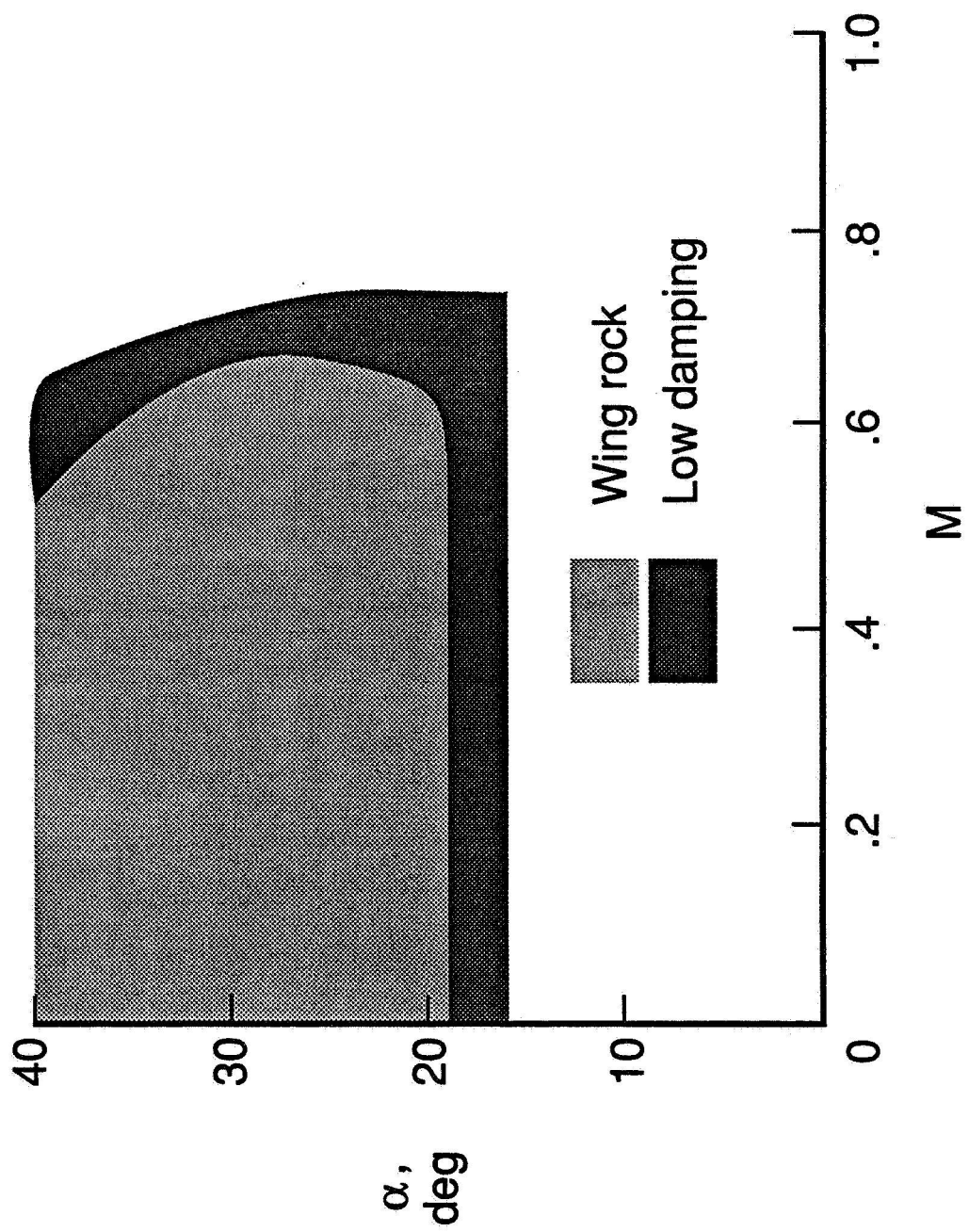


Figure 10. Wing Rock Envelope for the F-14 aircraft (Ref. 17)

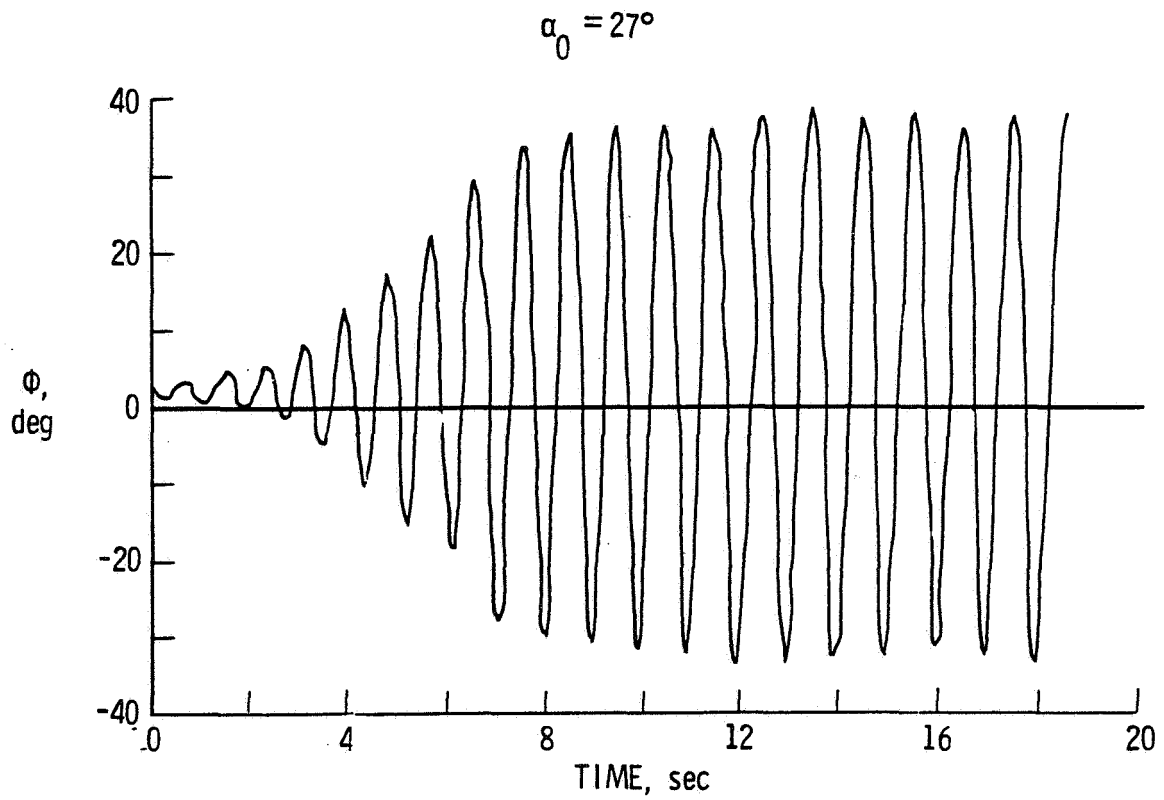


Figure 11. Wing Rock Build Up for the 80° Delta Wing (Ref. 18)

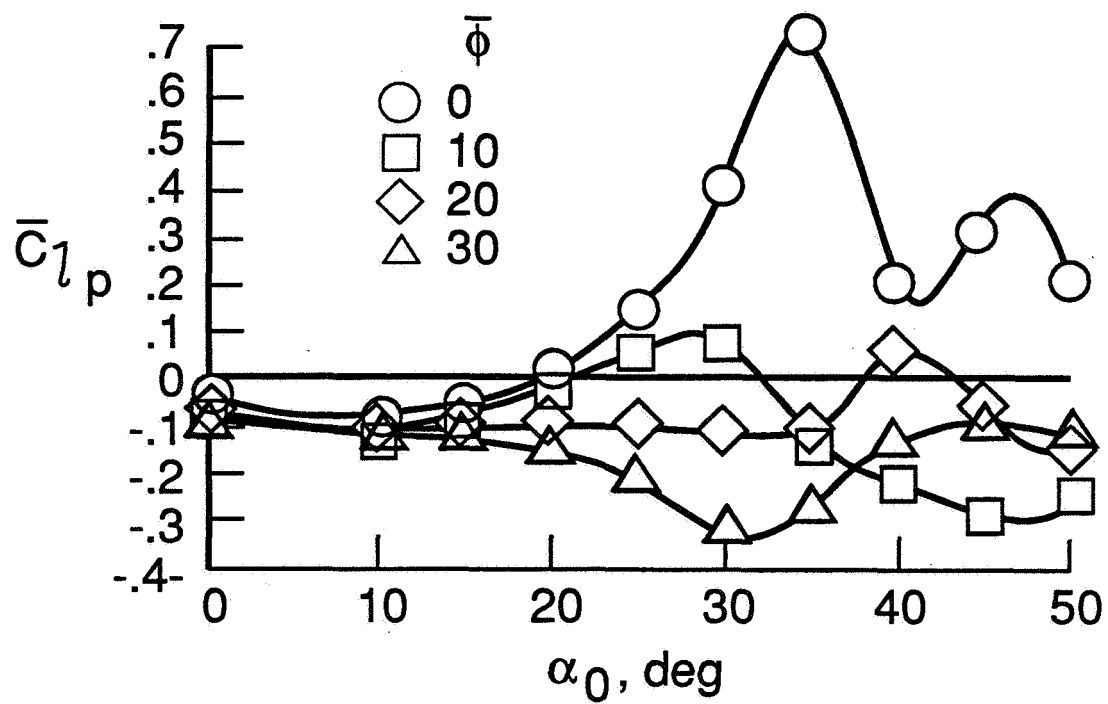


Figure 12. Roll Damping Variation with Sideslip for the 80° Delta Wing (Ref. 19)

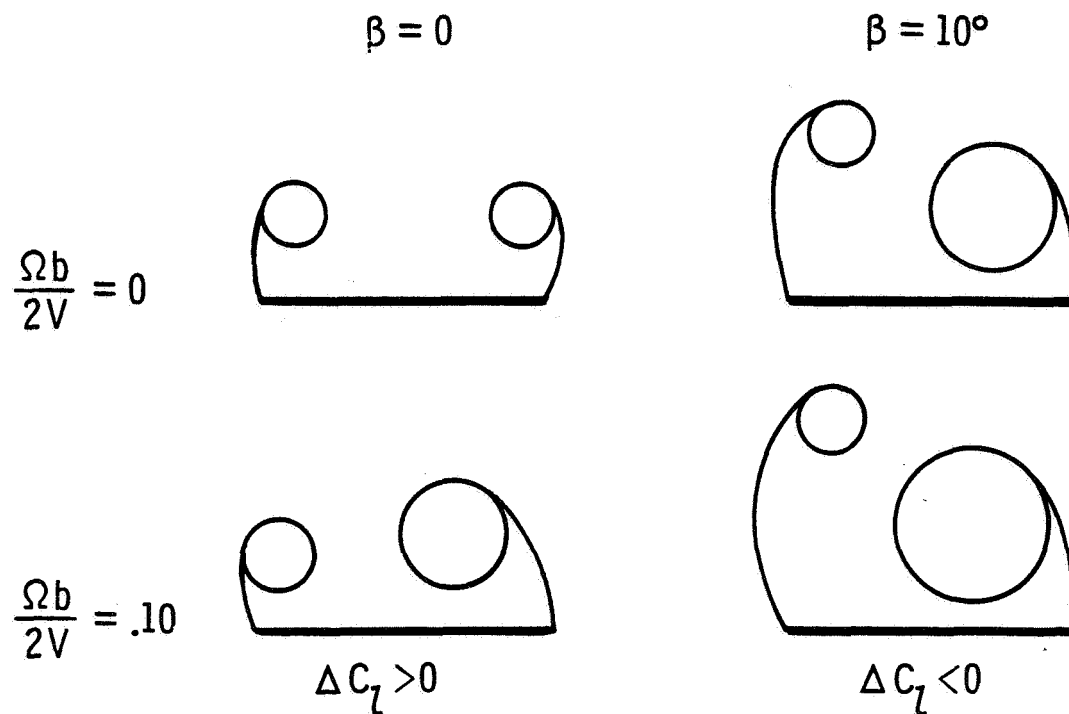


Figure 13. Vortex Patterns for the 80° Delta Wing.(Ref. 18)

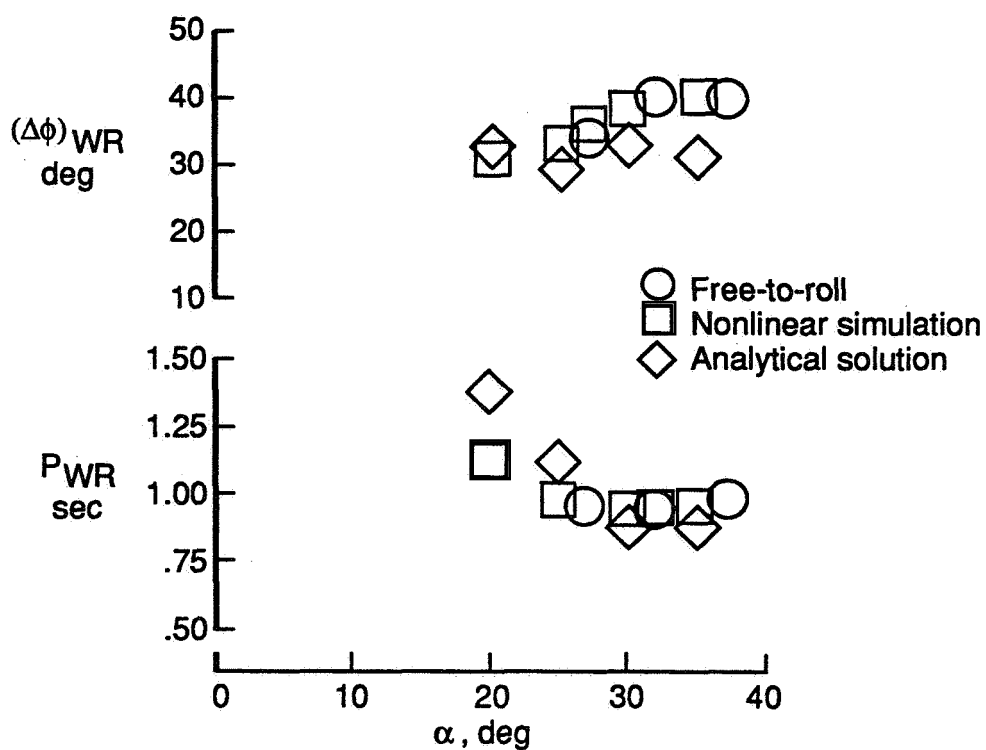


Figure 14. Comparison of one D.O.F. Results for the 80° Delta Wing.(Ref. 18)

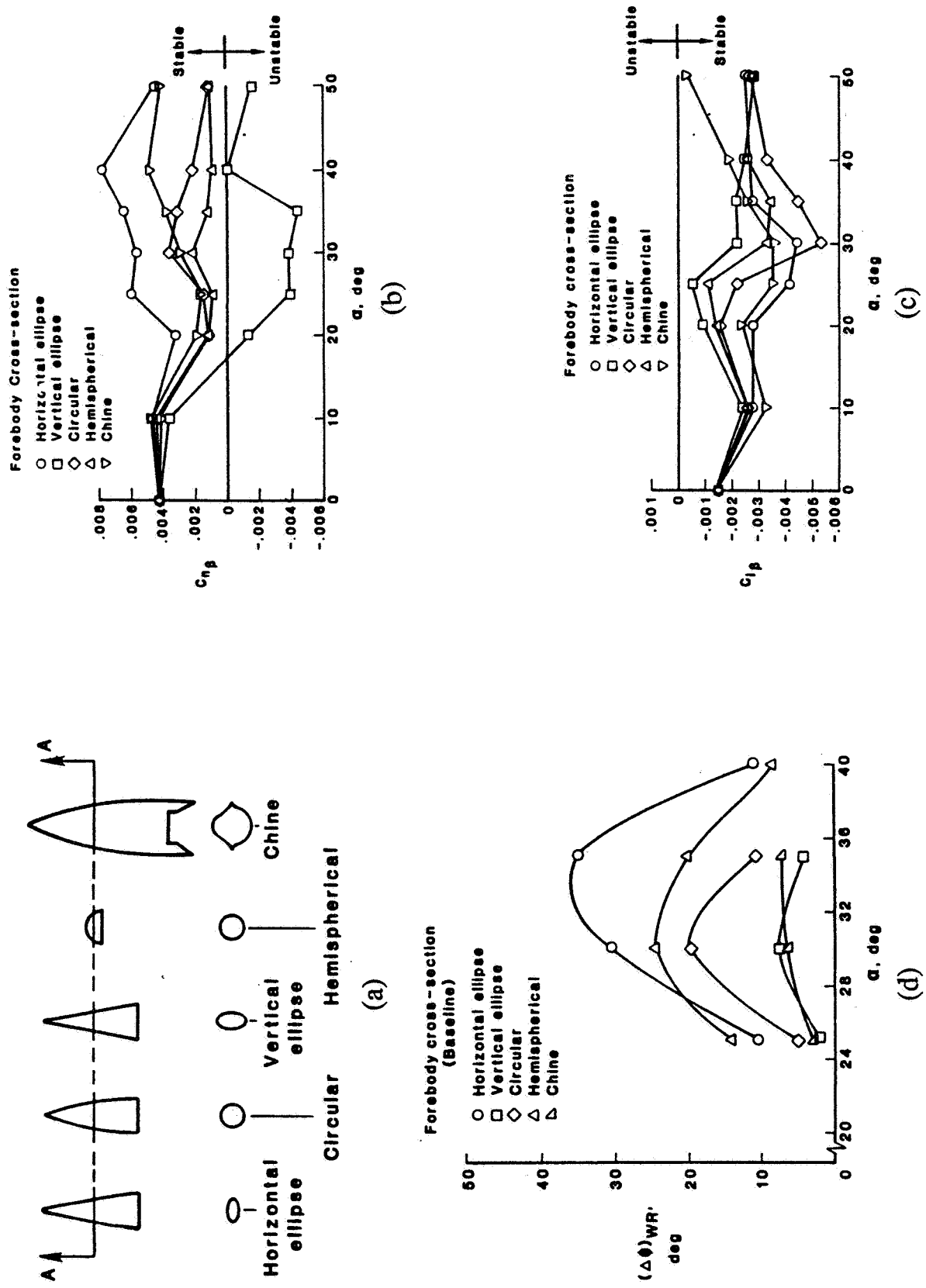


Figure 15. Forebody Study for a Generic Fighter Model (Ref. 34)

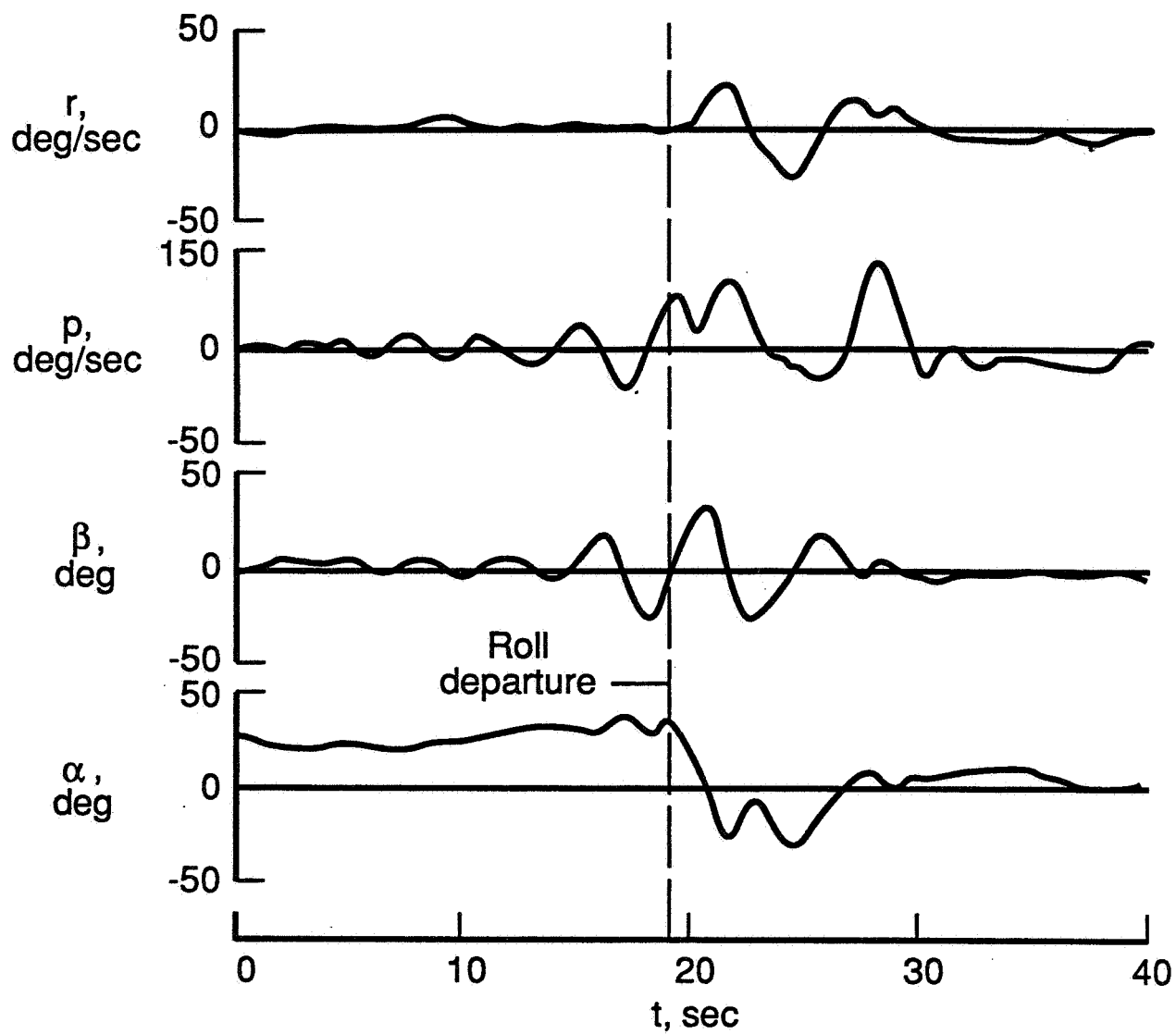


Figure 16. Wing Rock on the X-29 Drop Model (Ref. 20)

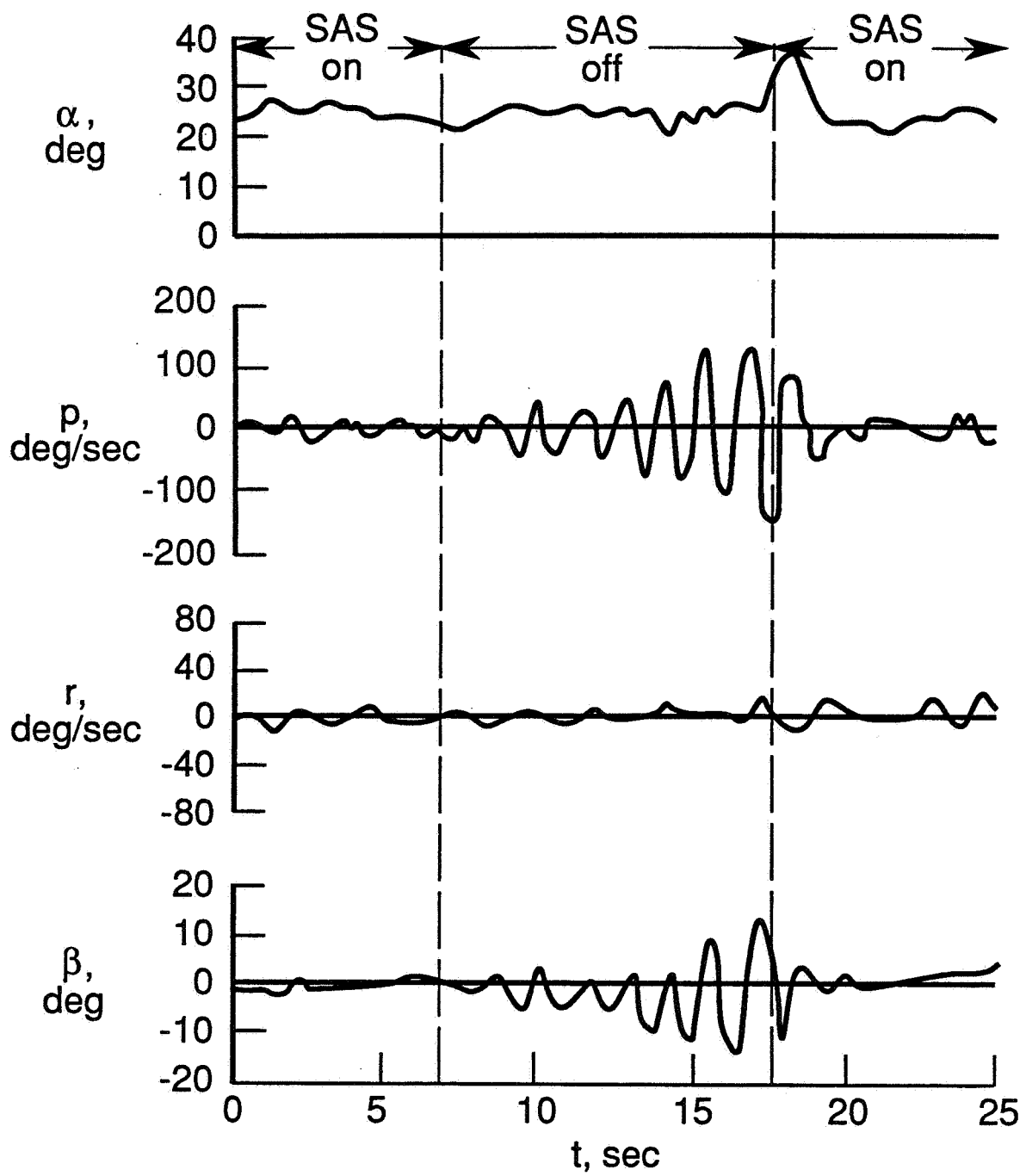


Figure 17. Roll Damper Effect on Wing Rock for the X-29 (Ref. 20)

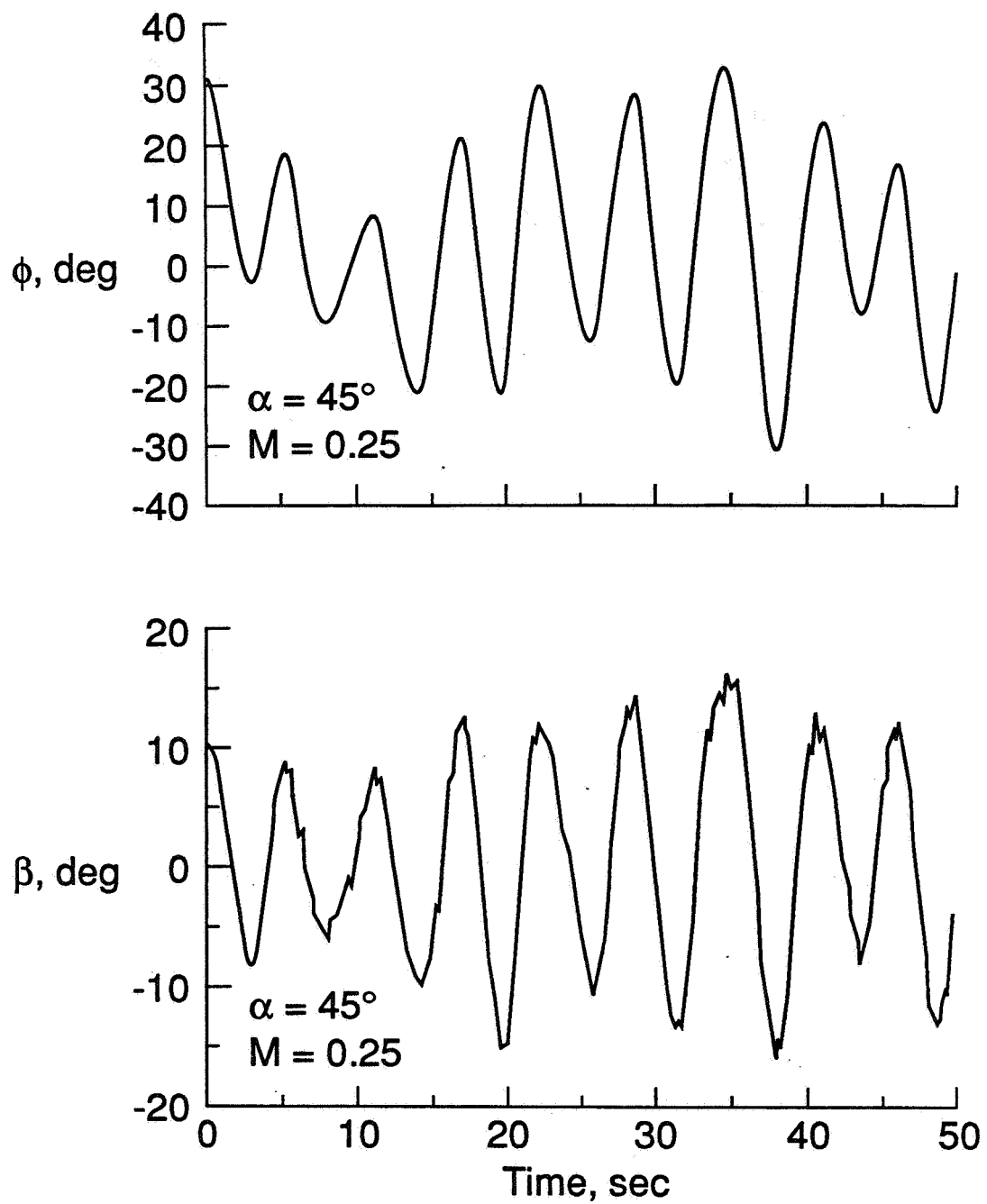


Figure 18. Wing Rock on the F-18 aircraft (Ref. 21)

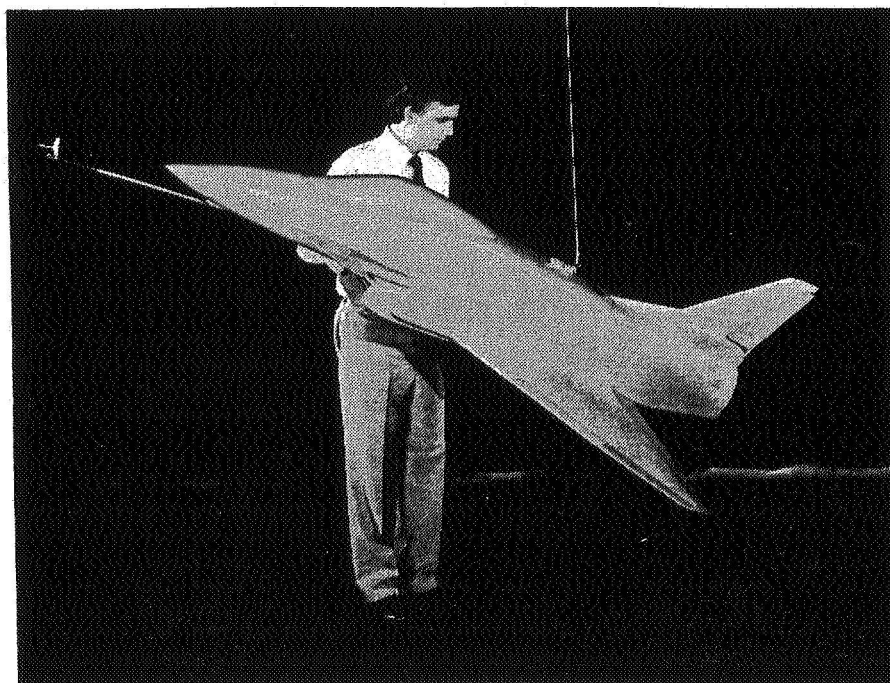


Figure 21. X-31 19-percent-scale Model

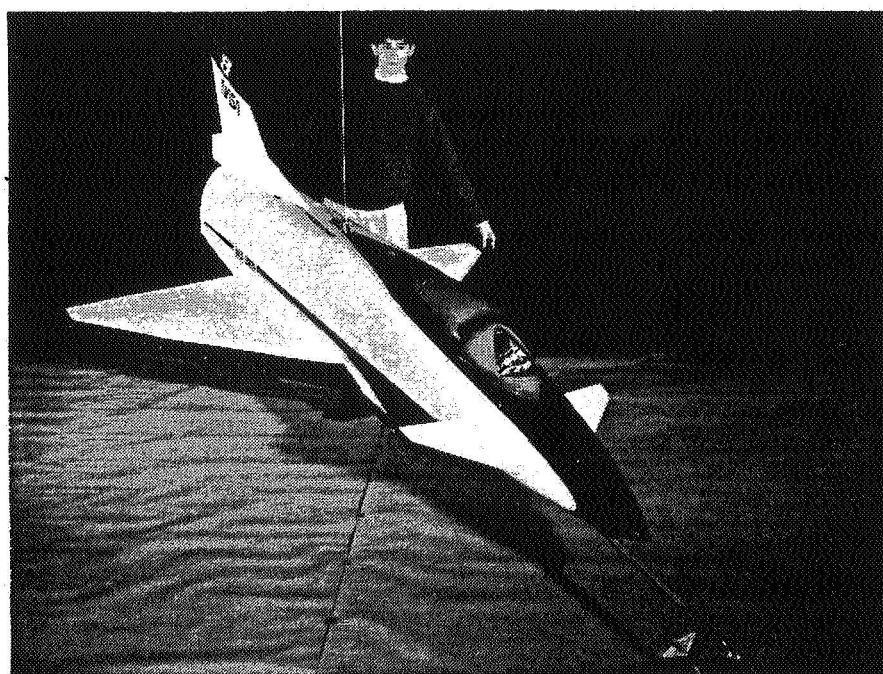


Figure 22. X-31 27-percent-scale Drop Model

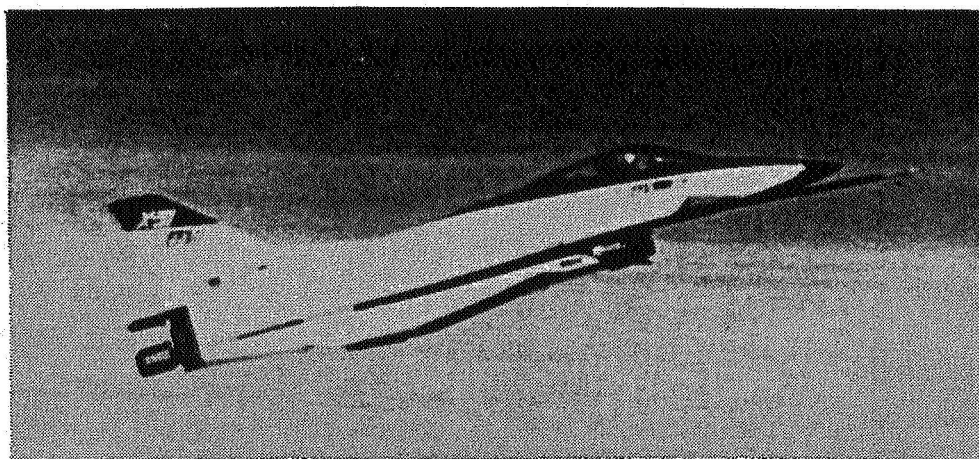


Figure 19. X-31 Full-Scale aircraft

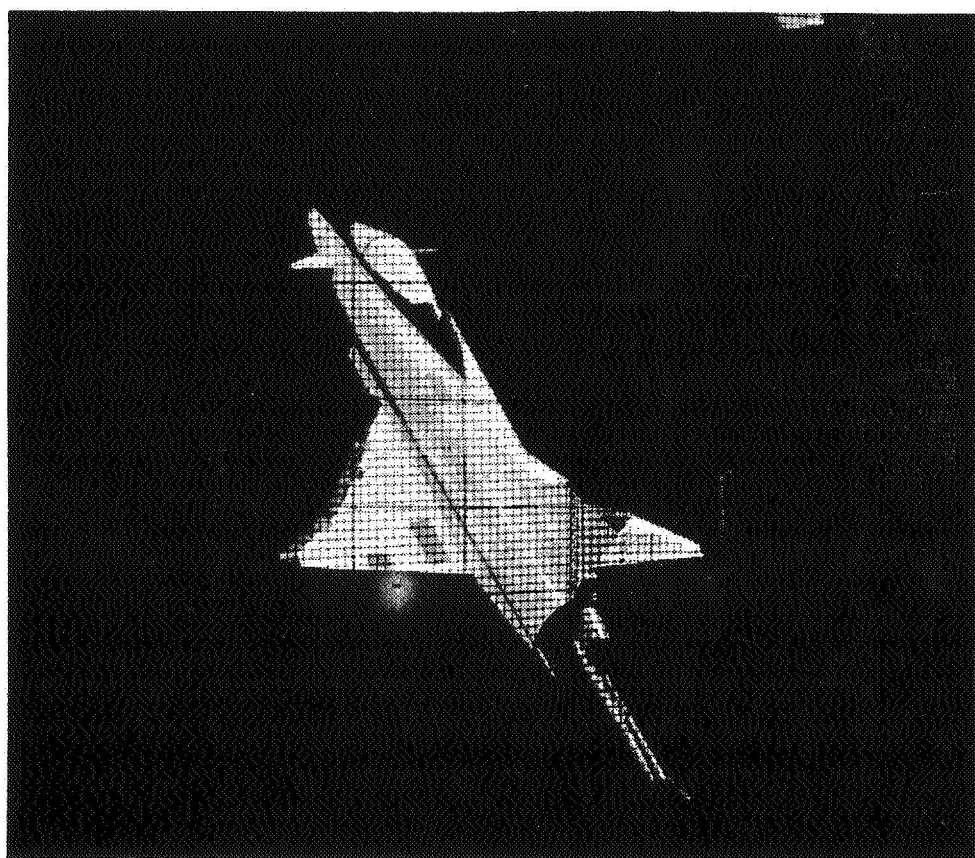


Figure 20. X-31 13.3-percent-scale Model

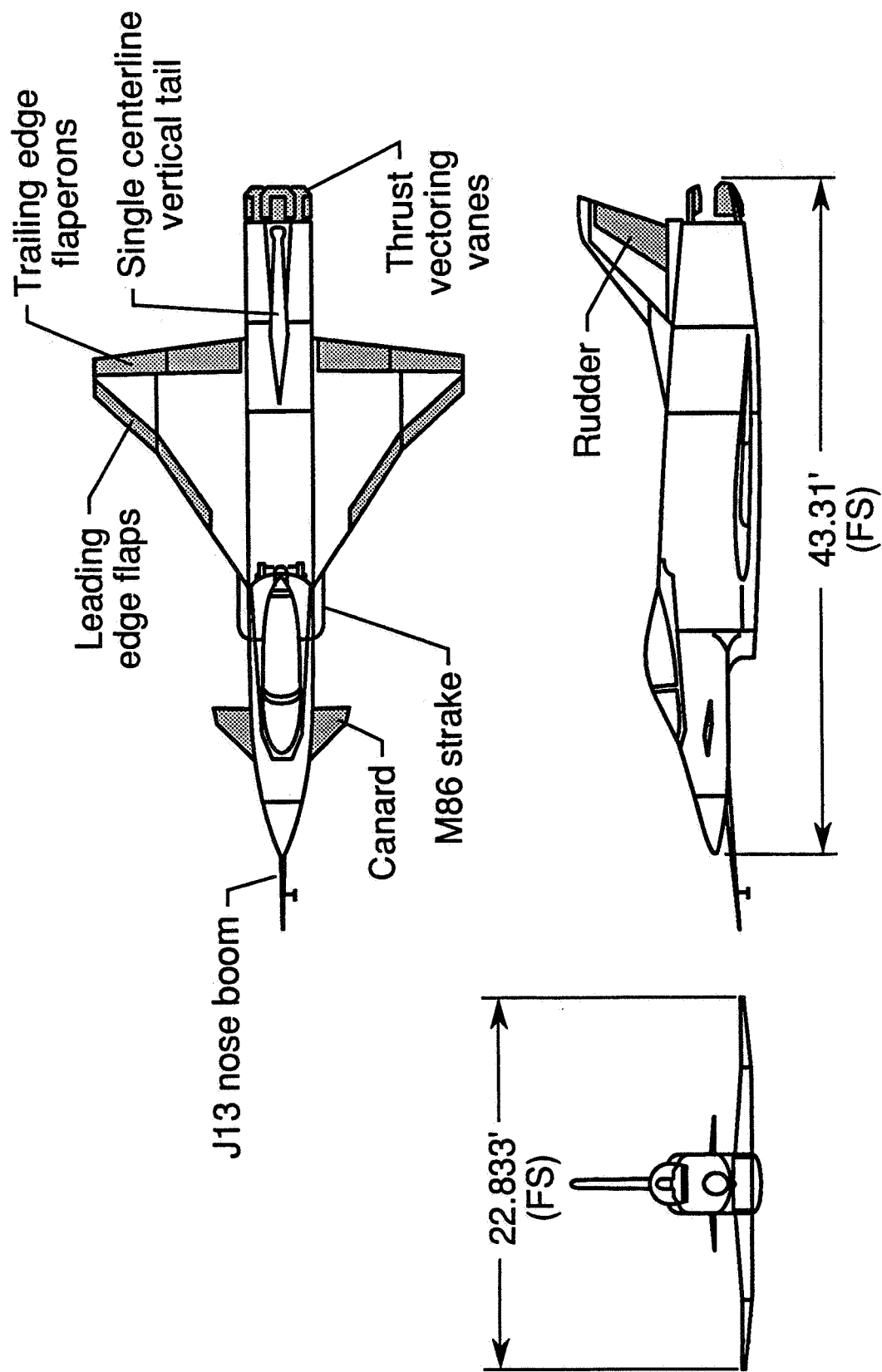


Figure 23. X-31 Full-Scale 3-D Configuration Drawing

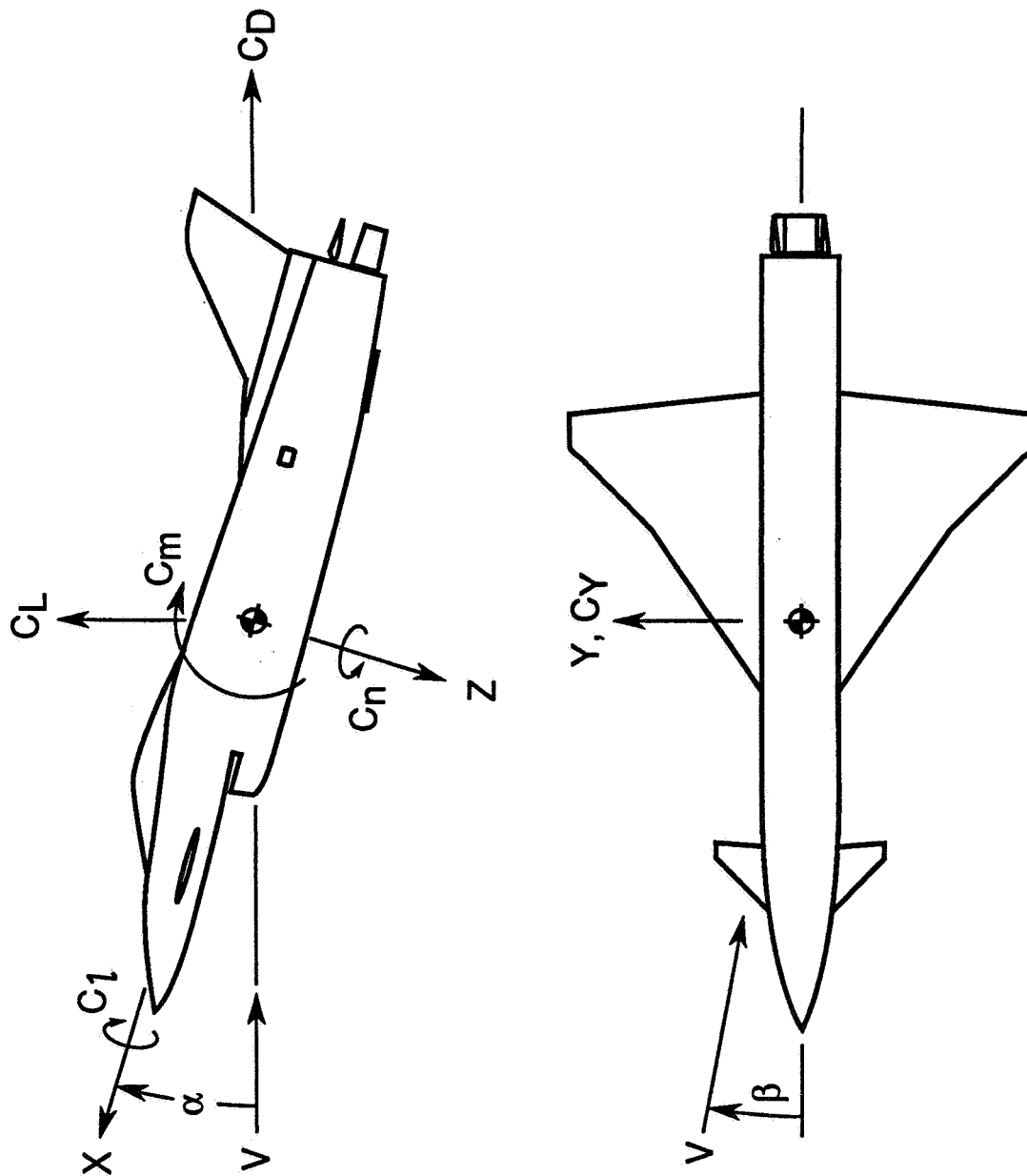


Figure 24. System of Axes

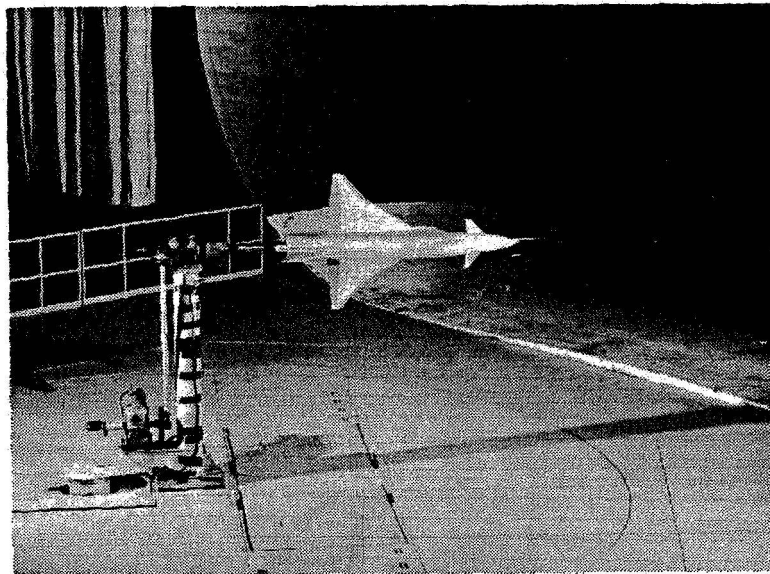


Figure 25. Forced-Oscillation Test Setup for Roll

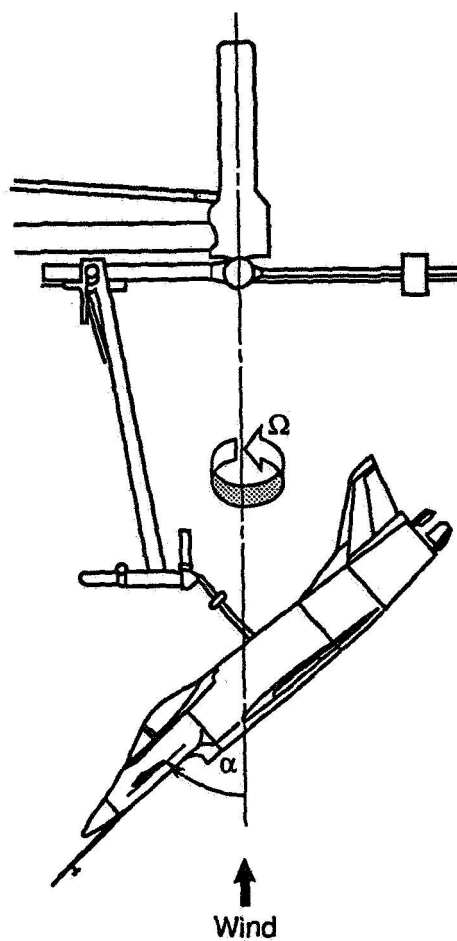


Figure 26. Rotary Balance Test Setup

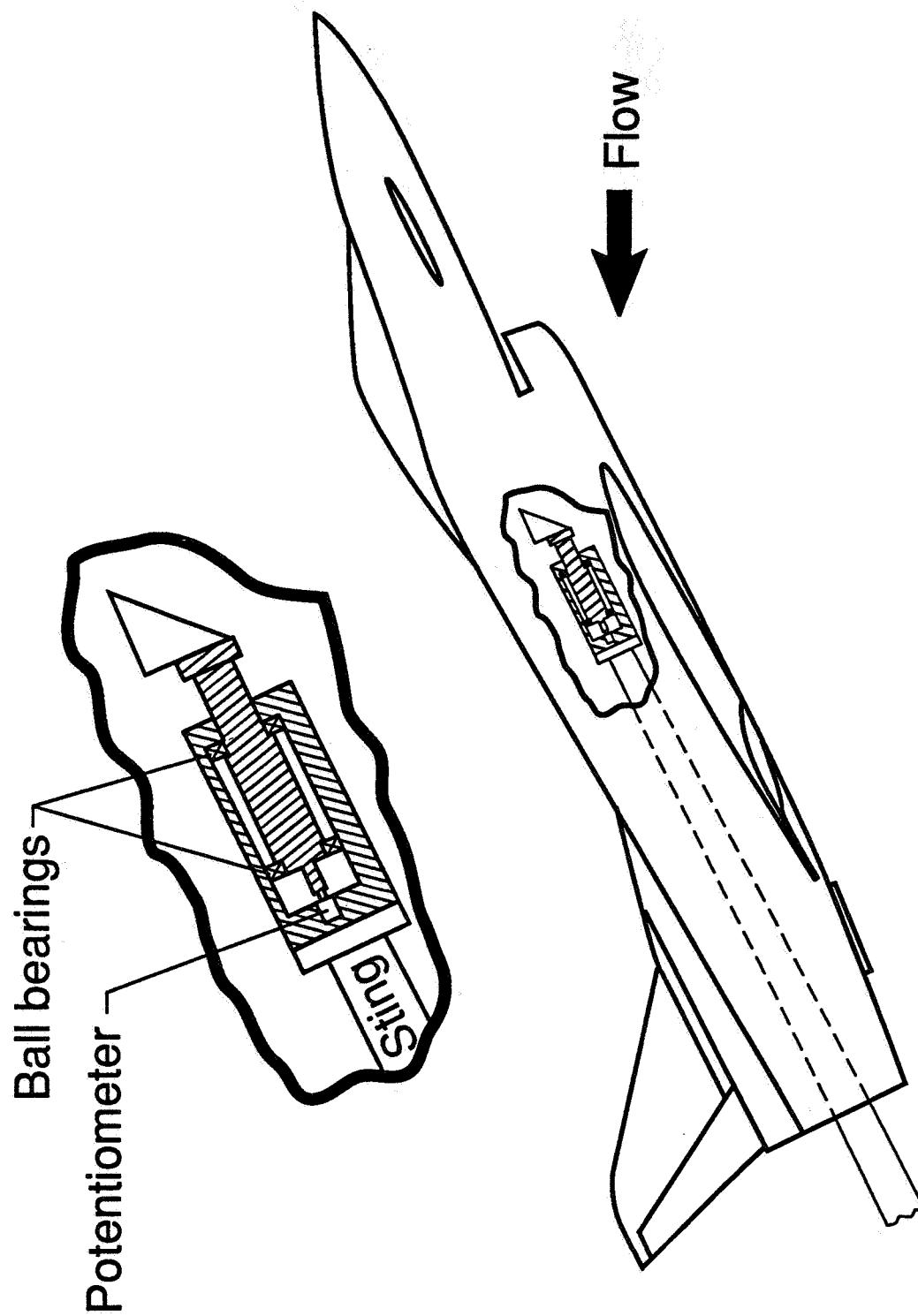


Figure 27. Free-to-Roll Test Setup

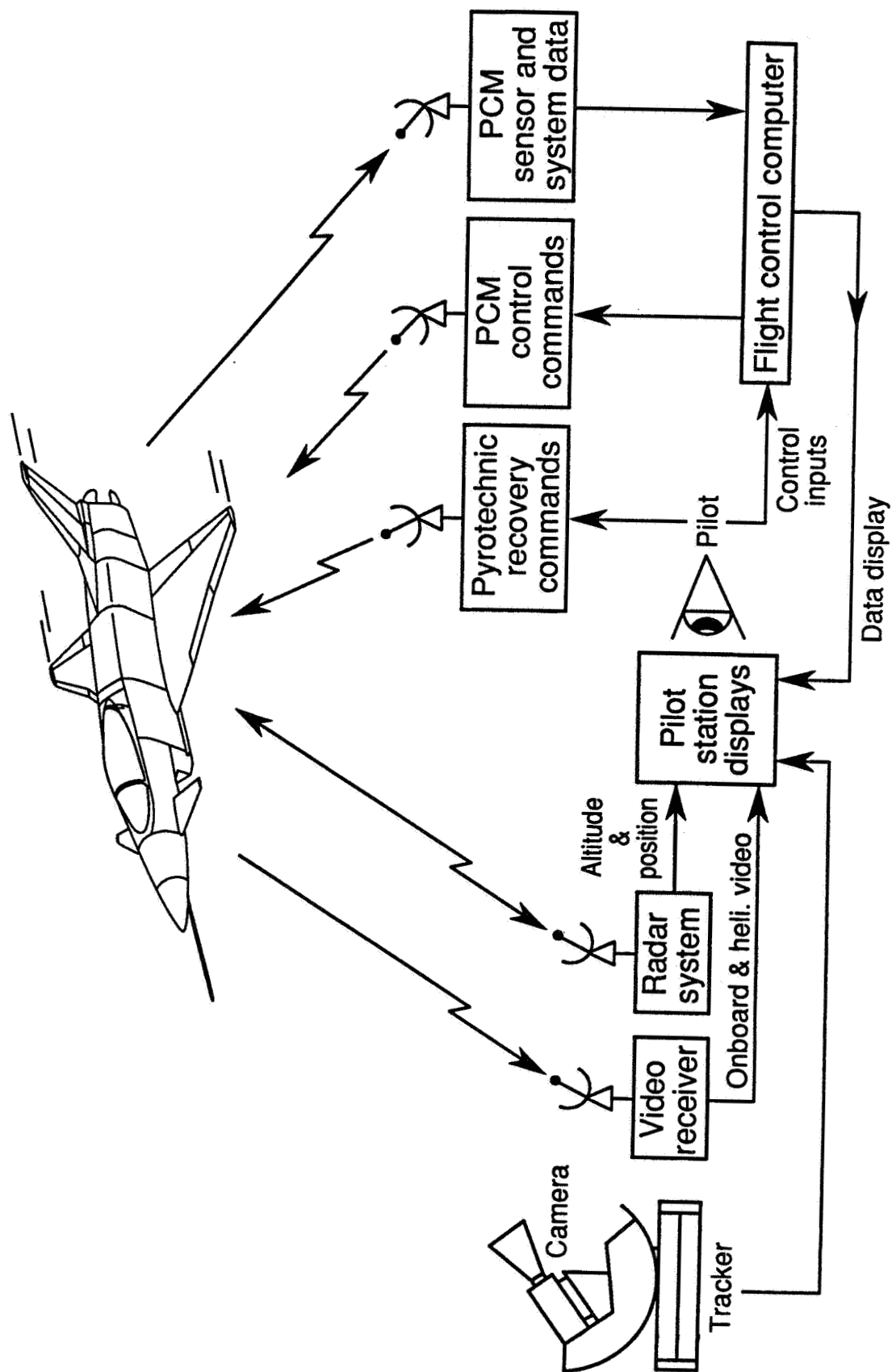


Figure 28. Drop Model Operation at the NASA Plumtree Test Facility

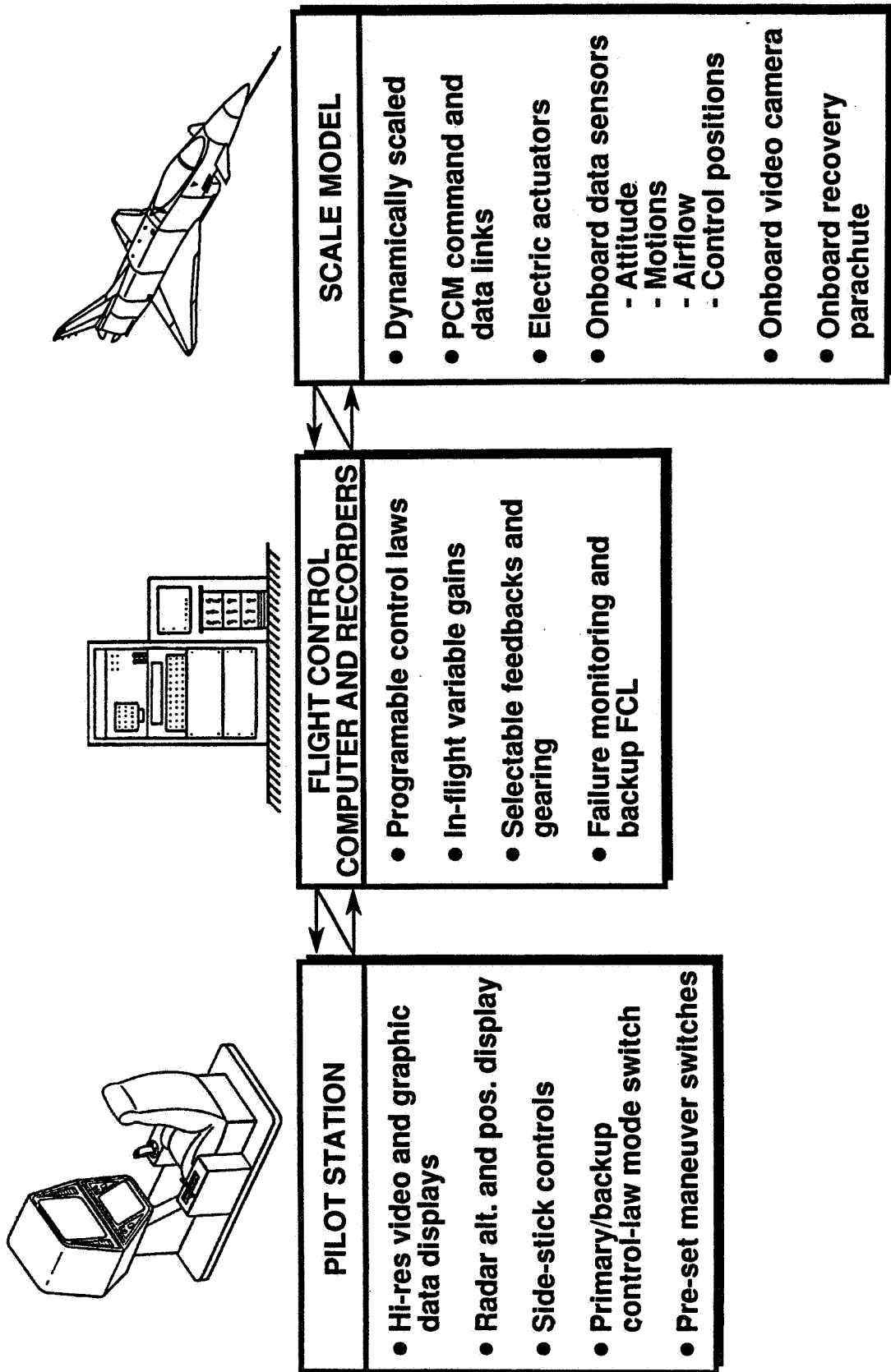


Figure 29. Drop Model Flight Control System

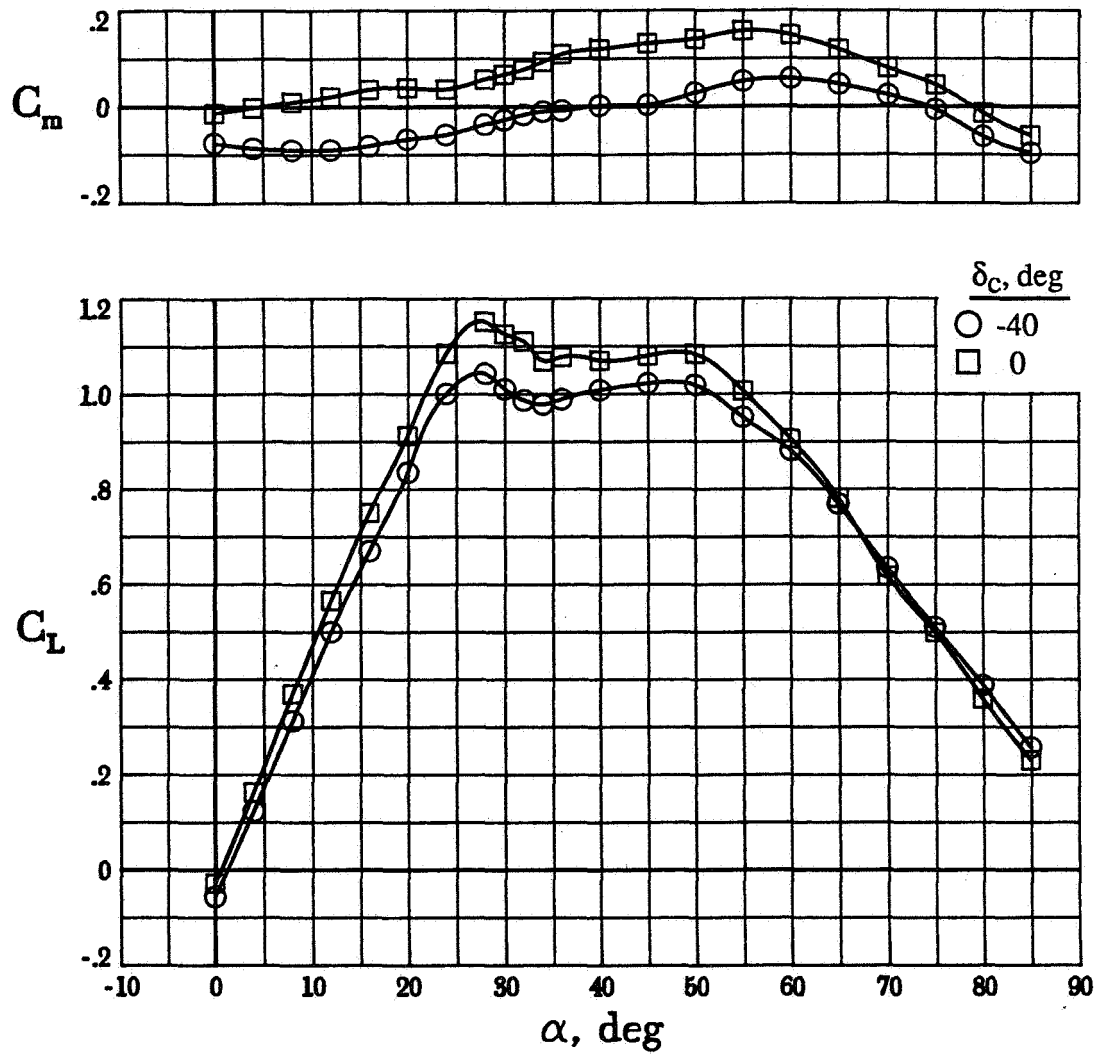


Figure 30. Canard Effect on Longitudinal Characteristics

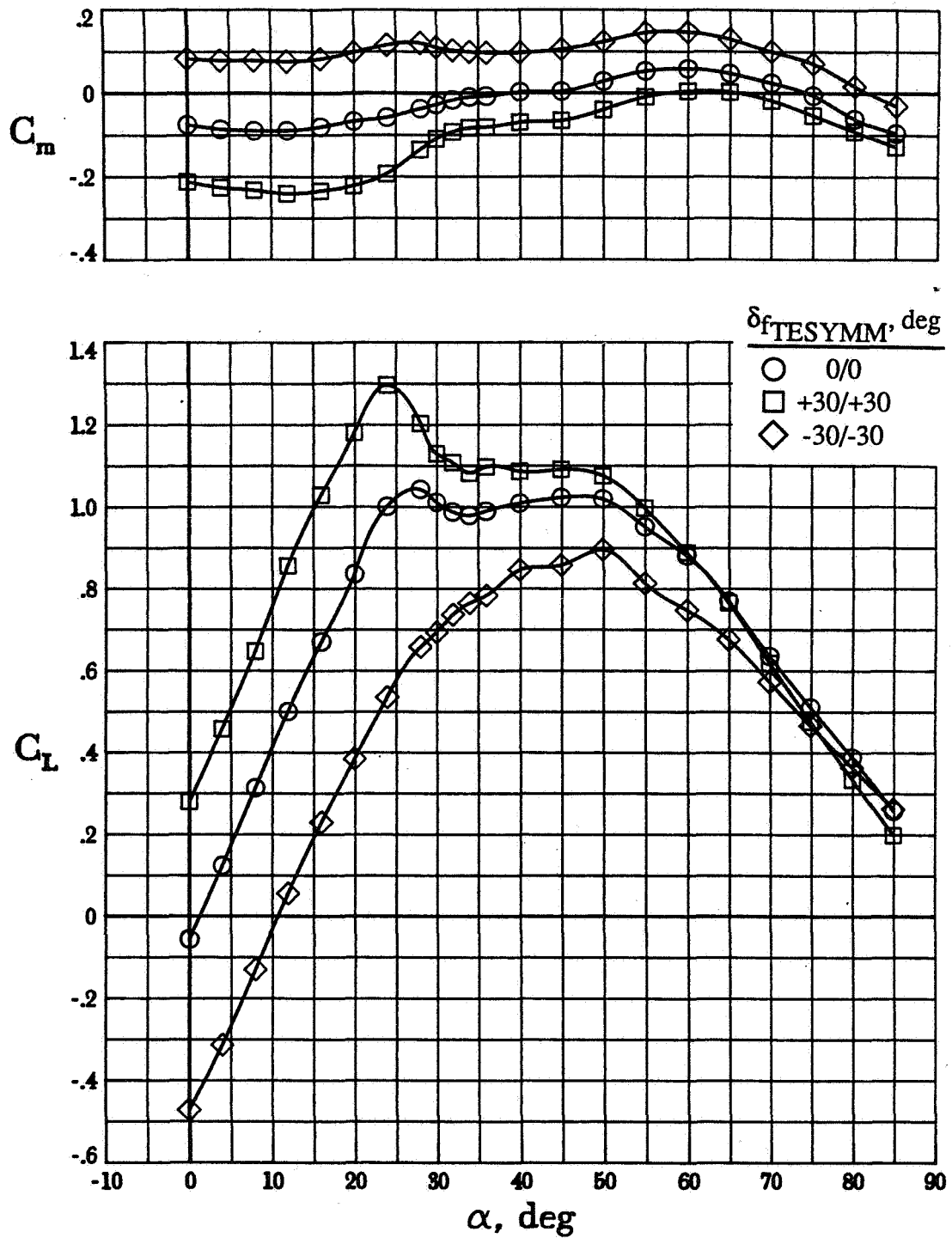


Figure 31. Trailing-edge Flap Effect on Longitudinal Characteristics

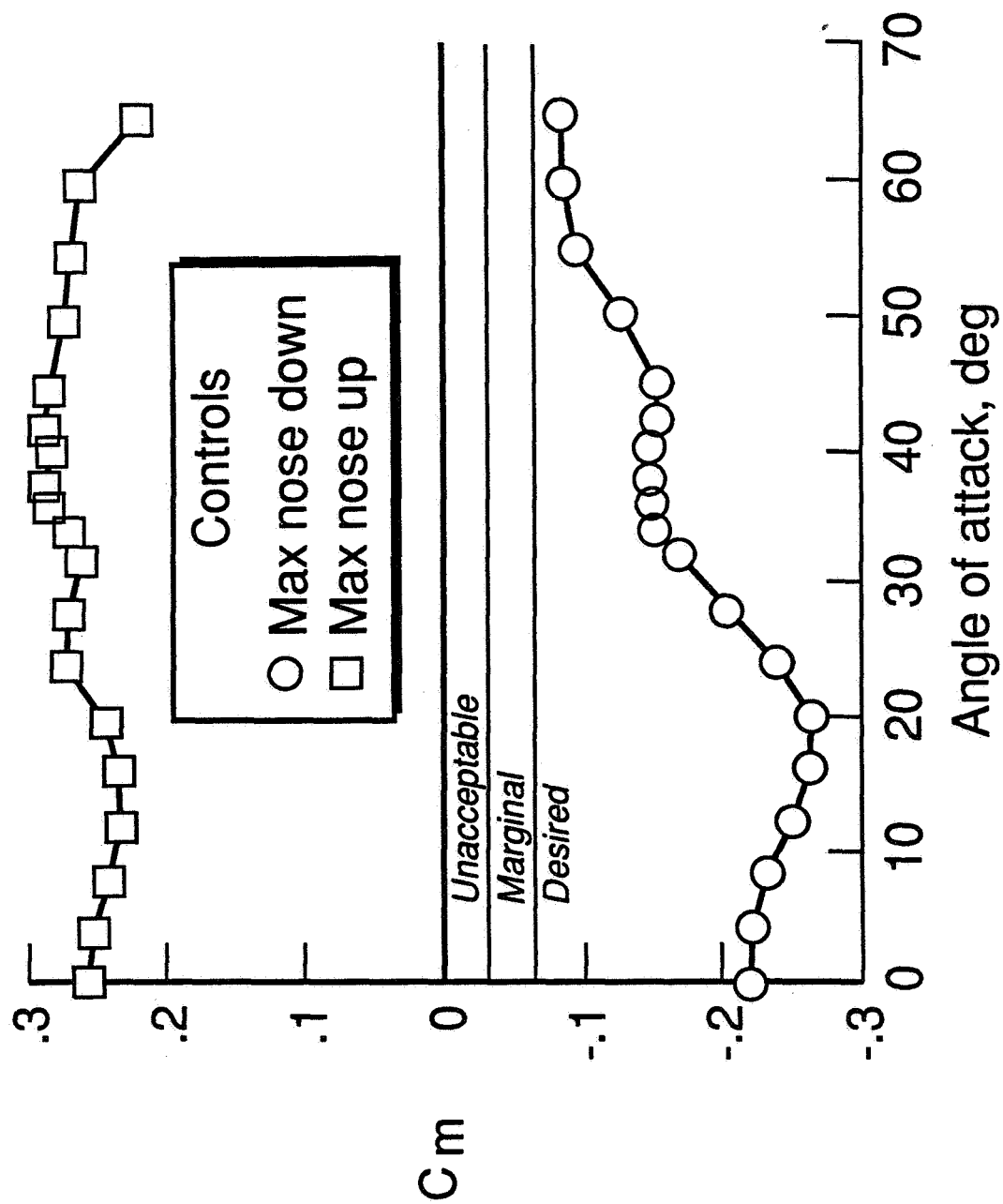
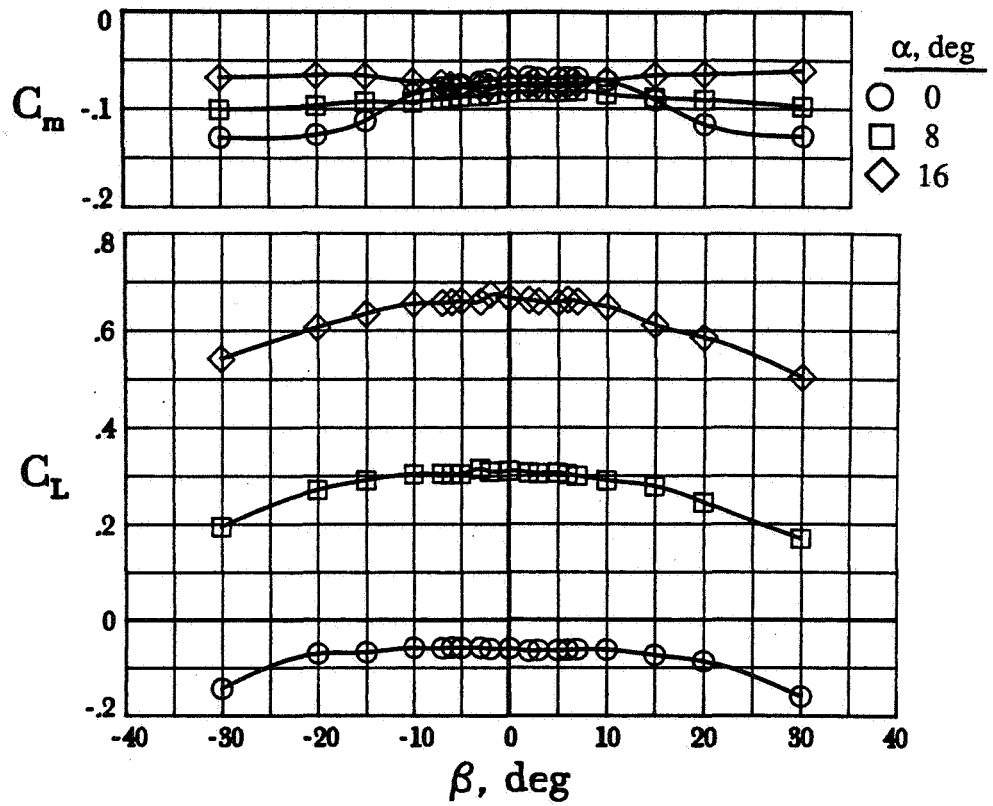
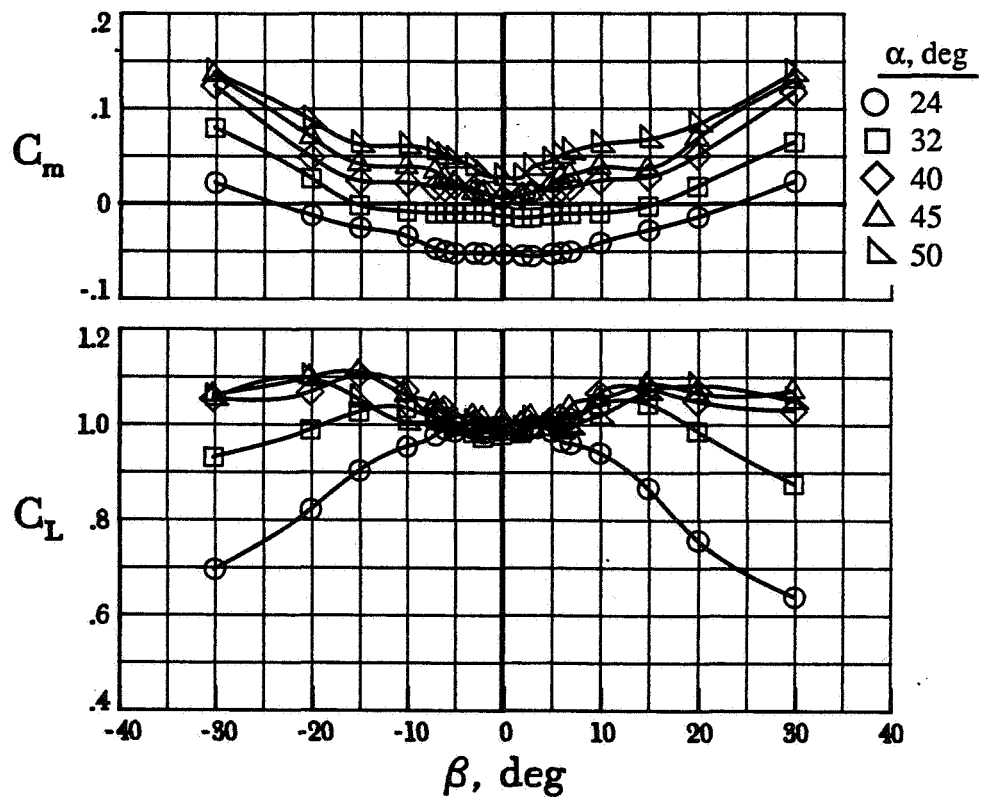


Figure 32. Maximum Nose-up and Nose-down Controls

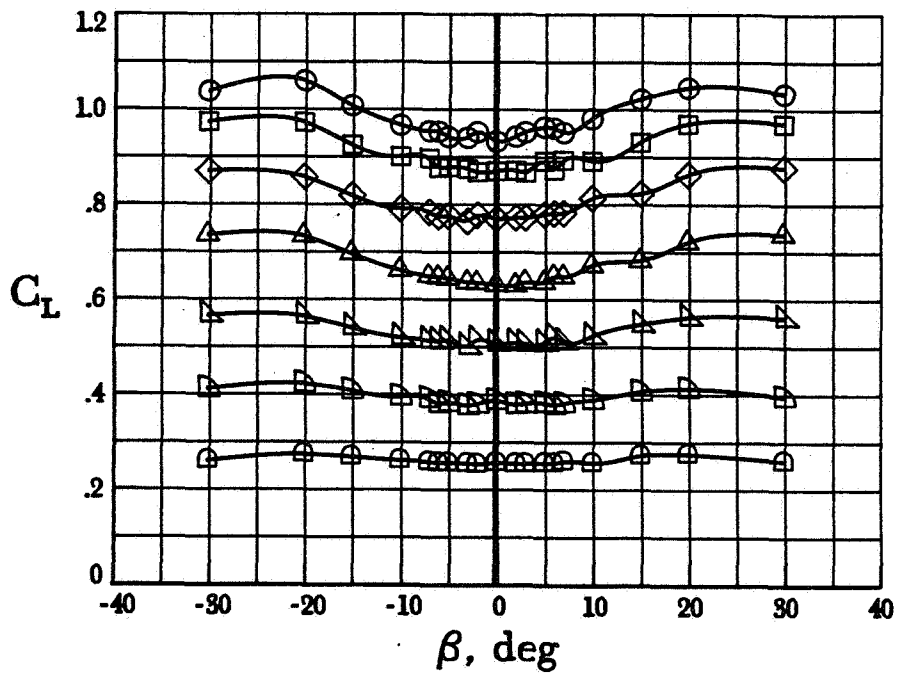
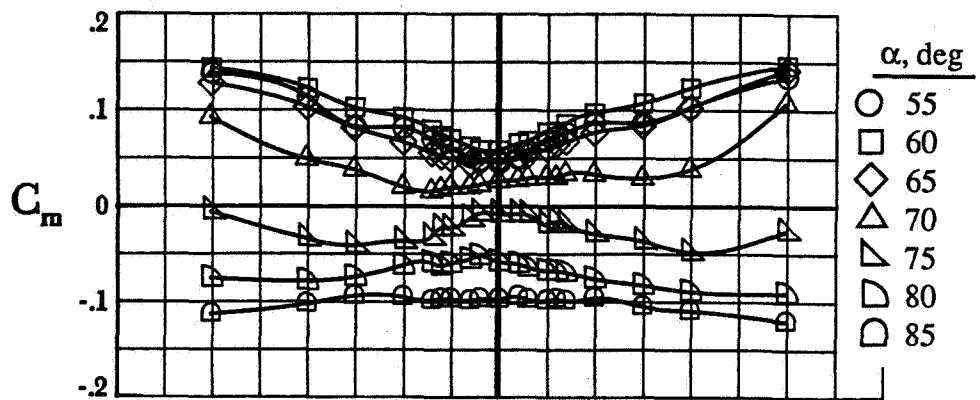


(a) Low Angles of Attack



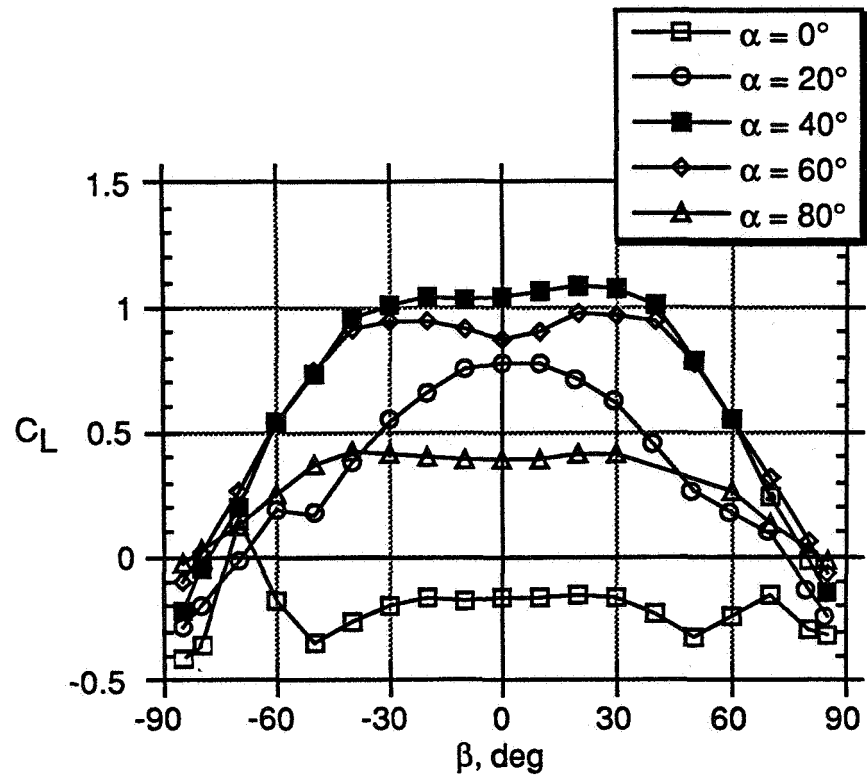
(b) Mid Angles of Attack

Figure 33. Sideslip Effect on Lift and Pitching Moment

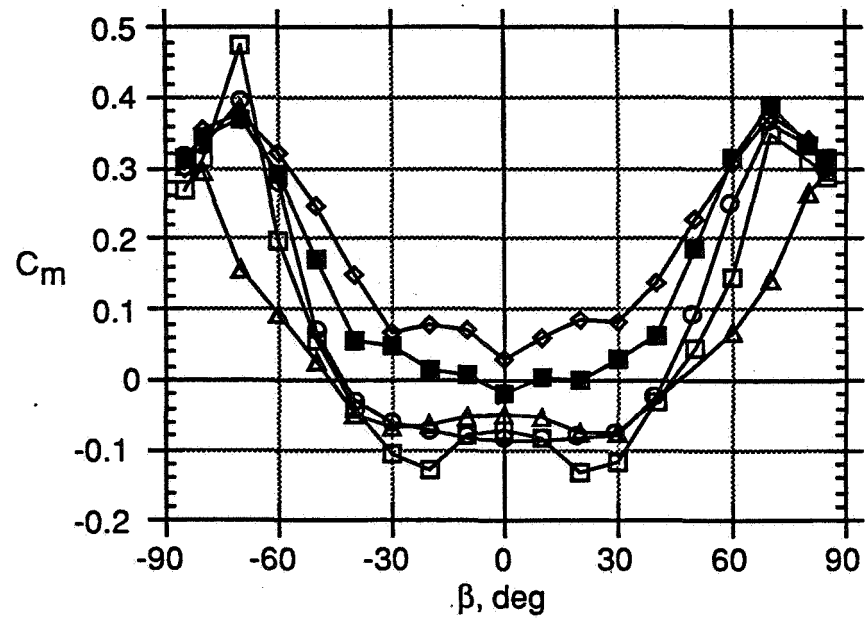


(c) High Angles of Attack

Figure 33. Concluded



(a) Lift



(b) Pitching Moment

Figure 34. Large Sideslip Effect on Lift and Pitching Moment

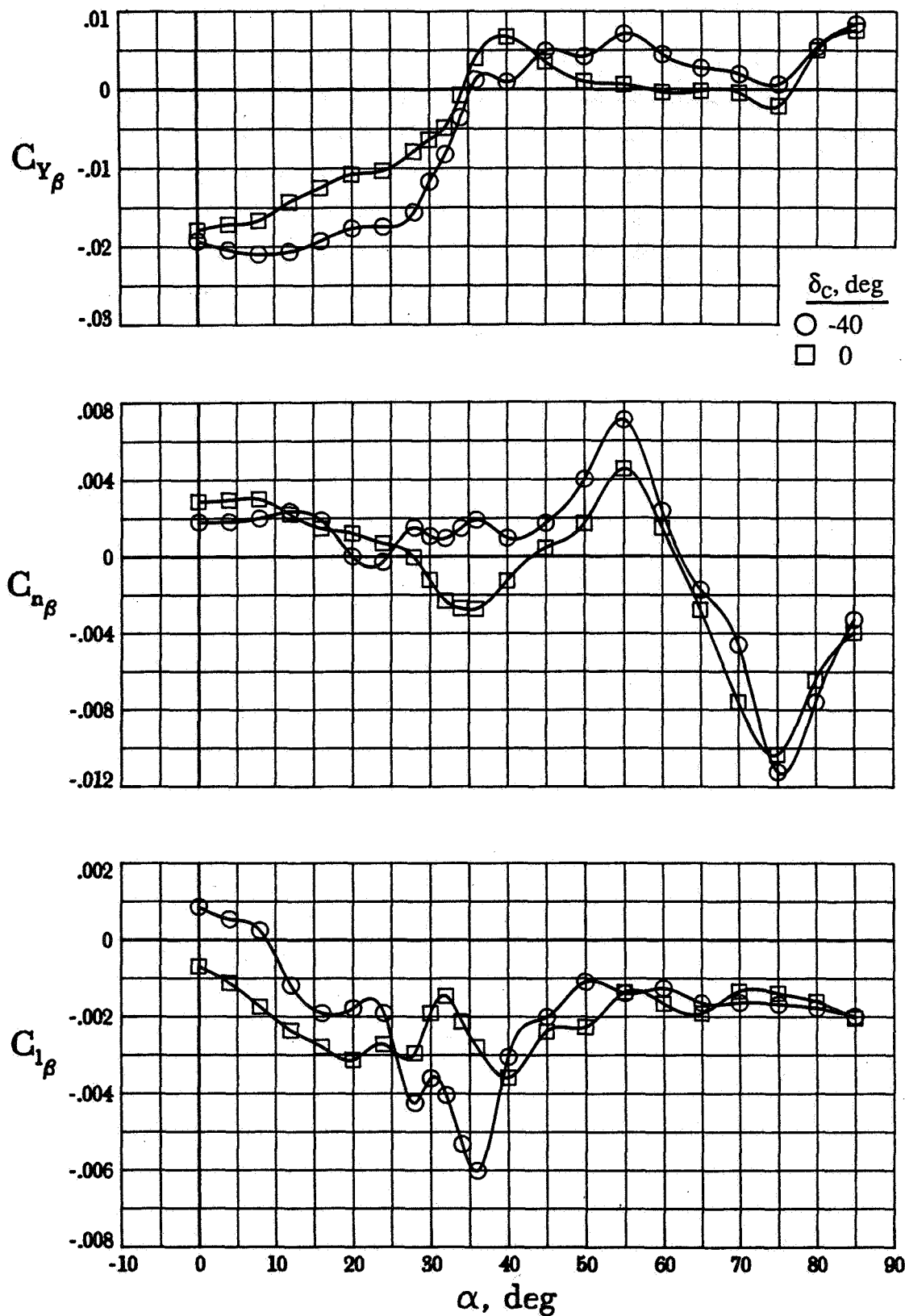


Figure 35. Canard Effect on Lateral-Directional Static Stability

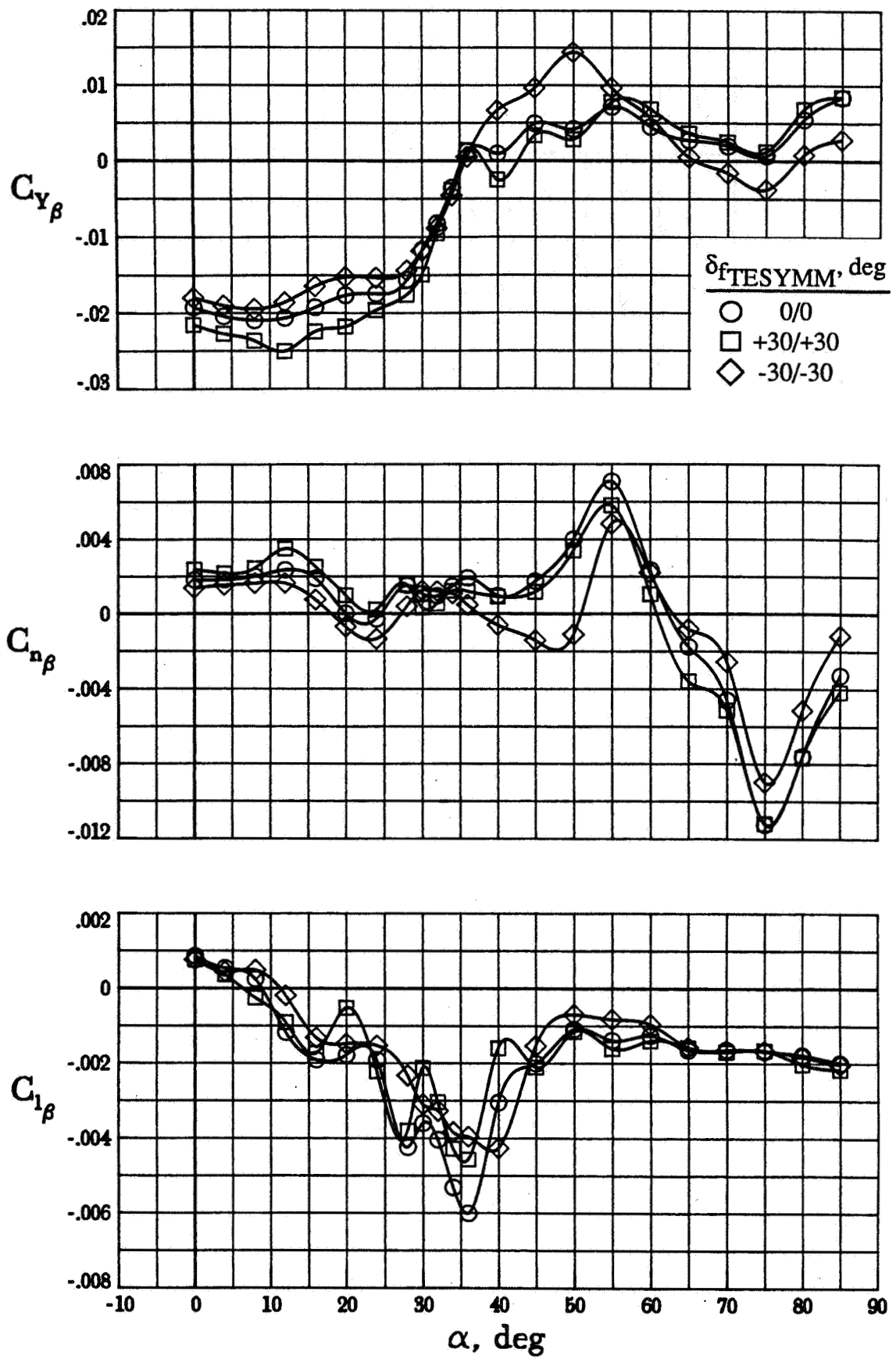


Figure 36. Flap Effect on Lateral-Directional Static Stability

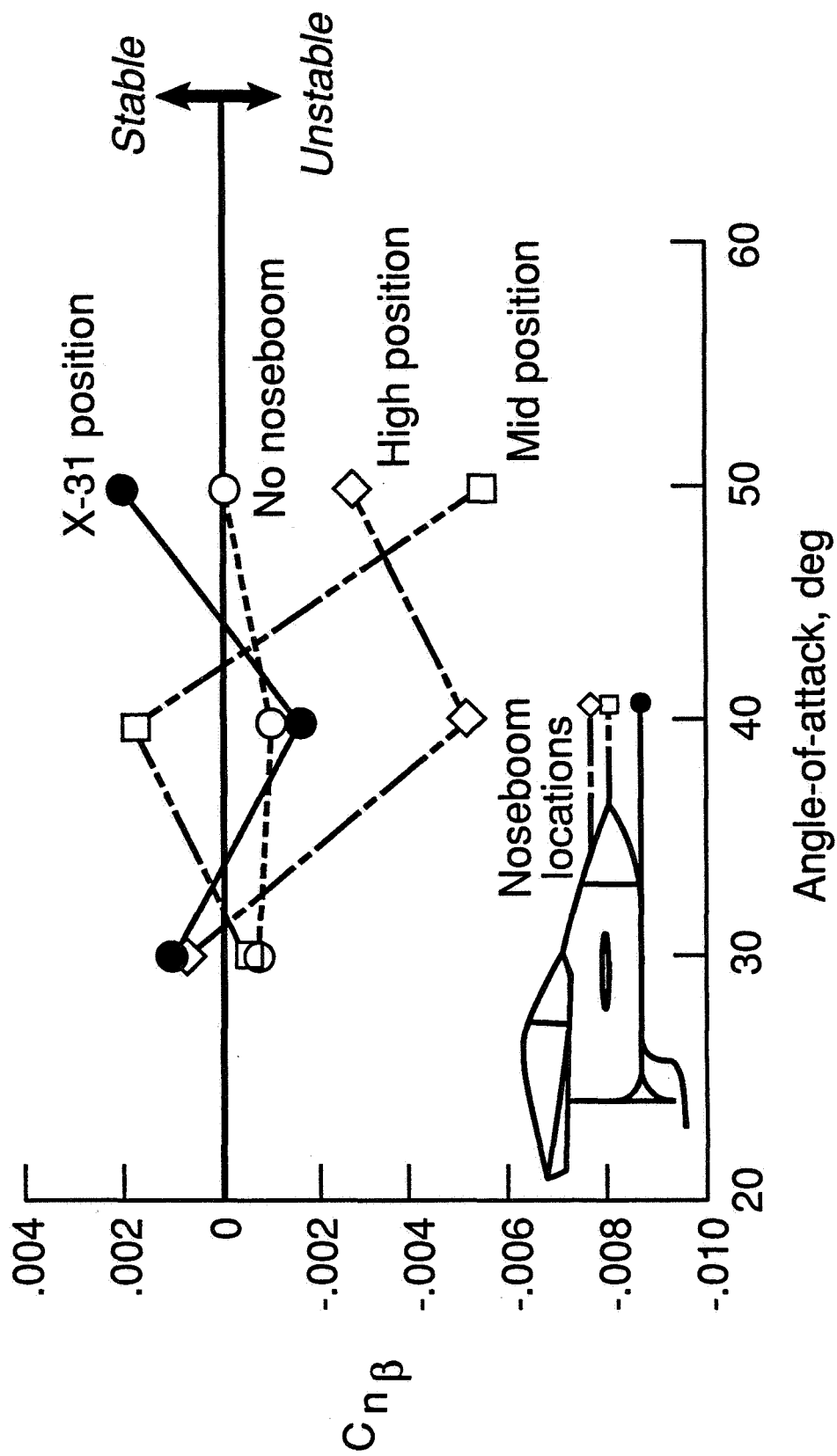


Figure 37. J13 Noseboom Effect on Directional Static Stability

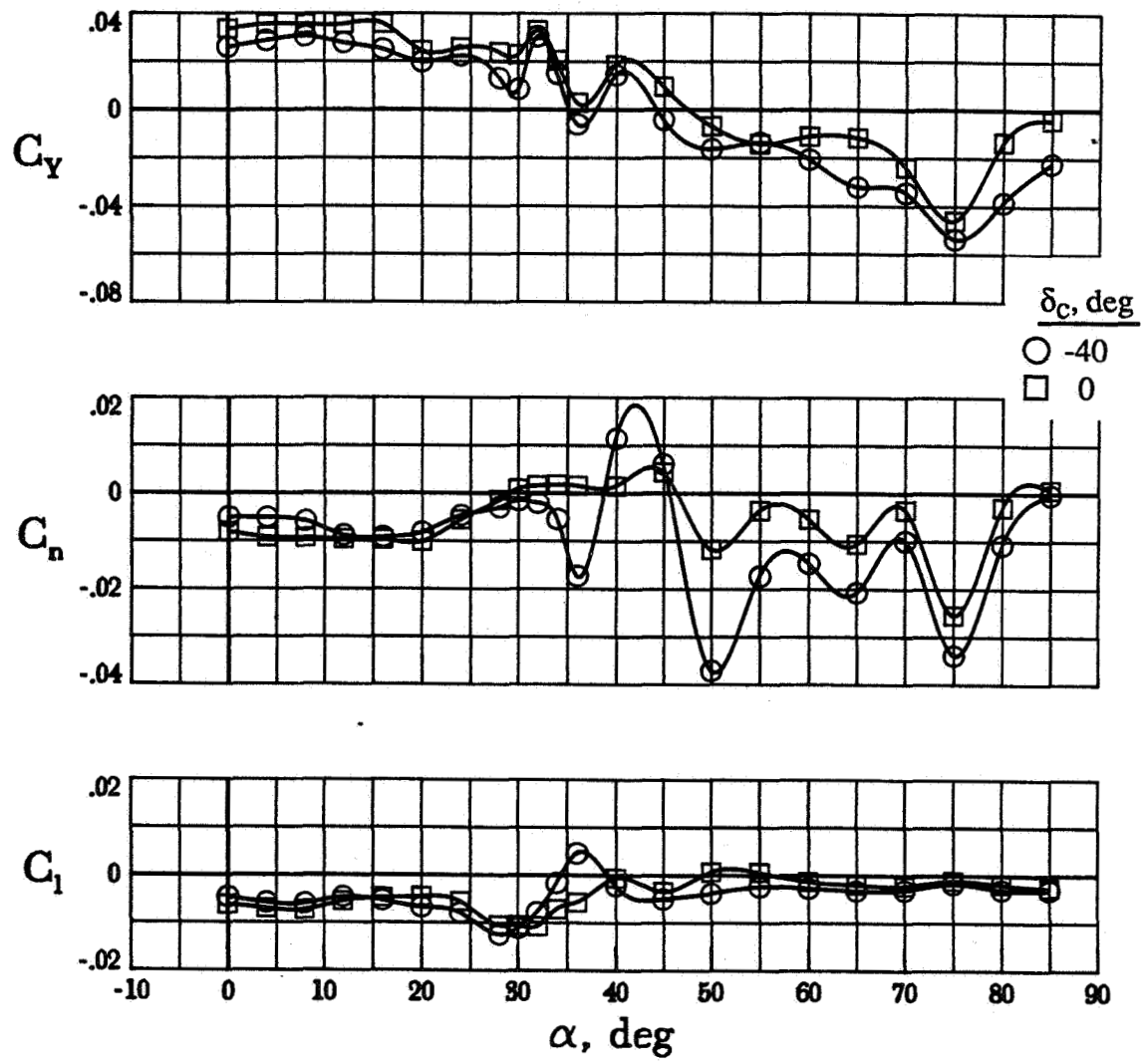


Figure 38. Canard Effect on Lateral-Directional Characteristics

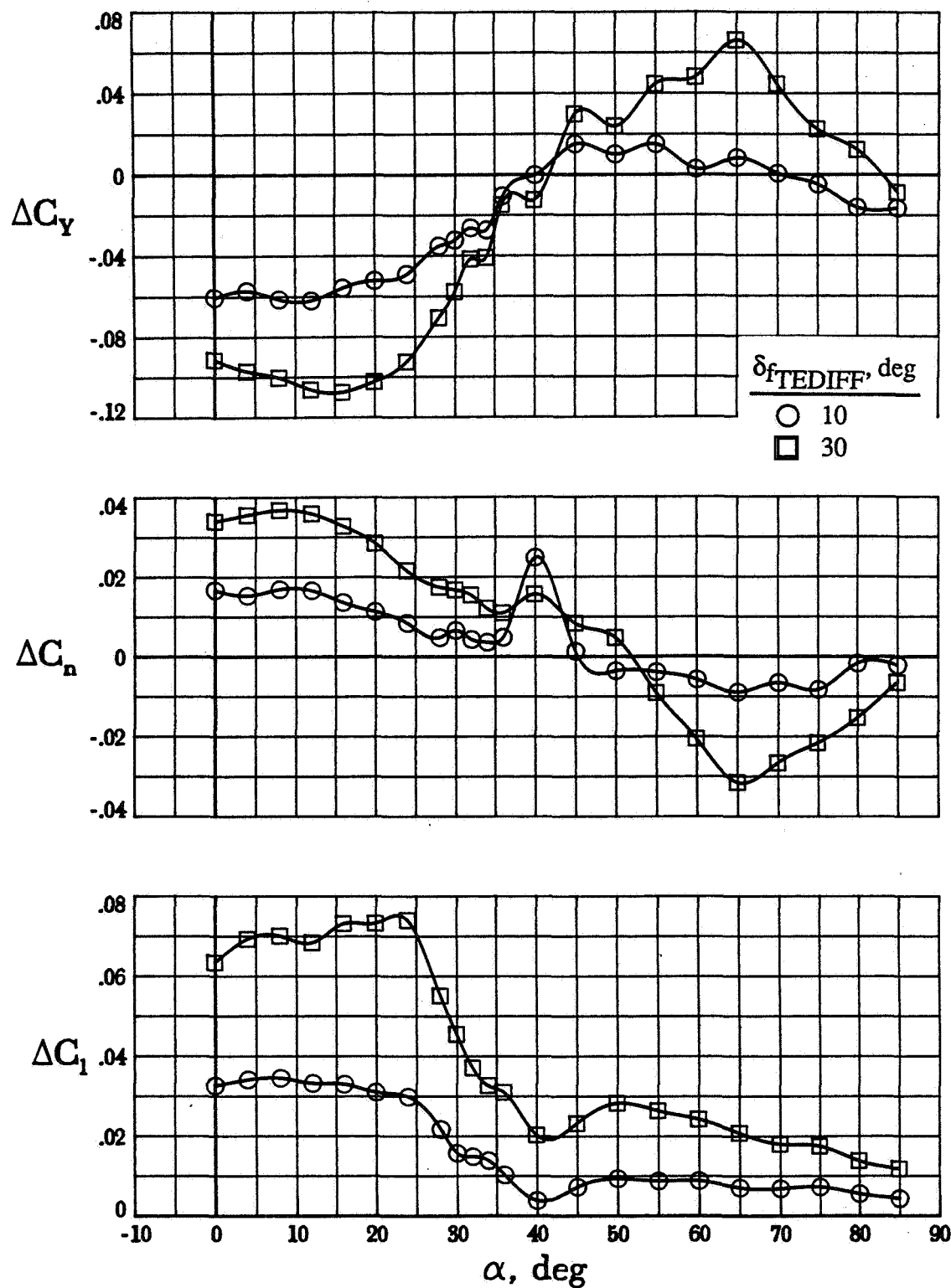


Figure 39. Lateral Control Power for Trailing-edge Flaps Differential

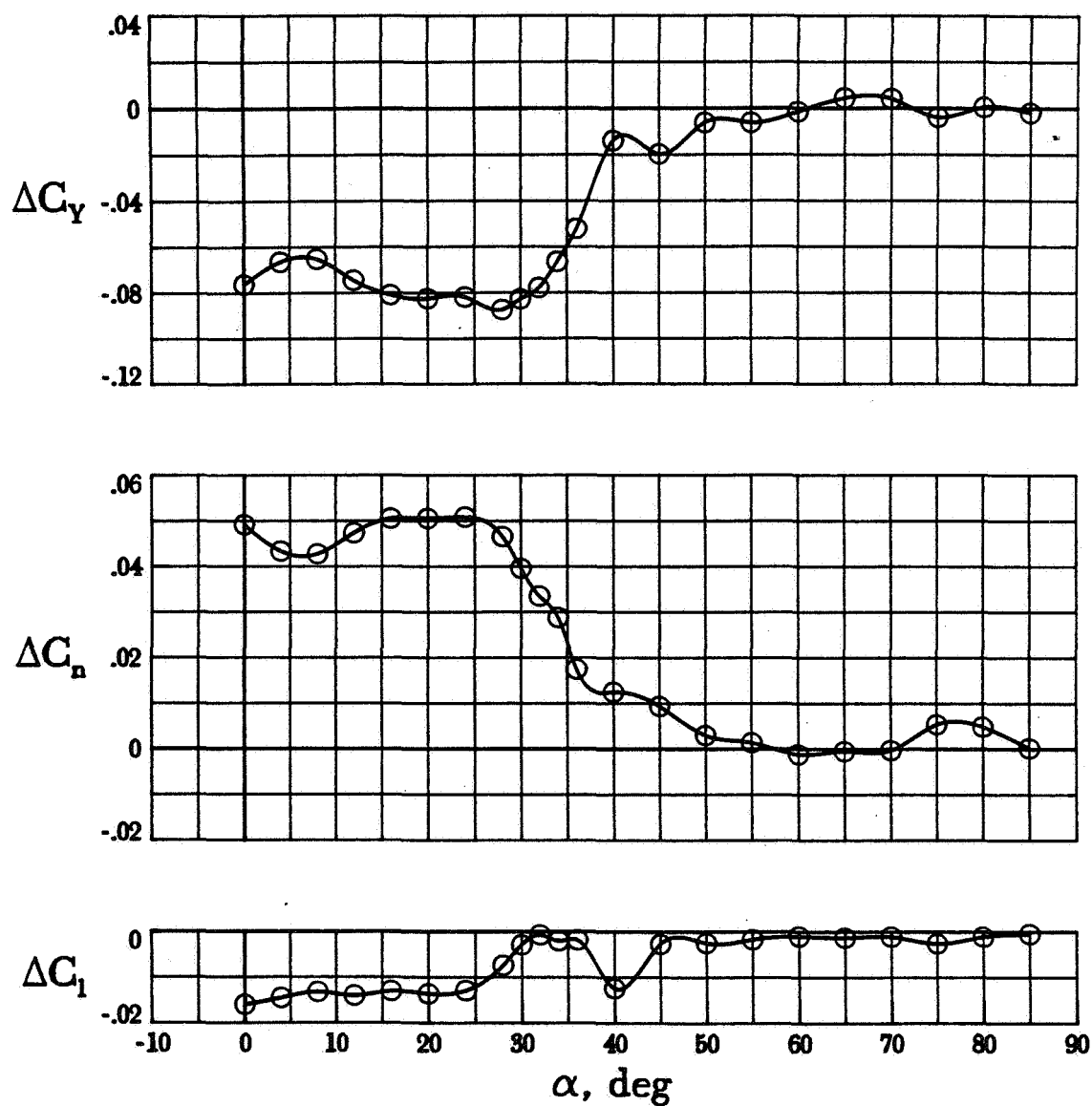
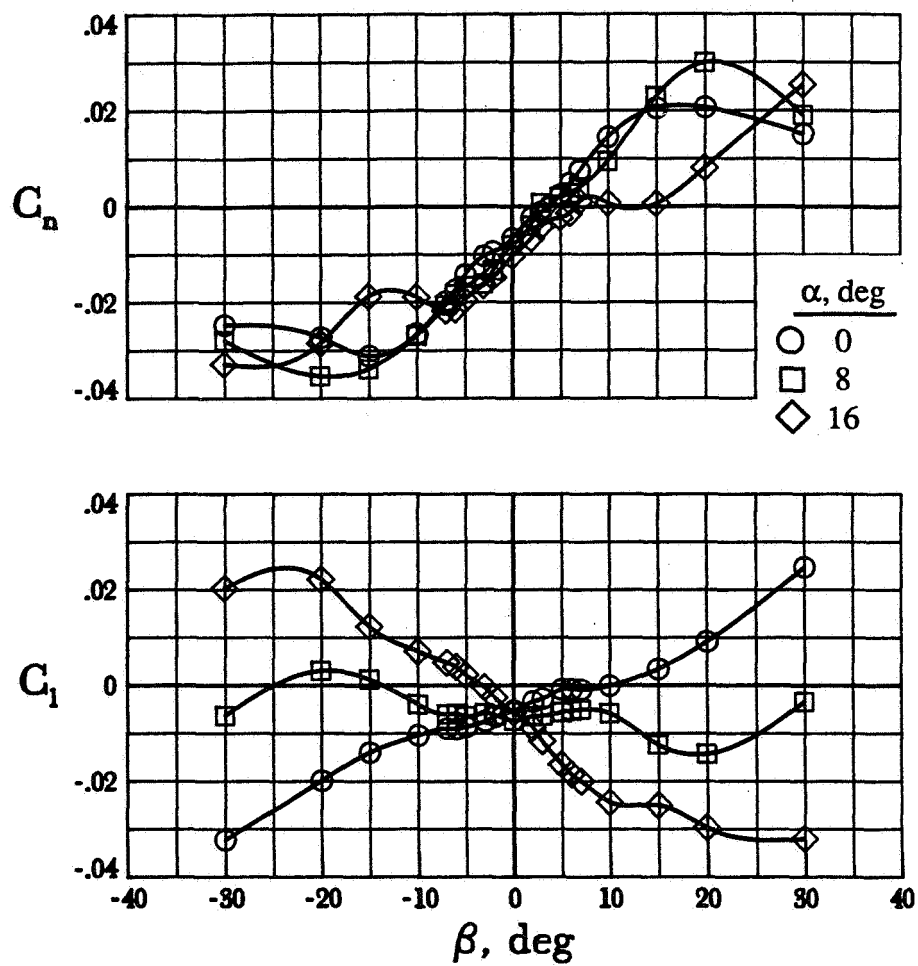
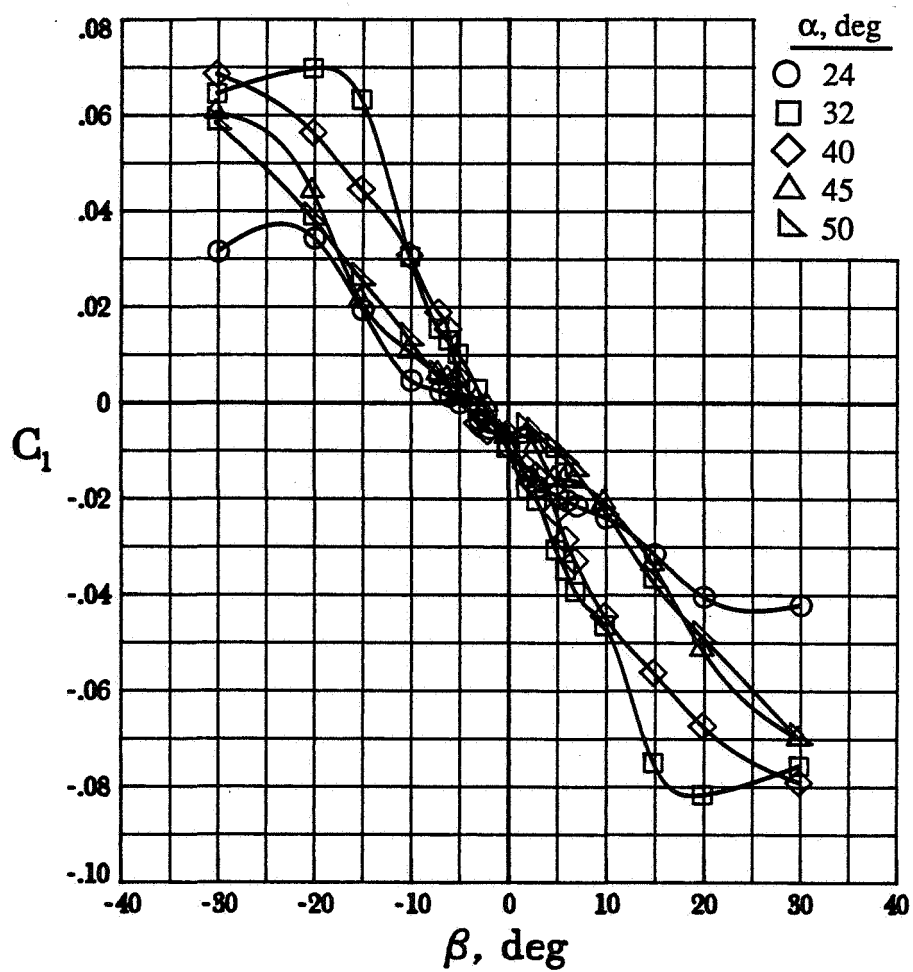
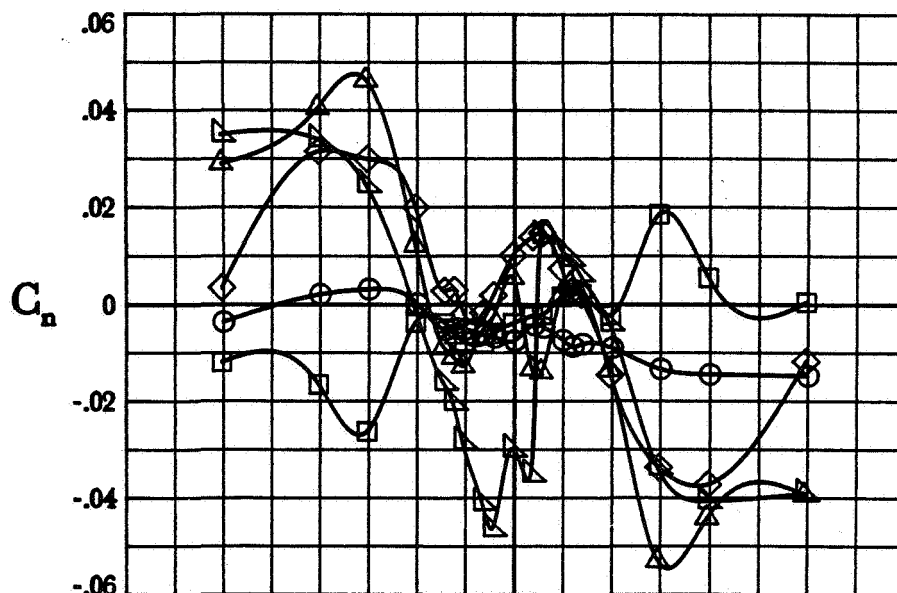


Figure 40. Directional Control Power for Rudder; $\Delta\delta_r=-30$



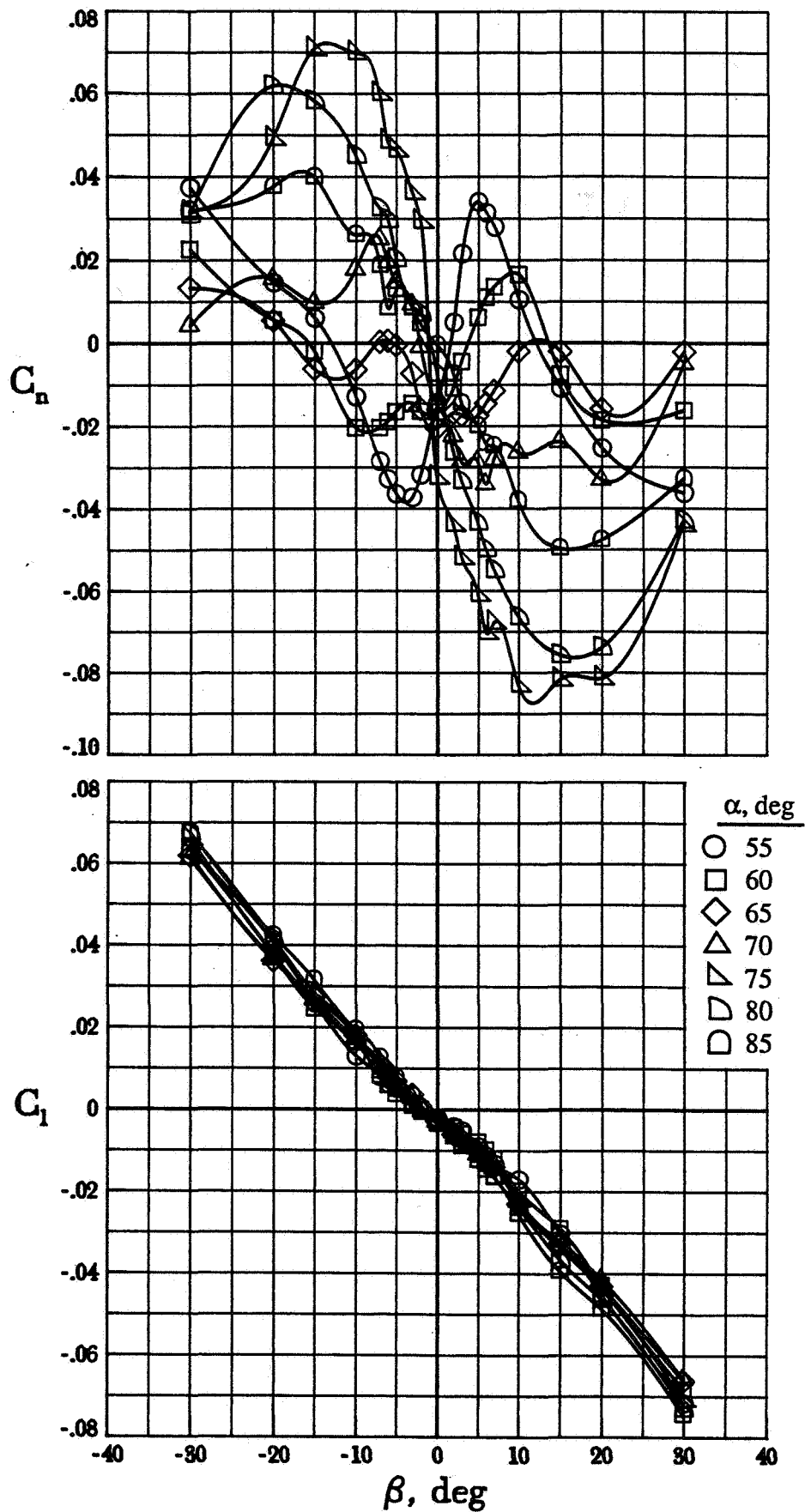
(a) Low Angles of Attack

Figure 41. Sideslip Effect on Rolling and Yawing Moments

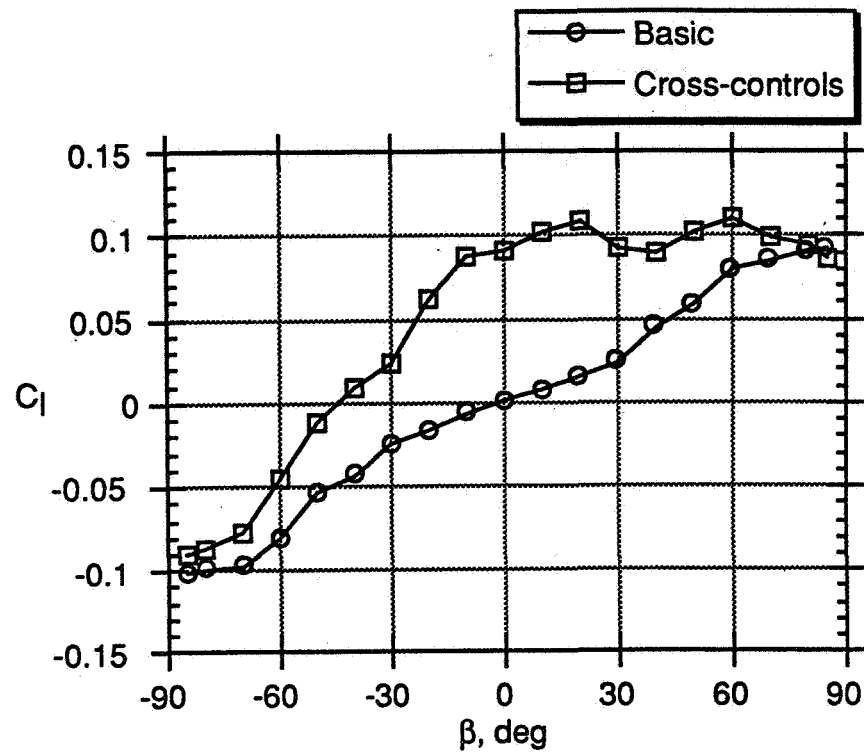


(b) Mid Angles of Attack

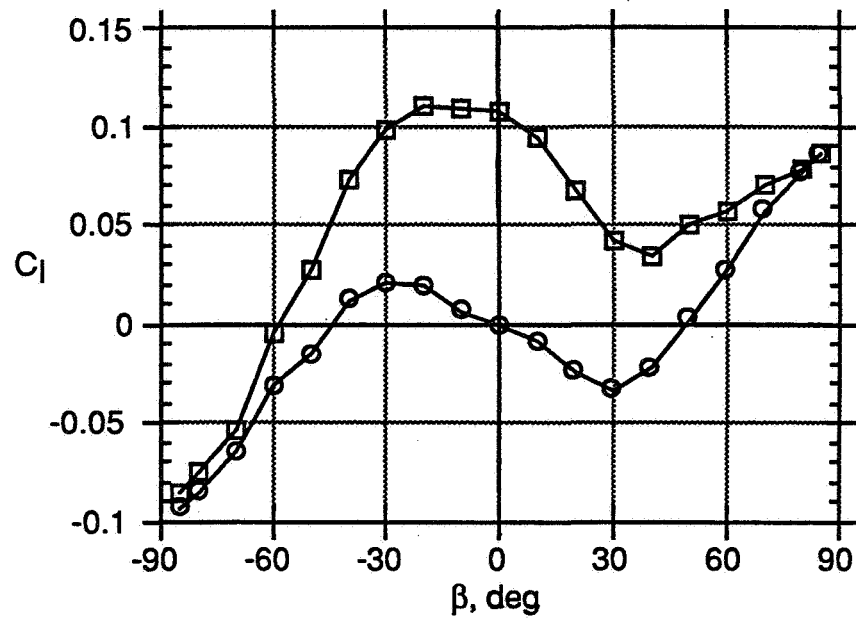
Figure 41. Continued



(c) High Angles of Attack
Figure 41. Concluded

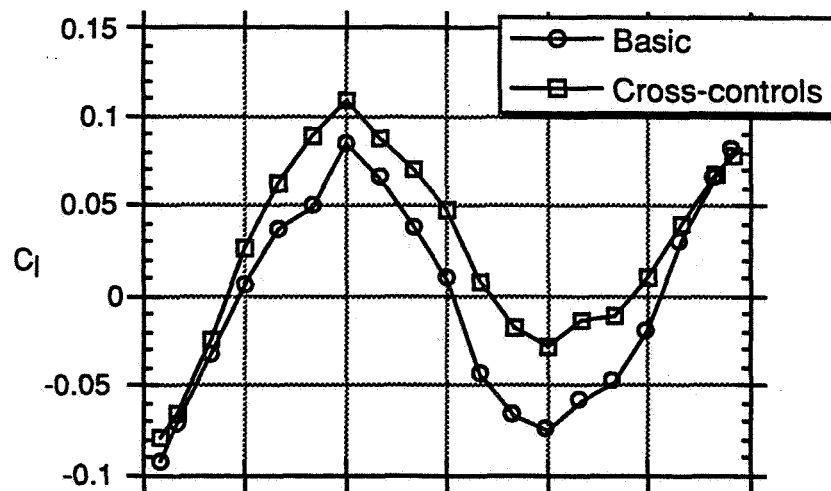


(a) $\alpha = 0^\circ$

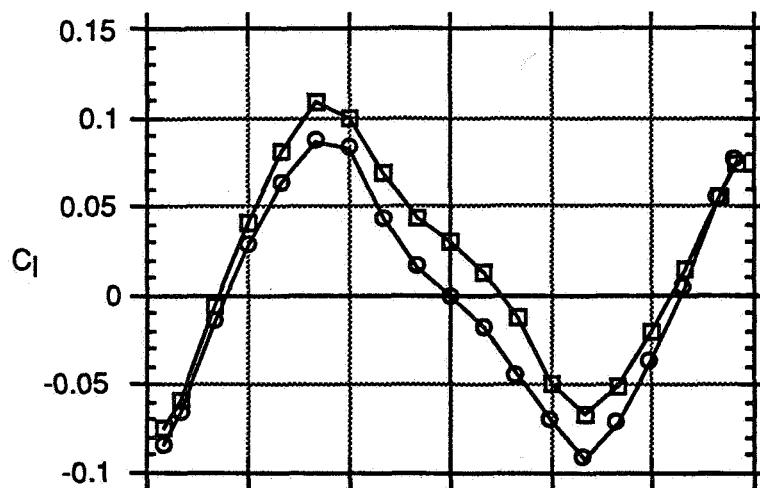


(b) $\alpha = 20^\circ$

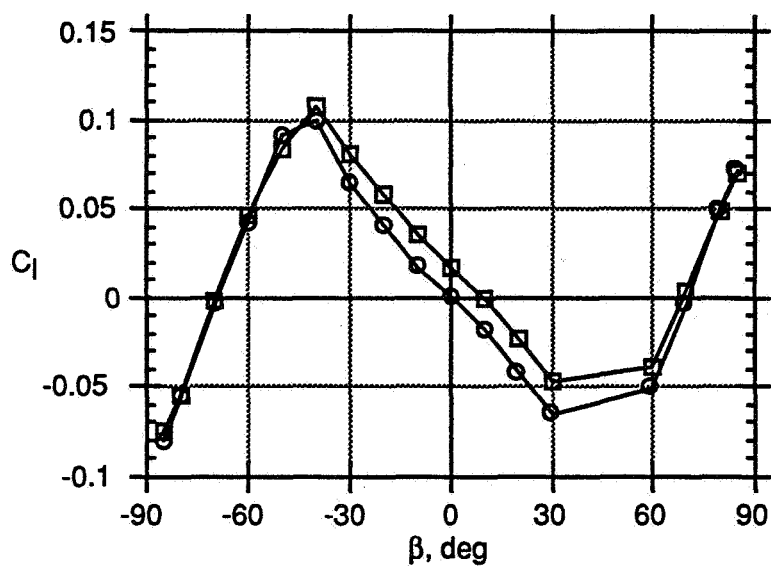
Figure 42. Large Sideslip Effect on Rolling Moment



(c) $\alpha = 40^\circ$

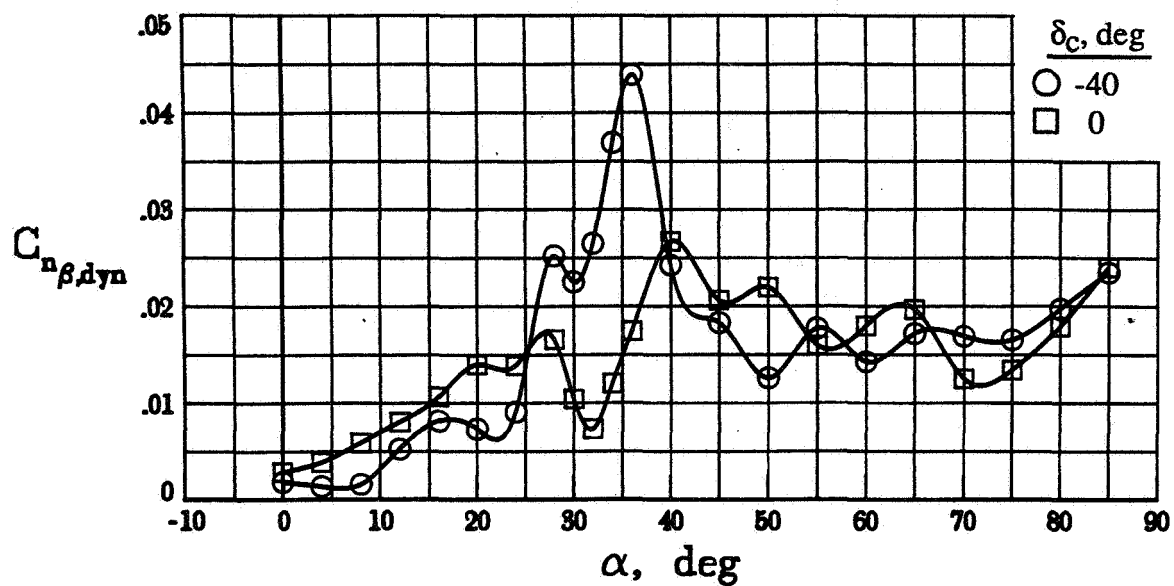


(d) $\alpha = 60^\circ$

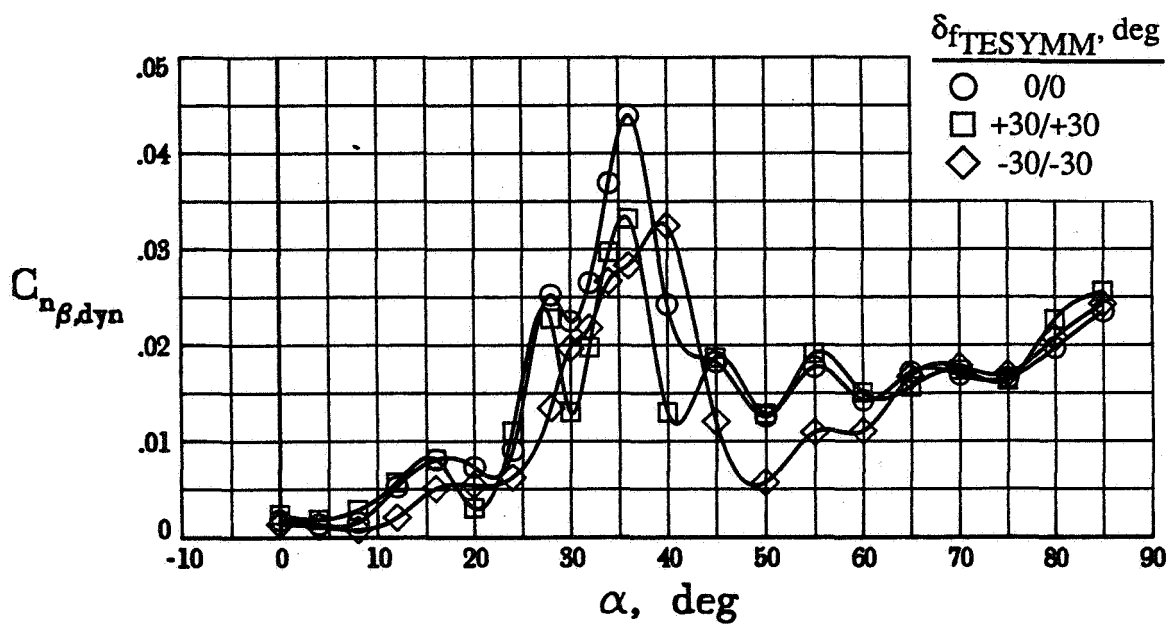


(e) $\alpha = 80^\circ$

Figure 42. Concluded



(a) Canard Effect



(b) Trailing-edge Flap Symmetric Effect

Figure 43. Longitudinal Control Effects on Dynamic Directional Stability

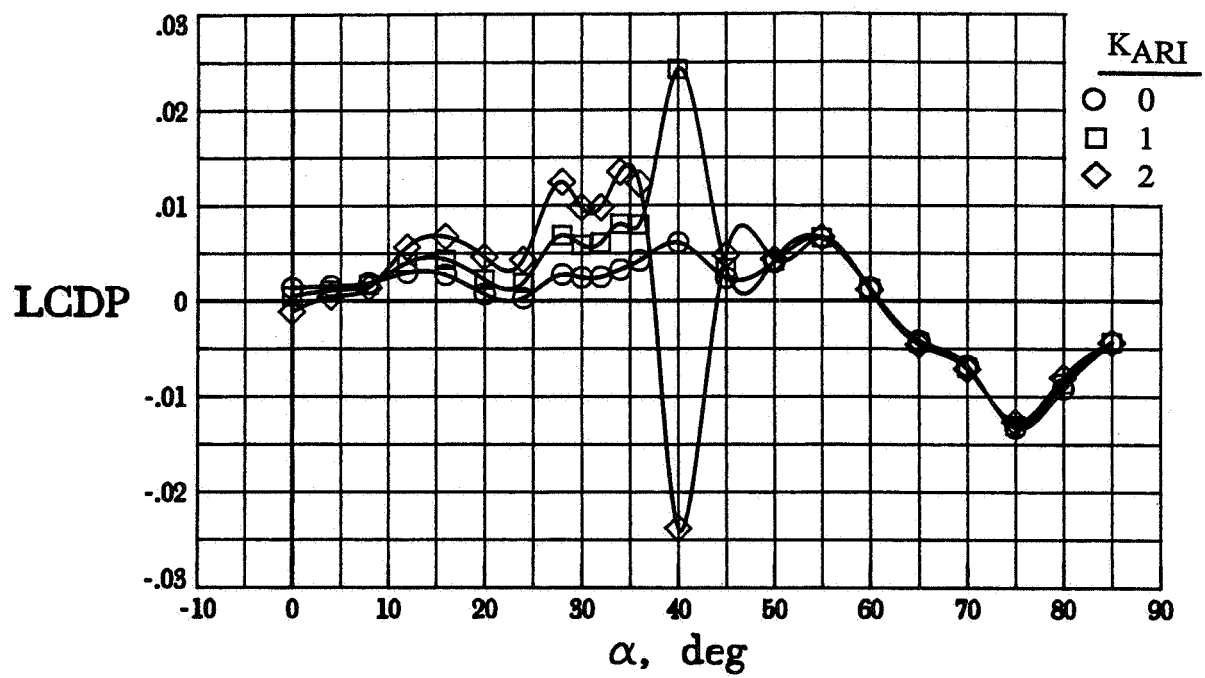
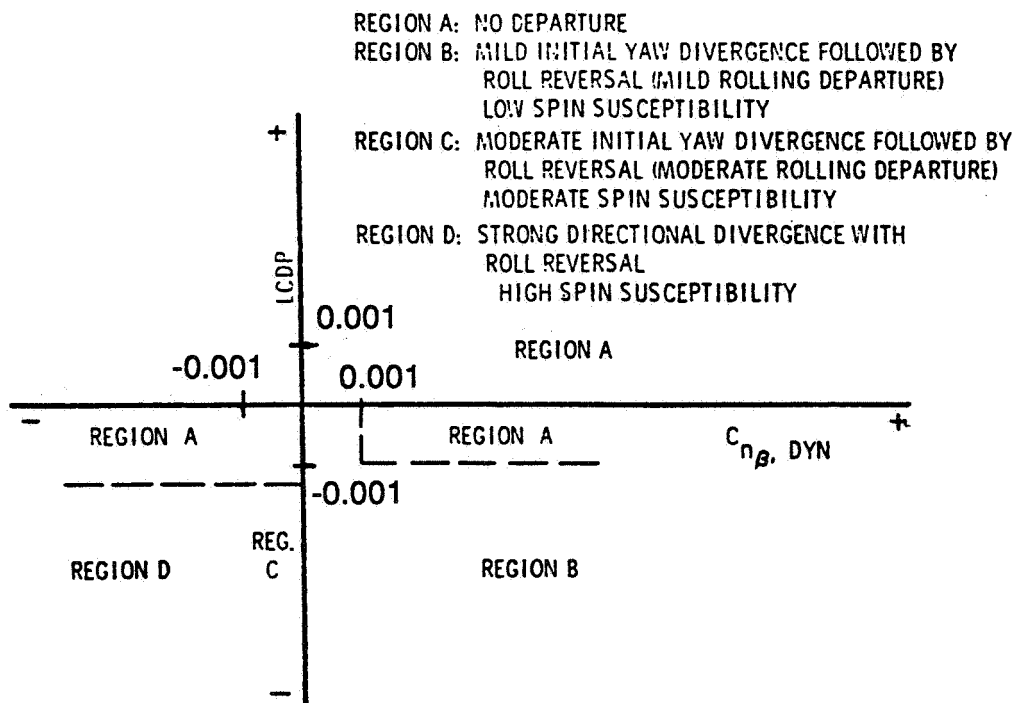
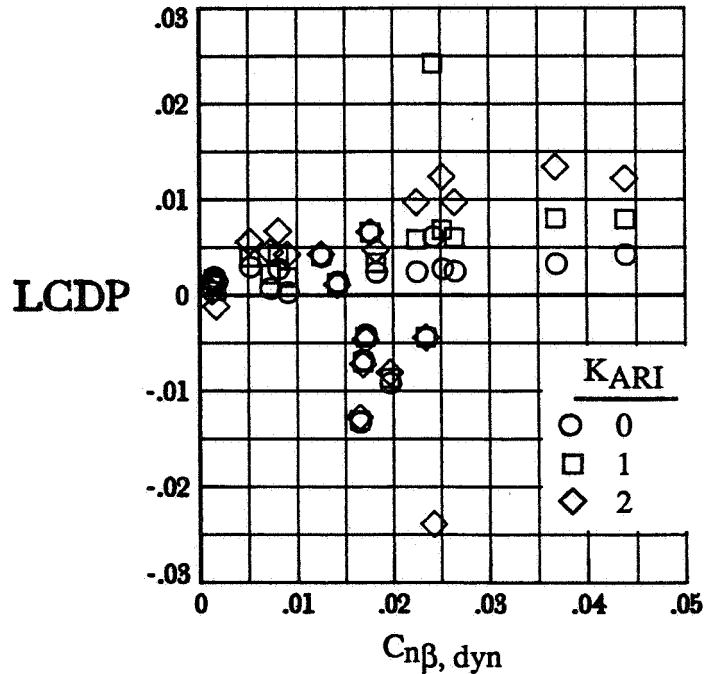


Figure 44. Aileron Rudder Interconnect Gain Effect on LCDP



(a) (Ref. 33)



(b)

Figure 45. Departure and Spin Susceptibility Criteria

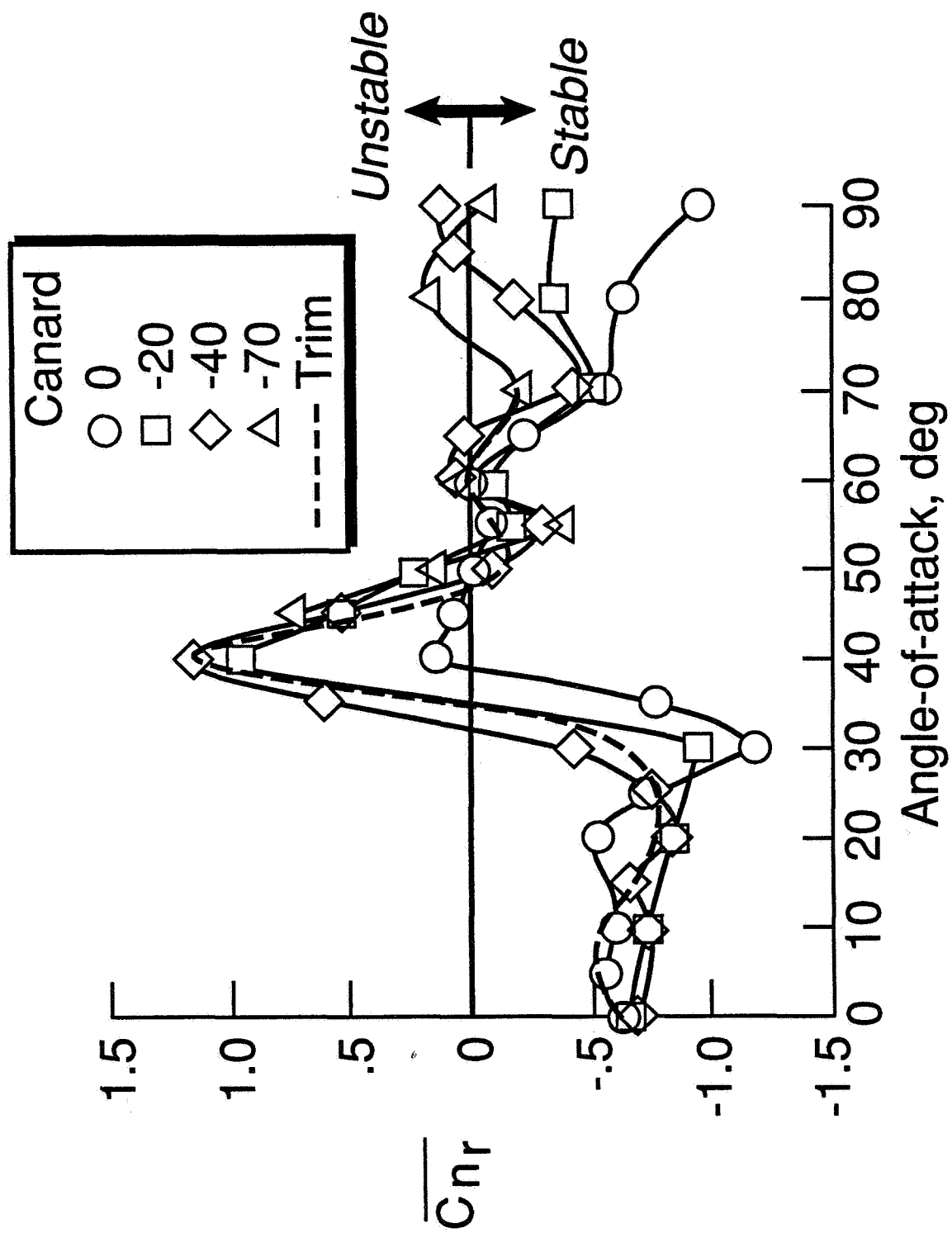


Figure 46. Canard Effect on Yaw Damping

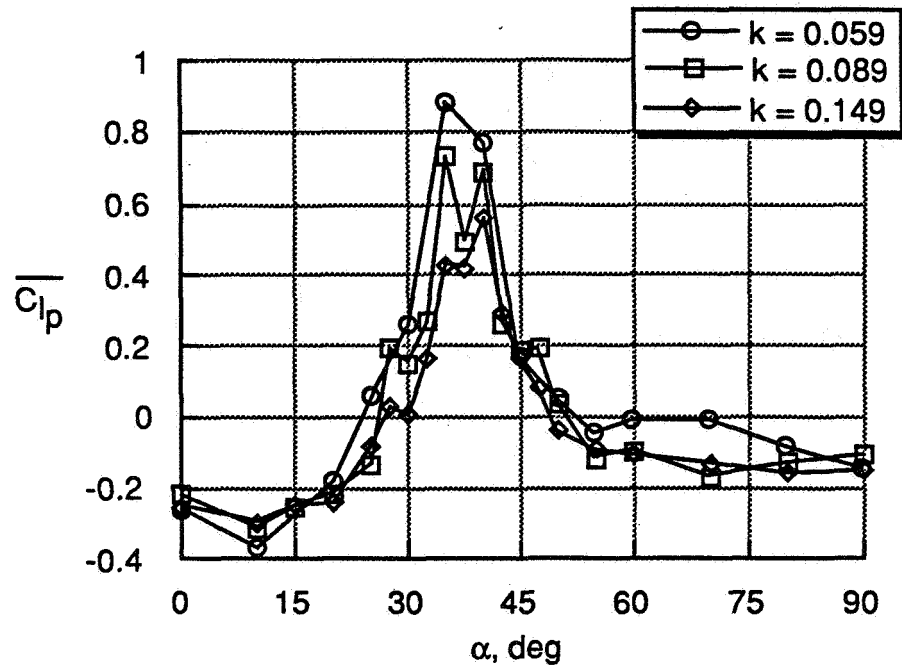


Figure 47. Frequency Effect on Roll Damping; $\Delta\phi = \pm 5^\circ$.

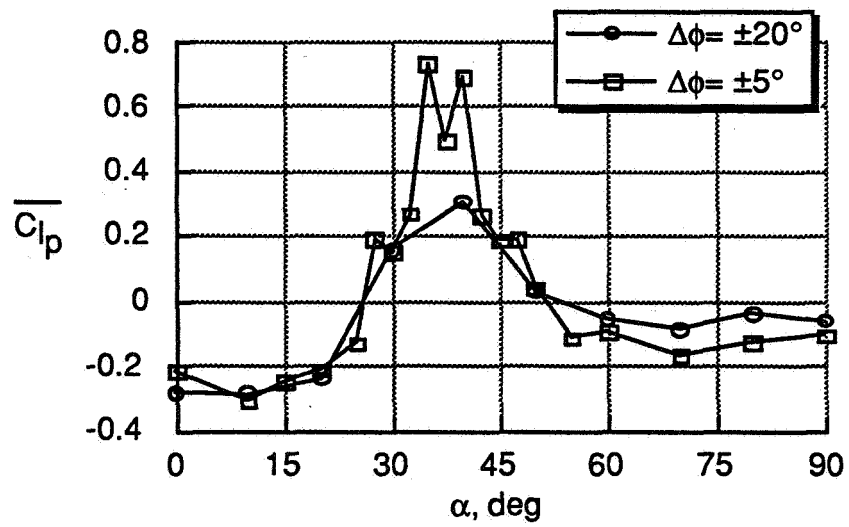


Figure 48. Amplitude Effect on Roll Damping; $k = 0.089$

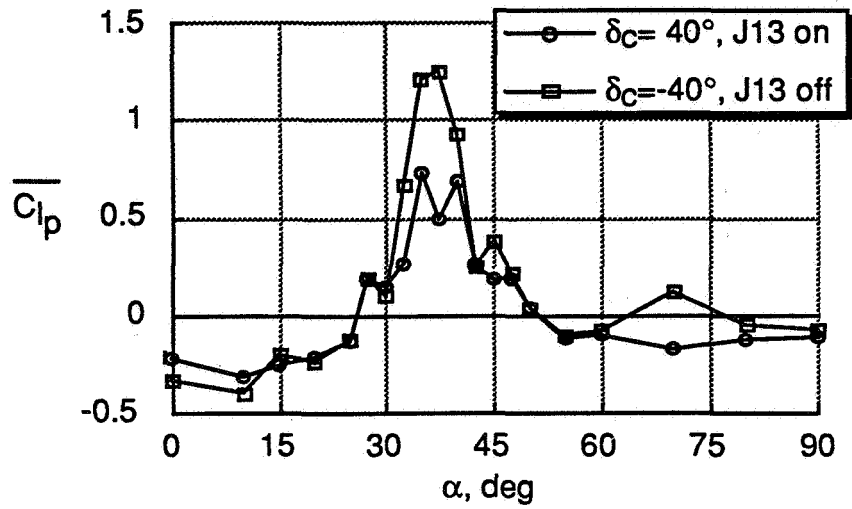


Figure 49. J13 Noseboom Effect on Roll Damping; $k = 0.089$

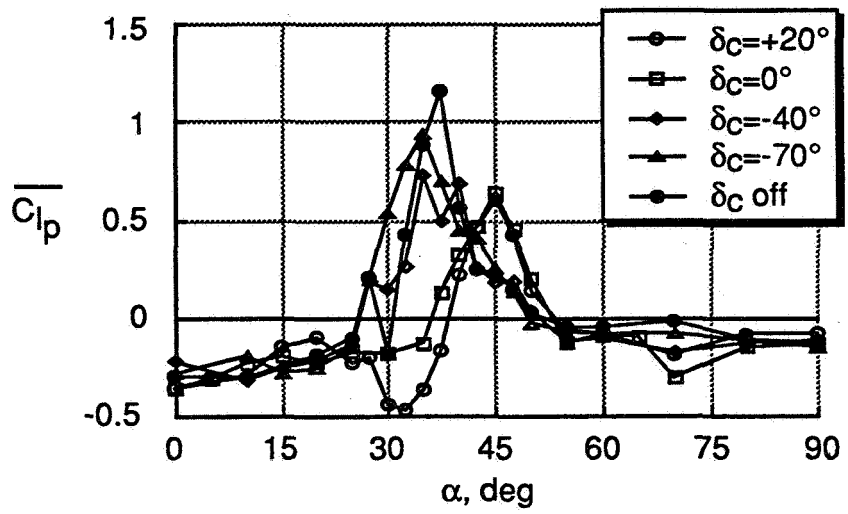


Figure 50. Canard Effect on Roll Damping; $k = 0.089$

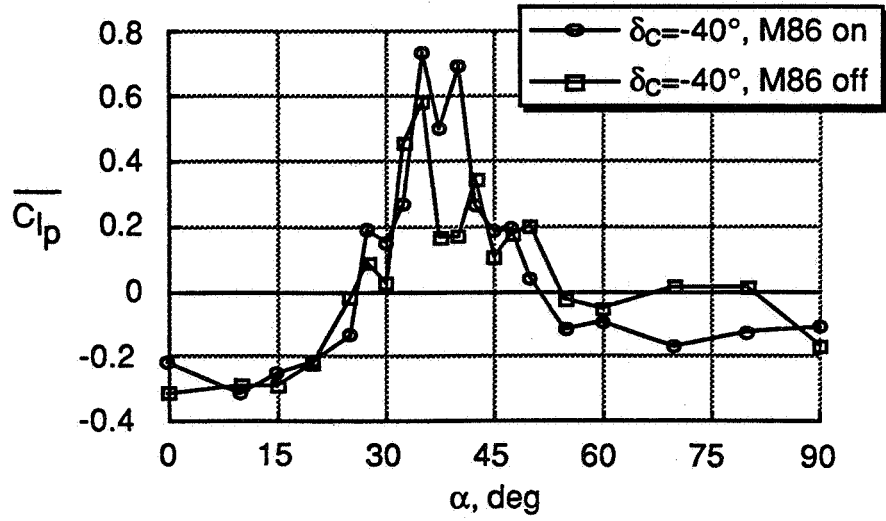
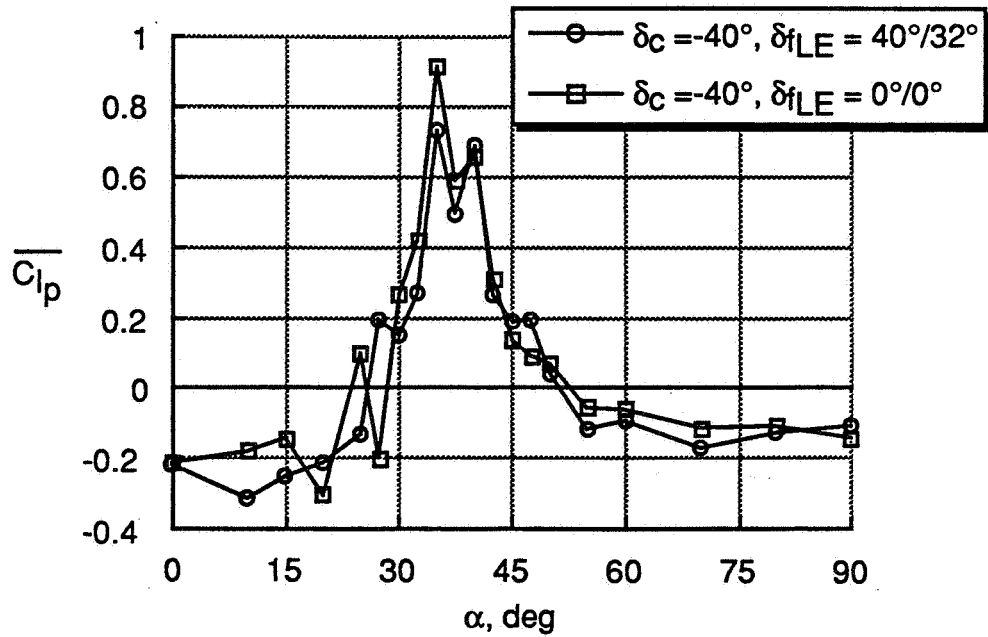
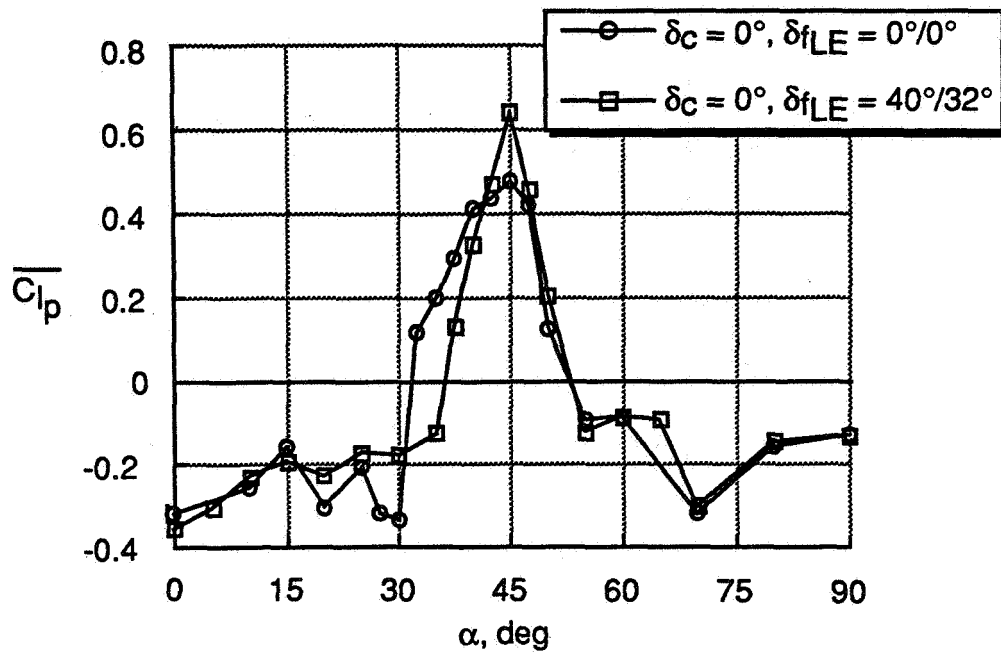


Figure 51. M86 Body Strake Effect on Roll Damping; $k = 0.089$



(a) $\delta_c = 0^\circ$

Figure 52. Leading-edge Flaps Effect on Roll Damping; $k = 0.089$



(b) $\delta_c = -40^\circ$

Figure 52. Concluded

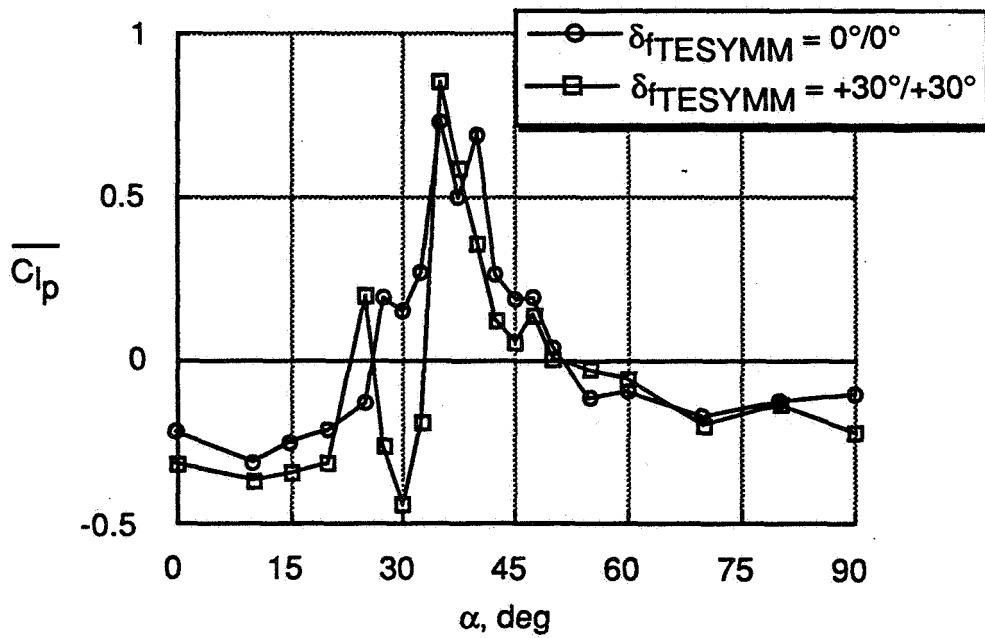


Figure 53. Trailing-edge Flaps Effect on Roll Damping; $k = 0.089$

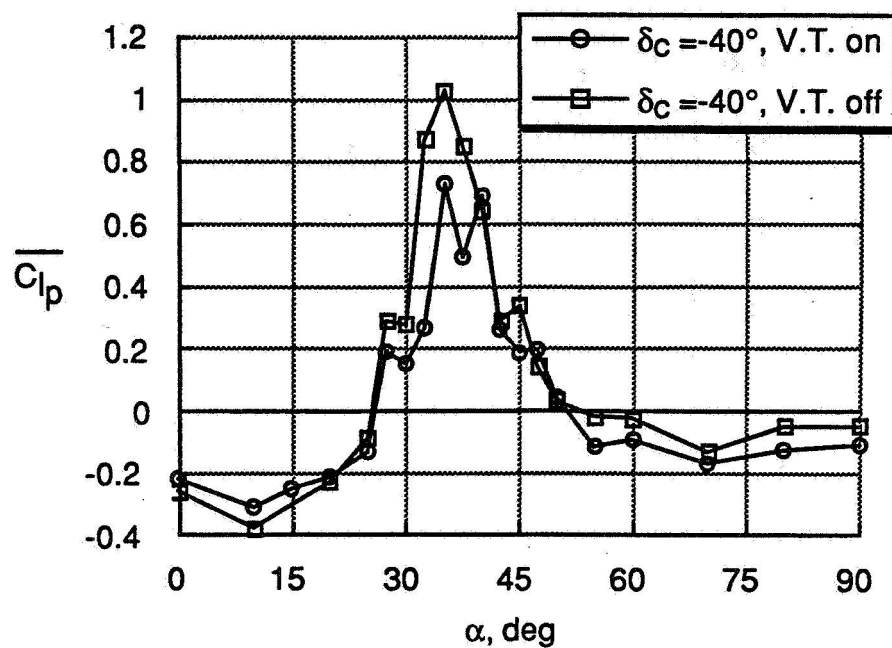


Figure 54. Vertical Tail Effect on Roll Damping; $k = 0.089$

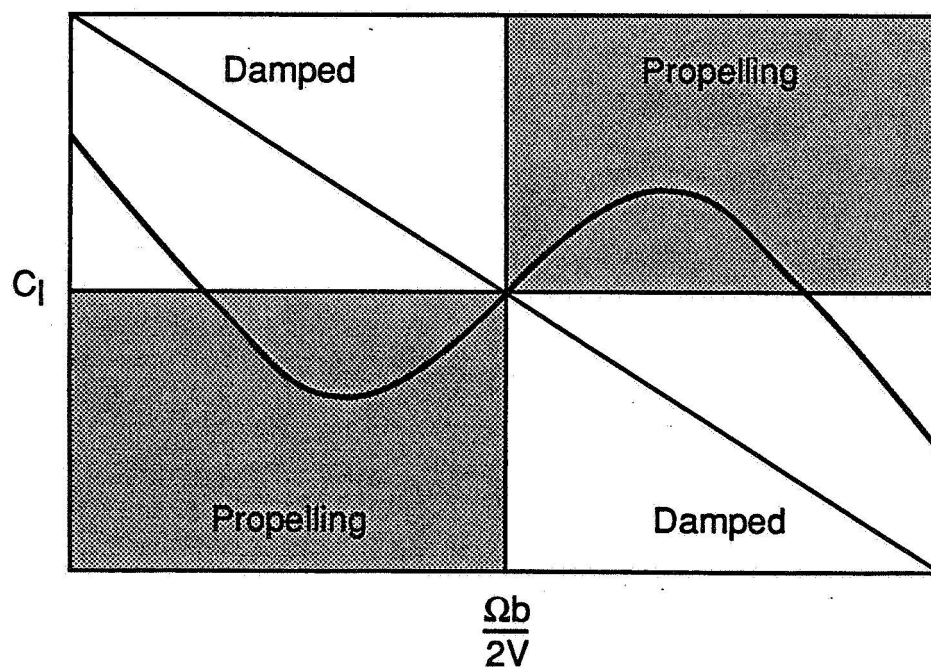
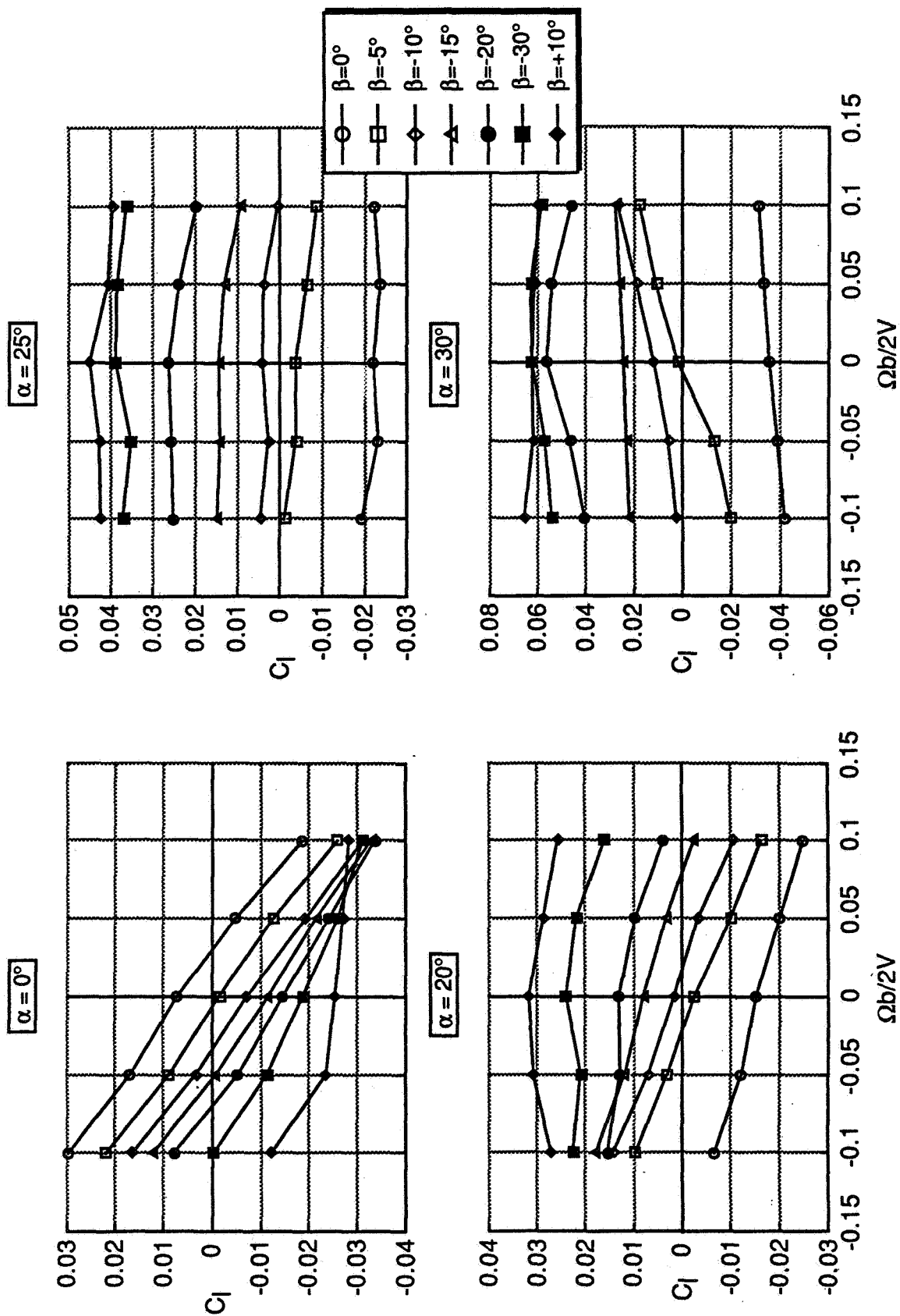
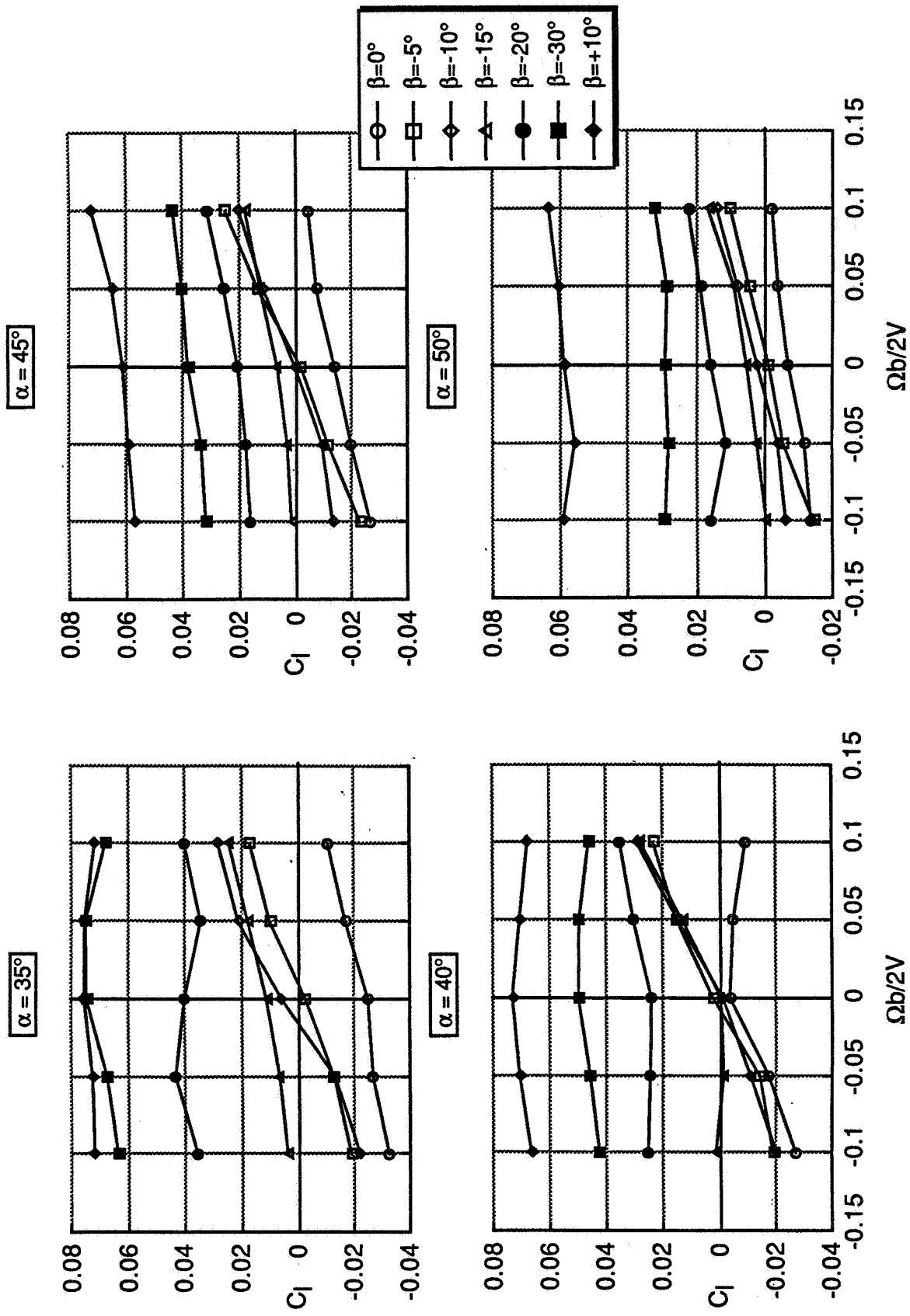


Figure 55. Moment Slope Criteria for the Rotary Balance Test Data.



(a)

Figure 56. Sideslip Effect on Rolling Moment from Rotary Balance Test.



(b)

Figure 56. Concluded

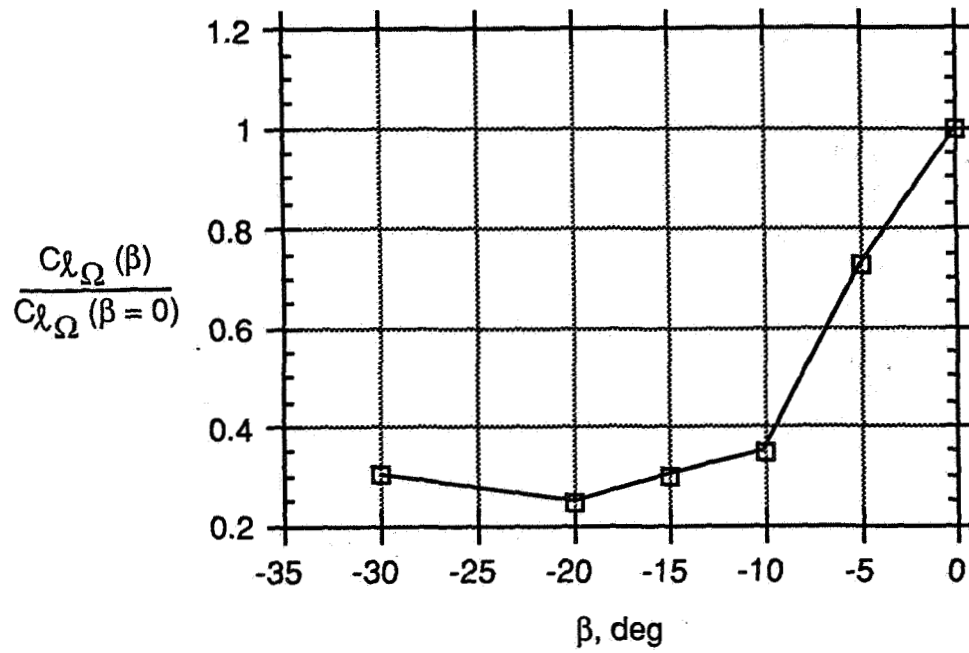


Figure 57. Normalized Sideslip Effect on Roll Damping from Rotary Balance Test Data; $\alpha = 45^\circ$.

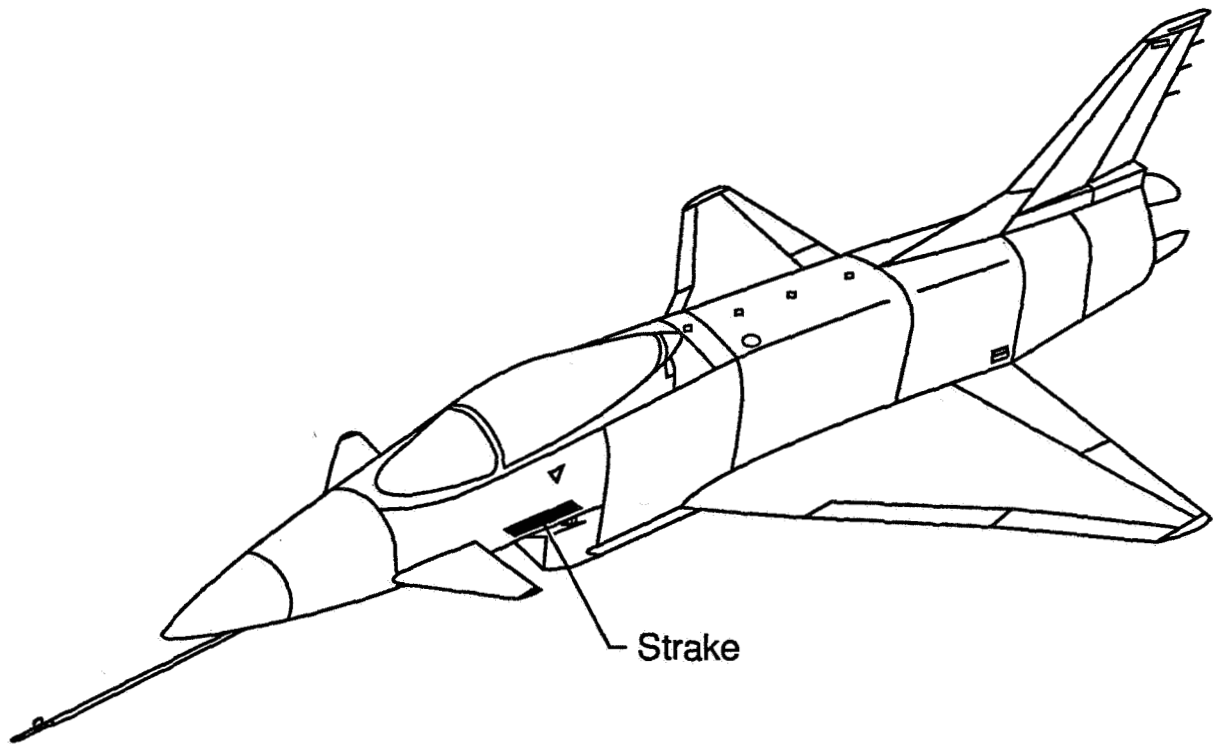
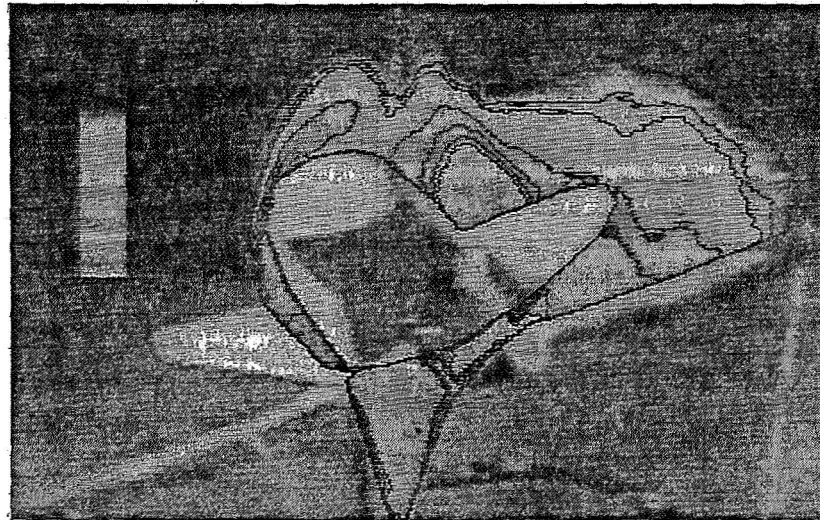
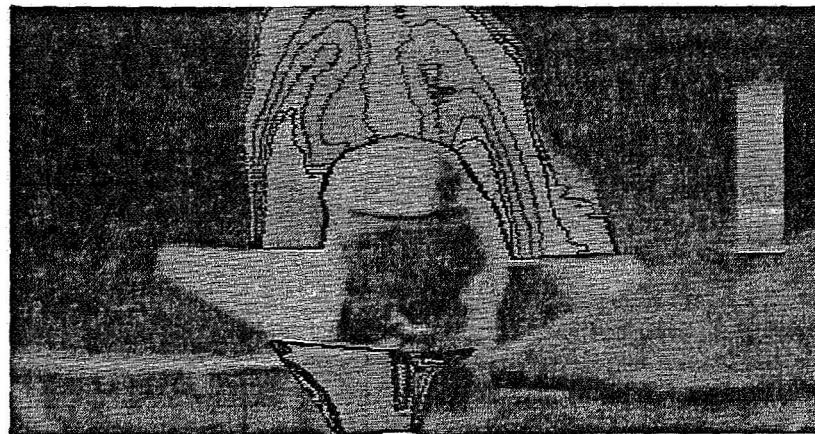


Figure 58. Wing Rock Suppression Body Strakes Location



(a) Right Roll



(b) Level



(c) Left Roll

Figure 59. Wing Rock Flow Visualization Results; Front View
Descending Order in Color Look-Up Table Represents Increase in Smoke Density

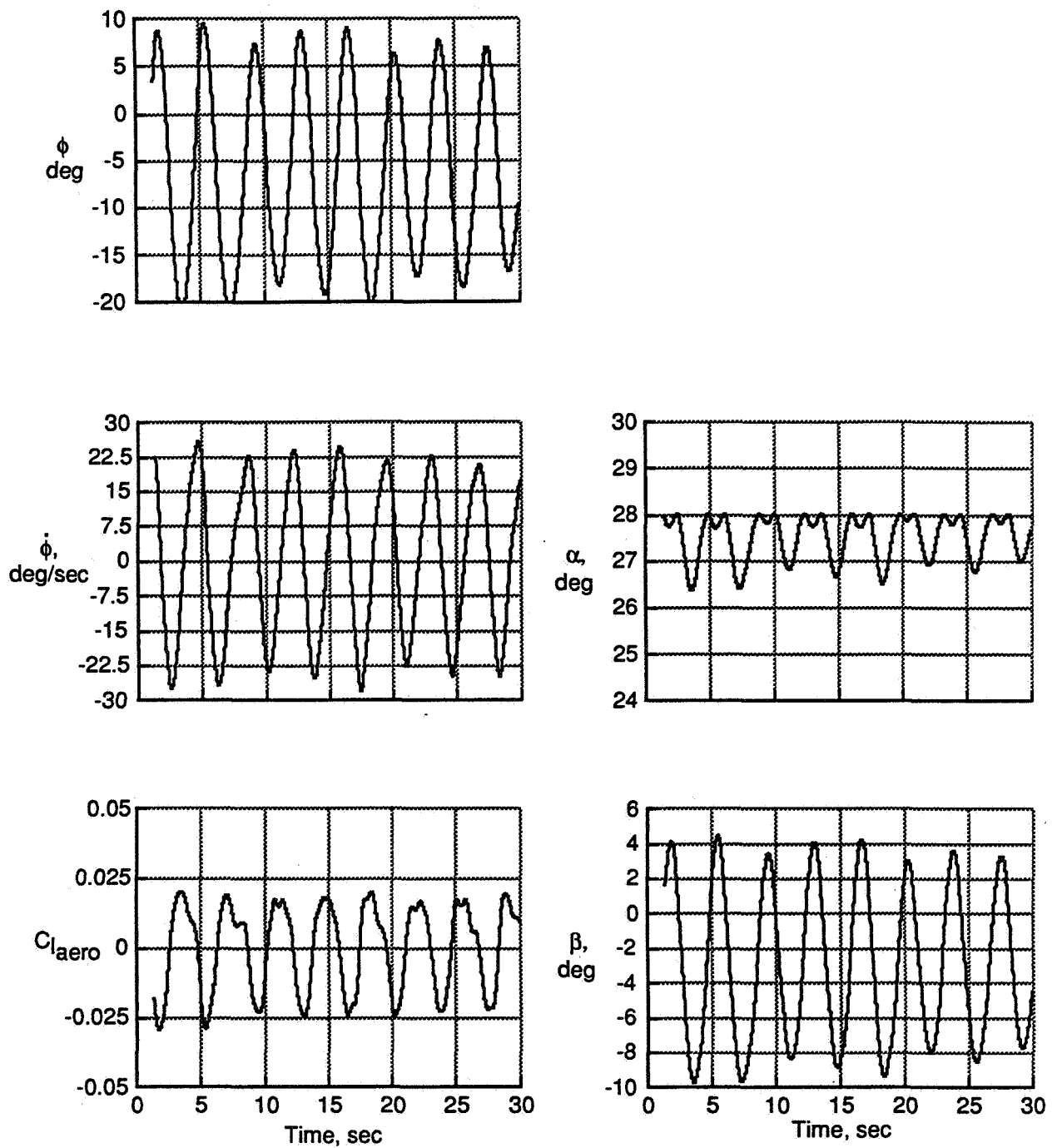


Figure 60. Free-to-Roll Results for $\theta_{sting} = 28^\circ$

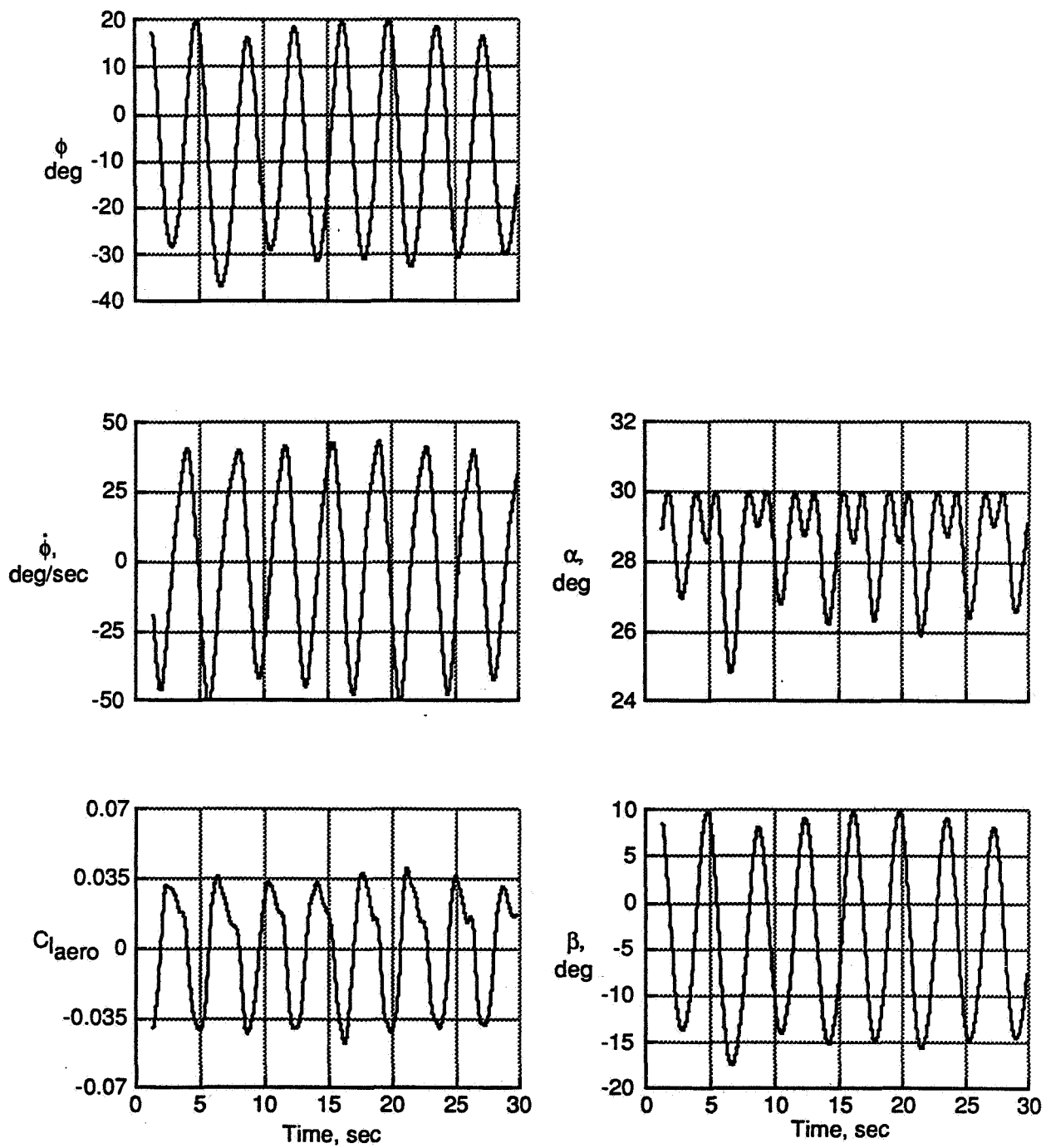


Figure 61. Free-to-Roll Results for $\theta_{sting} = 30^\circ$

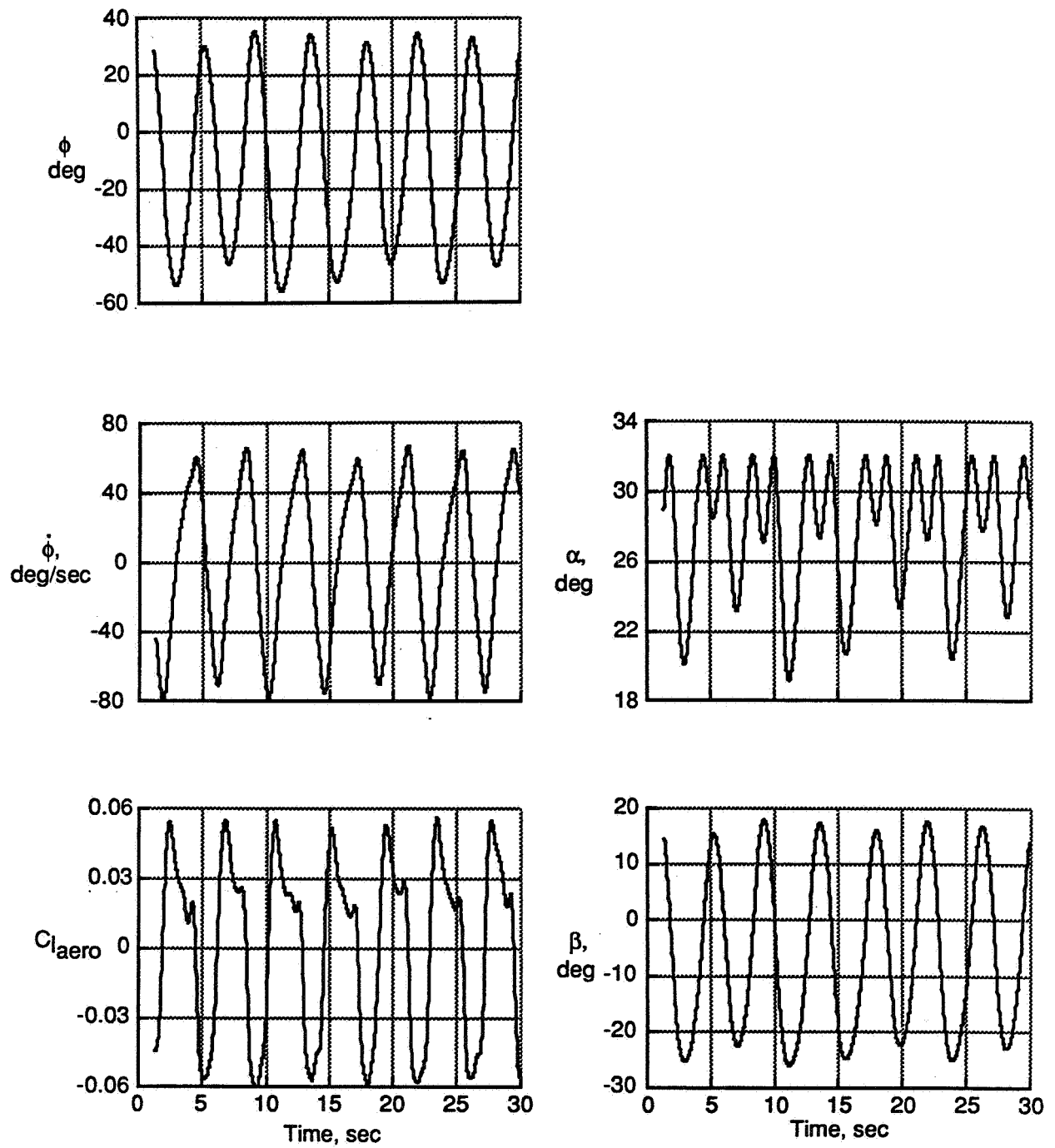


Figure 62. Free-to-Roll Results for $\theta_{sting} = 32^\circ$

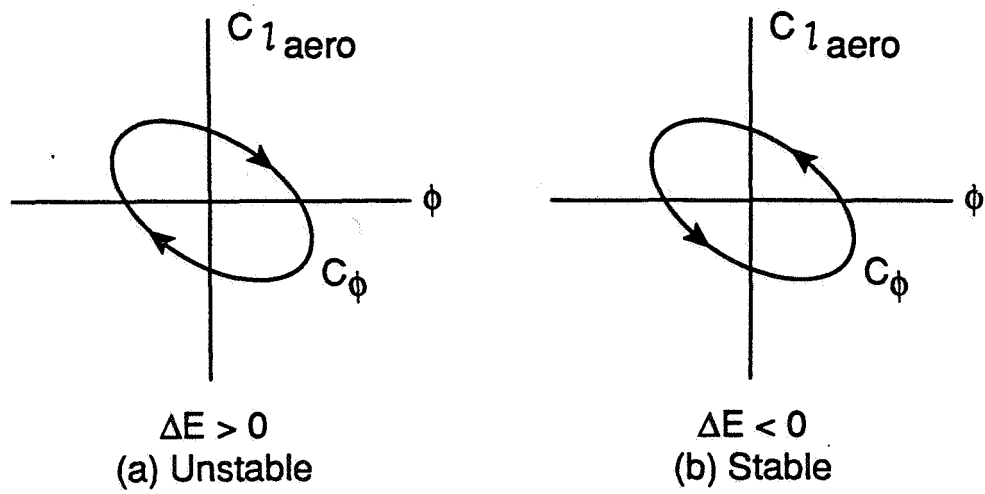
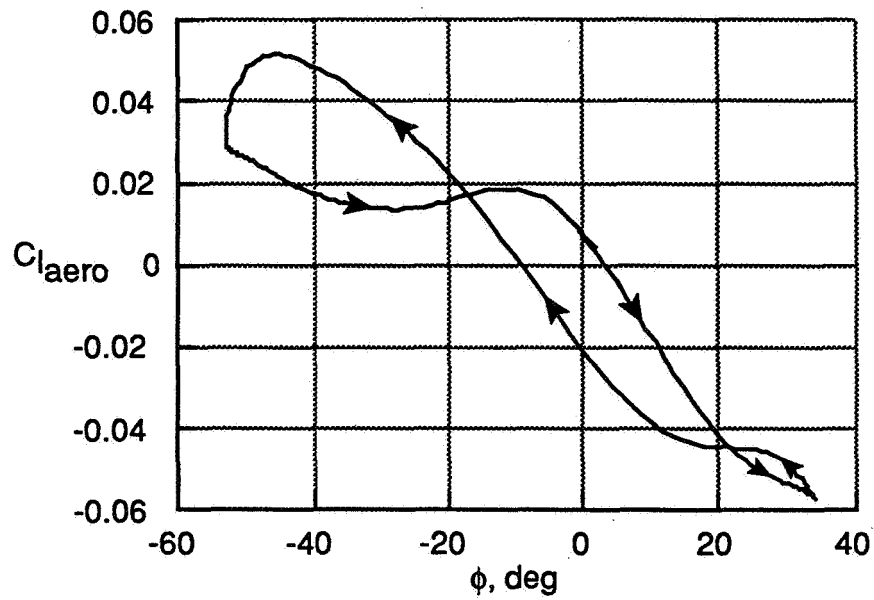
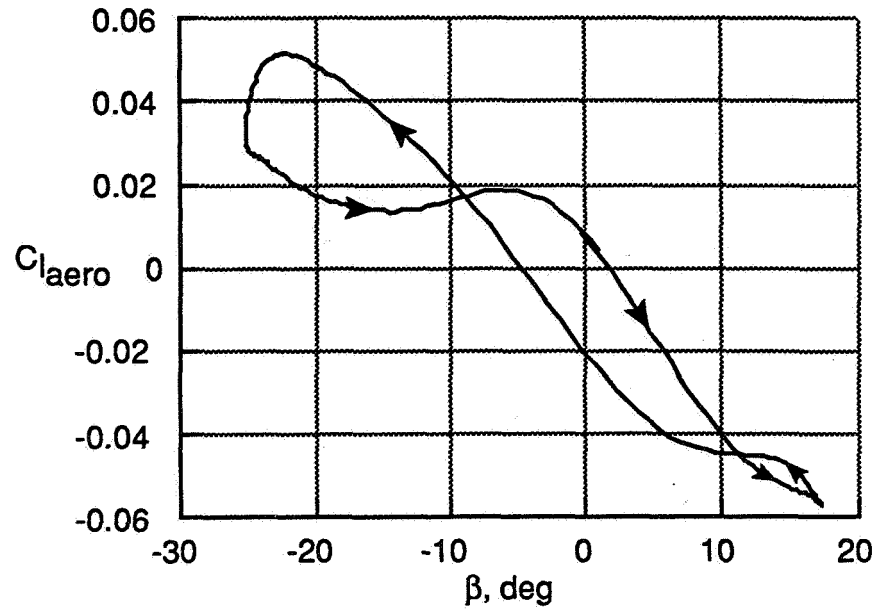


Figure 63. Energy Exchange Effect on Rolling Moment



(a) Roll Angle Effect

Figure 64. Roll and Sideslip Angle Effects on Rolling Moment



(b) Sideslip Angle Effect

Figure 64. Concluded

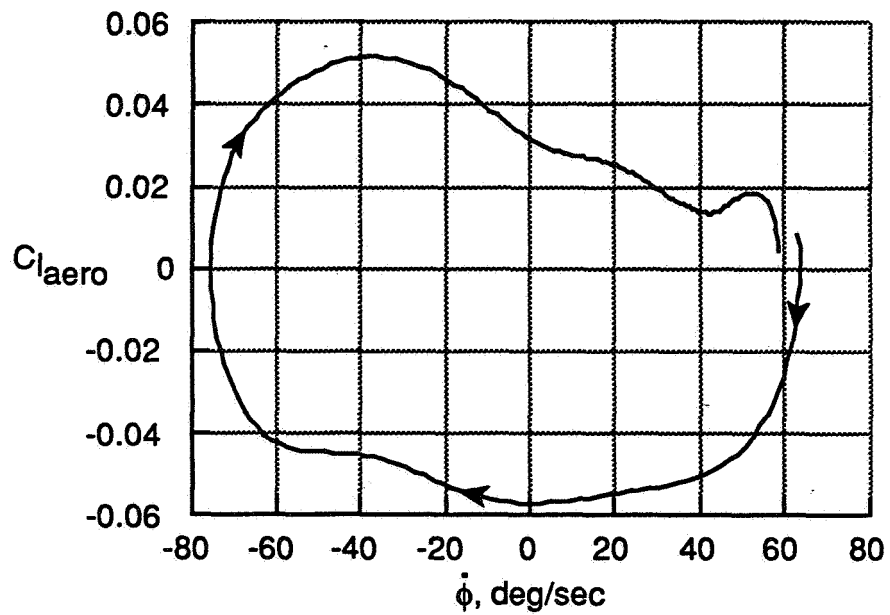
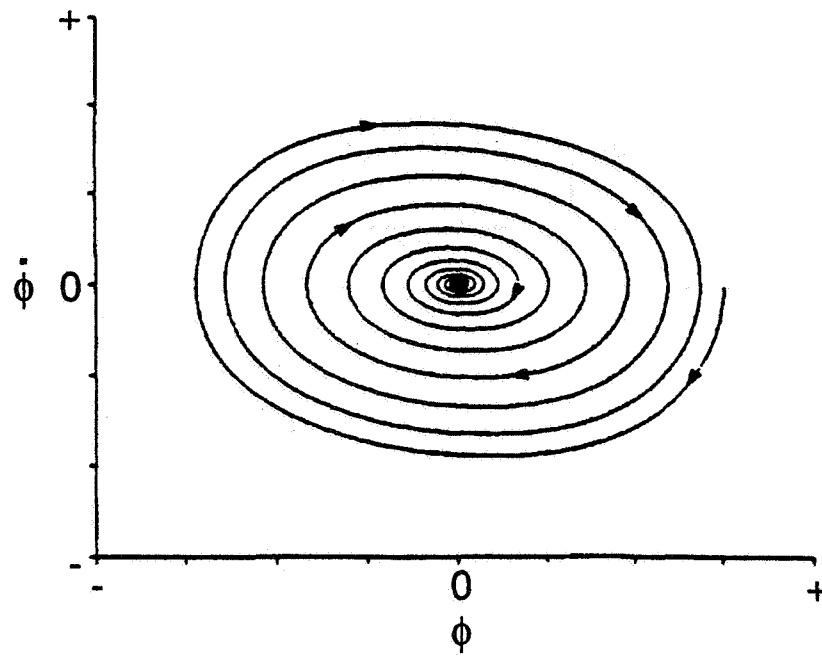
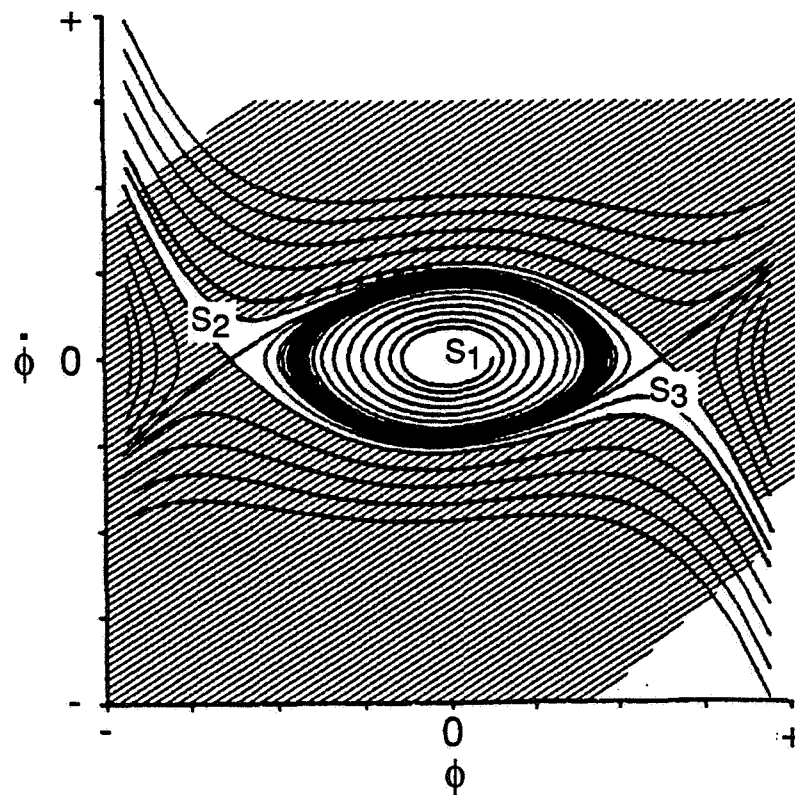


Figure 65. Roll Rate Effect on Rolling Moment for $\theta_{sting} = 32^\circ$

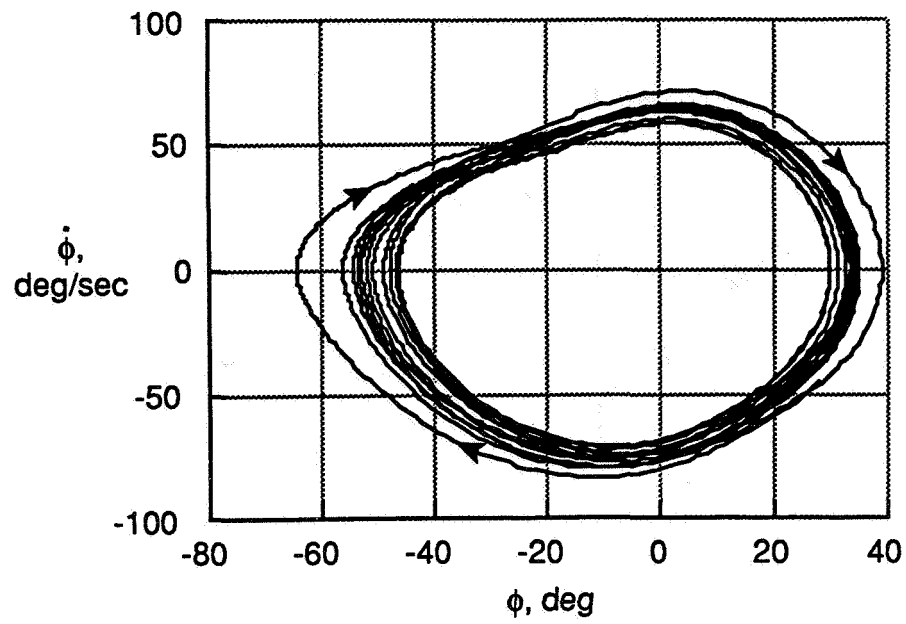


(a) Stable Focus

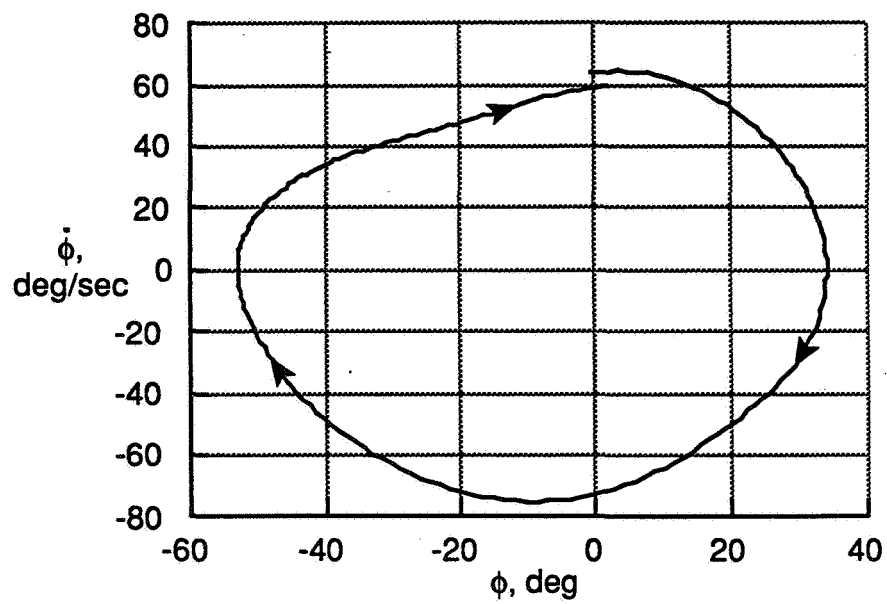


(b) Unstable Focus and Saddle Points

Figure 66. Phase Plane Theoretical Diagram

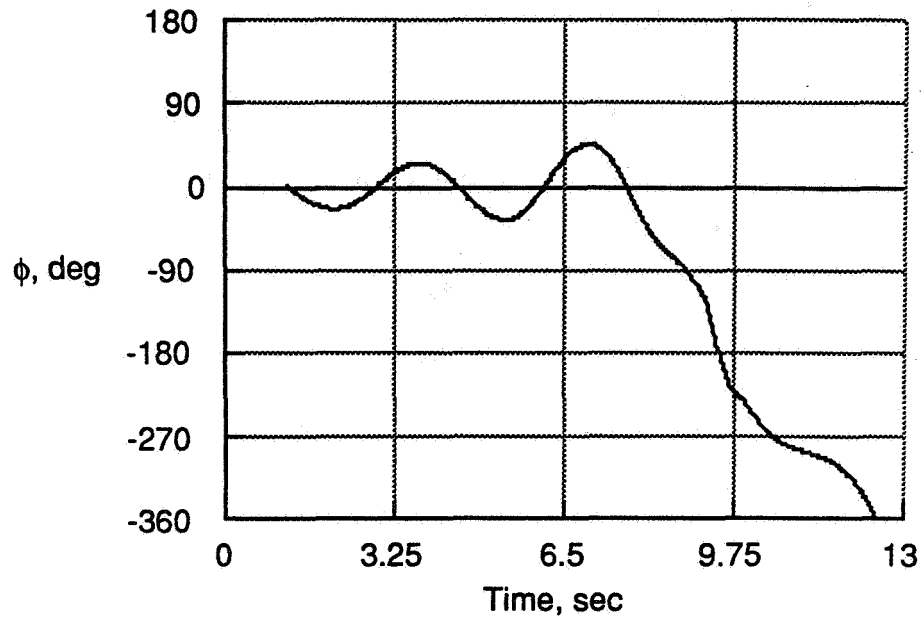


(a) Multiple Cycles

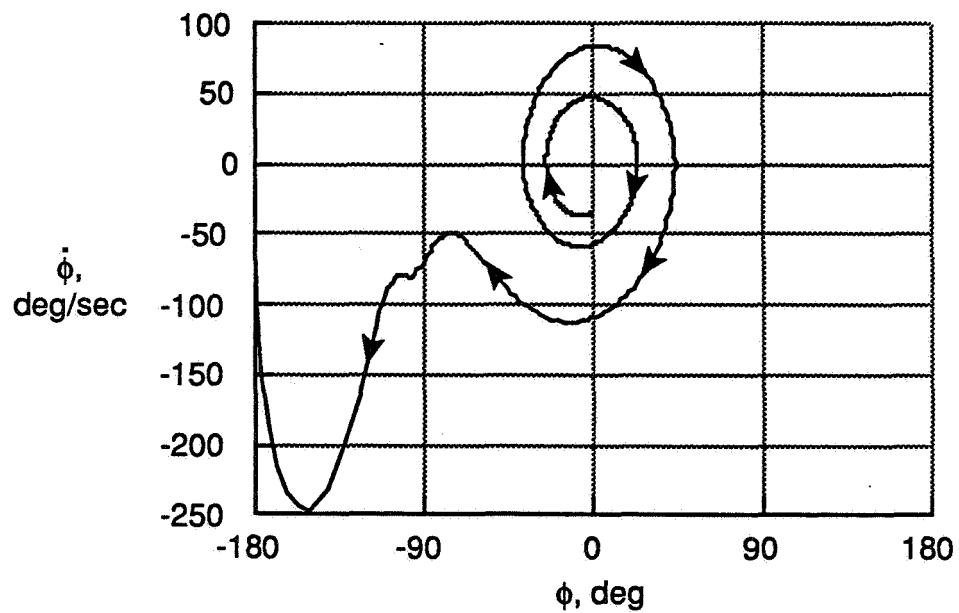


(b) Single Cycle

Figure 67. Phase Plane Diagram for $\theta_{\text{sting}} = 32^\circ$

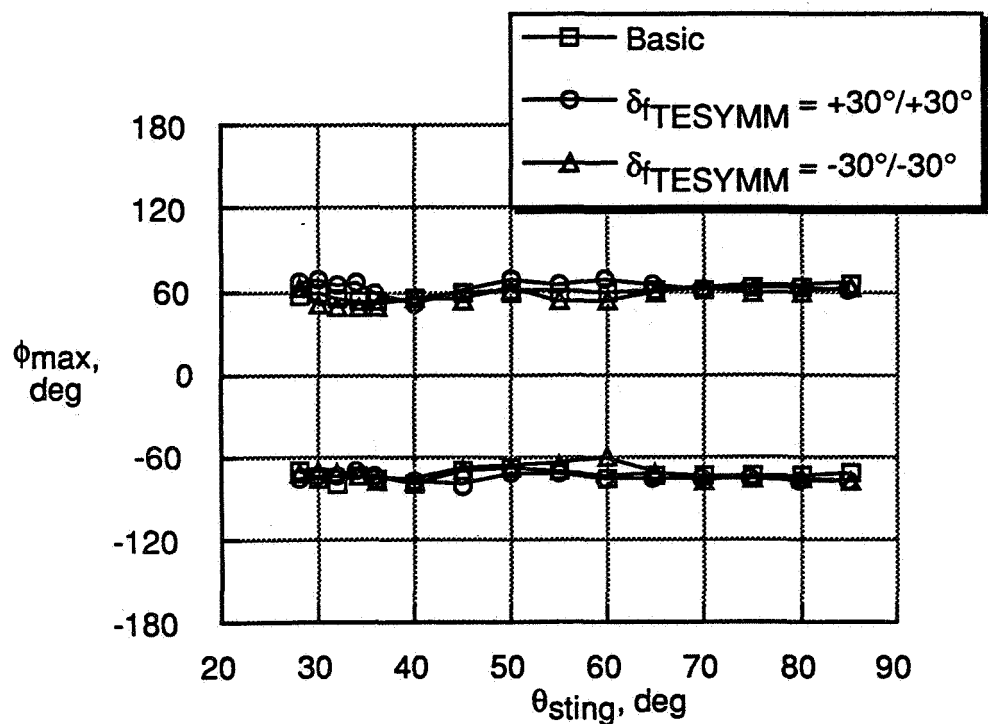


(a) Wing Rock Build Up into HIKR Departure

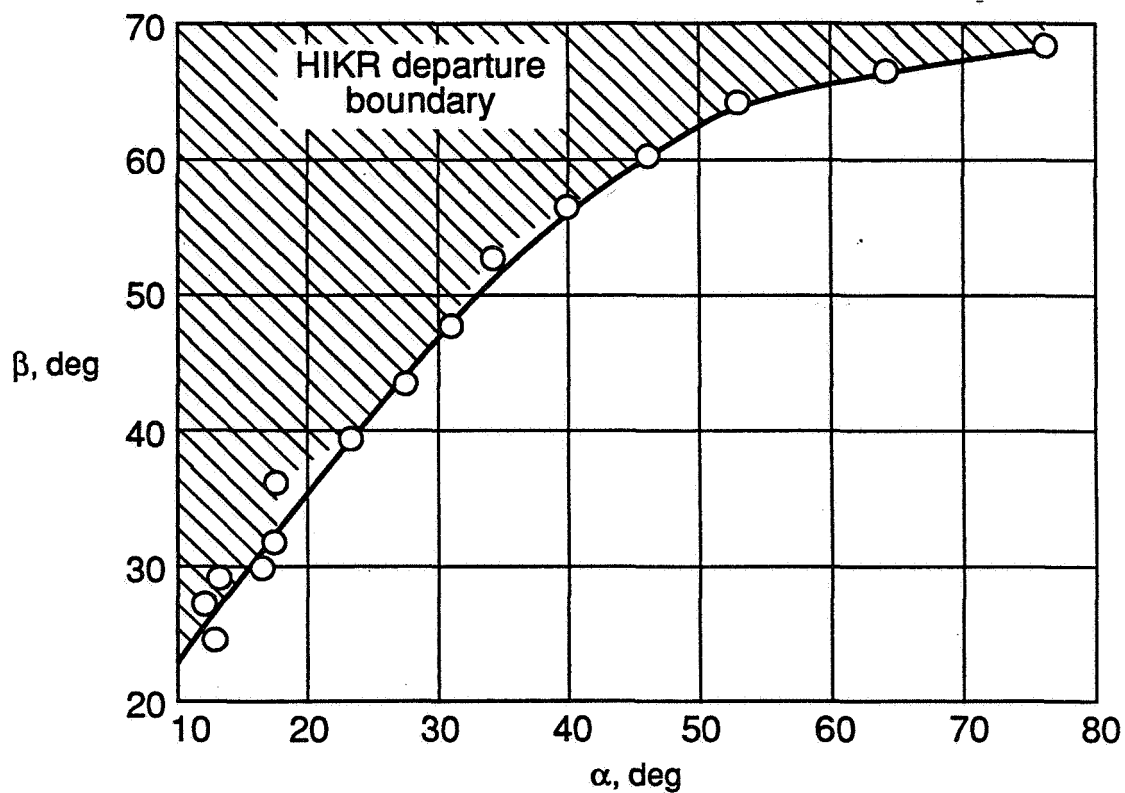


(b) Phase Plane Diagram

Figure 68. Free-to-Roll Results for $\theta_{\text{sting}} = 45^\circ$



(a) Static Departure Roll Angles from Free-to-Roll Tests



(b) Flight Envelope Guideline for HIKR Departure Based on Free-to-Roll Test Data

Figure 69. HIKR Departure Characteristics from Free-to-Roll Tests

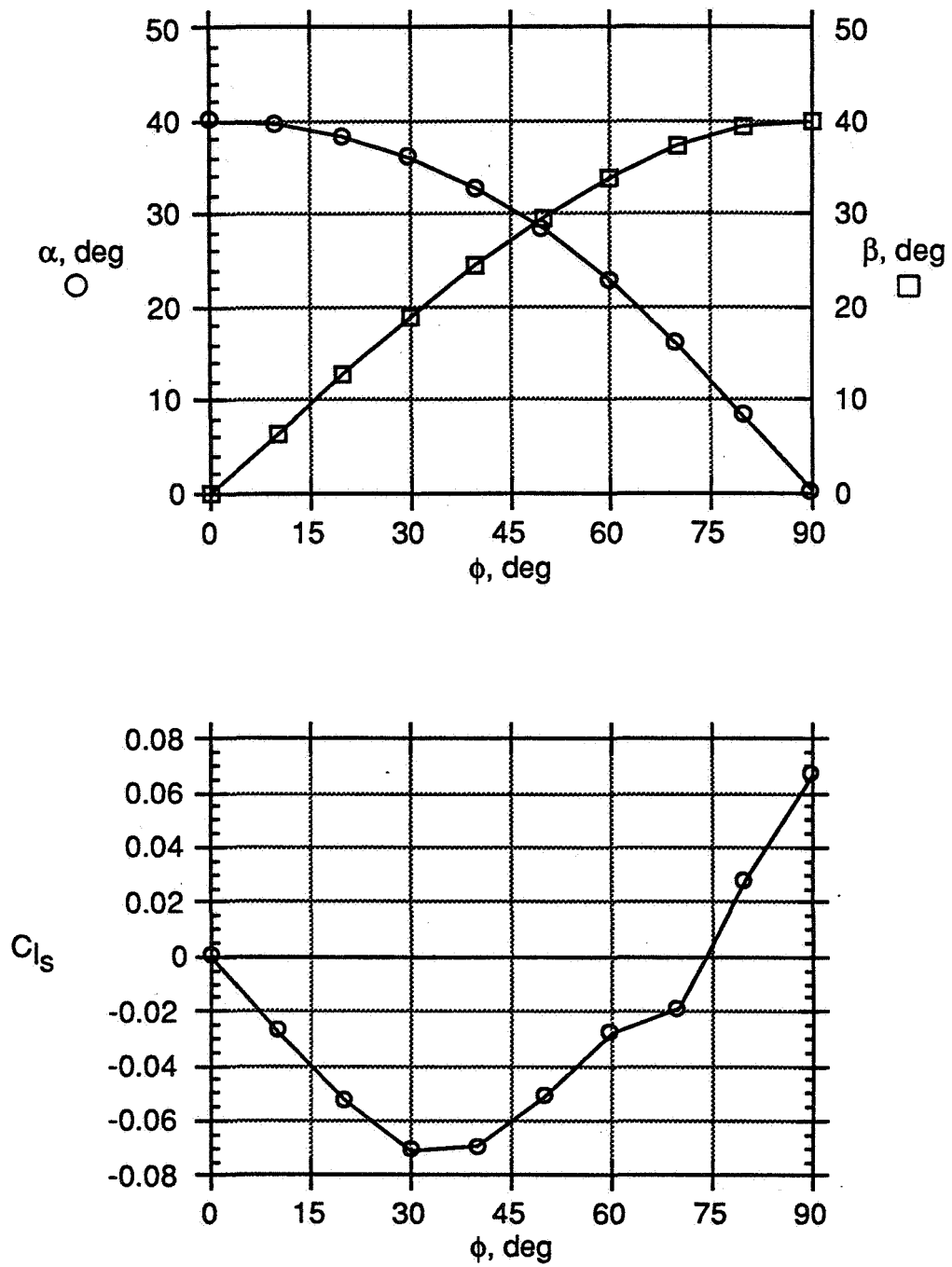
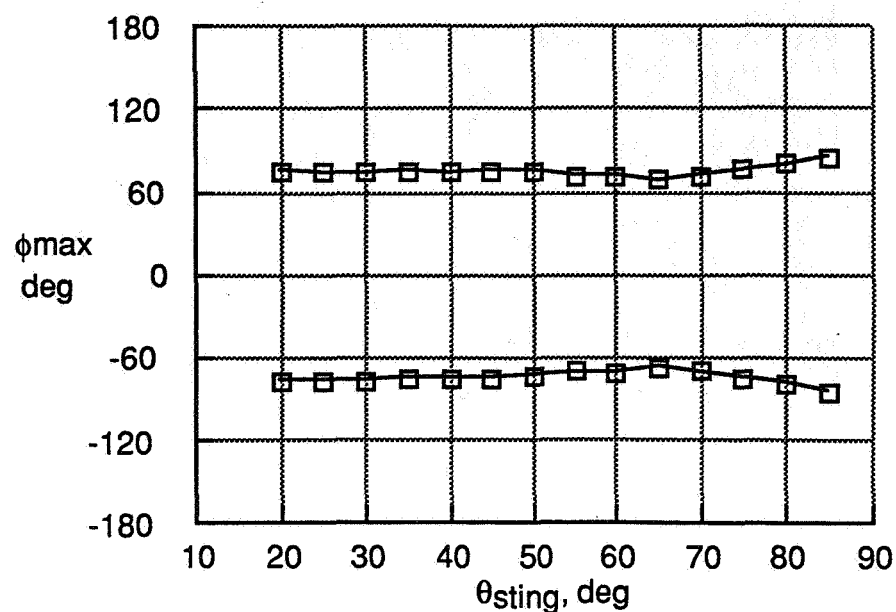
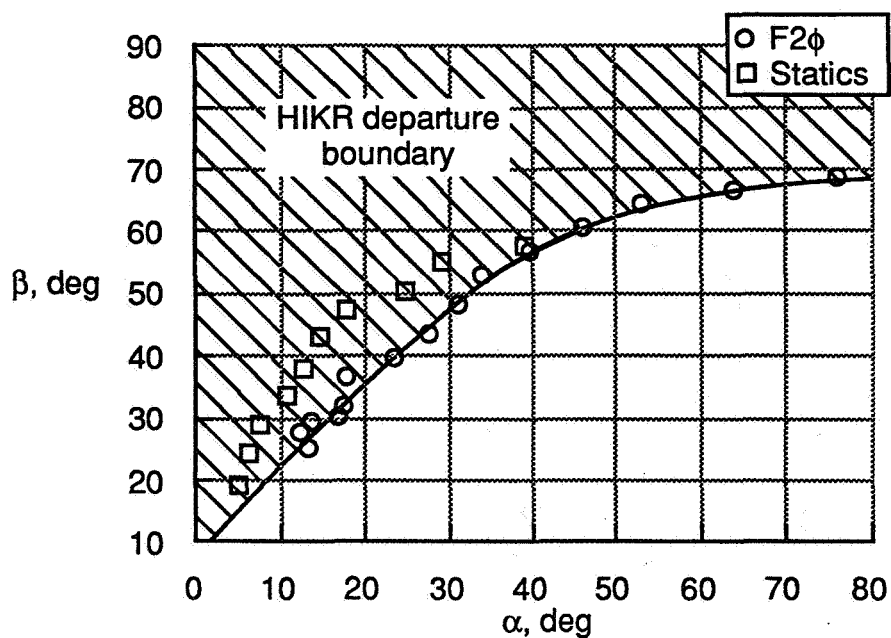


Figure 70. Static Rolling Moment Dependence with Roll Angle; $\theta_{\text{sting}} = 40^\circ$

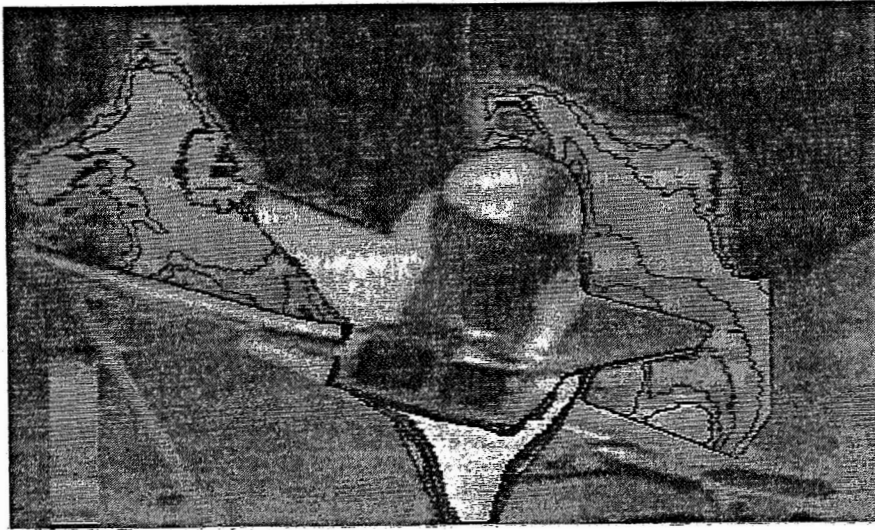


(a) Static Departure Roll Angles from Static-Force Tests

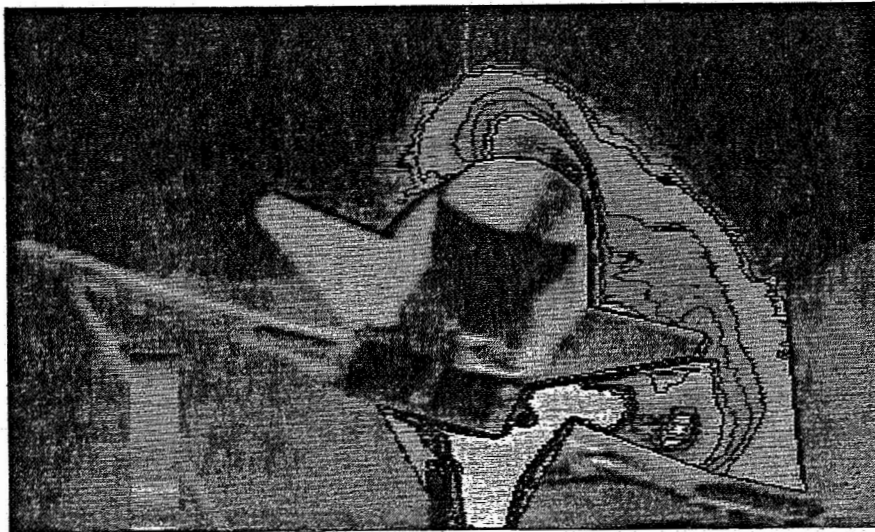


(b) Flight Envelope Guideline for HIKR Departure Based on Static-Force Test Data Compared to Free-to-Roll Test Data

Figure 71. HIKR Departure Characteristics from Static-Force Tests



(a) Small Left Roll



(b) Moderate Left Roll

Figure 72. HIKR Departure Flow Visualization Results; Front View
Descending Order in Color Look-Up Table Represents Increase in Smoke Density



(c) Large Left Roll



(d) Left Roll HIKR Departure Point

Figure 72. Concluded

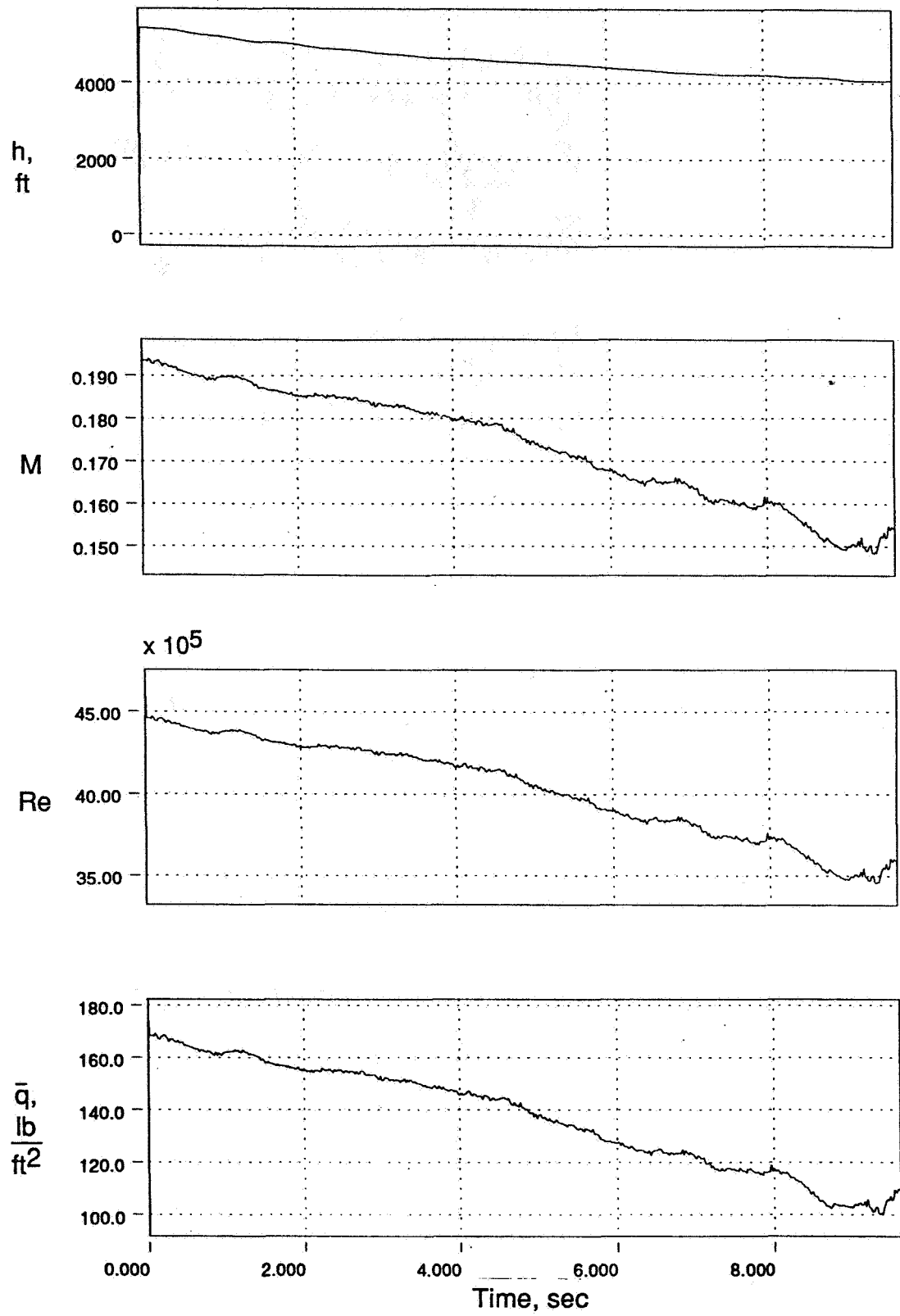


Figure 73. Wing Rock Drop Test Results

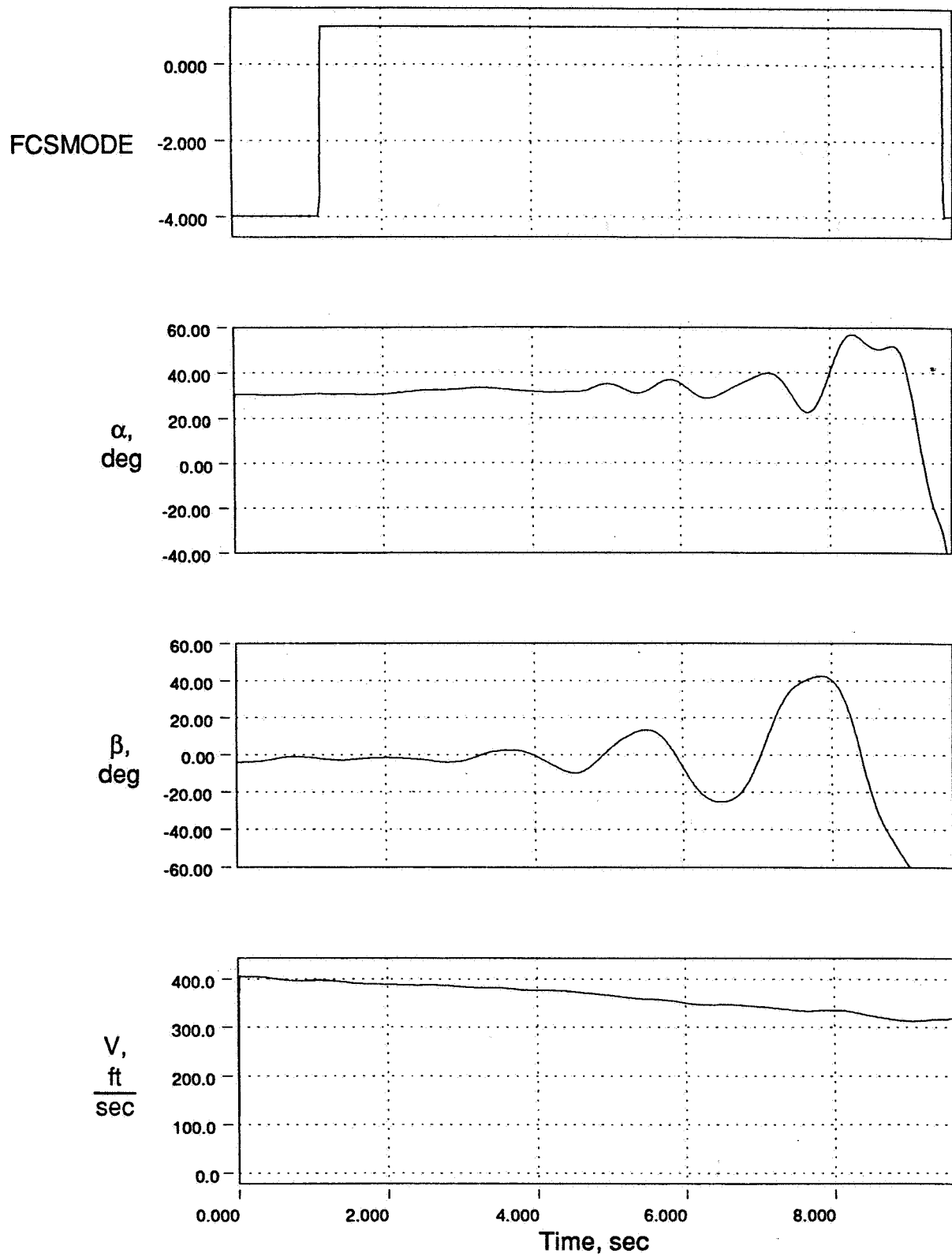


Figure 74. Wing Rock Drop Test Results

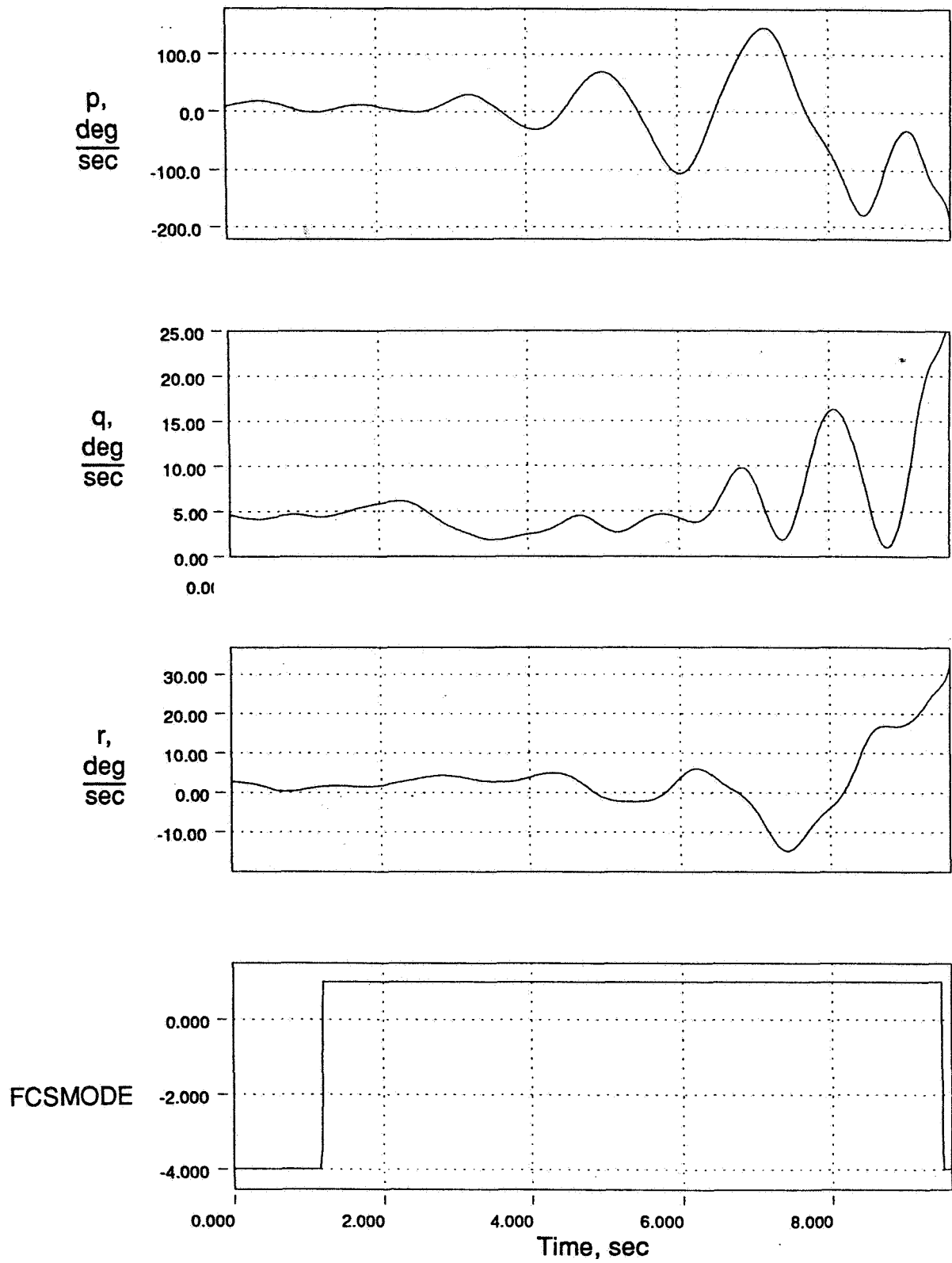


Figure 75. Wing Rock Drop Test Results

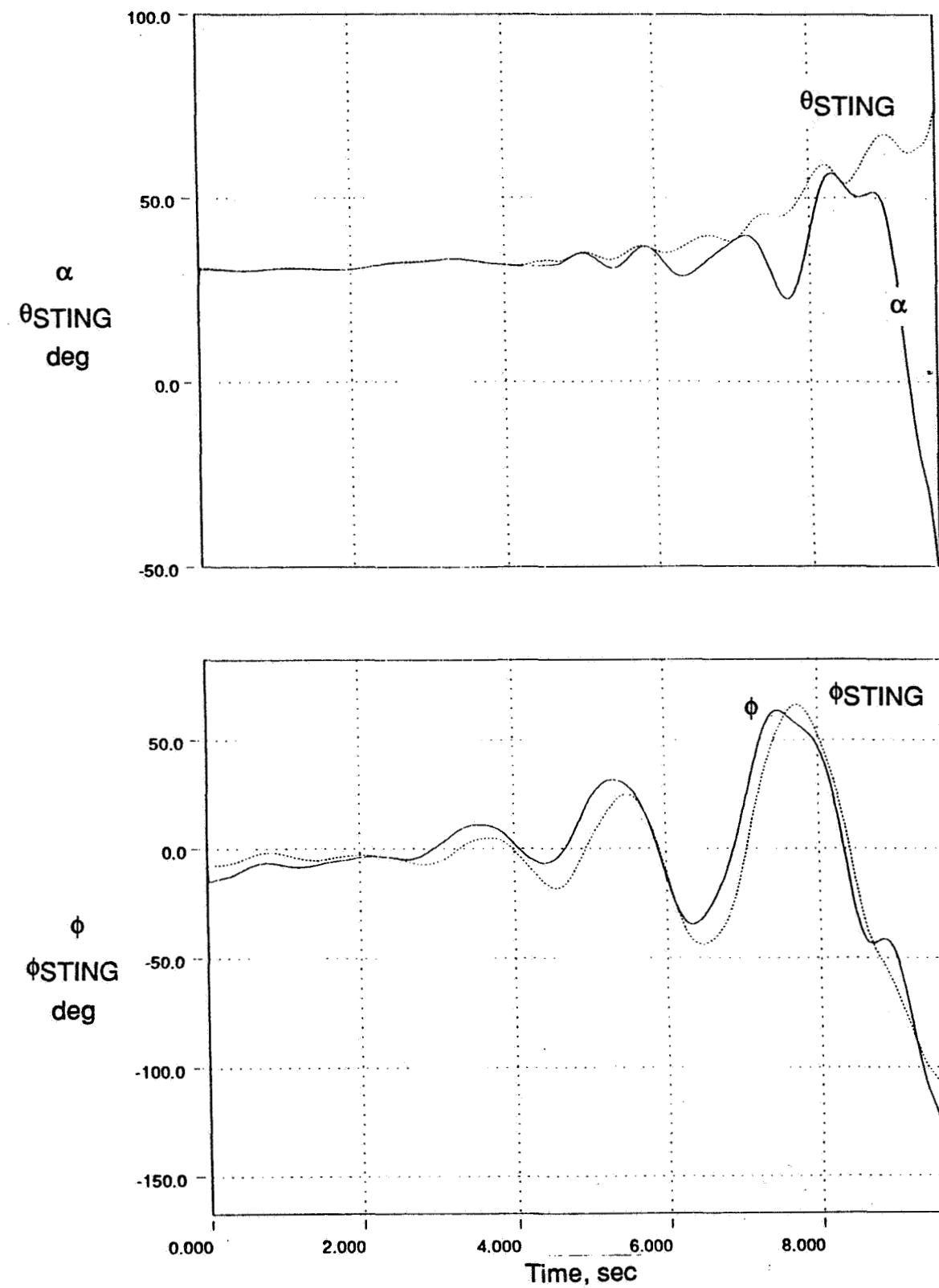


Figure 76. Wing Rock Drop Test Results

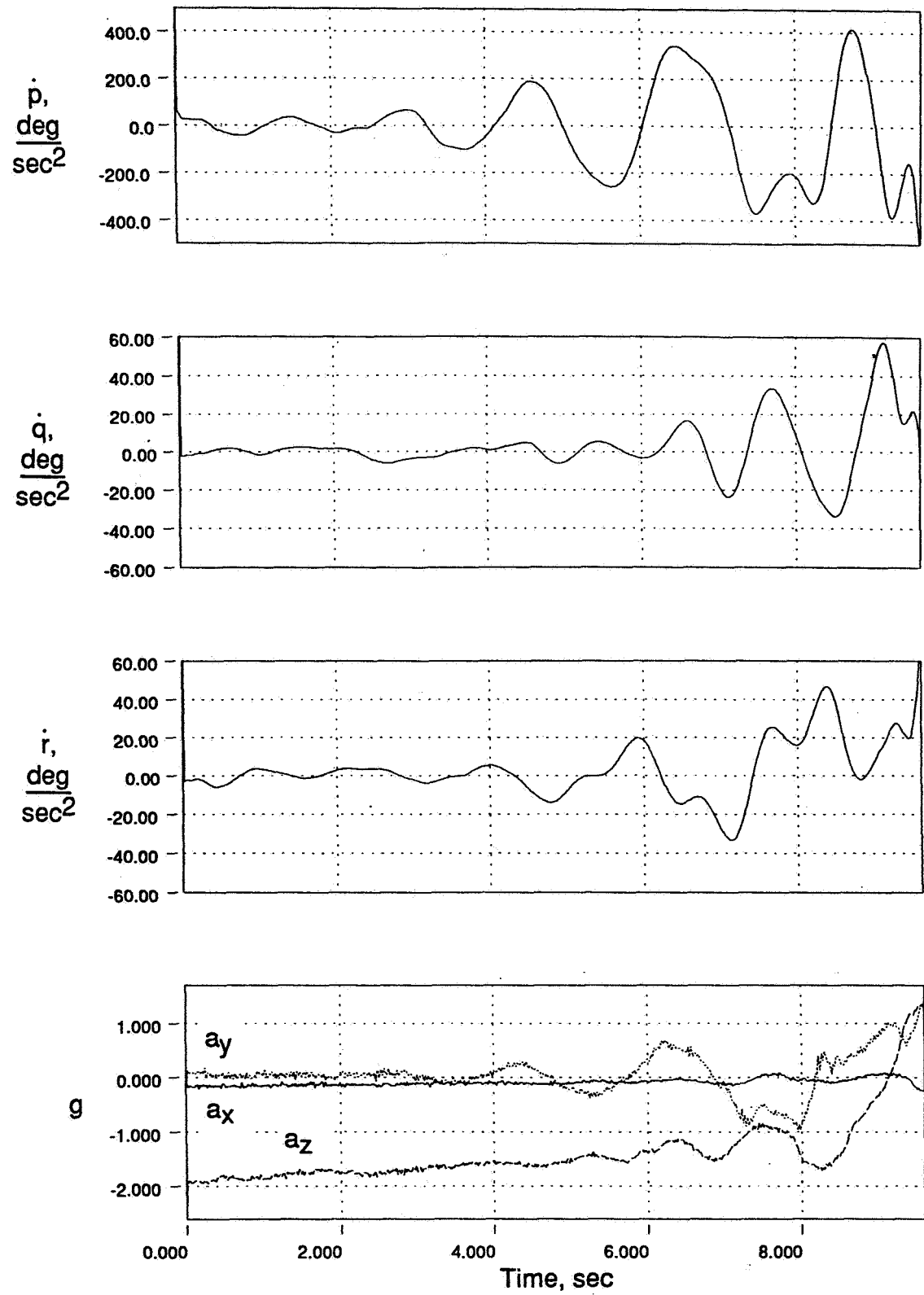


Figure 77. Wing Rock Drop Test Results

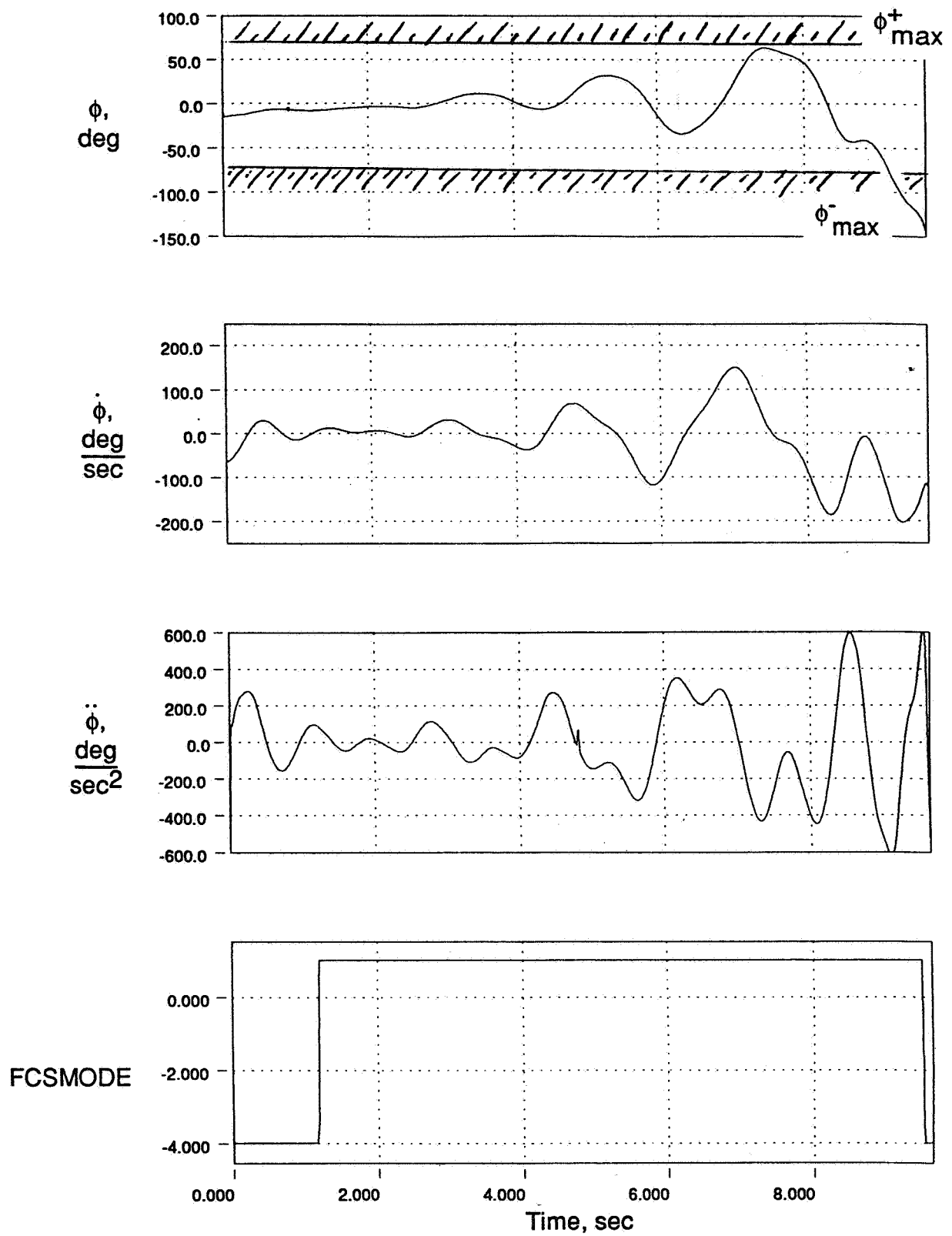


Figure 78. Wing Rock Drop Test Results

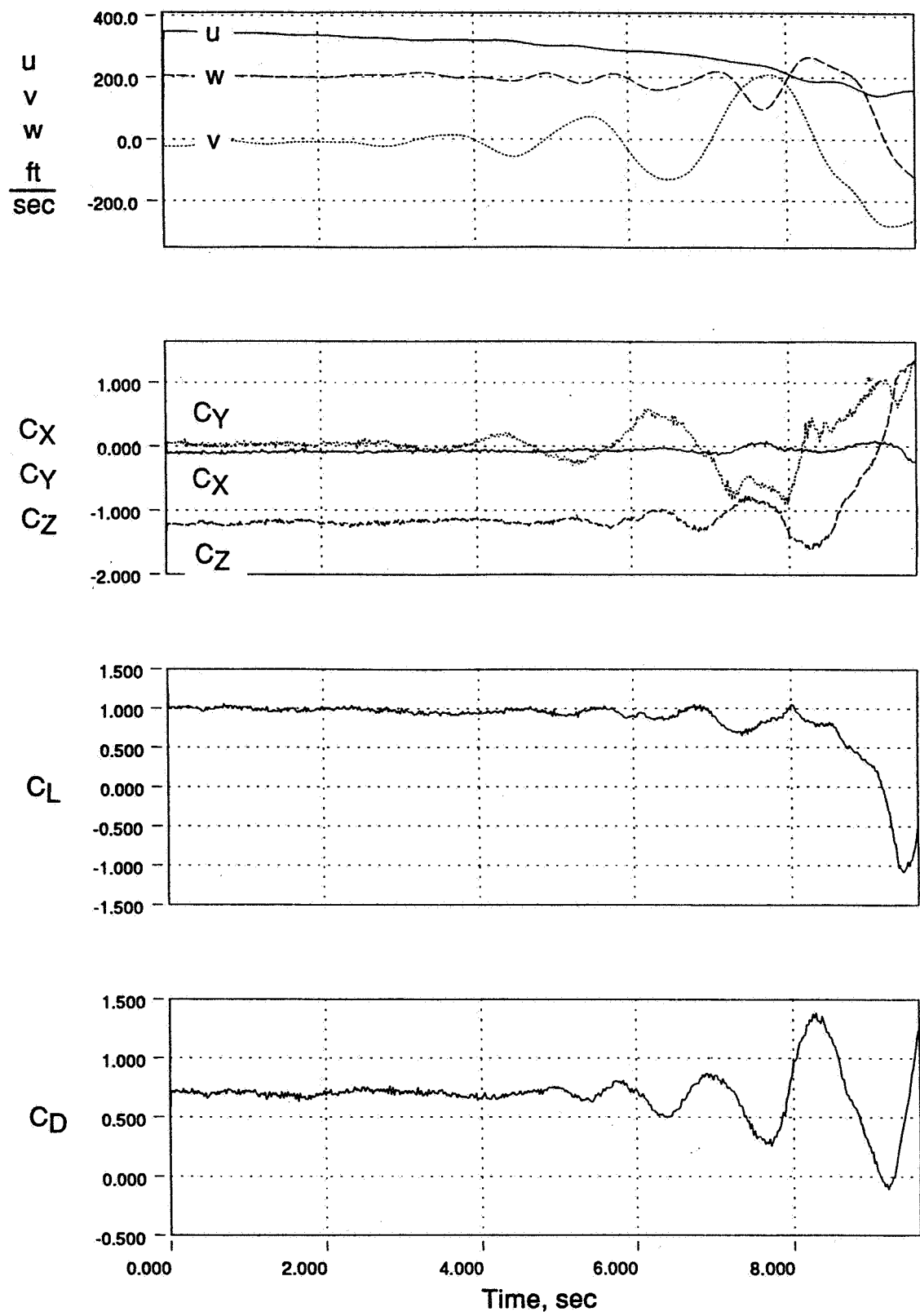


Figure 79. Wing Rock Drop Test Results

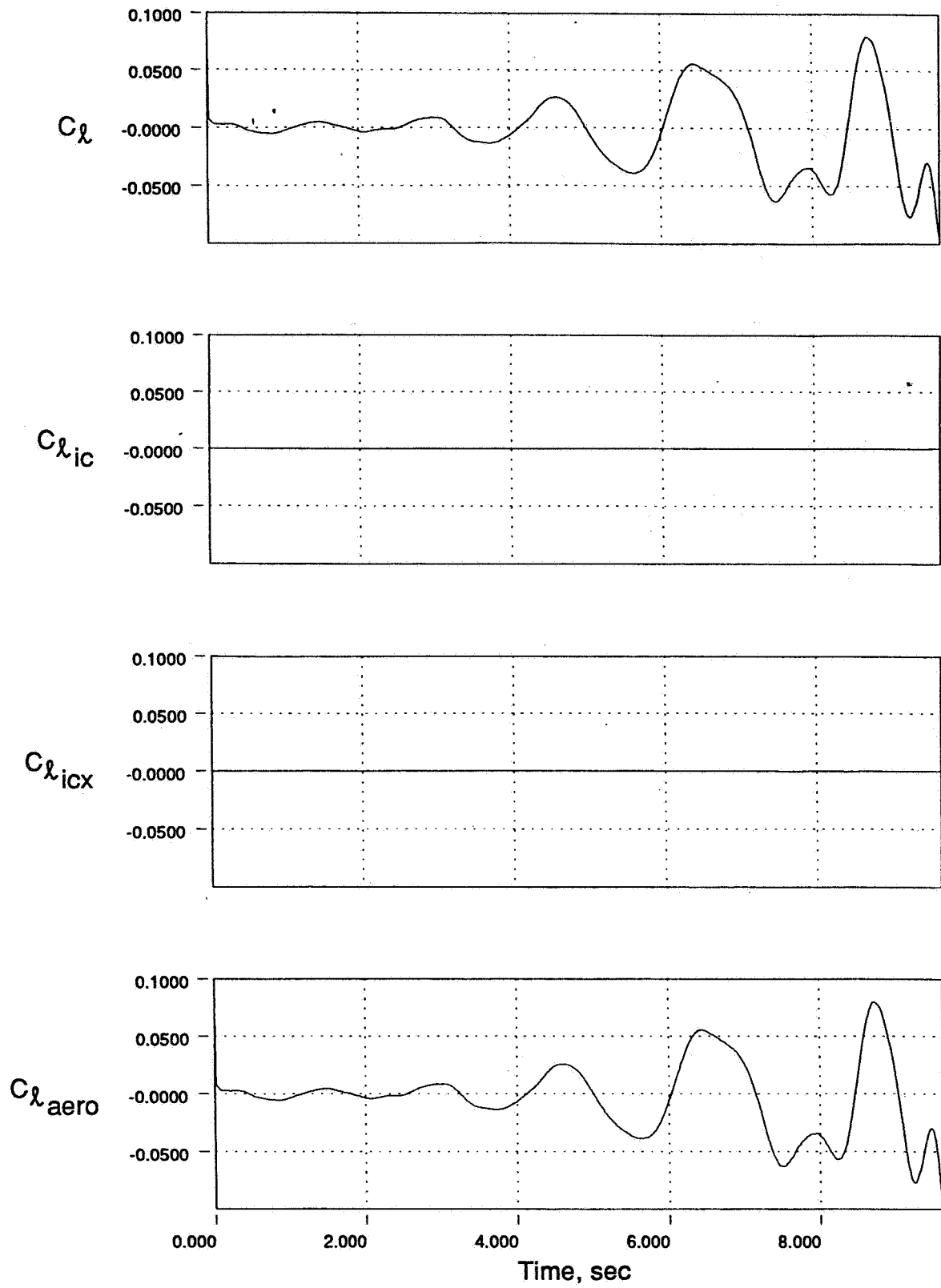


Figure 80. Wing Rock Drop Test Results

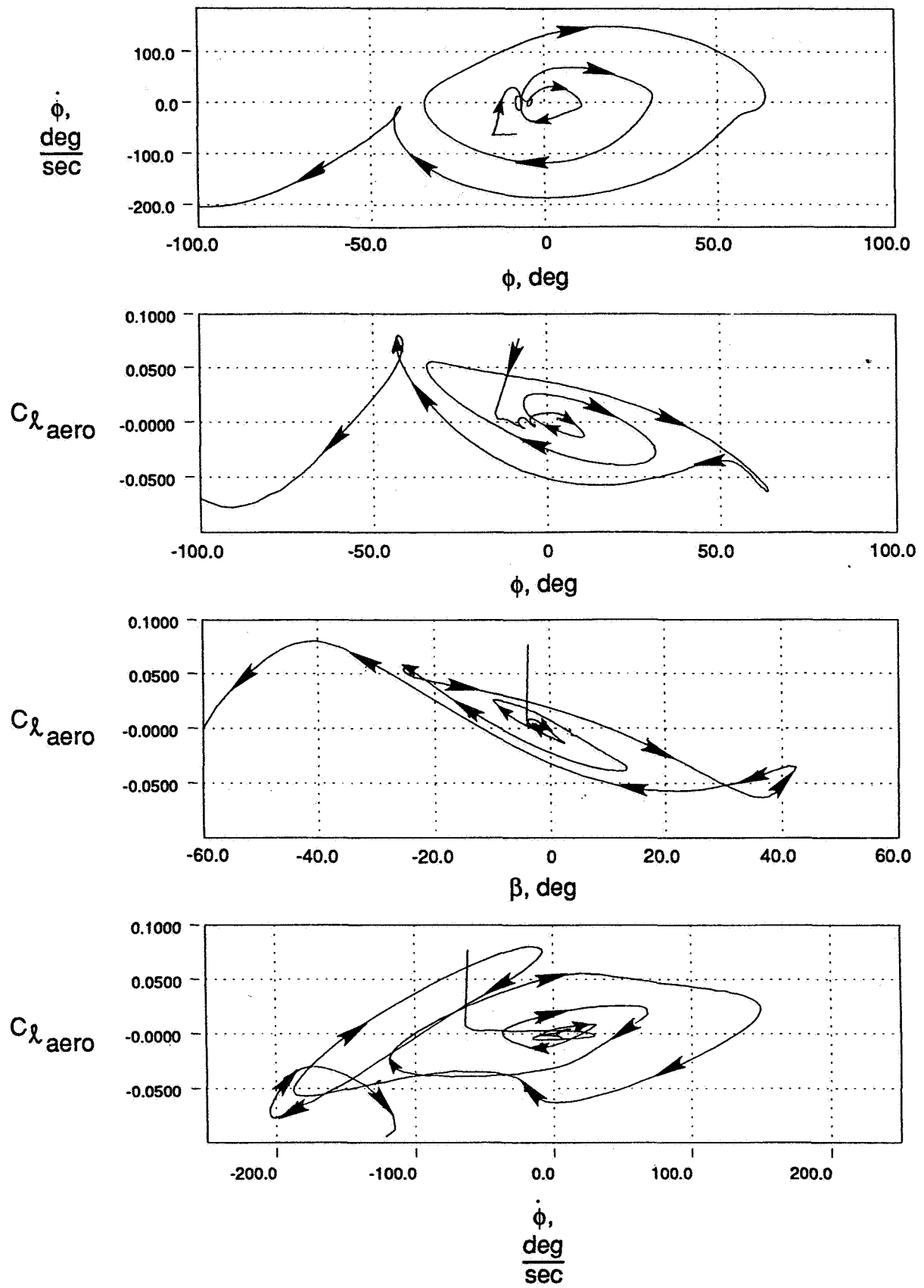


Figure 81. Wing Rock Drop Test Results

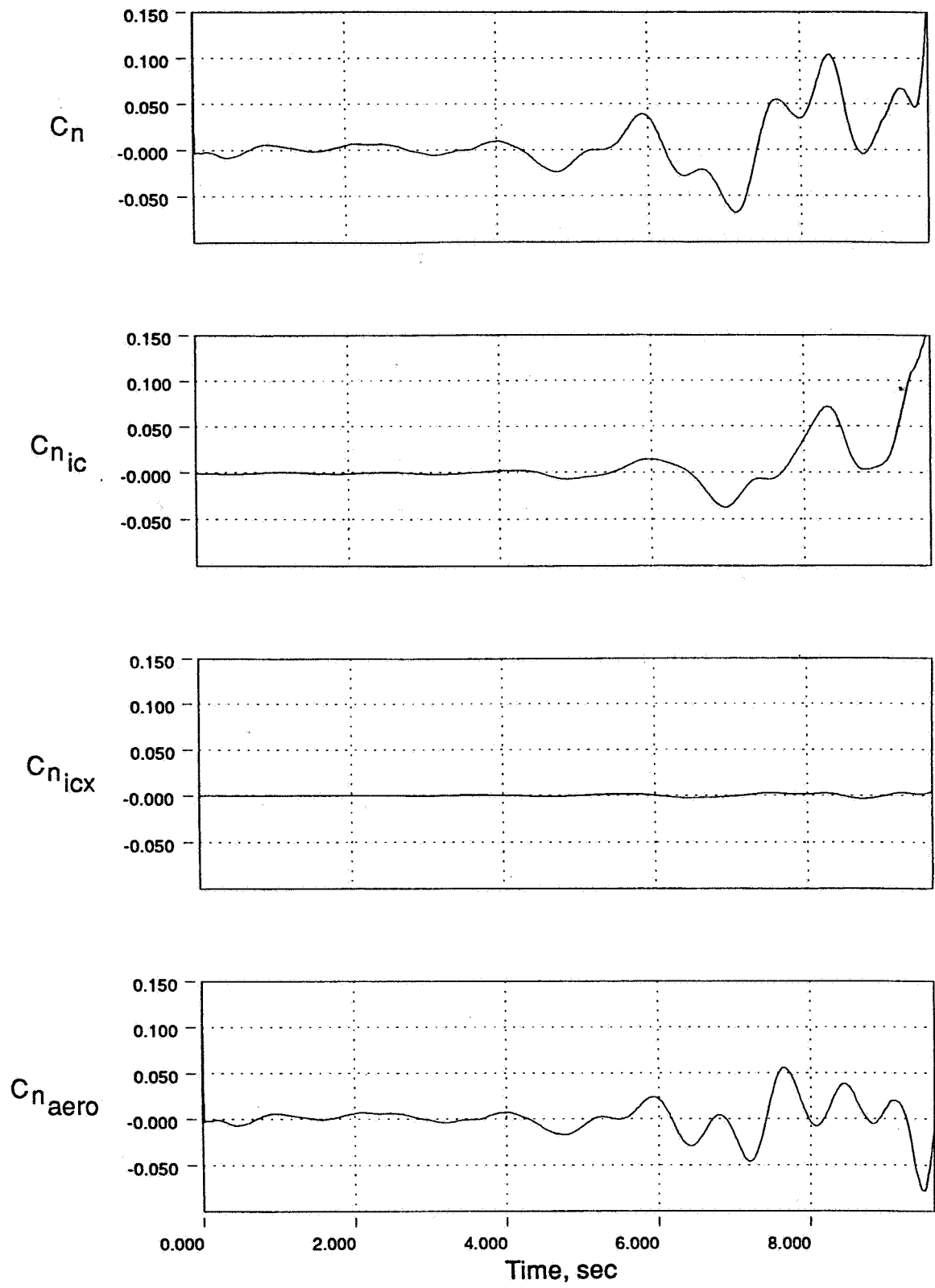


Figure 82. Wing Rock Drop Test Results

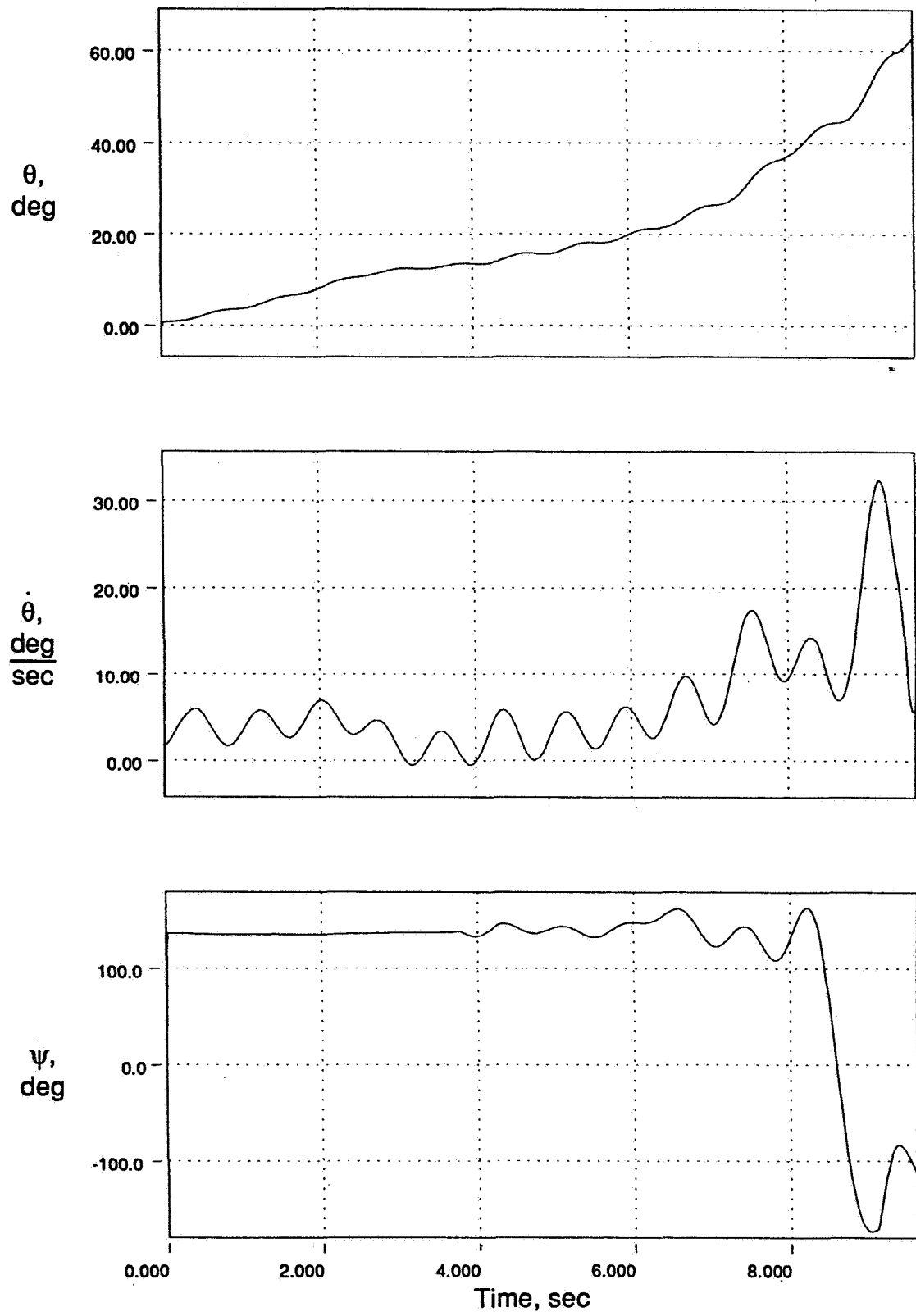


Figure 83. Wing Rock Drop Test Results

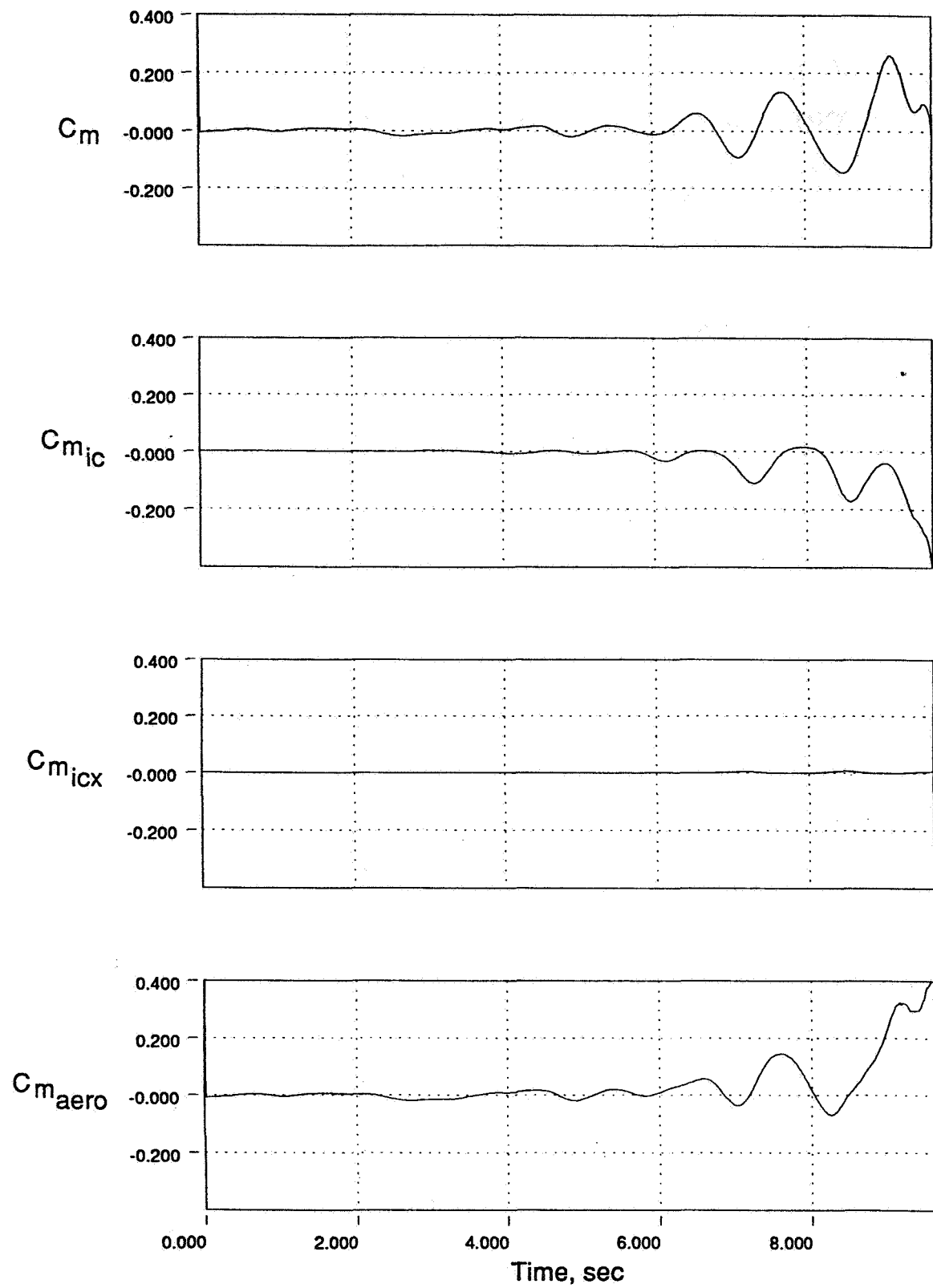


Figure 84. Wing Rock Drop Test Results

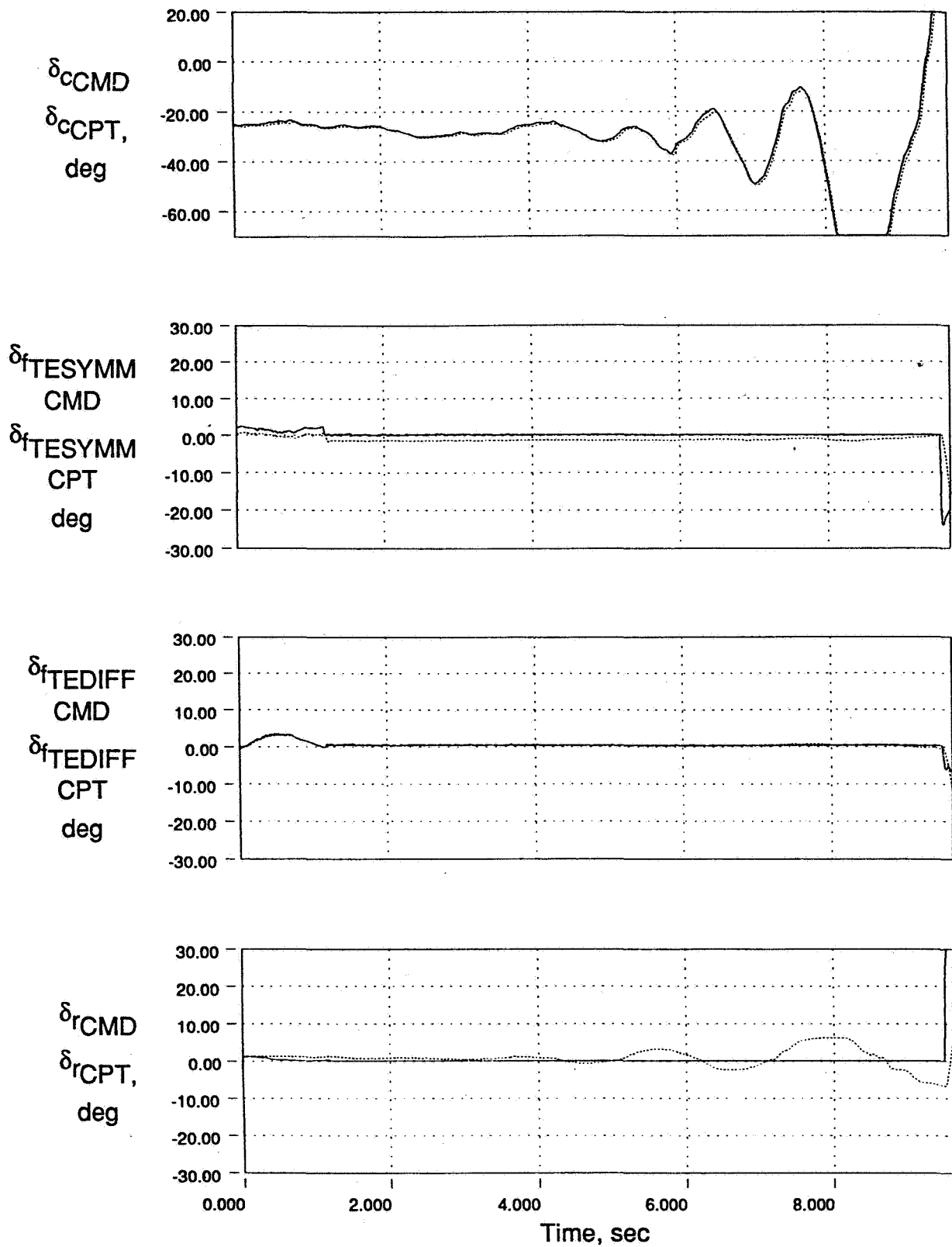


Figure 85. Wing Rock Drop Test Results

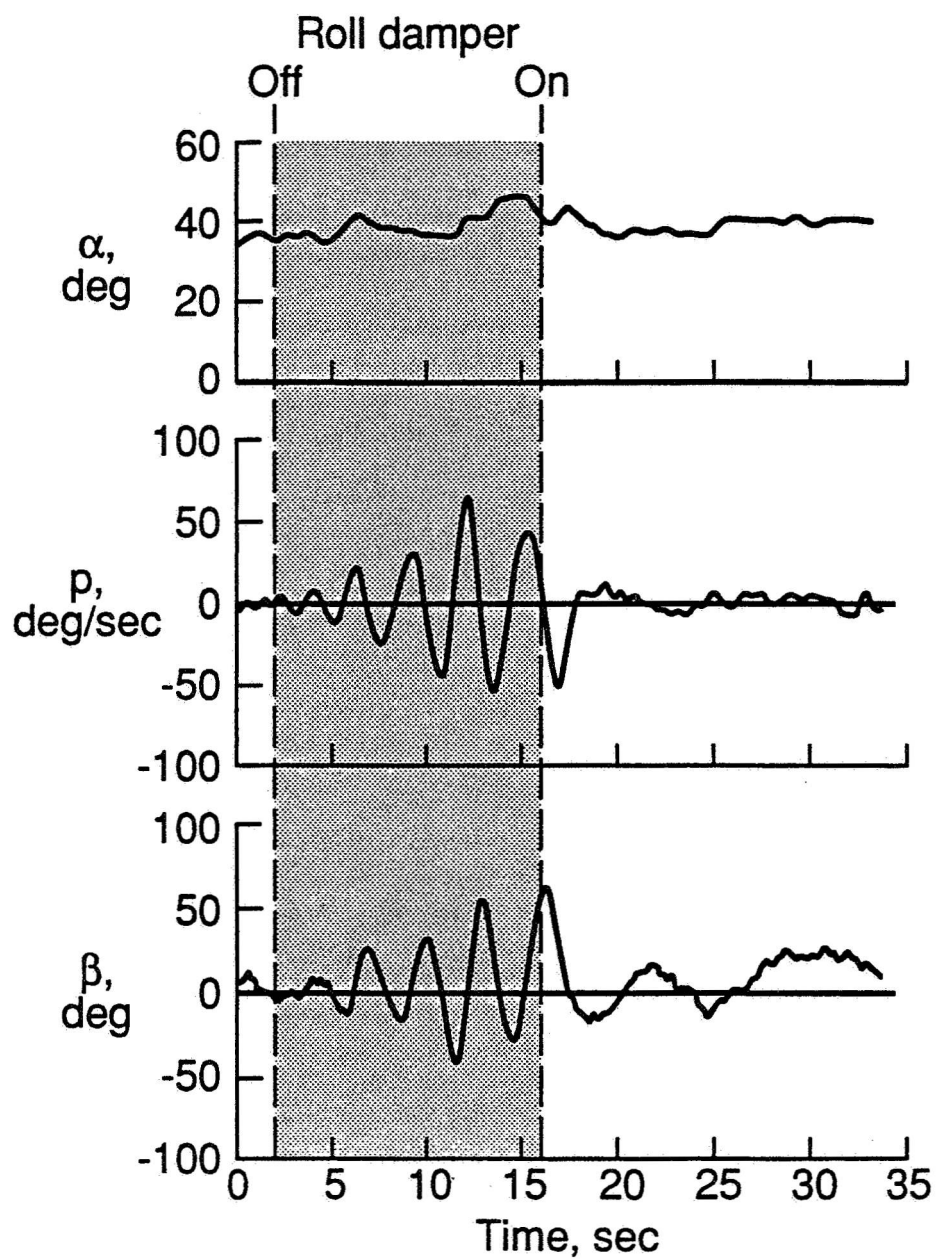


Figure 86. Wing Rock Suppression Results from X-31 Free-Flight Test

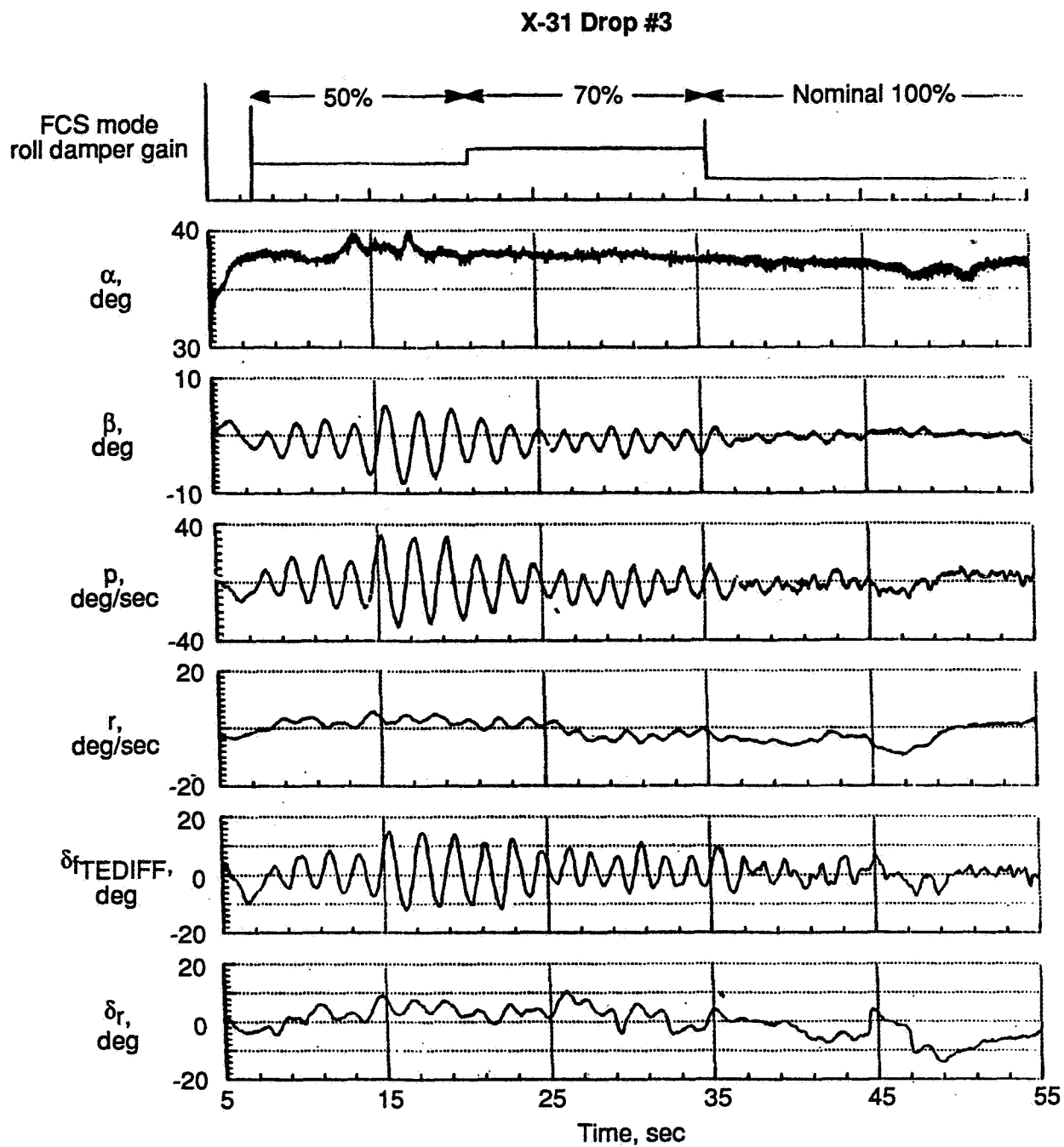


Figure 87. Roll Damper Gain Variation Effect on Wing Rock

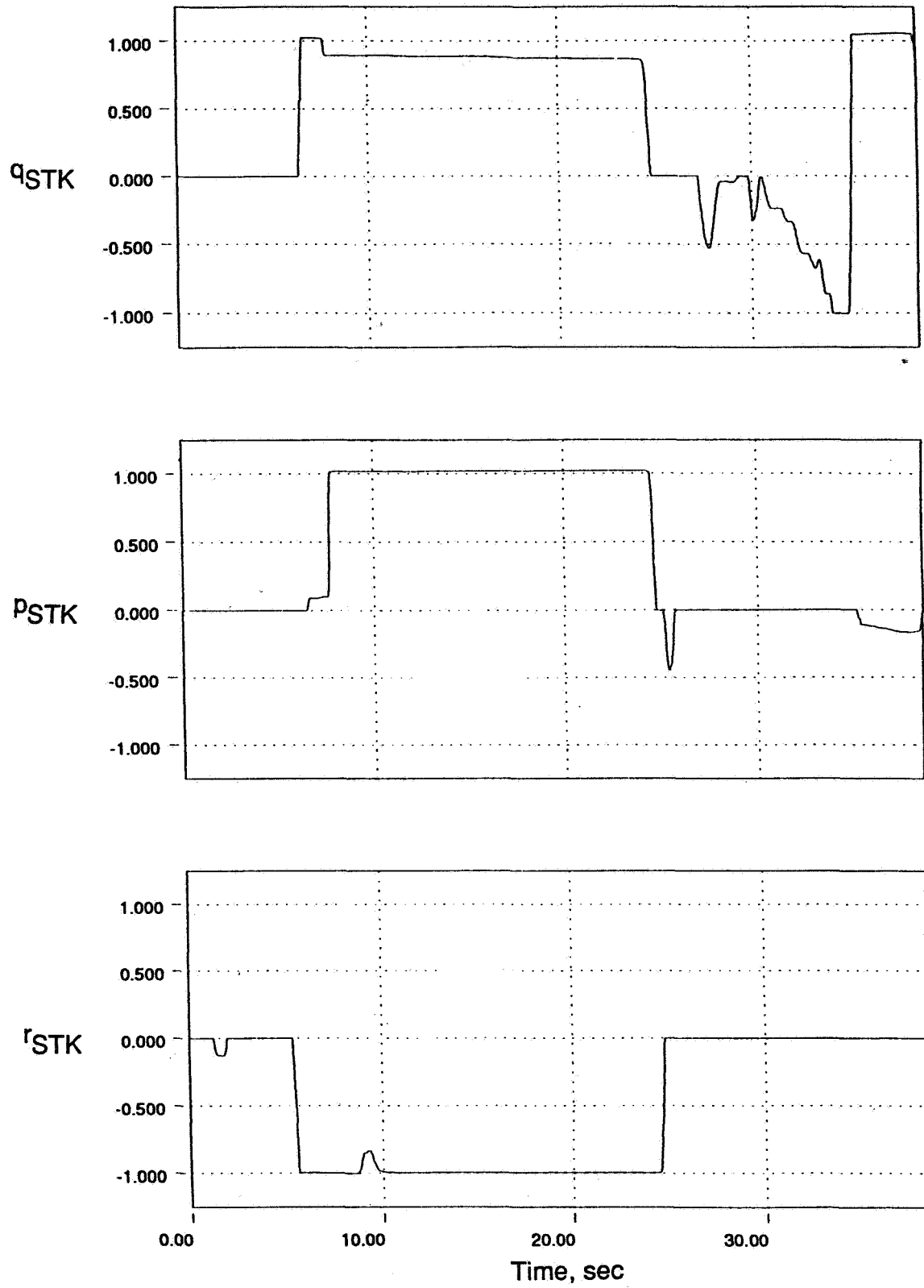


Figure 88. HIKR Departure Drop Test Results

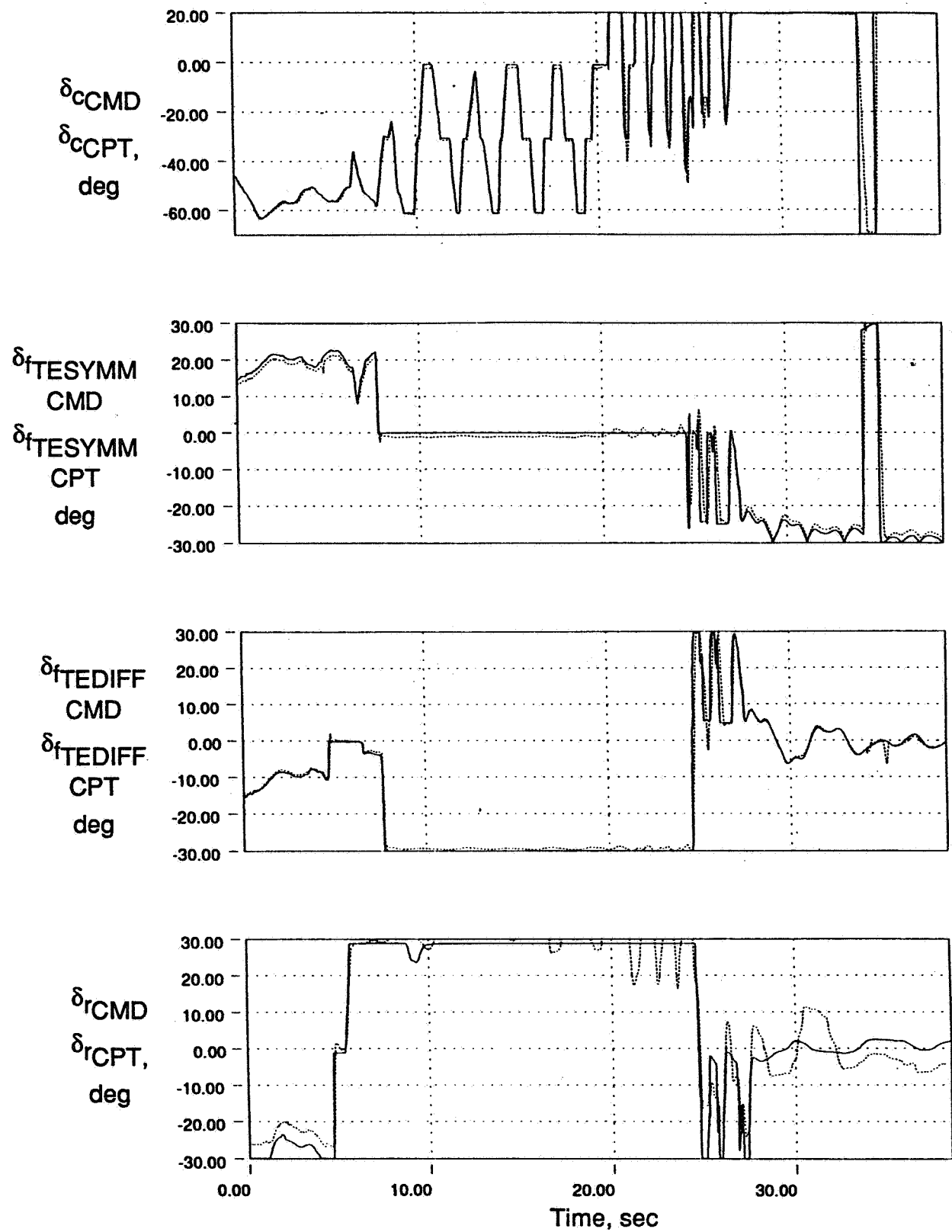


Figure 89. HIKR Departure Drop Test Results

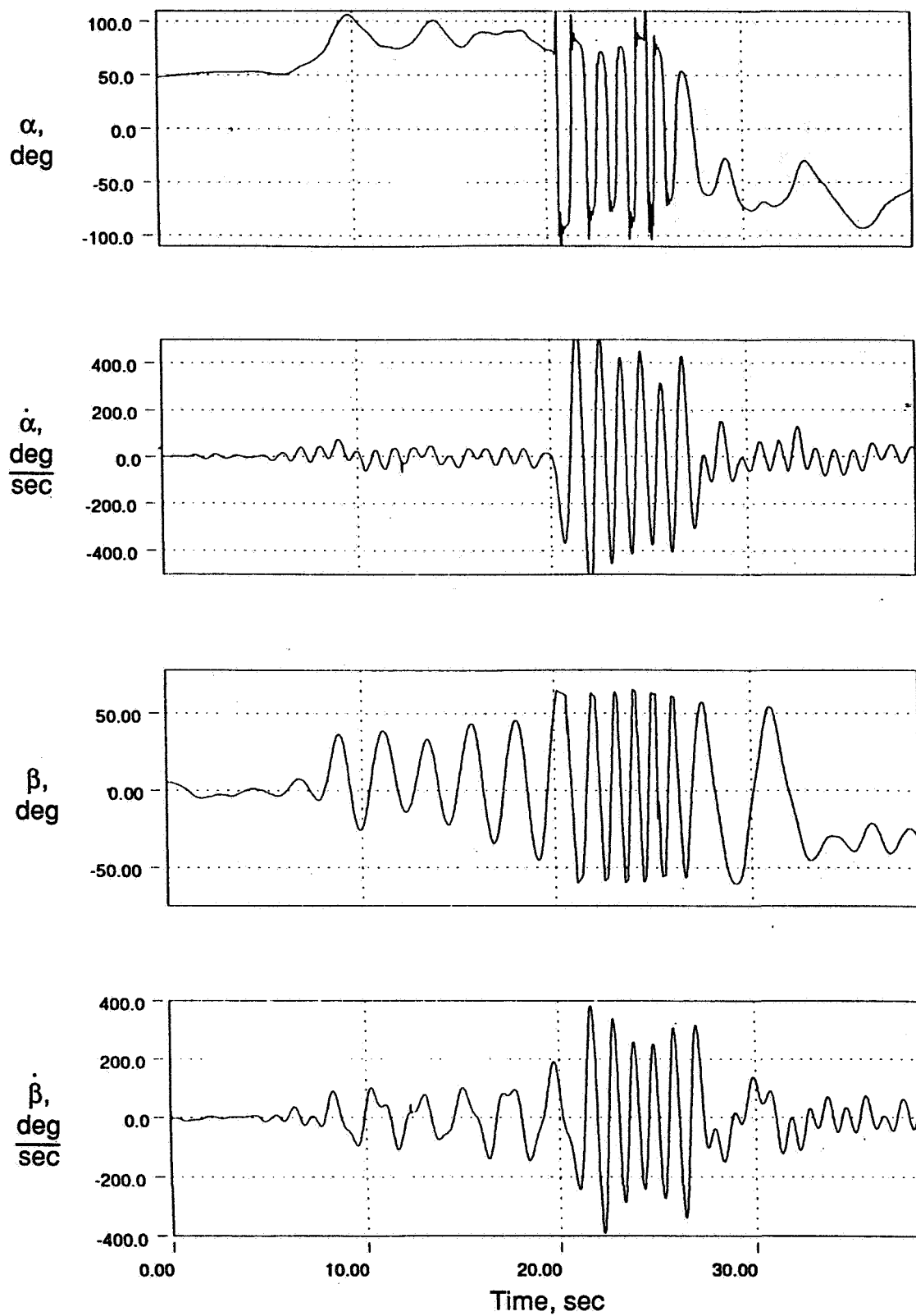


Figure 90. HIKR Departure Drop Test Results

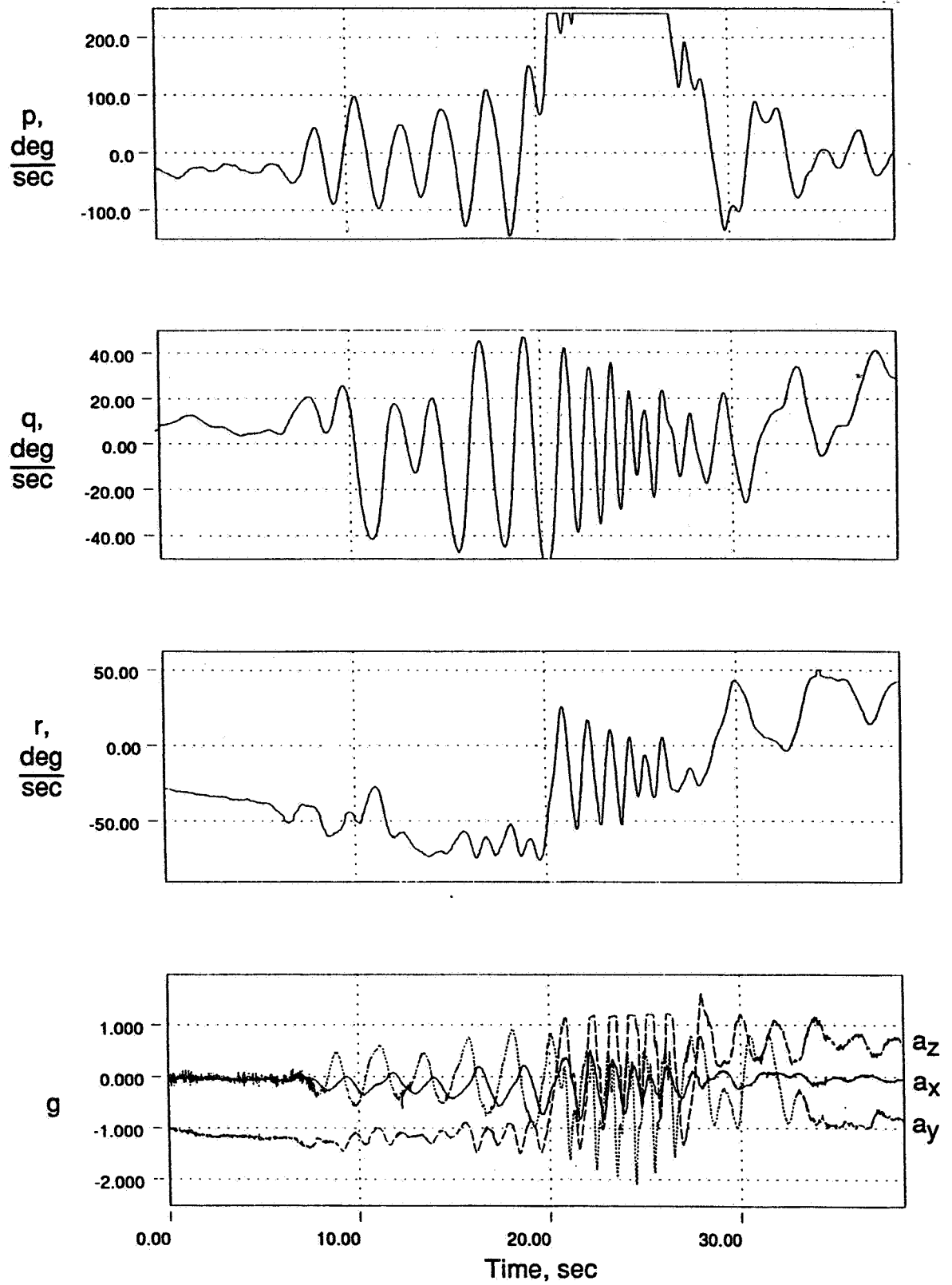


Figure 91. HIKR Departure Drop Test Results

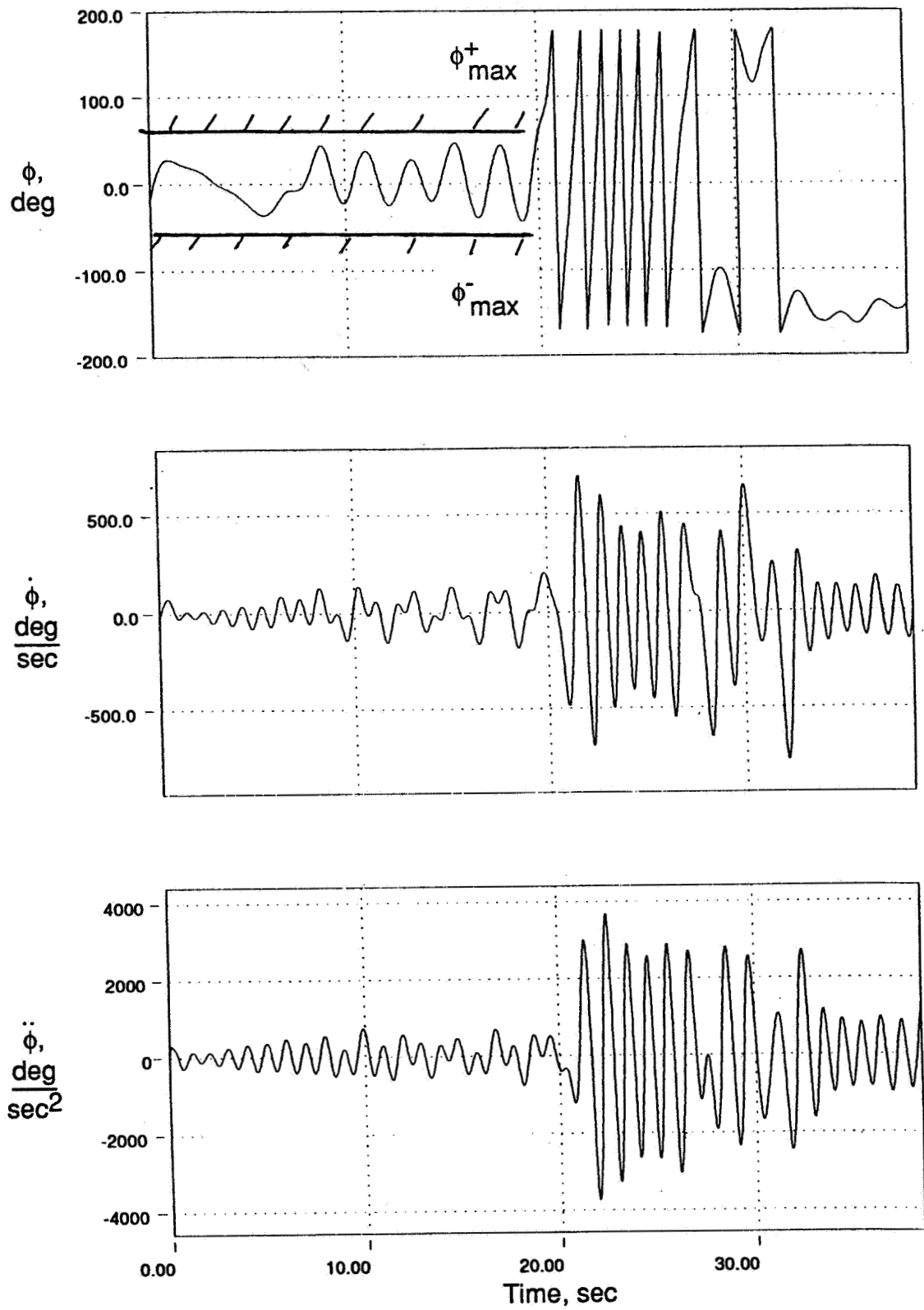


Figure 92. HIKR Departure Drop Test Results

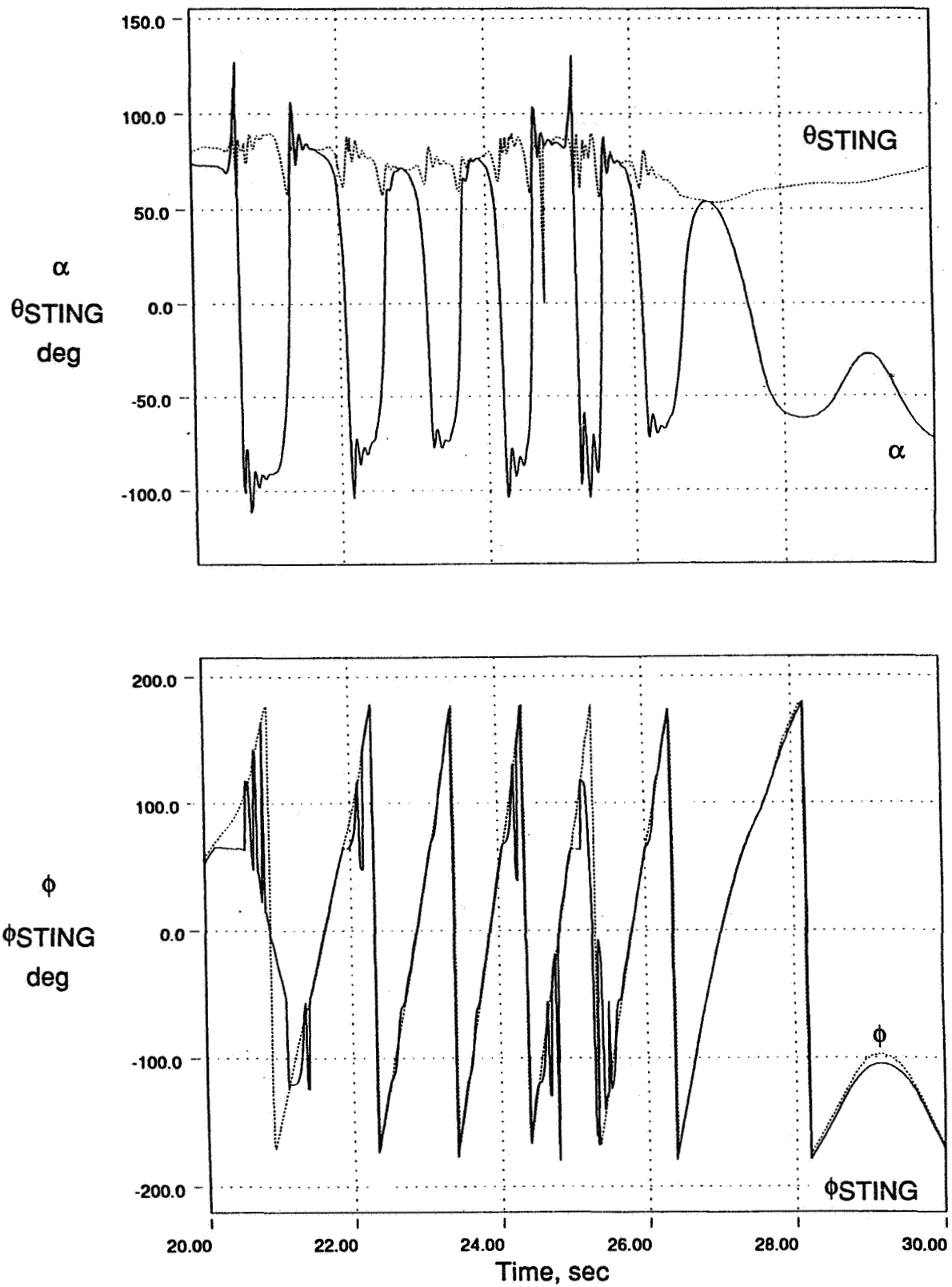


Figure 93. HIKR Departure Drop Test Results

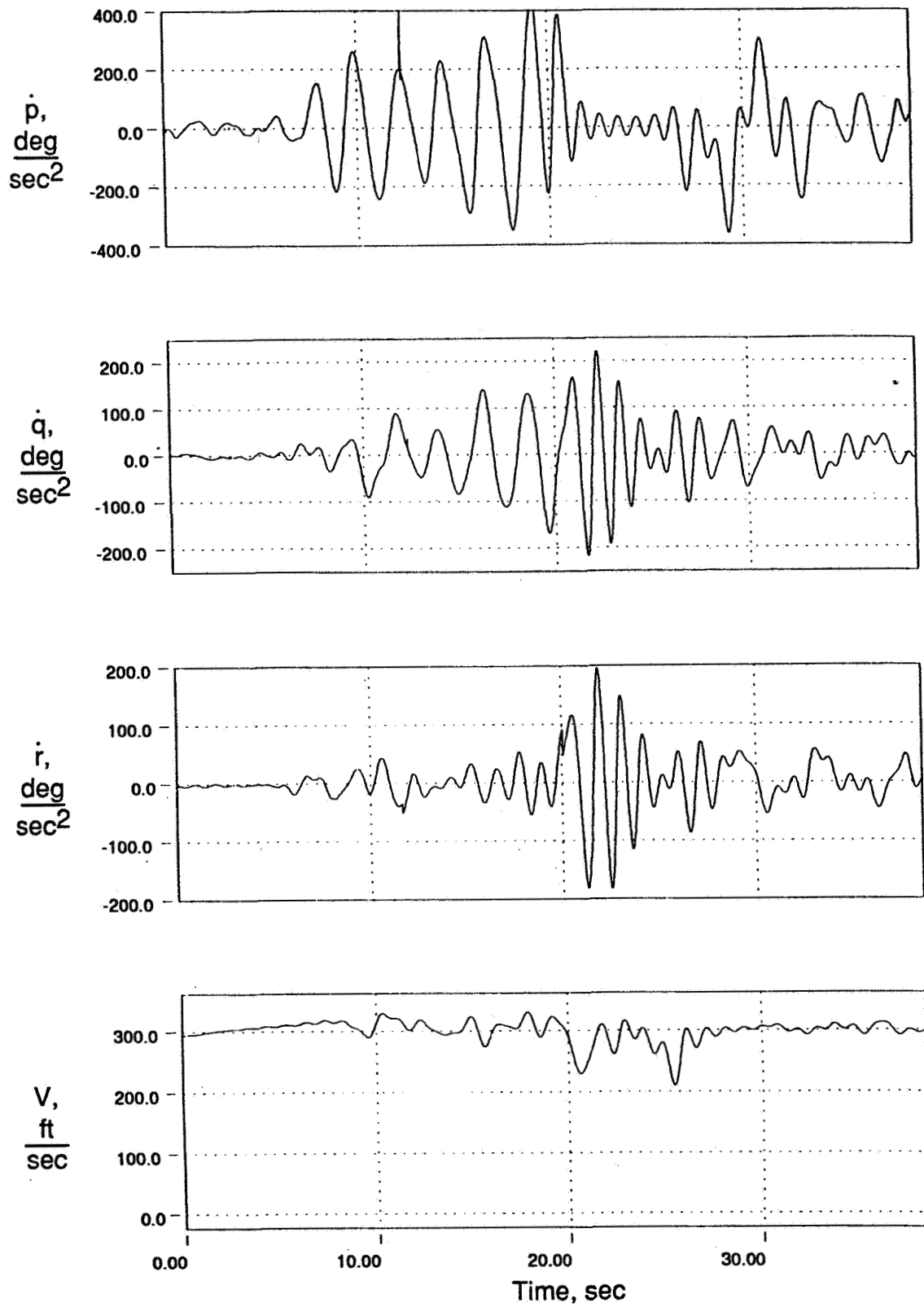


Figure 94. HIKR Departure Drop Test Results

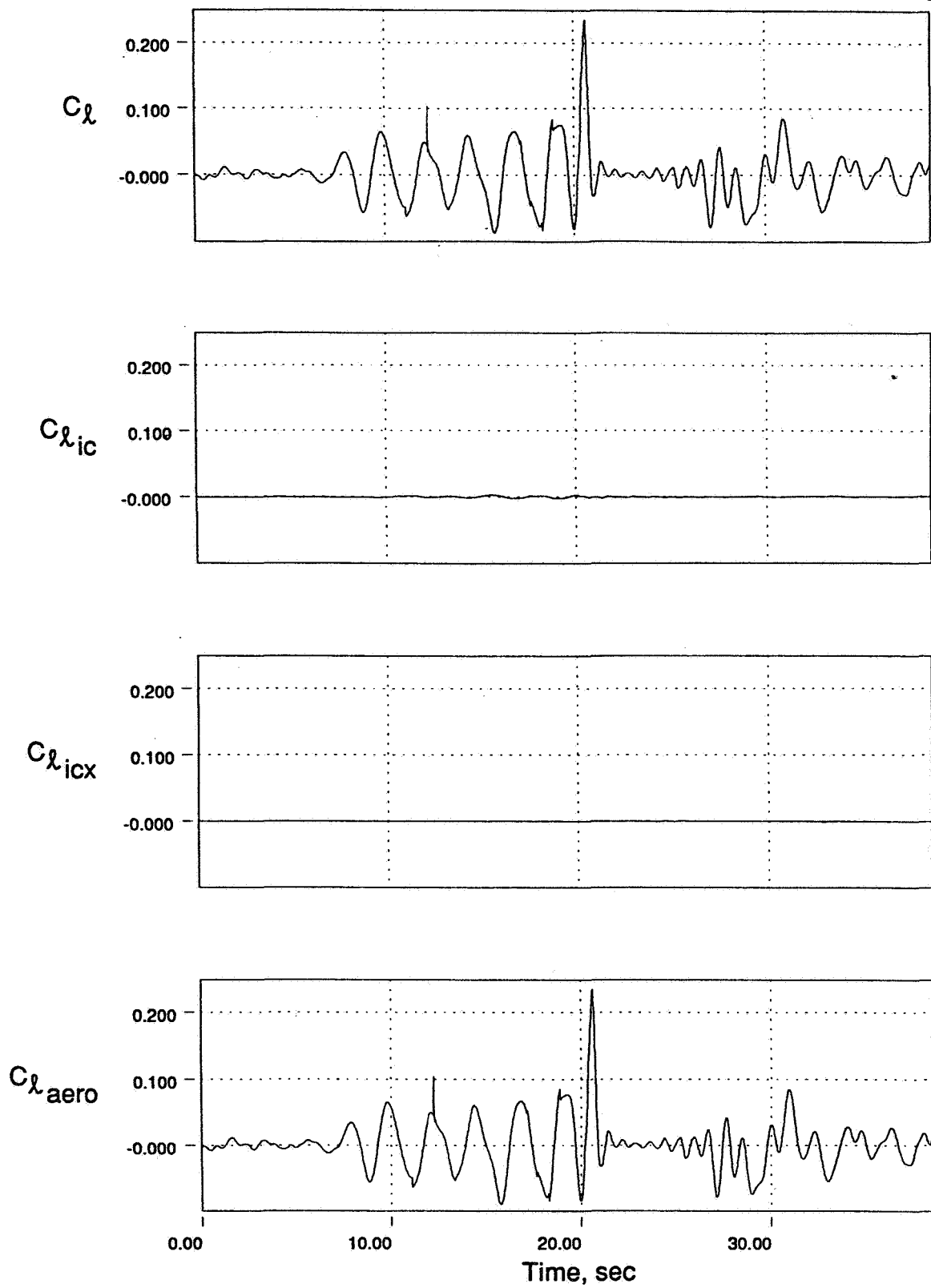


Figure 95. HIKR Departure Drop Test Results

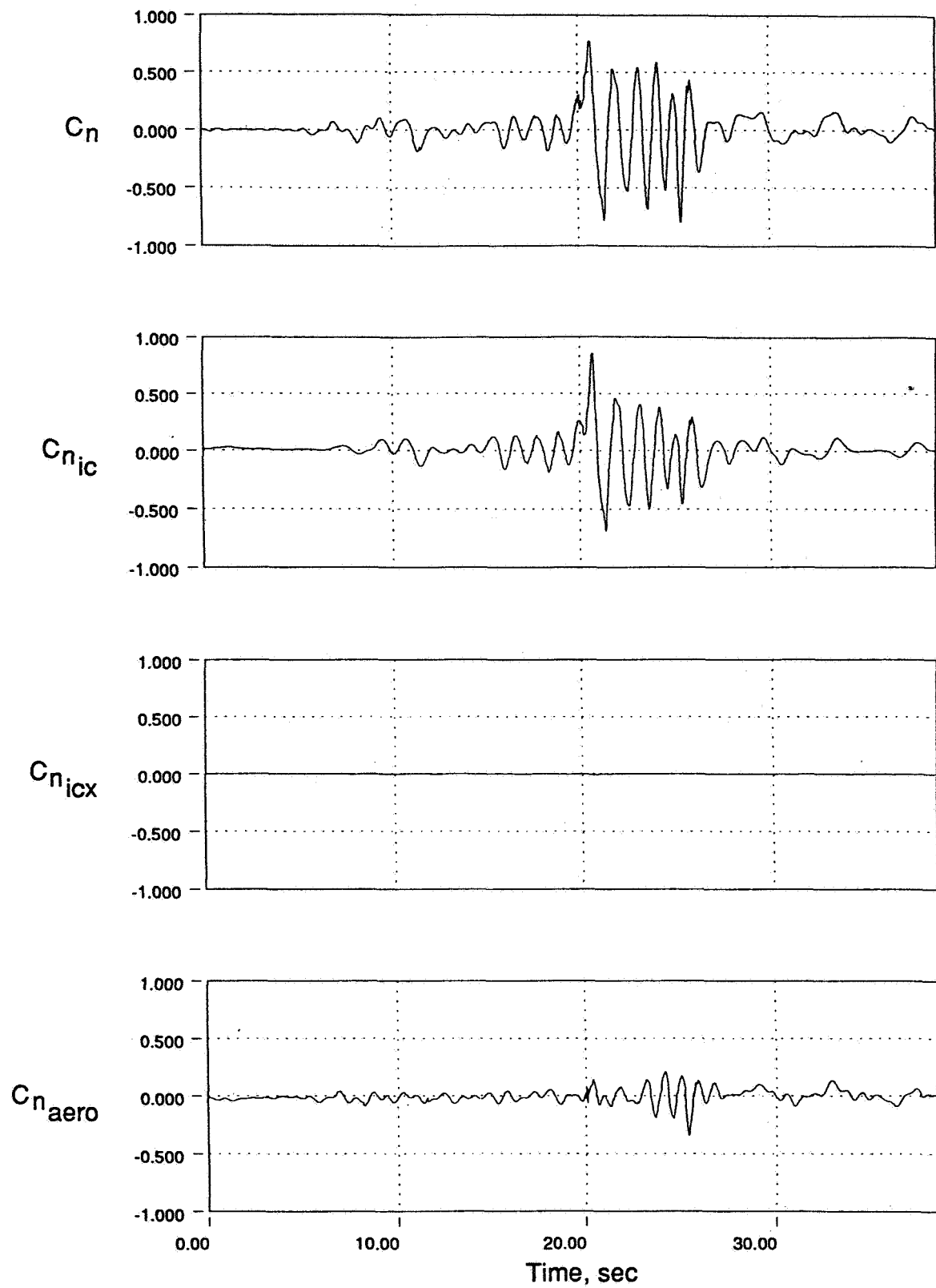


Figure 96. HIKR Departure Drop Test Results

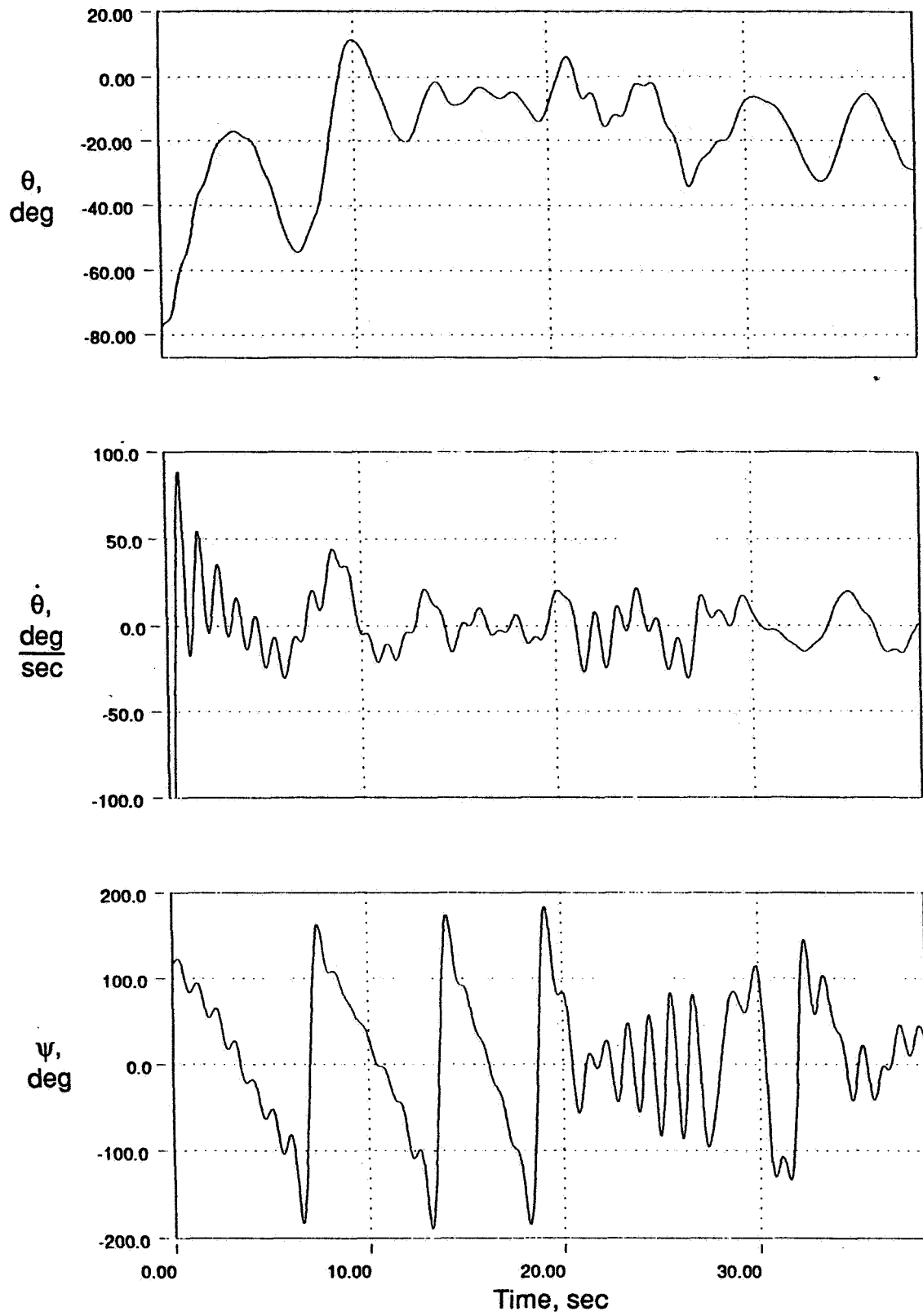


Figure 97. HIKR Departure Drop Test Results

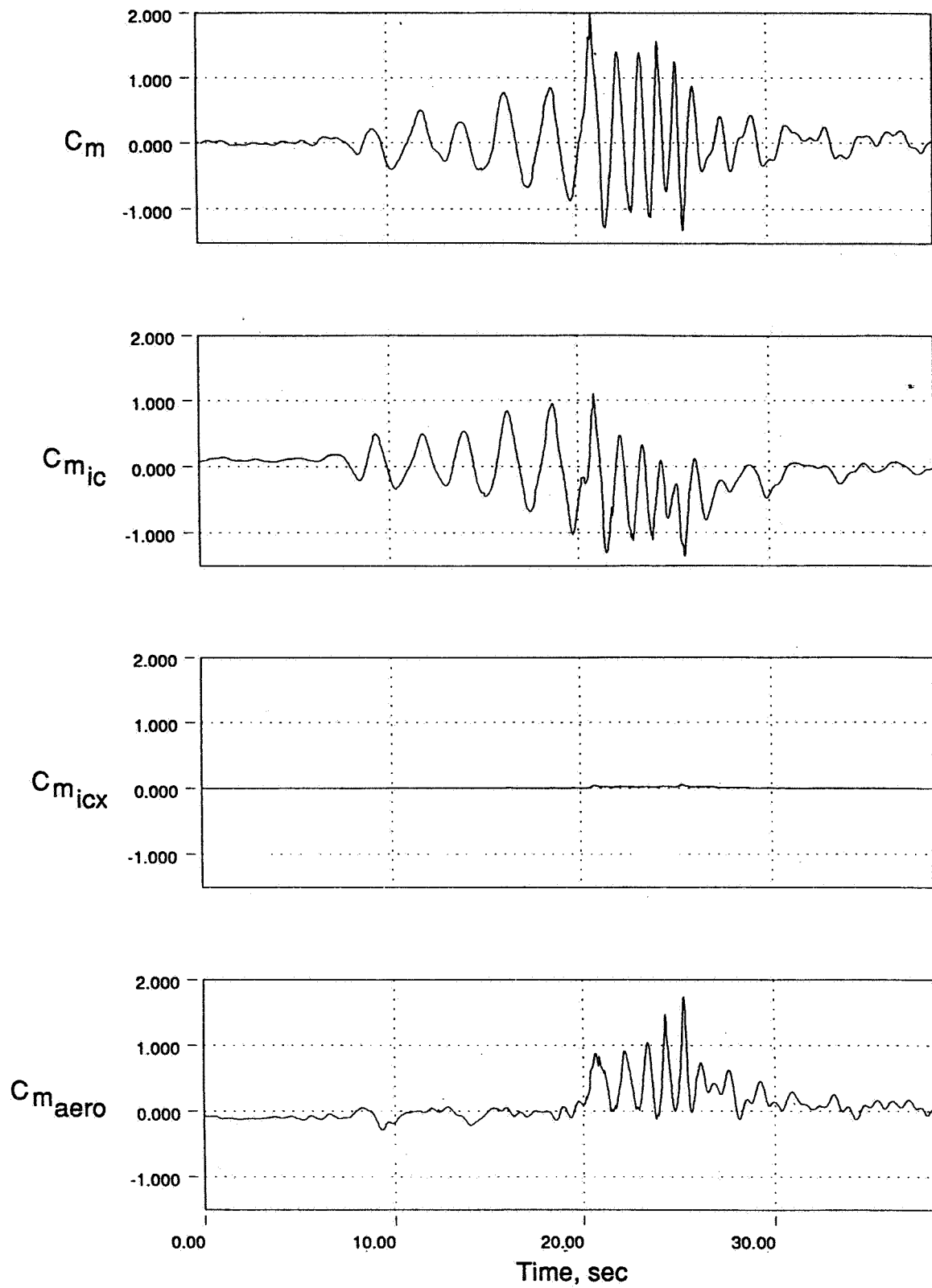


Figure 98. HIKR Departure Drop Test Results

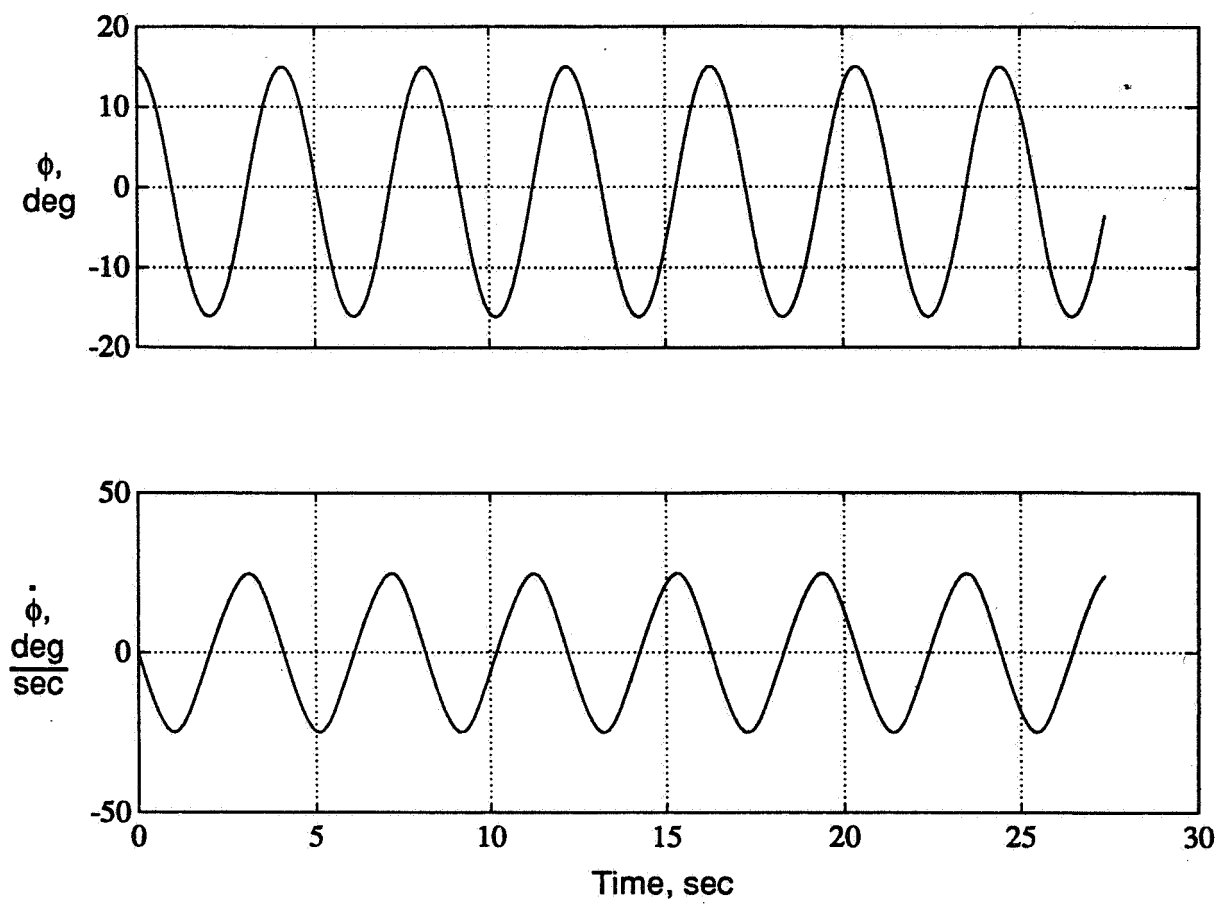


Figure 99. Nonlinear Simulation Results for $\theta_{\text{sting}} = 28^\circ$

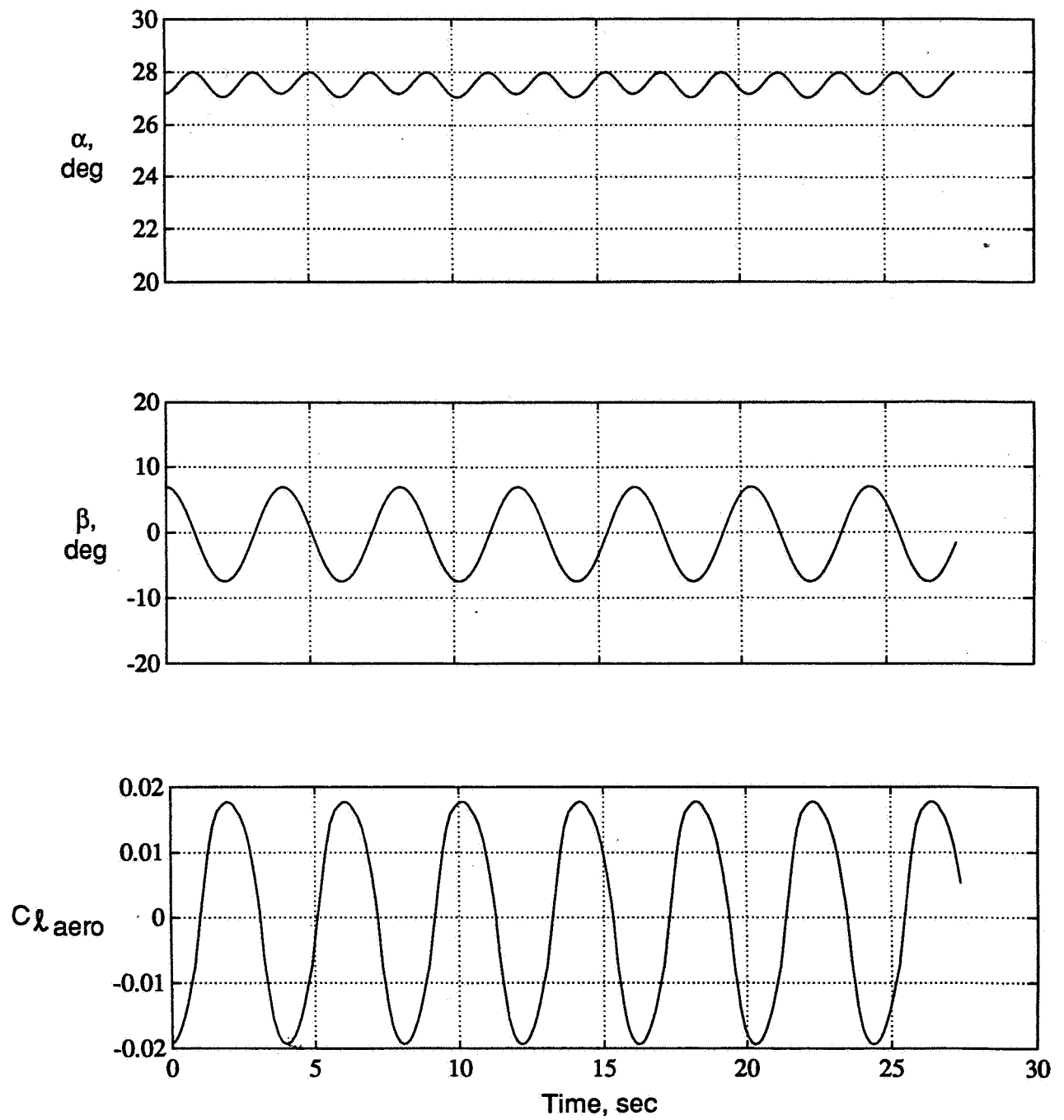


Figure 100. Nonlinear Simulation Results for $\theta_{sting} = 28^\circ$

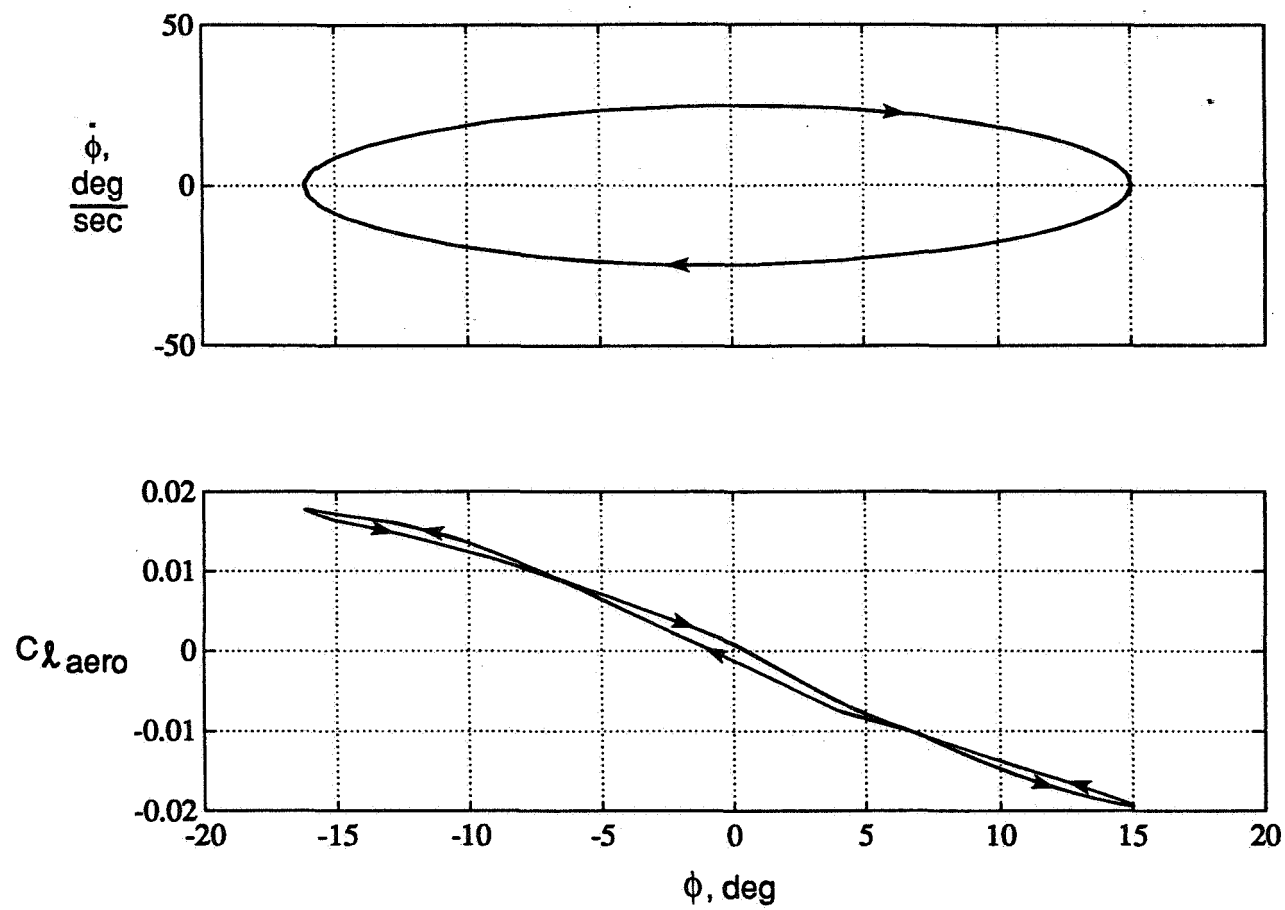


Figure 101. Nonlinear Simulation Results for $\theta_{sting} = 28^\circ$

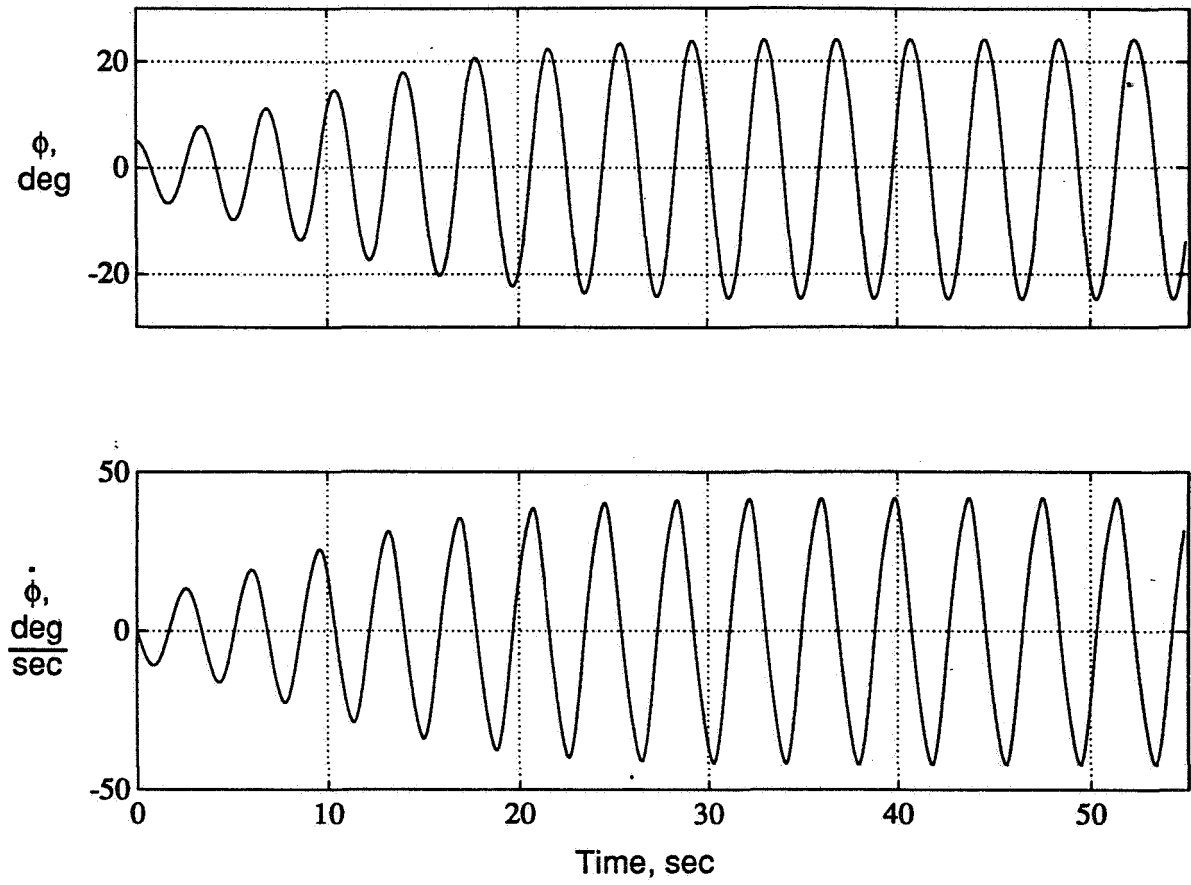


Figure 102. Nonlinear Simulation Results for $\theta_{\text{sting}} = 30^\circ$

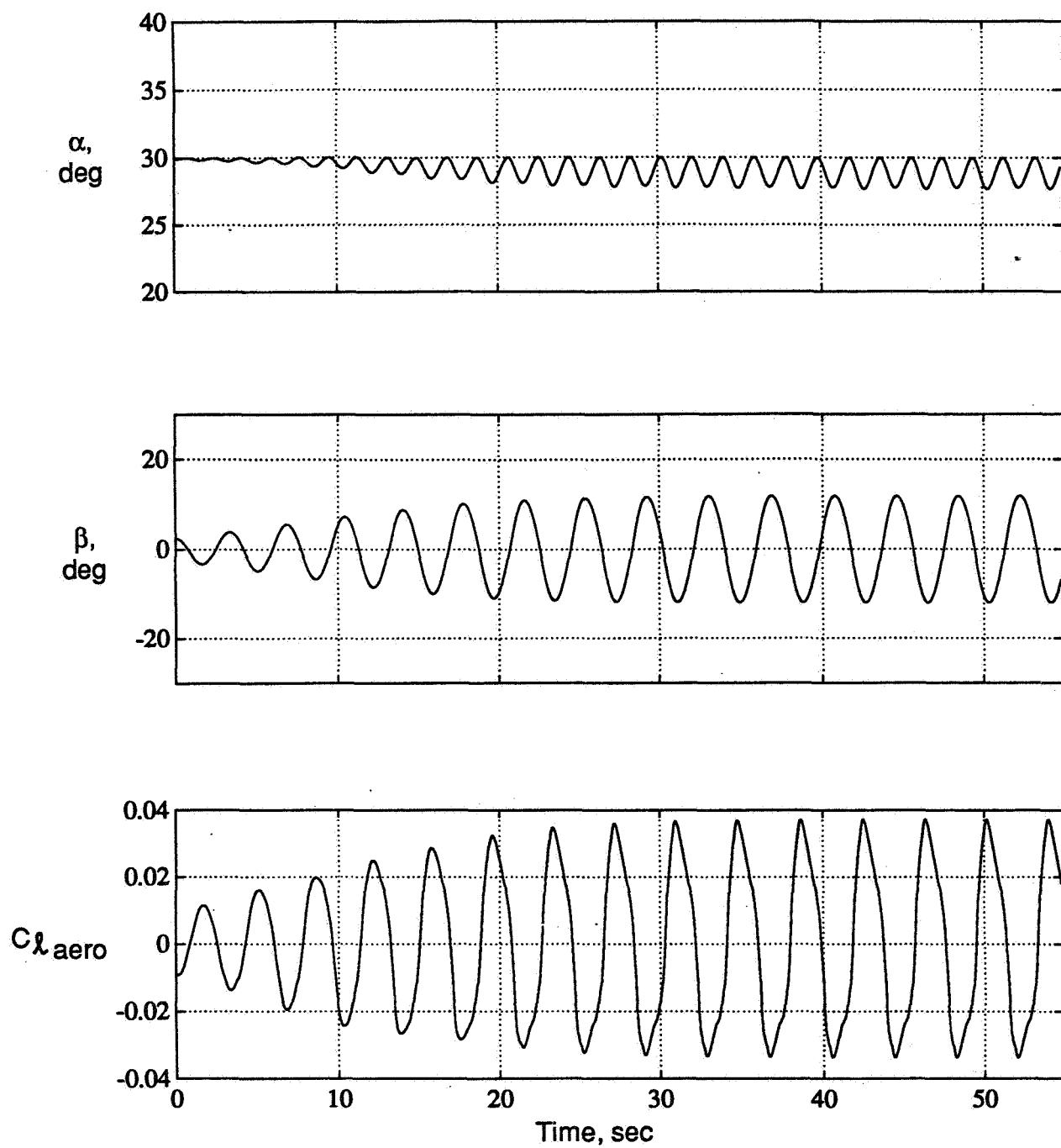


Figure 103. Nonlinear Simulation Results for $\theta_{sting} = 30^\circ$

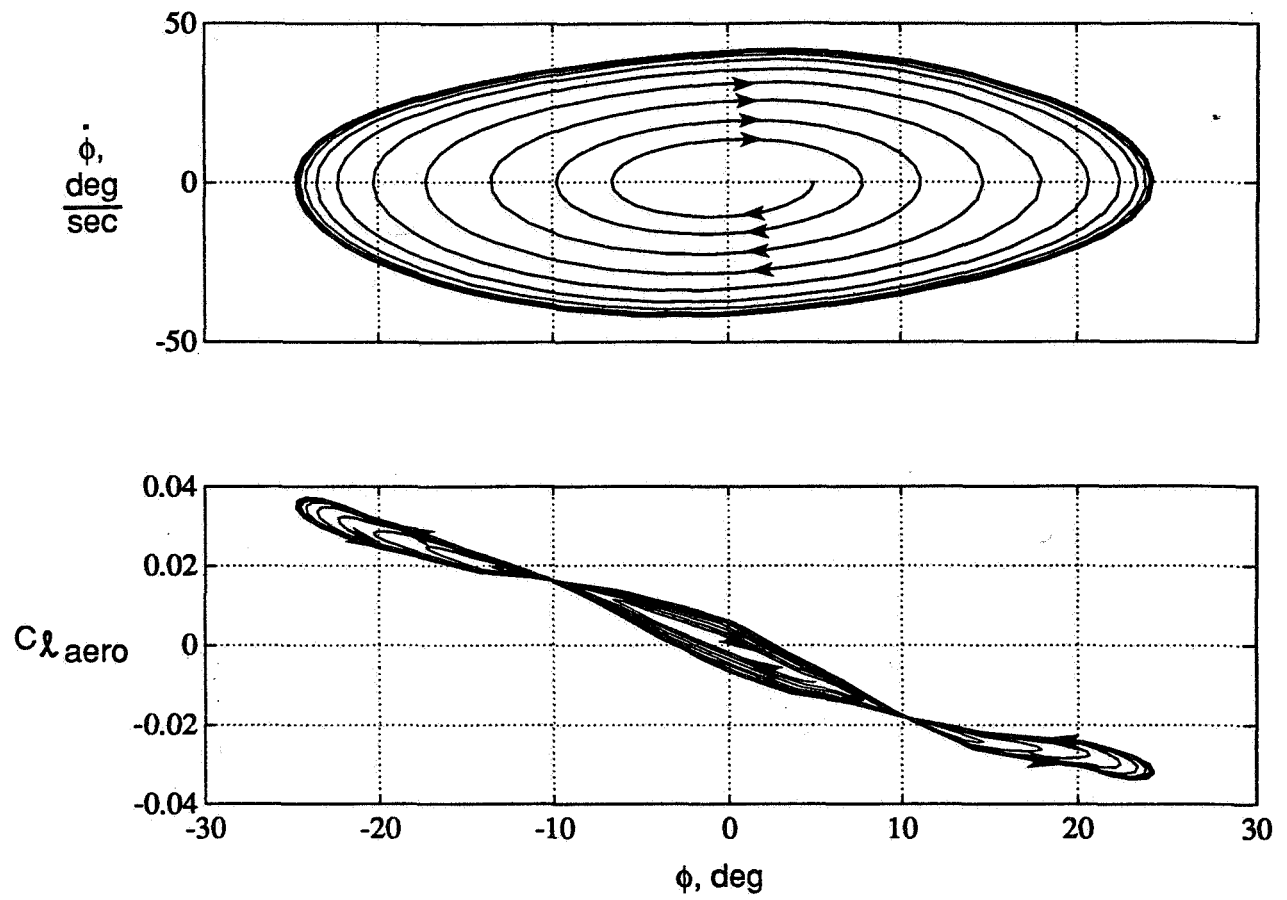


Figure 104. Nonlinear Simulation Results for $\theta_{sting} = 30^\circ$

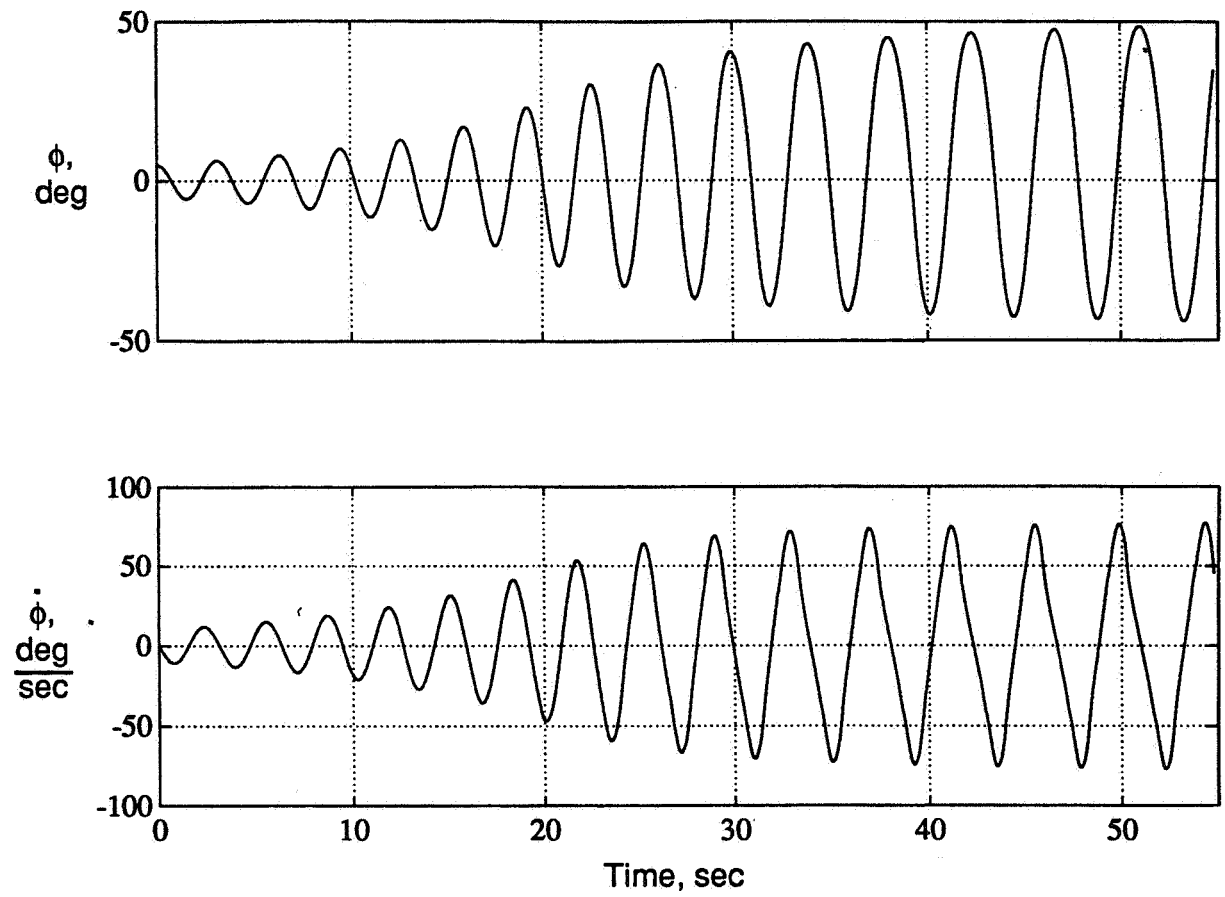


Figure 105. Nonlinear Simulation Results for $\theta_{\text{sting}} = 32^\circ$

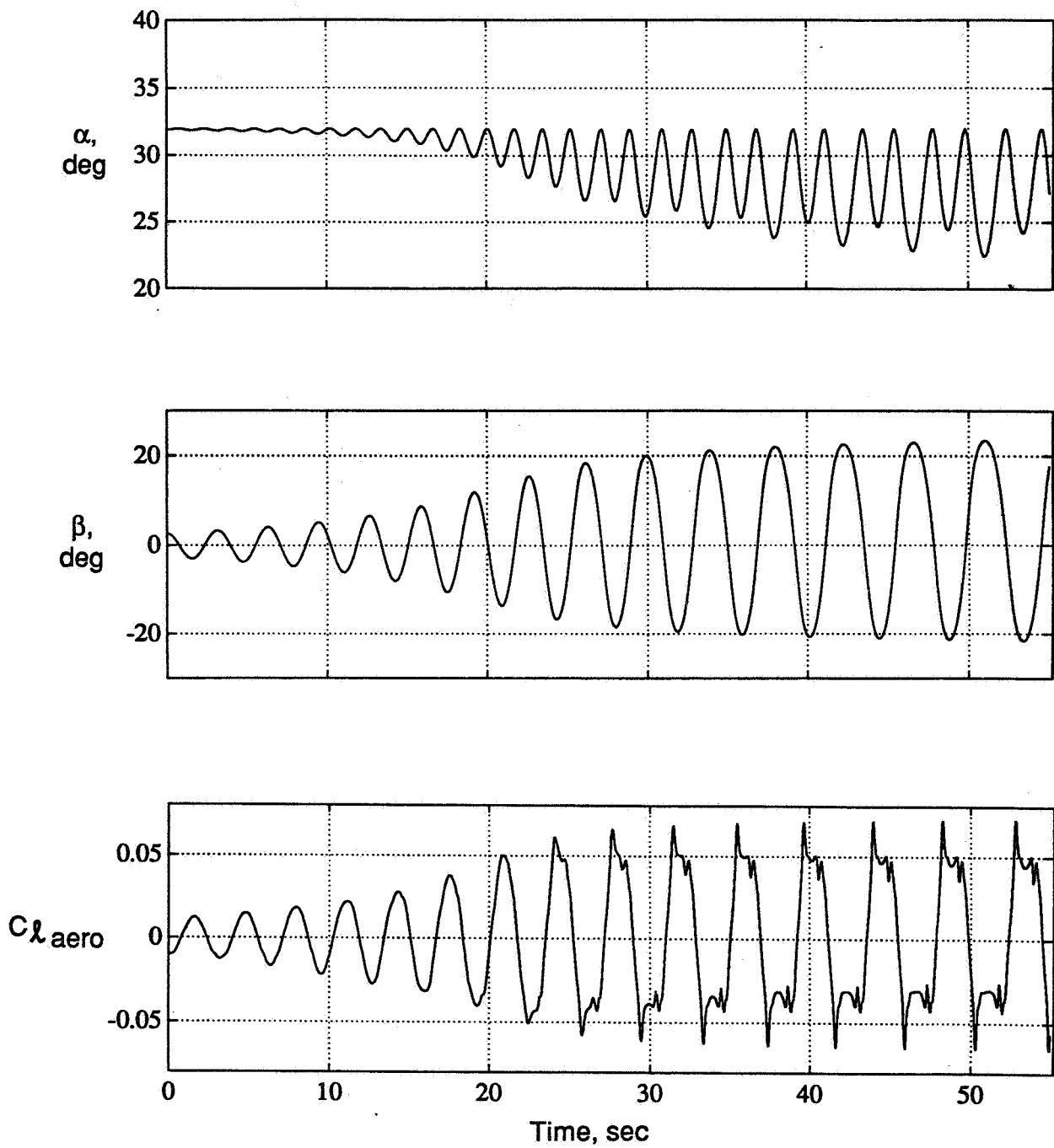


Figure 106. Nonlinear Simulation Results for $\theta_{sting} = 32^\circ$

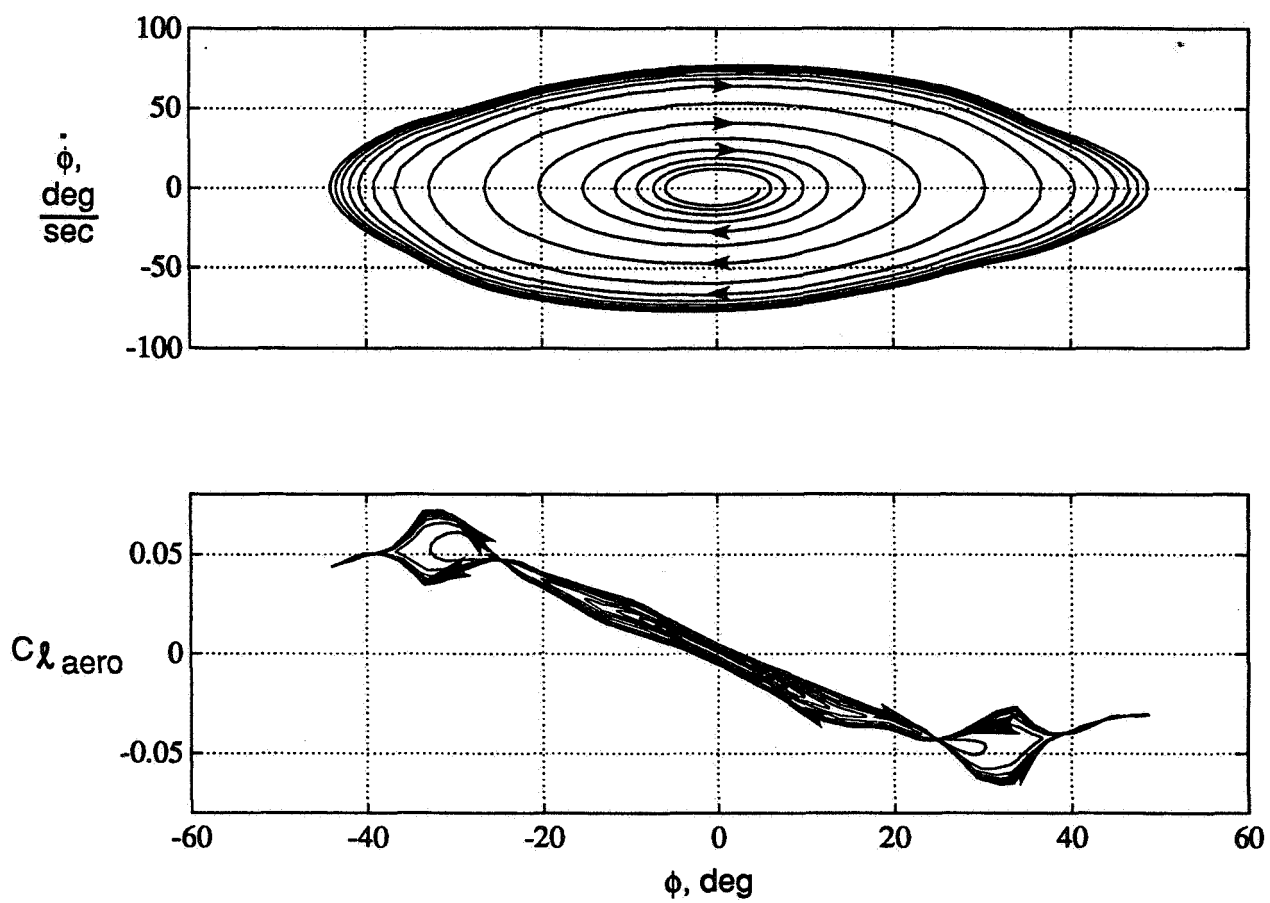


Figure 107. Nonlinear Simulation Results for $\theta_{sting} = 32^\circ$